2014

Monitoring the Integrity of CO2 Storage Sites Using Smart Field Technology

Seyed Alireza Haghighat

Monitoring the Integrity of CO_2 Storage Sites Using Smart Field Technology

Seyed Alireza Haghighat

Dissertation submitted to the
Benjamin M. Statler College of Engineering and Mineral Resources
at West Virginia University
in partial fulfillment of the requirements for the degree of

Doctor of Philosophy
in
Petroleum and Natural Gas Engineering

Shahab. D. Mohaghegh, Ph.D., Chair
Samuel Ameri, M.S., P.E.
Grant Bromhal, Ph.D.
Ebrahim Fathi, Ph.D.
Eduardo A. Proano, M.S., P.E.
Thomas H. Wilson, Ph.D.

Petroleum and Natural Gas Engineering Department

Morgantown, West Virginia
2014

Keywords: CO_2 Leakage; Pressure Down-hole Gauge (PDG); Neural Network; Reservoir Pressure, Smart Well

ABSTRACT

Monitoring the Integrity of CO_2 Storage Sites Using Smart Field Technology

Seyed Alireza Haghighat

Capability of underground carbon dioxide storage to confine and sustain injected CO_2 for a very long time is the main concern for geologic CO_2 sequestration. If a leakage from a geological sink occurs, it is crucial to find the approximate amount and location of the leak in order to implement proper remediation activity.

An overwhelming majority of research and development for storage site monitoring has been concentrated on atmospheric, surface or near surface monitoring of the sequestered CO_2. This study is different it aims to monitor the integrity of CO_2 storage at the reservoir level. This work proposes developing in-situ CO_2 Monitoring and Verification technology based on the implementation of Permanent Down-hole Gauges (PDG) or "Smart Wells" along with Artificial Intelligence and Data Mining (AI&DM). The technology attempts to identify the characteristic of the CO_2 leakage by de-convolving the pressure signals collected at the Smart Well sites.

Citronelle field, a saline reservoir located in Mobile County (Alabama, US) was considered for this study. A reservoir simulation model for CO_2 sequestration in the Citronelle field was developed and history matched. The presence of the PDGs were considered in the reservoir model at the injection well and an observation well. High frequency pressure data from sensors were collected based on different synthetic CO_2 leakage scenarios in the model. Due to complexity of the pressure signal behaviors, a Machine Learning based technique was introduced to build an Intelligent Leakage Detection System (ILDS).

The ILDS was able to detect leakage characteristics in a short time (less than a day) demonstrating high precision in quantifying leakage characteristics subject to complex rate behaviors. The performance of ILDS was examined under different conditions such as multiple well leakages, cap rock leakage, availability of an additional monitoring well, presence of pressure drift and noise in sensor and uncertainty in the reservoir model.

To my beloved wife Neda and my family
Specially my father whose memory was my motivation

ACKNOWLEDGMENTS

I would like to express my appreciation and gratitude to all people supported me during my PhD. study. Special thanks and gratitude is for Dr. Shahab D. Mohaghegh, my supervisor, for involving me in this research. He is a dedicated instructor, supportive supervisor and sincere friend. Working with him will be remembered as a great experience.

Great appreciation also goes to my committee members Mr. Ameri, Dr. Bromhal, Dr. Fathi and Dr. Wilson for their interest in this work and useful suggestions and comments that improved the quality of this dissertation. Special thanks to Mr. Eduardo Proano who traveled two times to Morgantown to join in my candidacy and final defense.

I also would like to appreciate my teammates in Petroleum Engineering and Analytics Research Lab(PEARL), especially Vida Gholami and Alireza Shahkarami for providing friendly and professional atmosphere in the office. Moreover, their hints, ideas and support helped me a lot to overcome some obstacles throughout this work.

I want to acknowledge Intelligent Solutions Inc. (ISI) for providing data mining software packages which acted as the core of this study. Likewise, I wish to express my thanks to Advanced Resources International (ARI) and specifically Mr. George Koperna for providing the field data and US Department of Energy for supporting this project at WVU.

Finally my heartfelt gratitude is for my mother for her unconditional affection and support in my life, my father whose memory will remain in my heart forever and my sister for her encouragements and cheers. My greatest and deepest appreciation goes to my beloved wife Neda for her eternal love, support, patience, companionship and understanding during my graduate study.

NOMENCLATURE

a = Tortuosity factor (1; default value)

A= Area of reservoir (acre)

c = Compressibility factor (1/psi)

c_{br} = Brine Compressibility factor (1/psi)

d_k = Desired values at neuron k

g = Acceleration of gravity (m/s^2)

h = Formation thickness (ft)

i,j = Indices

K= Permeability (md)

$K1$=First order Bessel function

K_0= Zero order Bessel function

Kh= horizontal permeability (md)

Kv=vertical permeability (md)

K_{rg} = Gas relative permeability

K_{rw} = Water relative permeability

m = Cementation factor

n = Saturation exponent

Nl = Noise level

P= Pressure (psi)

P_b = Bubble point pressure (psi)

P^0 = Reference pressure(psi)

q = Flow rate (m^3/s, ft^3/day)

r = Radius (m)

$r_{p=}$ Radius of pore pores (cm)

$r_{t=}$ Radius of pore throats (cm)

Rs = Solution gas ration (ft^3/bbl)

Rw = resistivity of the formation water (ohm.m)

Rt = True formation resistivity (ohm.m)

s= Laplace transform

S = saturation (Fraction, dimensionless)

S_{CO_2} = Saturation of CO_2 (Fraction, dimensionless)

T = Transmissibility (m3)

T = Temperature (◦F)

V= Threshold value for activation function

V = bulk volume (reservoir m^3)

Vsi= Shale concentration in layer I (Fraction, dimensionless)

V_{CO_2} = Theoretical maximum storage capacity (reservoir m^3 of CO_2)

x_i = Neural network input

X= Leakage coordinate (ft)

y_i = Neural network output

w_i = Neural network connection weight

Zi= Thickness of layer i (ft)

α = Neural network learning rate

φ = Rock porosity(Dimensionless)

ρ= Leak monitor distance (m)

ρ_{br} = Brine density @ reference pressure (lb/ft^3)

ρ^o_{br} = Brine density (lb/ft^3)

ρ_{CO_2} = density of CO_2 at storage conditions(lb/ft^3)

ρ_o = Oil density (lb/ft^3)

ρ_w= Water density (lb/ft^3)

δ =Neural network error gradient

μ = Viscosity

η = Diffusivity (m^2/s)

γ = Interfacial tension (dyn/cm)

γ_g = Gas specific gravity

γ_o = Oil specific gravity

TABLE OF CONTENTS

LIST OF FIGURES

LIST OF TABLES

LIST OF ACRONYMS

Acronym	Definition
AI	Artificial Intelligence
ANN	Artificial Neural Network
AOI	Area of Interest
CCS	Carbon Capture and Storage
CLR	CO_2 Leakage Risk
CMG	Computer Modeling Group
DM	Data Mining
EM	Electro Magnetic
EOR	Enhanced Oil Recovery
GA	Genetic Algorithm
GM	Gas Migration
GRNN	Generalized Regression Neural Network
ILDS	Intelligent Leakage Detection System
KPI	Key Performance Indicator
LDL	Leak Detection Log
LGR	Local Grid Refinement
OOIP	Original Oil In Place
PDG	Pressure Down-hole Gauge
PSD	Pressure Sensor Drift
R-ILDS	Real-time Intelligent Leakage Detection System
SCVF	Surface Casing Vent Flow
SCP	Sustained Casing Pressure
SGR	Shale Gouge Ratio
SP	Spontaneous Potential
SRM	Surrogate Reservoir model
TDM	Top Down Model

Chapter 1 INTRODUCTION

Geological sequestration of carbon dioxide is one of the most prominent technologies developing to reduce the emission of CO_2 and mitigate greenhouse effects. Known as CCS (Carbon Capture and Storage), this technology captures the CO_2 from production sources such as coal or gas fired power plants and transfers it to a sink or storage site (geologic unit). Hydrocarbon reservoirs, deep saline aquifer and coal bed formations are different types of geological CO_2 storages. The last step of the CCS is injection of the CO_2, preferably in supercritical phase into the underground CO_2 storage. It is important to verify that the stored CO_2 remains in the underground storage for a very long time period.

1.1 Description of problem

It is possible that the sequestered CO_2 leaks back into the atmosphere through some leakage paths and negates the benefits of geologic CO_2 sequestration. The leakage can also have harmful ecological effects such as risks for human health and global warming. For the long term CO_2 storage, it is necessary for the target reservoir to be sealed by the impervious cap rock. Under unfavorable conditions, the integrity of the cap rock can be damaged by the improperly cemented wells, unsealed faults, high permeable regions and fractures. To assure the cap rock's integrity, CO_2 storage sites must have active monitoring systems to detect CO_2 leakage and be prepared to take remedial action in the event that leakage occurs. This needs adequate knowledge of the leakage and its behavior to determine appropriate monitoring systems.

There are several monitoring techniques that can be implemented on the geological storages based on the site infra-structure, CO_2 injection program and duration of project. With each monitoring system, a specific parameter is being measured continuously or periodically in order to indicate the possible leakage. Usually these parameters are formation or reservoir pressure, formation temperature, resistivity, seismic velocity, multi frequency EM data and CO_2 concentration.

In the past 2 decades, Smart Fields has gained advancements and practicality in petroleum industry. Permanent Down-hole Gauges and valves have been used for continuous monitoring of pressure, flow rates and automatic flow controls. This technology can be used in the underground CO_2 reservoirs to monitor the pressure in real time. The reservoir pressure data provides valuable information in order to history match and update the reservoir simulation model. More importantly, by analyzing the reservoir pressure behavior there is a possibility to determine the location and rate of the leakage.

1.2 Research Objectives

The objective is to use real-time pressure data from Permanent Down-hole Gauges (PDGs) for estimation of the location and the rate of CO_2 leakage to ensure that 99 percent of the injected CO_2 remains in the injection zone. During this project the aim is to model and demonstrate the application of this technology to a real CO_2 sequestration project such as one of the Regional Carbon Sequestration Partnership Projects (Citronelle).

PDGs monitor the pressure changes in the formation and transmit high frequency data streams to the surface. The pressure changes in the reservoir are indications of fluid flow in the formation which can be caused by leak in the reservoir. The complex and highly convoluted real-time data transmitted by multiple PDGs is cleansed, summarized, processed and modeled using state-of-the-art Artificial Intelligence and Data Mining (AI&DM) technology in order to identify the approximate location and amount of the CO_2 leakage which causes the pressure change in the reservoir. This methodology will be verified and tested over different conditions and uncertainties.

1.3 Review of Chapters

This dissertation consists of six chapters. In chapter 1, the overall problem is briefly discussed with the solution method, goals and objectives. Chapter 2 contains the literature review which introduces Carbon Capture and Storage (CCS) with an emphasis of geological saline aquifers. Additionally, CO_2 leakage from underground storages is reviewed through explanations about CO_2 leakage conduits and relevant monitoring techniques for storage sites and is followed by describing Smart Well technology which

can be considered as a practical tool for CO_2 storage site monitoring. At the end of Chapter 2, neural networks and their applications in different areas are explained.

Chapter 3 explains all the steps for building reservoir simulation model for CO_2 injection in a saline aquifer at Citronelle field. Initially, geology of the storage formation is discussed including the procedure for preparation of geological model; following this, reservoir simulation model is described with the prediction for reservoir pressure and CO_2 plume extensions. The last part of this chapter discusses sensitivity analysis of reservoir simulation results subject to some uncertain reservoir parameters.

In Chapter 4, presence of the actual field measurements (injection and pressure data) is considered in the reservoir simulation model. Based on availability of real field data, all the steps for matching reservoir simulation results with actual measurements are described. After that, the reservoir model is validated with three months of data that was not used during history matching process.

The development process of Intelligent Leakage Detection System (ILDS) is the main subject of Chapter 5. This process is initially applied to a simple and homogenous reservoir simulation model which predicts reservoir pressure subject to different synthetic leakage scenarios. Then, data summarization method for handling high frequency data and its conversion to the appropriate format for pattern recognition technology is explained. The final part of this chapter talks about neural network training procedure with results and discussions. The same procedure is repeated for the complex, history matched and heterogeneous reservoir simulation model.

Chapter 6 discusses enhancements and complementary studies for ILDS. At the beginning, the procedure of building R-ILDS which can detect leakage characteristics in real time is explained. After that leakage detection time is determined for different leakage locations and rates and R-ILDS is tested for multiple geological realizations. Then, capability of R-ILDS for detection of leakage at different vertical locations along the wells is investigated. The other important studies in this chapter relate to effect of pressure drift on the R-ILDS results and the possibility of using well-head pressure rather than PDG for leakage detection. R-ILDS also improves with capability of detecting variable rates, multi-wells and cap-rock leakages. Presence of PDG in the injection well is considered to test if R-

ILDS can detect leakages accurately. Finally, two methods for removing noise and outliers from high frequency pressure data are explained.

Chapter 2 Literature Review

2.1 Carbon Capture and Storage

It has been documented that the biggest source of the global CO_2 emissions is the combustion of fossil fuels. This emission is one of the main causes of climate change with serious impacts on a variety of issues such as weather pattern, health, wild life and the rise in the sea level. It seems to be widely accepted that a comprehensive switch from fossil fuels to green fuels will take several decades to be completed; other CO_2 emission mitigation options like CCS (Carbon Capture and Storage) must be implemented. Geologic sequestration of carbon dioxide has been identified as one of the most viable options for long term carbon storage.

2-1-1 Global Impact of CO_2 Emission

Growing trend in greenhouse gases and especially CO_2 concentration, about 72% of greenhouse gases consists of CO_2, in the atmosphere has been causing global warming and consequently severe changes in the climate. Global average temperature which showed an approximate increase of 1.4 ^{0}F in 20th century can be considered as the main indicator for global climate change. Global temperature changes have been almost proportional to the CO_2 concentration in the atmosphere which increased from 280 ppm in year 1880 to 385 ppm in year 2010(Figure 2-1).

Three different technological options have been proposed in order to mitigate global CO_2 emissions. The first option considers energy consumption reduction by enhancing energy conversion and utilization efficiency. In the second option, high-carbon fuels (e.g. coal) are replaced with low-carbon fuels such that renewable and nuclear energy. Final option deliberates capture and sequestration of some portion of emitted CO_2 from fossil fuels.

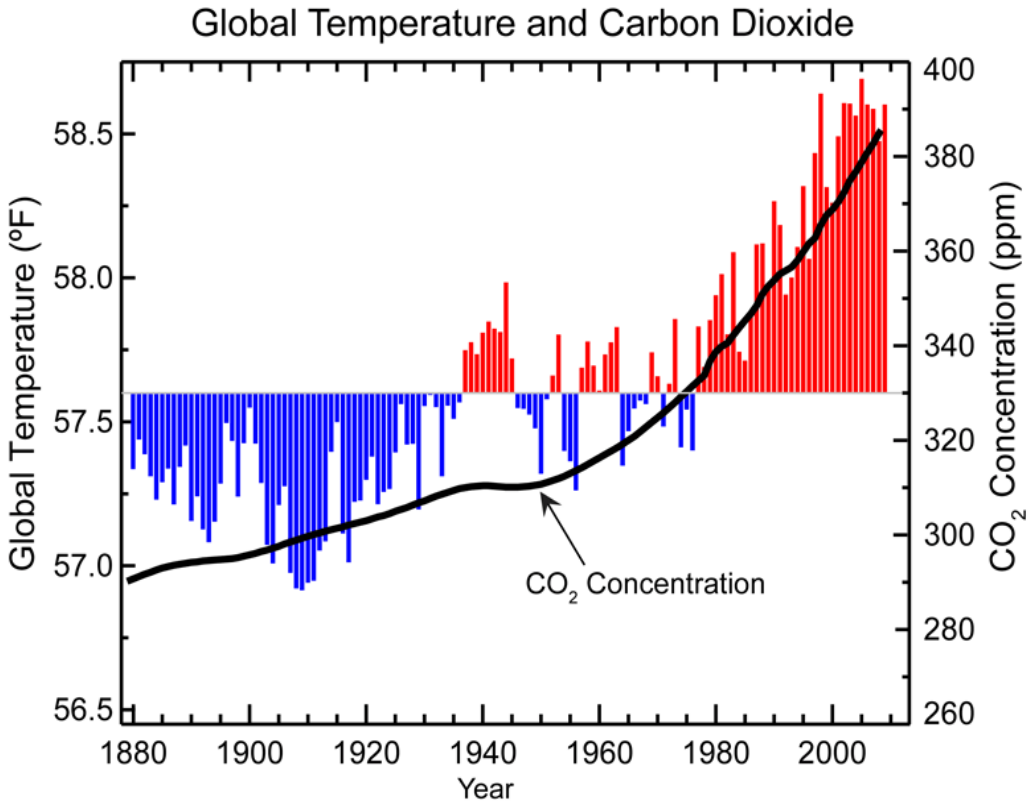

Figure 2-1: Global temperature and CO_2 concentration history [1]

2-1-2 Carbon Capture and Storage (CCS)

It seems to be widely accepted that a comprehensive switch from fossil fuels to green fuels will take several decades to be completed; other CO_2 emission mitigation options like CCS (Carbon Capture and Storage) must be implemented.

CCS can be considered as a bridging technology while a transition from fossil fuels to more environmentally ones is taking place [2]. Generally CCS process is described as separating CO_2 at industrial level(power plants, refineries, cement plans and steel mills),transporting to target storage sinks, and finally injecting mainly into the underground formations(research for storing CO_2 deeply in the oceans is under way - [2]).

There are different potential sites for geological CO_2 sequestration as: depleted oil and gas reservoirs, deep saline aquifers, deep un-mineable coal seams and storage in association with CO_2/EOR.

Few commercial CCS projects are operational currently due to lack of business and economical justifications excluding CO_2 /EOR projects. Because stored CO_2 lacks any commercial value, commencement of CCS for companies does not make profitable sense. Due to the industry's efforts, large-scale CCS projects are operational; assembling new legal and regulatory frameworks to provide commercial reasoning for CCS deployment is necessary.

Every CCS project consists of four different transitional phases [2]. "Site Selection and Development," the first phase, covers geological, commercial and regulatory evaluation which takes approximately from 3 to 10 years to purchase and secure space for surface facilities and geological storage. In addition, permission acquirement and infrastructure construction are completed in this phase. The "Operation" phase follows and includes CO_2 injection and further technical site monitoring. Depending on storage capacity and operational designs, this phase may take decades. After "Operation," the "Closure" phase begins with implementation of different monitoring systems to assure no risk is associated with the stored CO_2. During "Closure," injection wells should be plugged following the removal of unnecessary infrastructures. Finally, the "Post-closure" phase is conducted with no involvement with the operator as some occasional observational or monitoring activities may be applied in this phase [2](Figure 2-2).

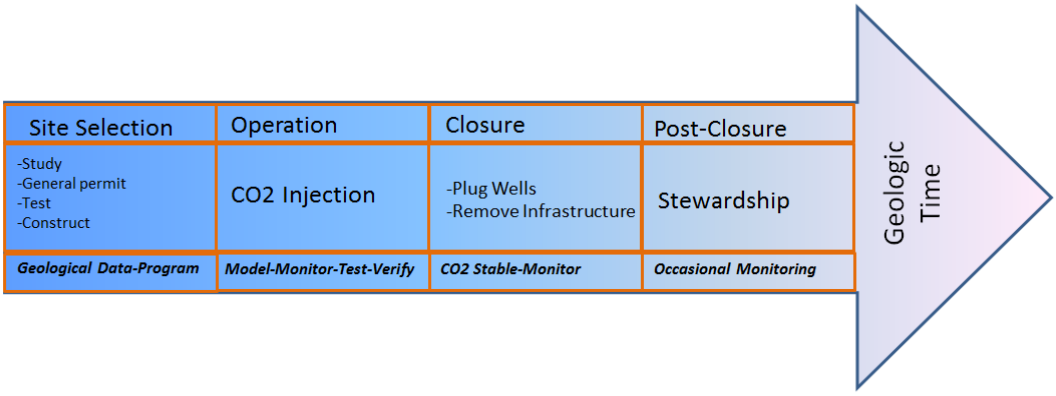

Figure 2-2: Phase of CCS projects [2]

To introduce the site selection phase, three fundamental characteristics of CO_2 storage sites are reviewed. The storage capacity indicates how much pore volume would be available in the reservoir for CO_2 to be stored in. The required depth for target underground geological

formations is more than 800 meters to 1000 meters at which CO_2 represents the supercritical phase behavior. Generally, storage capacity can be determined through Original Oil/Gas in Place-OOIP calculations by knowing area of site, formation thickness, rock porosity, density of CO_2 at storage conditions, storage efficiency (maximum CO_2 saturation) and rock/brine compressibility factor. Depending if the formation type is composed of carbonate or clastic rock, favorable minimum porosity values for CO_2 storage sites vary between the values of 10% and 15%. Additionally, the minimum required formation thickness for storage sites is twenty meters. Another storage characteristic for a favorable CO_2 storage site is the continuous sealing system that closes the reservoir to prevent fluid flow in the upward direction. Prior to the injection, the integrity of the seal should be verified to assure secure storage containment. "Injectivity," which represents rock/fluid capability for CO_2 flow in the reservoir, is another storage site characteristic. The ideal permeability values for CO_2 storage sites are more than 100 mD. However, very high permeability formations may provide conductive pathways causing rapid enhancement of CO_2 in specific areas results in effective storage reduction [2].

2-1-3 Geological Saline Aquifers

Geological formations composed of deep sedimentary rocks which are saturated with water and brine containing a considerable amount of salt concentration are known as saline aquifers. While it is not economically or conventionally viable to use high salinity brines for practices such as drinking or irrigation, deep saline aquifers have been used for low-power geothermal energy generation as well as injection of chemical waste, drilling slurries, and radioactive waste [3].

Supporting evidence suggests deep saline aquifers have enough volumetric capacities to sequester enormous amounts of CO_2. Despite of the limited locations for oil and gas reservoirs, deep saline formations are widely spread geographically, providing more available options to store CO_2 from emission sources. Based on Yamasaki study [4], storage capacity of saline aquifers is much more than the capacity found in oil/gas fields and un-minable coal beds (Table 2-1). The retention time for CO_2 stored into saline aquifers is estimated to support up to thousands of years, representing the most viable storage option amongst the other geological formations. Reservoir characterization is a

concern for saline aquifer storages as it drastically lacks available information in comparison with depleted oil and gas reservoirs.

Table 2-1:CO_2 Storage Capacity [4]

Options	Capacity[Gt-C]
Depleted Oil Field	120
Depleted Gas Fields	188
Un-minable Coal Beds	11
Saline Aquifers	109-2727
Oceans	1400-20000

2-1-3-1 Storage Capacity

Storage capacity calculations require estimations of total affected space which represents the whole region that is affected due to CO_2 injection. The void space that is required to store the injected CO_2 is created by compressing the whole formation, including rock and fluids composed of CO_2 and brine, by increasing the reservoir pressure. Ultimate storage capacity is also determined by the maximum average reservoir pressure allowed which varies upon regulations (i.e., 10 bars or 10% of the initial reservoir pressure). Assuming rock/brine compressibility effects and maximum allowable average pressure in a multi-layer reservoir the maximum storage capacity can be calculated by the following formula [5]:

$$V_{CO2}=\sum_{l=1}^{L}\sum_{i=1}^{I} V_l \emptyset_l S_i^l (C_l + C_i)\Delta\overline{P}_l$$

V_{CO2} = theoretical maximum storage capacity [reservoir m3 of CO_2]

V = bulk volume [reservoir m3]

$\emptyset$ = porosity [fraction]

S = saturation [fraction]

C = compressibility [1/Pa]

ΔP = average pressure difference p − p0 [Pa]

Considering above equation, to predict the storage capacity it is necessary to obtain reasonable values for affected space or reservoir boundary, compressibility, and maximum allowable pressure. Typically, three types of pressure increase during CO_2 injection are as local (bottom hole pressure), regional (reservoir pressure), and total (affected space pressure). Due to estimating techniques proposed from establishments such as the Carbon Sequestration Leadership Forum (CSLF) and the United States Department of Energy, it is important to note there is a variation of methods which may be used to calculate storage capacities in CBM, oil/gas reservoir, and saline aquifers [6].

The storage efficiency factor is another parameter in storage capacity calculations and can be determined similar to an Original Oil in Place calculation. The "available space" which is covered by sealing the cap-rock includes total pore space for CO_2 storage. A portion of the "available space" is filled by CO_2 after the end of injection, a function of reservoir characteristics, is defined as "used space." The efficiency factor simply represents the "used space" to "available space" ratio (Figure 2-3, [5]).

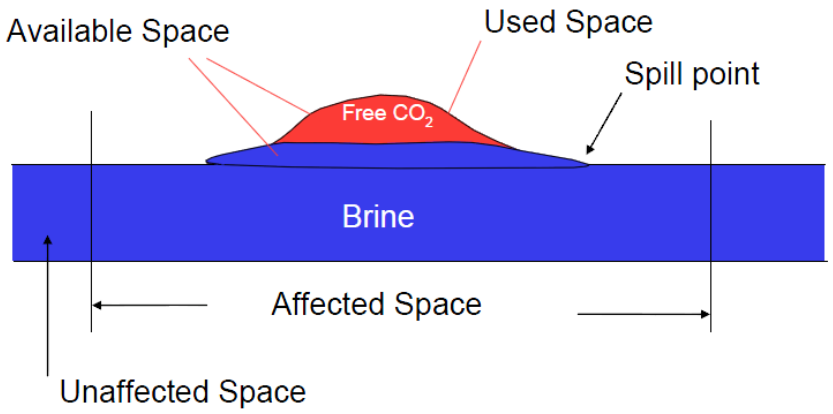

Figure 2-3: Different regions in a saline aquifer after CO_2 injection [5]

2-1-3-2: Saline Aquifer Distribution

Various studies proposed several sedimentary regions all around the world which are suitable for CO_2 storage (Figure 2-4). Sediments that are located in the mid-continent or close to the edge of continental plates are considered to be suitable for CO_2 storage due to

stability and structure. Basins that are located behind mountains (formed by plate collision) like Appalachian, Andean, Rocky Mountain in US, Alps and Carpathians in Europe and Zagros, Himalayas in Asia are good potentials for storage [7]. Plate edges are not ideal locations for the basins due to the subduction occurring between active mountains which creates highly folded/faulted regions and includes paths for leakage. Other important characteristics to determine good reservoir options for storage consist of depth, temperature gradient (colder basins are more suitable for storage), reservoir pressure, porosity, thickness, and reservoir dip.

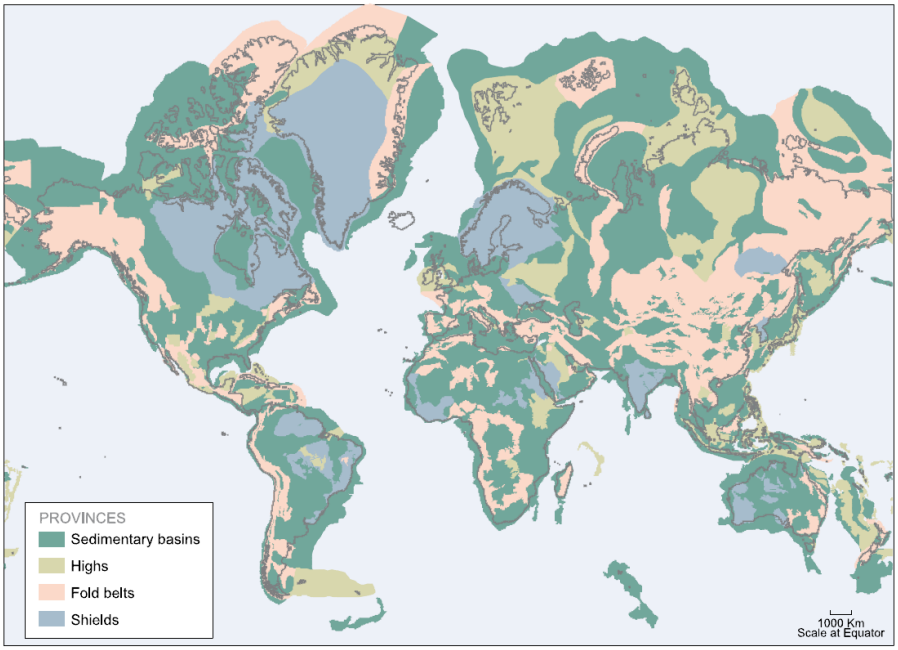

Figure 2-4 : Sedimentary basin distribution suitable for CO_2 storage [7]

As mentioned in section 2-1-3, saline aquifers provide very large volumes for CO_2 sequestration. Based on the source (coal-fired power plants)-sink (saline aquifer) distribution atlas in the United States, it is estimated [8] that more than 95% of the main CO_2 sources in US are in proximity of 80 km from a potential underground storage. In Figure 2-5 estimates [9] for saline aquifer storage capacities in the United States are shown for each state/province. The national total storage capacity for saline aquifers reported to range from 1,820 to more than 22,260 million Tons (low and high estimates). Texas,

Louisiana, Montana, Wyoming, Mississippi, New Mexico, Colorado, California, and Washington represent the largest CO_2 Storage resources.

*CO_2 Storage Resource Estimates for Saline Formations by State/Province**

State/ Province	Million Metric Tons		Million Tons	
	Low Estimate	High Estimate	Low Estimate	High Estimate
Alabama	11,760	161,630	12,963	178,167
Alaska				
Alberta	35,150	39,240	38,746	43,255
Arizona	120	1,580	132	1,742
Arkansas	4,320	59,420	4,762	65,499
British Columbia	1,590	2,120	1,753	2,337
California	30,070	413,490	33,147	455,795
Colorado	30,860	424,330	34,017	467,744
Connecticut	0	0	0	0
Delaware	20	80	22	88
District of Columbia	0	0	0	0
Florida	15,750	216,910	17,361	239,102
Georgia	490	23,200	540	25,574
Hawaii				
Idaho	50	720	55	794
Illinois	8,490	115,330	9,359	127,130
Indiana	14,370	85,440	15,840	94,181
Iowa	10	150	11	165
Kansas	1,190	16,400	1,312	18,078
Kentucky	1,350	9,450	1,488	10,417
Louisiana	149,360	2,053,760	164,641	2,263,883
Maine				
Manitoba	310	310	342	342
Maryland	860	5,050	948	5,567
Massachusetts	0	0	0	0
Michigan	14,620	58,490	16,116	64,474
Minnesota				
Mississippi	45,450	624,940	50,100	688,878
Missouri	20	310	22	342
Montana	120,710	1,653,720	133,060	1,822,914
Nebraska	22,860	76,840	25,199	84,702
Nevada	0	0	0	0

State/ Province	Million Metric Tons		Million Tons	
	Low Estimate	High Estimate	Low Estimate	High Estimate
New Brunswick				
New Hampshire				
New Jersey	0	0	0	0
New Mexico	32,120	441,650	35,406	486,836
New York	1,700	6,820	1,874	7,518
Newfoundland & Labrador				
North Carolina	1,320	18,170	1,455	20,029
North Dakota	103,220	120,070	113,781	132,355
Northwest Territories				
Nova Scotia				
Ohio	3,970	15,900	4,376	17,527
Oklahoma	0	0	0	0
Ontario	10	20	11	22
Oregon	7,080	97,390	7,804	107,354
Pennsylvania	5,900	27,620	7,606	30,446
Quebec	0	0	0	0
Rhode Island	0	0	0	0
Saskatchewan	980	8,820	1,080	9,722
South Carolina	200	9,660	220	10,648
South Dakota	17,390	155,990	19,169	171,950
Tennessee	490	6,650	540	7,330
Texas	333,400	4,584,250	367,511	5,053,271
Utah	20,990	288,680	23,138	318,215
Vermont	0	0	0	0
Virginia	80	390	88	430
Washington	29,930	411,570	32,992	453,678
West Virginia	4,480	17,930	4,938	19,764
Wisconsin	0	0	0	0
Wyoming	87,430	1,202,200	96,375	1,325,199
Offshore	491,080	6,756,360	541,323	7,447,612
TOTAL	1,652,550	20,213,050	1,821,625	22,281,074

* States/Provinces with a "zero" value represent estimates of minimal CO_2 storage resource, while states/provinces with a blank represent areas that have not yet been assessed by the RCSPs.

Figure 2-5: CO_2 storage resource estimates for saline formations in US [9]

2-1-3-3: CO_2 Trapping Mechanisms

Sequestration of CO_2 in the saline aquifer may occur by various types of trapping mechanisms which control the movement of the injected gas in the reservoirs; the trapping mechanisms are hydrodynamic, solubility, residual, and mineral trapping. In hydrodynamic or geologic trapping, the injected CO_2 compresses water/rock and occupies the free pore space of the reservoir rock. Although the compressibility of water is small, large volumes of water and sufficient injection pressure make it possible that gas bubbles form [2]. In solubility trapping, injected gas dissolves in the aquifer based on water salinity, temperature and pressure (Figure 2-6). Notably, complications may arise where CO_2 reacts with water yielding carbonic acids or other carbonates. If the CO_2 causes rich brine to flow, dissolved CO_2 may move in the reservoir. When the brine is completely saturated with CO_2, an increase in the water density occurs; this phenomena leads to natural convectional flow in the reservoir which can enhance diffusion rate of CO_2 in the reservoir brine.

The residual trapping mechanism works as the CO_2 saturation in the reservoir reaches below the minimum gas saturation required initiating the flow of gas, residual gas saturation, and the gas becomes immobile in the pores. Residual gas saturation mainly depends on the end point relative permeability. Although residual CO_2 remains buoyant, it represents no mobility due to capillary forces as it is not connected to mobile CO_2 clusters (Figure 2-7).

The mineral trapping process occurs as dissolved CO_2 reacts with some of the reservoir rock minerals rich in calcium, magnesium, and iron and forms carbonate compounds (Figure 2-7). There is supporting evidence that for most reservoirs the mineral trapping mechanism will have minimal impacts in the first years [2]. Due to the insufficient understanding in the subsurface characteristics, there are noticeable uncertainty in CO_2 reactions and corresponding rates.

Notably, the trapped CO_2 in the hydrodynamic mechanism represents higher potential for leakage due to the mobility of the free CO_2. In solubility, residual, and mineral trapping, the form of geological CO_2 storage is more stable or permanent. The amount of CO_2 trapped by each mechanism at a site will impact site security. The focus in this work is on hydrodynamic-trapped CO_2.

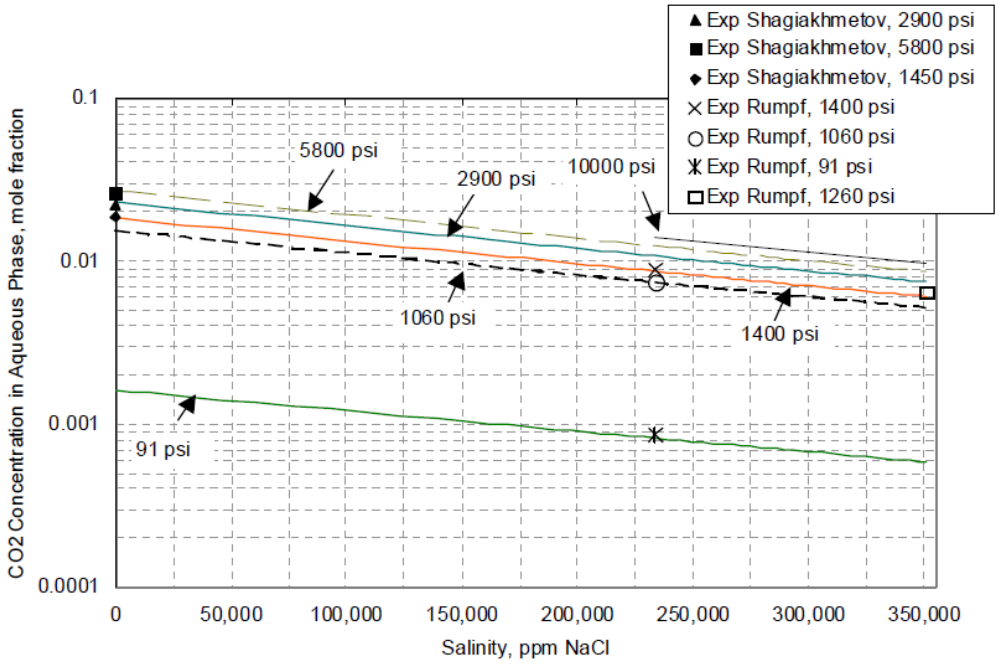

Figure 2-6: Effect of Salinity and pressure on CO_2 solubility in brine [10]

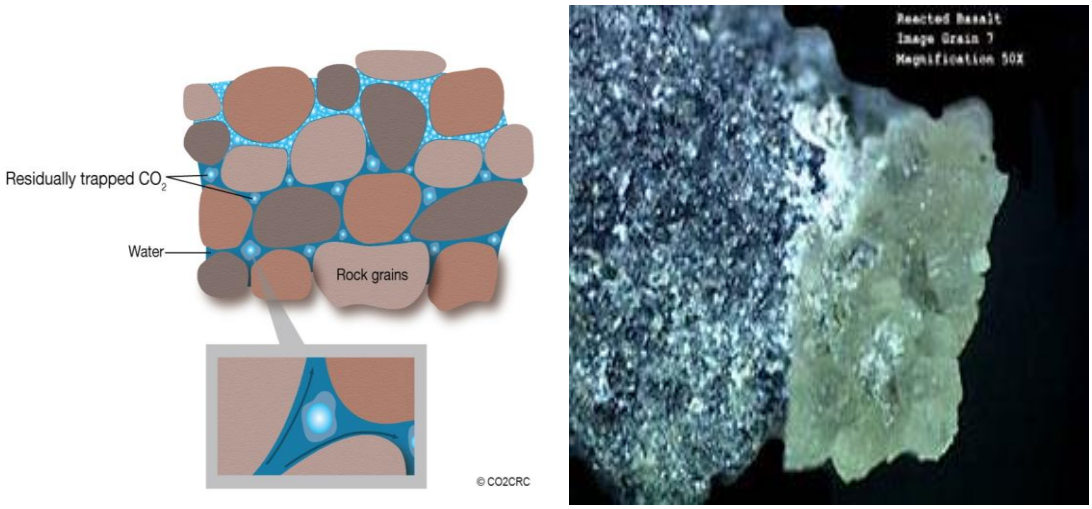

Figure 2-7: left: Schematic of residual trapping [11], right: Metallic ions in basalt and certain other rocks lock CO_2 into stable mineral form [12]

2-1-3-4 Case Studies for CO_2 Storage in Saline Aquifers

In this section some practical CO_2 sequestration in saline aquifer projects will be discussed briefly. These projects are located in Norway and US.

2-1-3-4-1 Sleipner(Norway)

Sleipner is a gas reservoir (divided into Sleipner West and Sleipner East) located in North Sea about 250 km from Stavanger, Norway. The field which is operated by Statoil produces natural gas (1.27 MMcf/day) which contains about 9.5% of CO_2 and condensate. The producing formation is sand stone which is located 2500m (8200ft) below sea level. Due to the sales regulations that enforced operator to limit CO_2 fraction up to maximum 2.5 %, separation units were installed on the offshore platform (Sleipner T treatment platform). Since release of captured CO_2 in the atmosphere was not environmentally allowable, CO_2 sequestration into a saline aquifer (Ustira formation) was planned for this field .This was the first CO_2 storage project in the world. Ustira Formation which is the target zone for storage consists of fine grained and high permeable sand located at 800m below sea level with reservoir thickness that ranges from 150 to 250 m (Figure 2-8). Injection started from 1996 with approximate rate of 0.9 MM ton/year. The cumulative injected CO_2 up to now is 14 MMt(the planned value is 17MMt).4D seismic studies indicated no CO_2 migration from the target layer into the other zones [13].

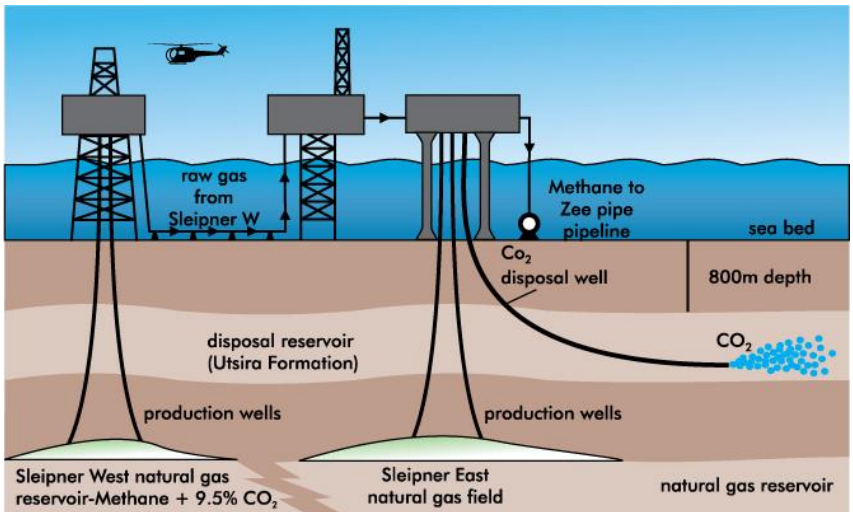

Figure 2-8: CO_2 injection Utsira formation-Sleipner Field [14]

2-1-3-4-2 Snohvit (Norway)

Snohvit gas field is located in the Barnet Sea, developed with no surface installations. In depth of 250-345 meters under the sea level, subsea production facilities were installed. The final production is from 9 wells and transported to land via 143 km pipeline (Figure 2-9). Gas production started from 2007 with average yearly rate of 7Bcf. Associated CO_2(0.7 MMcf/year) was removed on the land and transferred back to the field to be injected in Tubaen sandstone which is 45-75 meters thick and located 2600 meters below the sea level. Injection started since 2008 and planned to reach to 31-40Mt [15].

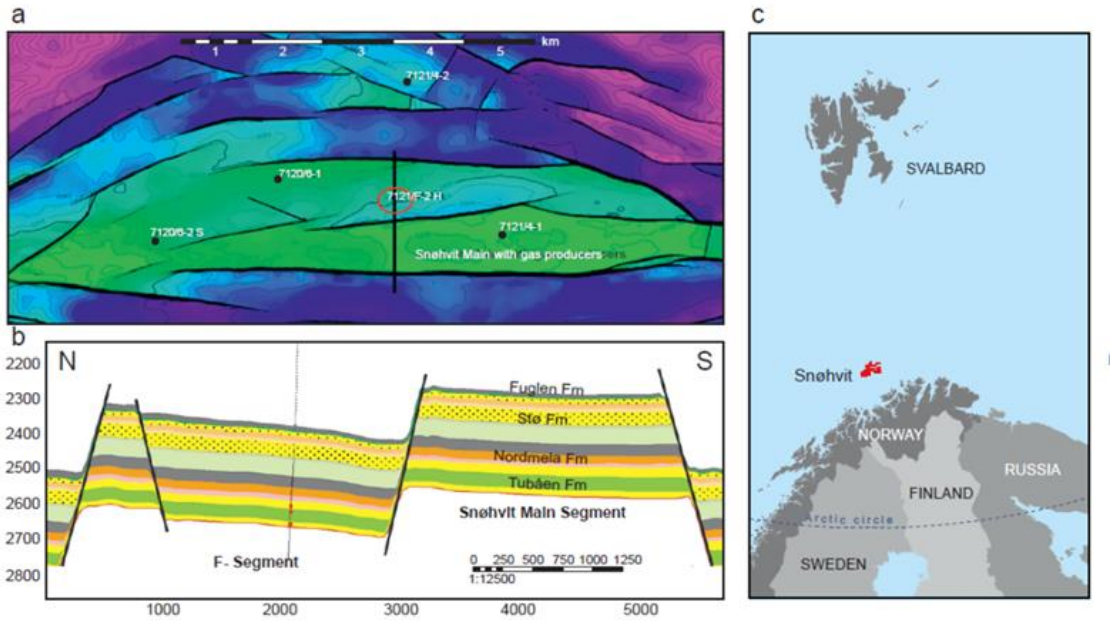

Figure 2-9: Location of the Snohvit fields [15]

2-1-3-4-3 The Mississippi Test Site (US)

The objective of this project is to verify safe geological storage of CO_2 captured from coal-fired power plant in Lower Tuscaloosa Massive Sand Unit which is located in the Gulf Coast region. Initial studies indicated that Tuscaloosa formation may represent favorable capacity to store CO_2. This formation is located at the depth of 8550 ft and appeared to have enough thickness (150-250 ft), porosity (15-33%) and extension (Figure 2-10). Middle Tuscaloosa shale with thickness of about 400ft, provides primary confining unit (seal) for

the target formation. An observation well, located 175 ft from the injection well, was drilled into the same formation before start of injection. In October 2008, about 3020 tons were injected in the reservoir (the planned goal was 3000 tons of CO_2). Reservoir simulation results showed that maximum CO_2 plume extension would be 190ft from the injection well [16].

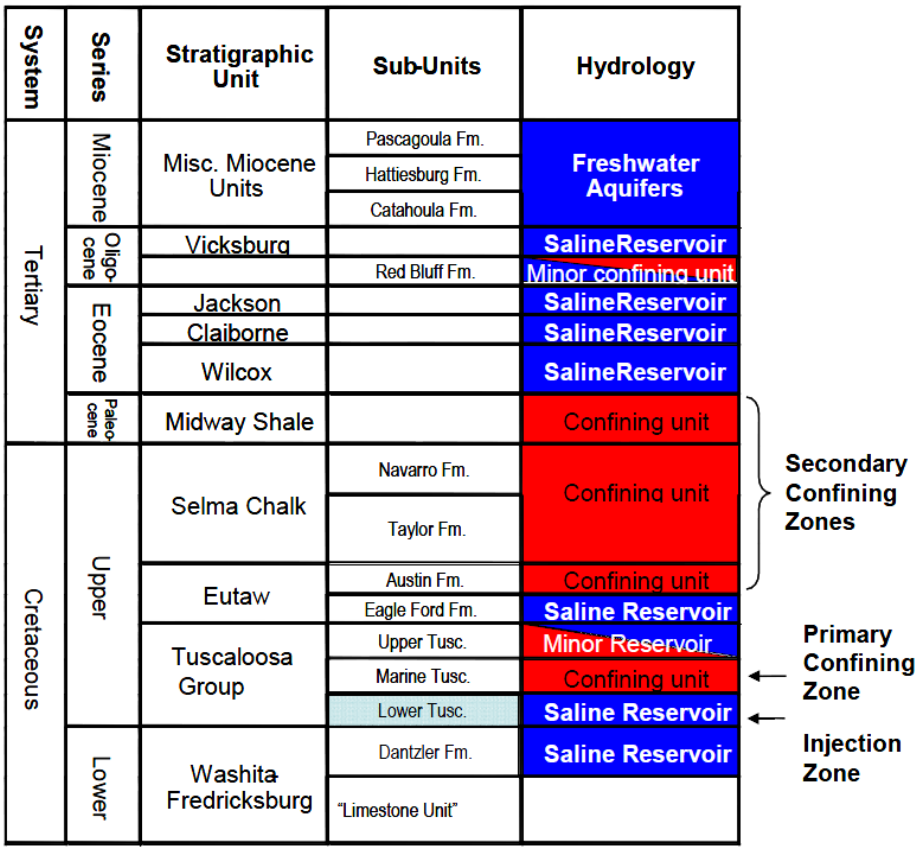

Figure 2-10: General Mississippi Stratigraphy [16]

2-1-3-4-4 In Salah (Algeria)

In Salah CO_2 storage project, started since 2004 in Algeria and operated by BP, Sonatrach and StatoilHydro. The reason for initiation of this project was high concentration of CO_2 (5 - 10%) in produced gas came from Krechba, Teg and Reg fields (export gas should contain 0.3% of CO_2). Joint venture companies spend more than $100 million to install CO_2 capture and transport facilities to be injected in a deep saline formation. The target storage

formation which is in down-dip of the production horizon, located about 1850m below gas reservoir level with thickness, porosity and permeability of 20m, 13-20% and 10mD respectively. The target formation is separated by 950 meters of Carboniferous mudstones (seal) from the production interval (Figure 2-11). During this project, 17 million tons of CO_2 was planned to be injected in the underground storage via three injection wells [2].

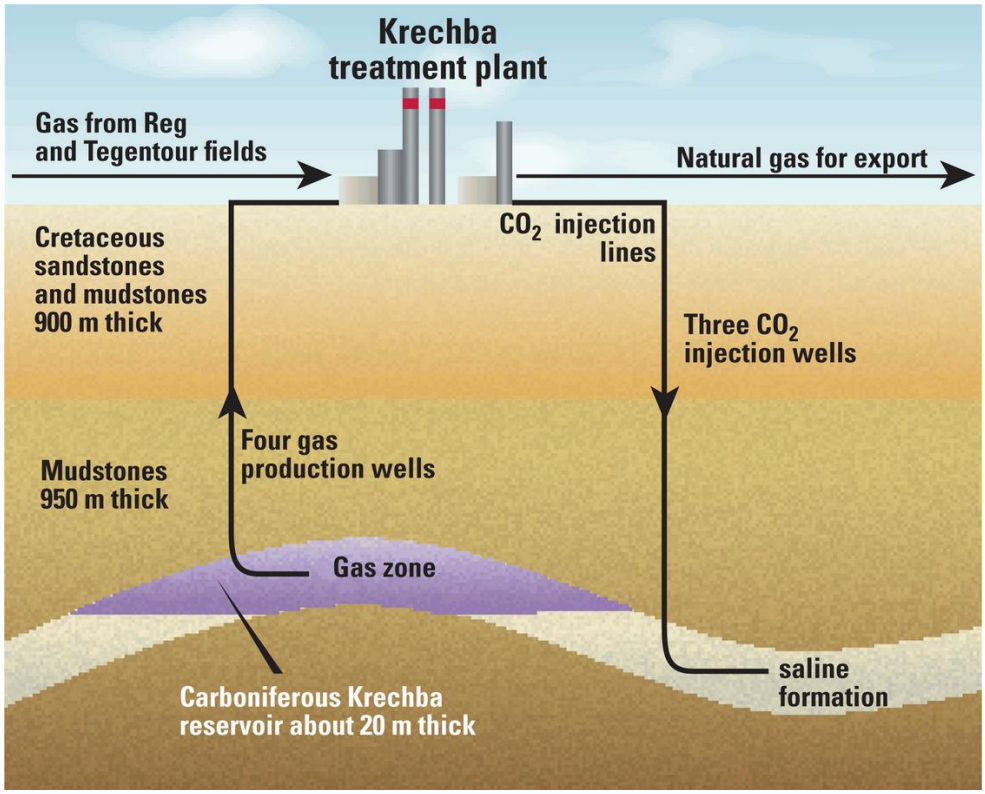

Figure 2-11: CO_2 storage saline aquifer of In Salah [17]

2-2: CO_2 Leakage from Underground Storages

As mentioned earlier in Section 2-1-2, Carbon Capture and Storage (CCS) is considered as the ideal short term strategy for sustaining or reducing global atmospheric CO_2 concentration. The technology for capturing and transporting CO_2 from producing sources

(power plants, petrochemicals, cement, metals and minerals) to the sinks (underground geological storages) has been widely used in chemical and petroleum industry. In the storing aspect of Carbon Capture and Storage, a complication arises as the operations are relatively new and need to be more investigated thoroughly in order to determine if the geological sinks are suitable to sequestrate CO_2 indefinitely. Notably, the potential for the CO_2 leakage from the underground storage to the atmosphere should be addressed.

The sinks for geologic CO_2 sequestration are depleted petroleum and gas reservoirs, deep saline aquifers and coal beds. Leakage in the underground CO_2 storage leads to negate the benefits of geologic CO_2 sequestration. Also leakage could have harmful ecological effects and present the risks for health other than global warming. Recently, the establishment for performance requirements for geologically sequestered CO_2 to be that of or less than the leakage rates of 0.1% annually [18]. To adjust to these standards, CO_2 storage sites must have active monitoring systems to detect CO_2 leakage and be prepared to take remedial action in the event a leakage occurs. In order to select an appropriate monitoring system, adequate knowledge of the leakage's related factors are required.

2-2-1 CO_2 Leakage Conduits

2-2-1-1 Well Leakage

Leak source, driving force, and leakage pathway are the three most probable causes for a leakage to develop in an underground storage. The leakage source is the injected CO_2. The driving force for CO_2 movement can be considered as buoyancy or mostly pressure difference between the source and surface due to the injection. In presence of source and driving force, the wellbore can be a pathway (Figure 2-12) if it includes poorly cemented casing, casing failure and abandonment failure [19]. These leakage conduits are a pre-existing condition of the well bore before CO_2 injection. Also after injection it is possible that CO_2 causes cement degradation and casing corrosion.

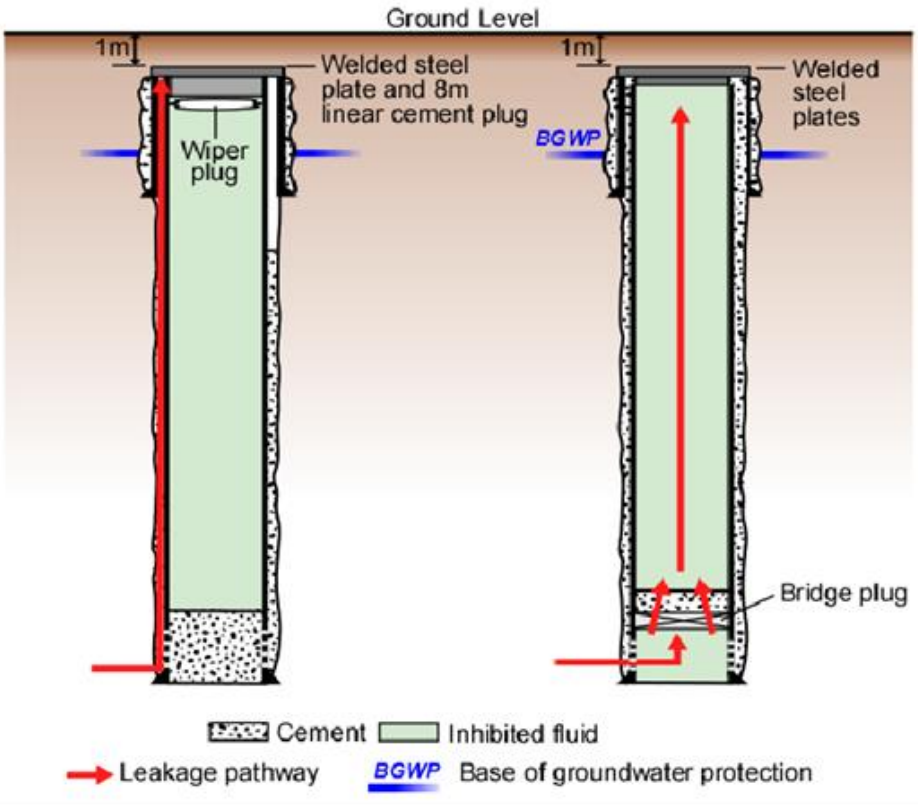

Figure 2-12: Different leakage pathways along wellbore [19]

Figure 2-13: CO_2 bubbles on casing cap [19]

Wells are especially important because they provide a direct and almost vertical pathway through the formations that otherwise act as a seal for CO_2. Well logs (especially sonic) examination is a good tool for describing the potential of the leakage from a well bore.

Abandoned wells have a higher probability to provide the pathway for the CO_2 to leak. After 2003, regulations require that all the surrounding permeable zones be isolated or covered to prevent any communication between the storage and geological formations. [19]. When the down-hole cement plugs have been installed it is necessary to keep the well open for inspection for 5 days. When the well is checked for the fluid level test or other signs of the leakage (such as bubble in the fluid-Figure 2-13), top of the casing is cut and capped almost 1 meter below the ground level [19].

In many cases in the wells that were abandoned before 2003, the wells were constructed with low annular cement top allowing a cross flow behind the casing. With current regulations, a cement squeeze is needed to achieve a good isolation in conjunction with putting some inhibitor liquids inside the casing. In addition, increasing the pressure to 7000 kilopascals and casing vent flow tests should also be performed to maximize efficiency. [19].

If any flow of gas is observed, repair process has to be done before abandonment. The test for surface casing vent flow, or SCVF, is referred to a situation where the pressure in the casing or annuls sustains, indicating that gas entered the production casing from a formation. The wells with positive SCVF, exhibits gas flow rates greater than 300 M^3/day or have stabilized build up pressure more than 9.8kpa/m must be repaired immediately [19]. The pressure build up in the SCVF can be used in order to determine the properties and characteristics of the leaked well specially the effective permeability of leak; this is done by assuming a continuous Darcy flow for the CO_2 movement along the well's leak path. Based on some laboratory tests a number of type curves were generated to be used for the leak effective permeability calculations (Figure 2-14).

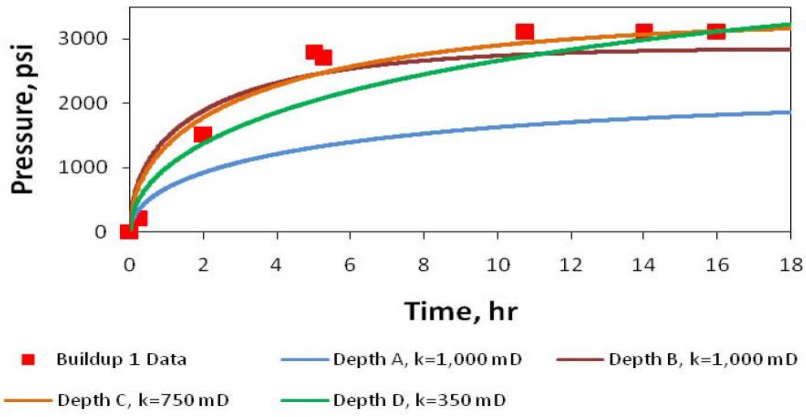

Figure 2-14: Type curves for well leakage permeability [20]

Another test that is required in some regulations is GM (gas migration). The GM test consists of boring small holes in the soil to a minimum depth of 50 cm in a test pattern radiating out from the wellbore. The holes are stopped to allow gas to build up a reading of Lower Explosion Limit is made to detect combustible gas (Figure 2-15). If gas is detected further investigation is conducted to determine if GM is present [19].

In a data mining study for about 316,500 wells in the province of Alberta in Canada, various factors were investigated to determine if the potential for leakage could be assessed based on well information. Briefly, the factors are categorized in Table 2-2.

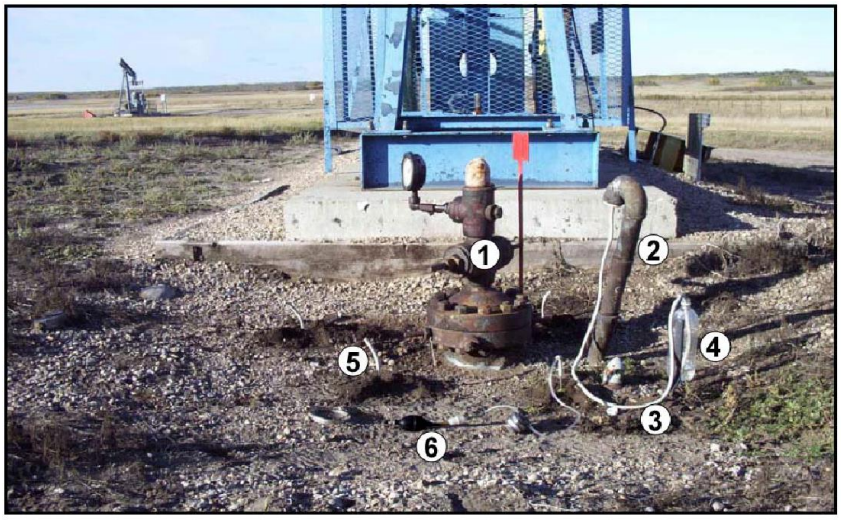

Figure 2-15: Wellhead with GM test [19]

Table 2-2: Factors that impact potential well leakage [19]

Factors showing no apparent impact	Factors showing minor impacts	Factors Showing major impact
Well Age Well Operational Mode Completion Interval H2S or CO_2 Presence	License surface Casing Depth Total Depth Well Density Topography	Geographic Area Wellbore deviation Well Type Abandonment method Oil Price ,regulatory changes Uncemented Casing /Hole Annulus

2-2-1-2 Cap Rock leakage

"Reservoirs are initially bounded by competent cap rock that is sealing, meaning that there is no communication between cap rock on one side and additional permeable media on the other. As pressures change in the reservoir, the pressures on one side of the seal may differ more and more from pressures on the other side; that is, a pressure deferential begins to appear across the cap rock [21]". "When this pressure drop becomes sufficiently large, the seal provided by the cap rock may be breached, and flow across the breach may occur [21]".

"At the moment of seal breakage, the cap rock may still have little conductivity across it. However, since the pressure drop across the cap rock may be driven higher by external influences and even though fluid can now move across it, further seal degeneration could occur resulting in larger outflow. Eventually, there will be some limit to this growth. There may also be a decline in outflow as the pressure drop becomes smaller as the seal somewhat heals, but never completely healing [21]".

In order to determine the cap rock leakage characteristics, stress distribution in the reservoir and cap rock should be determined by geo-mechanical models or measurements. These models also can orientate minimum principal stresses which are mostly prone to be fractured and provide a leakage path for CO_2 [22]. The best result for leakage

characterization will be achieved if coupled geo-mechanics and flow models are used. Reservoir simulator computes pressure and temperature, which is used as input for the geo-mechanical models in order to determine stress distribution and consequently rock failure and leakage permeability.

The fracture permeability is described as the permeability which occurs due to rock breaching during pressurizing the reservoir by CO_2 injection. If the cap rock crack finds a way to an overlaying permeable layer, CO_2 can escape from the reservoir. Barton –Bandis [22] model is generally used to demonstrate fracture permeability behavior in the reservoir. Based on this model no fracture exists in the matrix before the pressure increase starts. Another assumption in this model is high brittleness of the rock resulting in maximum value for the permeability at the beginning of the fracturing. . From the beginning the fracture aperture remains open until the pressure in the rock drops [22]. This pressure reduction leads to a decrease in the fracture aperture and consequently leakage permeability (Figure 2-16).

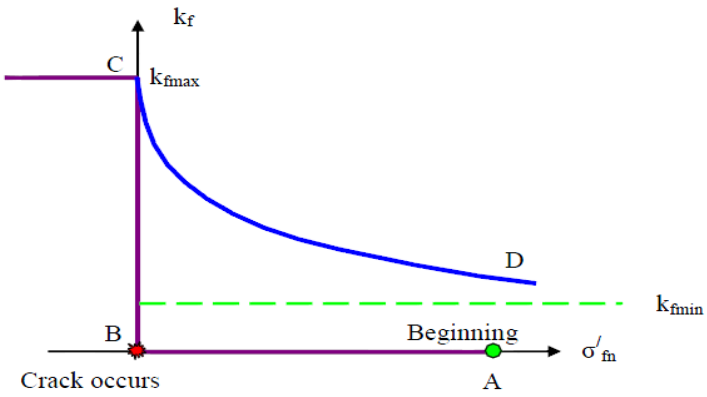

Figure 2-16: Barton-Bandis model [22]

Another factor that prevents a cap rock to act as a seal is the displacement of the connate water in the pores or fractures due to buoyancy forces. In other words, the capillary entry pressure of the largest interconnected pore throat must be bigger than the pressure that is exerted to the cap rock by CO_2 (buoyancy). The difference between water and CO_2 densities in addition to the height of CO_2 column determine the magnitude of buoyancy force. The factors determining the magnitude of the resistant force are the rock wettability, the largest connected pore throat radius, and the gas–water interfacial tension [23]. By

applying the force balance, cap rock seal strength corresponds to the height of CO_2 column that can be retained in the reservoir may be found as:

$$Critical\ height = \frac{2\gamma\ \times [{}^{1}/_{r_t} - {}^{1}/_{r_p}]}{g\ \times [\rho_w - \rho_{CO2}]}$$

Where:

γ = Interfacial tension

r_t = Radius of pore throats

r_p = Radius of pores

g = Acceleration of gravity

ρ_w = Water density

ρ_{CO2} = CO_2 density

2-2-1-3 Fault leakage

Faults are considered as potential pathways that results in CO_2 migration from target formation into the atmosphere or other subsurface formations. Due to the existence of faults in most of the sedimentary basins, fault-fluid interaction evaluation should gain more attention, especially for CO_2 storage risk assessment. Two important parameters are involved in fault evaluation as "fault sealing capacity" and "fault region petro-physical description" [24]. "Fault seal capacity" indicates if a fault acts as a barrier to flow. If the fault is non-sealed, its conductivity can be considered by fracture or matrix permeability which limits the flow but does not stop it. Seal capacity of a fault can be quantified by Shale Gouge Ratio or SGR. SGR can be defined as an estimate of amount of shale in the fault based on averaging or mixing rule (Figure 2-17):

$$SGR = \frac{\sum \Delta z_i Vs_i}{Throw} \times 100\%$$

Vsi= Shale concentration in layer i

Zi= Thickness of layer i

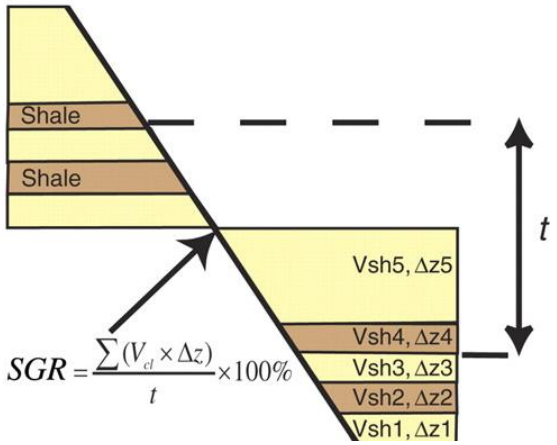

Figure 2-17: Shale Gouge Ratio Calculation [24]

Another parameter that affects fault conductivity is membrane sealing which is actually minimum capillary entry pressure that must be overcome before a non-wetting phase(CO_2 in this case) can enter into fault's pore throat(fault is mainly filled with ground particles). Understanding these two parameters helps to quantify how long it takes for buoyant CO_2 to migrate from the fault region to the atmosphere and how much CO_2 leaks through the fault [24]. The main fault characteristics are presumed to be functions of lithology (clastic or carbonate), fault structure and sealing mechanisms. Due to the difficulty and practicality issues (it is preferred to keep the integrity of the fault) associated with sampling (core) fault rocks in the deep formations, fault property specification is so challenging.

Some examples of CO_2 leaking faults in different locations exist, such as Crystal geyser which is 4.5 miles from Green river in Utah. Faults in this area contain travertine deposits and were charged by CO_2. Based on studies, faults in this region have leaked more than 2Gt-CO_2 over many years [25].

2-2-2 CO_2 Leakage Impacts

Underground CO_2 sequestration is associated with two types of risks—the risk of CO_2 leakage through the paths to the overlaying formations during and after injection(discussed in section 2-2-1) and the risk of the aquifer over-pressurizing during the injection. When the CO_2 is injected in saline formations, it creates a pressure build up that may lead to damaging seal formation, such as fracturing or fault activation, or brine leakage out of the

reservoir. CO_2 Leakage Risk or CLR depends on the probability of CO_2 leakage and its consequences and impacts.

CLR=Total Probability × Impact

The impact of the CO_2 leakage can be assessed by its flow rate and concentration as higher flow rates represent severe impacts. Total Probability of the leakage is divided into three separate probabilities [10]. The first probability (1) considers the chance that CO_2 plume intersects existing leakage paths (faults, wells) in the reservoirs. Second probability (2) deals with likelihood of path connection to other compartments or atmosphere. In final Probability (3), the chance of conductivity or sealing of the leakage path is taken into account.

Total Probability = Probability (1) × Probability (2) × Probability (3)

CO_2 leakage may result in serious effects on humans, animals, and the ecosystem. Humans, animals, and organisms which rely on gaseous oxygen may experience death or serious complications if they are exposed to high CO_2 concentrations. Since CO_2 is heavier than the O_2 in the air, the releases result in high accumulations in cellars and valleys with fatal consequences. CO_2 leakage into shallow ground level may contaminate and affect the quality of water, soil, and mineral resources. An increase in CO_2 concentration in water decreases the pH, which leads to an increase in the hardness of water [24].

2-2-3 Storage Site Monitoring Techniques

2-2-3-1 Well Monitoring

CO_2 injection well can be considered as the most possible leakage path in the underground storage sites. The well is supposed to keep its integrity over the injection period and during the post injection time for an estimated 10,000 years. Integrity refers to safe operation of

the well throughout its service life to reduce the risk unintended CO_2 release. Well monitoring provides a preventive verification to see if the integrity is maintained. LDL or Leak Detection Log, Tubular Inspection, Production (injection) Profile, Neutron, Spectral and Cement Bound Logs can be used as the cased-hole logs for validation of cement integrity, pressure isolation, corrosion and injection profile [2].

2-2-3-2 Pressure Down-hole Gauges (PDG)

Reservoir pressure is a good parameter for understanding subsurface flow behavior. PDG has been used in oil and gas industry for decades to measure well pressure over different time periods to analyze reservoir behavior and characteristics. Advancement of the technology enables operators to install permanent down-hole gauges which transduce real time and instantaneous data. Real time pressure data can be used for detecting fluid movement in the reservoir that is an indicator for CO_2 migration [2].

2-2-3-3 Seismic Imaging

The petroleum industry has been working with seismic waves in order to get subsurface images for underground geological modeling and interpretation. In this technique, sound waves are emitted into the subsurface. Reflected waves are altered to key information about subsurface rock geometry, distribution, properties, and boundaries.

Recently, the advancement in interpretation tools has resulted usage of time-lapse seismic images (4-D seismic) for monitoring CO_2 movements in underground storage sites. In this method, initial seismic images for an area of interest, would be compared with seismic images that are taken from the same area at different time intervals. Movement of CO_2 in the subsurface makes some changes in pore/fluid properties that can be observed by time-lapse seismic [2]. Usage of four-dimensional seismic for CO_2 monitoring in depleted gas or low porosity reservoirs is not practical because the sound waves' responses to CO_2 movement are not detectable. Four-dimensional seismic images from Sleipner field are good practical examples for demonstration of CO_2 movement in an underground storage site as seen in (Figure 2-18).

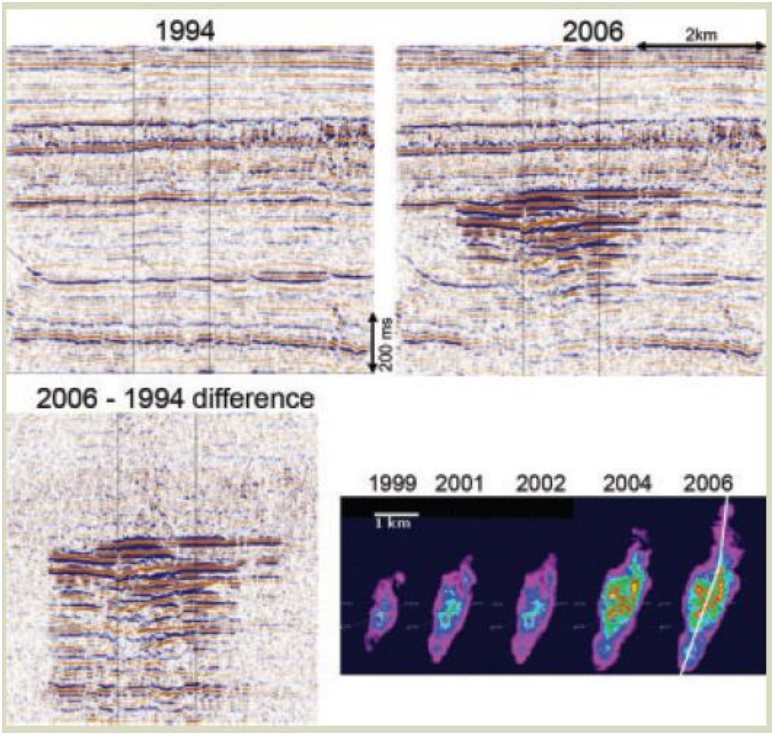

Figure 2-18: Seismic monitoring of CO_2 injection in Sleipner Field [2]

2-2-3-4 Gravity Survey

Changes in the vertical columns' rock densities may be calculated by gravity measurements. Due to the displacement of saline brine within the subsurface by CO_2, reduction of average column density may occur, but by implementing attentive gravity measurements as a monitoring tool can reveal where the CO_2 leakage arises. Gravity survey is ideally applicable for shallow reservoirs with high porosity and thickness. Unfortunately, CO_2 movement in the reservoirs with porosity and thickness less than 10% and 10 meters, respectively, and depths more than 2500 meters is typically not possible to be detected by gravity measurements. For practical CO_2 monitoring, fixed gravimeters with high accuracy of about 5 micro-gals are needed [2].

2-2-3-5: Satellite Imaging

Currently, using satellite platforms to measure vertical ground elevations in different time periods is a viable option. Maps of surface deformation over time are generated based on returned microwave energy analysis. In the petroleum industry, some studies from satellite

image observation showed ground level subsidence or uplift are due to oil production or gas injection, respectively. Prior to use of this monitoring technique, ground uplift response of one millimeter based on corresponding volume of injected CO_2 should be determined and calibrated. Deviation of ground level uplifts from calibrated values may be an indicator for CO_2 leakage [2].

2-2-4- Strategy for Leakage Prevention and Remediation

To select a safe and secure site as the geological storage, leakage pathways, cap rock integrity, and assured natural confinement must be considered along with assured well bore integrity and sufficient reservoir capacity. Among these components, consideration should be emphasized on the long-term well integrity at the CO_2 storage site. Descending in rank of importance, a series of reservoir simulations based modeling should be conducted to track and project the movement of the CO_2 plume. The overall CO_2 monitoring system at the storage site's installation purpose is to serve as early warning system and provide online information about the movement and immobilization of the CO_2 plume. By developing a pre-established mitigation strategy, a rapid response would be available when a leakage is detected. Reducing the pressure in the storage formation, increasing the overlying formation pressure, or re-injecting the CO_2 in more secure formations is other possible options to stop a leakage. [26]

2-3- Smart Well Technology

The concept of Smart Field, which is also recognized in the industry by names such as, i-fields, e-fields, field of the future, etc., is a new technical area which is rapidly gaining support and recognition in the oil and gas industry. Smart Well Technology is mainly based on down-hole measurements and the control of the wellbore in the reservoir. The advancement in the technology involving drilling and completion allows the installation of Permanent Down-hole Gauges, or PDGs, which are capable of operating in harsh environments for extended durations. PDGs collect and transmit high frequency data streams to the remote offices to be analyzed and used for reservoir management.

2-3-1 Smart Well Definition

Smart Wells are generally utilized with equipment capable of performing down-hole measurements and/or controlling the production process in the reservoir level. A list of equipment or technologies can be added to conventional wells and converted to smart ones which shown in Figure 2-19.

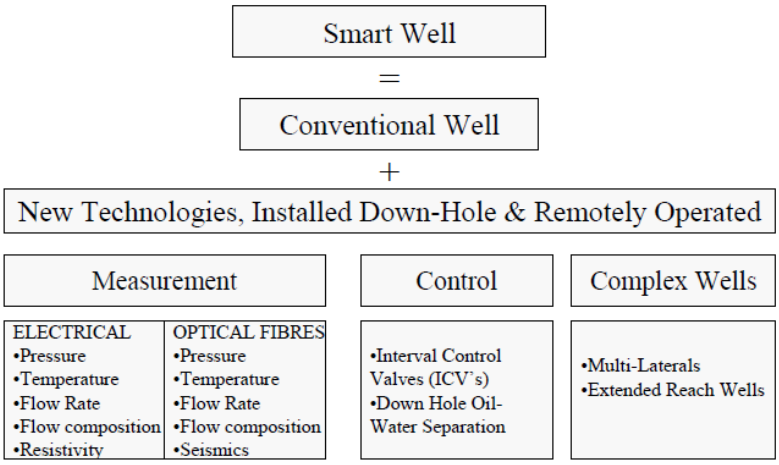

Figure 2-19: Smart Well instruments and technologies [27]

2-3-2 Smart Well Application

Several reservoir management applications exist with the ability to control and measure variables at reservoir level. In comingled or stacked pay zones, well production cannot reach the optimal value due to differences in reservoir pressure at different compartments. Utilization of down-hole chokes would allow the reservoir to produce from multiple layers with minimum cross flow or fluid loss [28]. Horizontal wells also benefit considerably from Smart Well technology, especially in thin oil rims. Thin reservoirs may experience early water/gas breakthrough which may be managed by installment of inflow control valve at different well locations to shut off unwanted flows. Additionally, secondary recovery mechanisms, such as gas/water injection, can be controlled optimally by Smart Wells to avoid excessive injected fluid production through high permeable zones [28].

Down-hole measurements also provide the capability of flow profiling by use of distributed temperature sensing fiber optics. By using fiber optics, down-hole measurements detect cross flows and flows behind the pipe. These implications are especially practical in wells

where production profiling is expensive. Another application of Smart Wells is the Auto Gas Lift, where oil producing wells cross different compartments with active gas cap [28]. Inflow control valves make it possible to use and to control gas from other layers and flow the oil based on artificial lift procedures. Future application for Smart Wells will be down-hole production testing. Permanent Down-hole Gauges transduce the well flowing pressure and flow rate data, which are collectively fundamental information for well test analysis. In addition, down-hole geophones may be installed in the well system enabling operators to perform repeatable seismic tests to obtain reservoir imaging data used in monitoring sweep efficiency [28].

2-3-3 Closed Loop Reservoir Management

The high frequency data streams can be used for real time monitoring, simulation/model updating, and finally optimal control of the oil and gas reservoirs. The combination of all the mentioned processes results in "closed loop reservoir management" as depicted in Figure 2-20. Data from sensors can be assimilated in to the simulator to update and history matches the reservoir models. Real time data indicates if the actual performance of the field is deviating from the planned targets. If deviation occurs, appropriate control actions would be necessary, based on optimization algorithms, to bring back performance toward the targets.

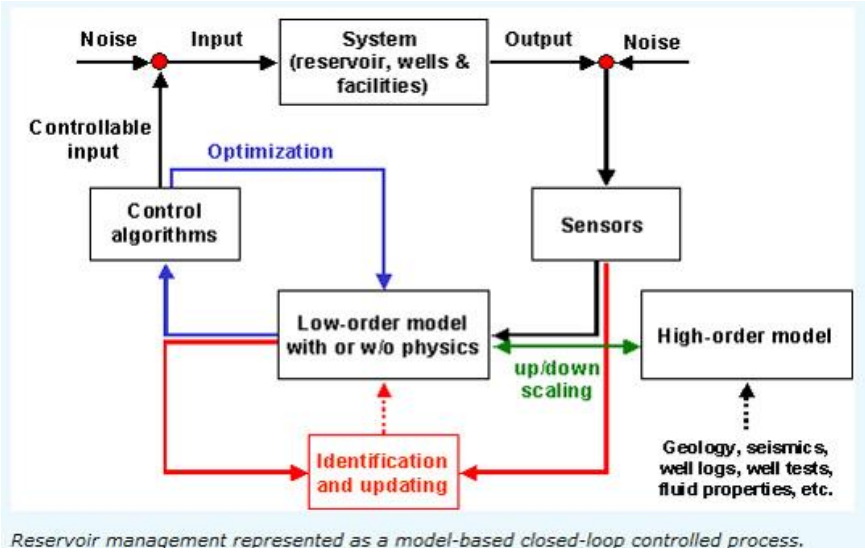

Figure 2-20: Closed Loop Reservoir Management [29]

In an underground CO_2 storage, it is possible to place an array of PDGs in the formation where the CO_2 is injected; notably, gauges may be placed in the injection/production wells and in the slim holes drilled specifically for this purpose. The pressure changes in the reservoir can be used during the injection to update the reservoir model and after the injection for reservoir monitoring [29].

2-4 Artificial Intelligence

Artificial Intelligence (AI) may be defined as the collection of analytical and numerical tools that tries to learn and imitate a process. When the learning process is accomplished, AI is capable of handling and responding to the new situations. Neural networks, Genetic Algorithms, and Fuzzy Logic are the main techniques considered as building blocks to Artificial Intelligence [30].

Neural network claims their artificial information processing correlates closely with biological neural networks. Artificial neural networks consist of main elements called neurons which pass signals between each other, similar to those of the human brain. The artificial neurons connect several inputs to one output by associated weighs and nonlinear activation functions. When data is provided to neural networks, it goes under a learning process, by specific algorithms, to find the appropriate weights that describe the behavior of the output with respect to multiple inputs.

Neural networks provide a good potential for exploring and analyzing large historical data bases that don't seem to be used in conventional modeling. [30]. In other words, neural networks should be applied in the cases where mathematical modeling is not practical. As a common situation in oil and gas industry where there are a lot of data available and the nature of problems are complex, these issues may be solved by unconventional methods such as Artificial Intelligence.

2-4-1Neural Networks

2-4-1-1 Biological Neural Networks

Artificial neural network was originally developed from behavior of biological neurons in the brain by McCulloch and Pitss [30]. The information processing in neural networks represent a lot of similarities with the issues that occur in biological systems. A schematic

of the nervous system block body, which is also called neuron, is shown in Figure 2-21. Generally, a neuron consists of cell body, axon, and dendrite which connected to another neuron with synaptic connection. Information communication is done by electrochemical signals that enter the cells through dendrites. Based on the characteristic of an input, the neuron is stimulated and releases an output signal that passes through the axons. The occurrence is known as "firing a signal" if a threshold is reached by a great enough electrical potential. [30]. The output signal from one neuron is an input for another neuron, which generates new electrochemical pulse as the output. Each module in the brain may have more than 100,000 neurons connecting to thousands of other neurons and form the complex architecture for neural networks; this neural network architecture is the basis for learning process in human brain.

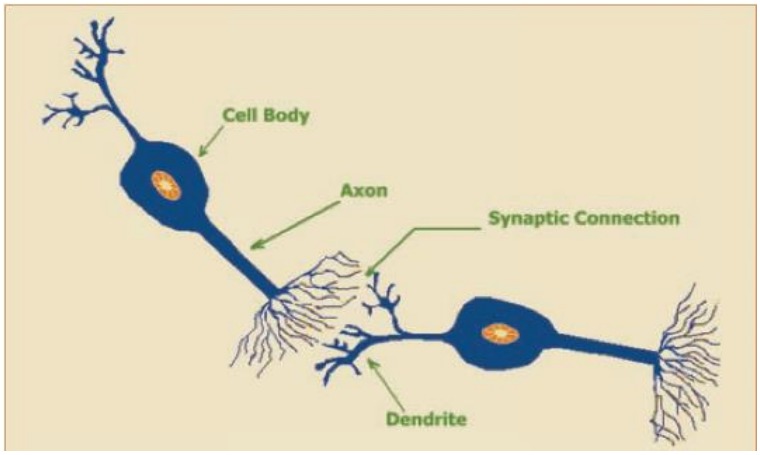

Figure 2-21: Sketch of biological neuron [30]

2-4-1-2 Mathematical Model

Artificial neural networks are mathematically modeled based upon functionality of biological neural networks. Synapses, which connect neurons to each other, of biological neurons are represented by weights (w). The weight, as a given value, is similar to strengths of the electrochemical signal. Excitatory reflections are designated by the weight's positive values, while inhibitory ones are identified by negative values [31]. The actual behavior of a neuron is represented by modification of all the inputs by weights

followed by summing them altogether which is referred as a linear combination (Figure 2-22).

$$Sum = \sum_{1}^{n} w_i x_i$$

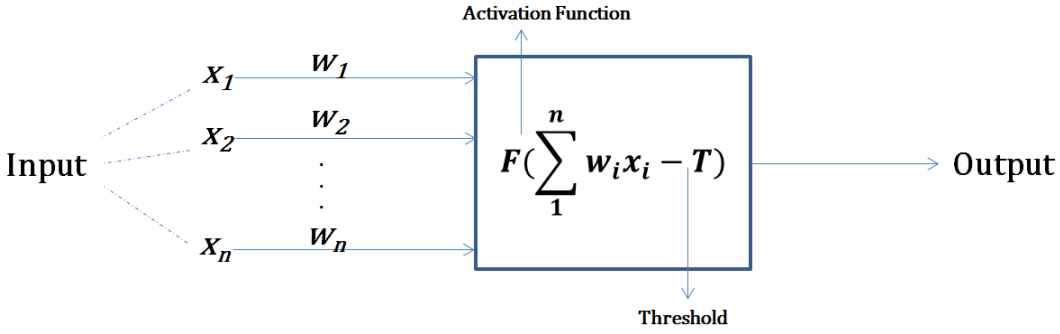

Figure 2-22: Mathematical form of a simple artificial neuron

The activation function decides the amplitude of the output signal. Based on the function type and a threshold value, the activation function generates a value between 0 and 1, or -1 to 1. Generally three types of activation functions (F) have been used in neural network models. By defining the difference between $\sum_1^n w_i x_i$ and threshold value (T) as V, the process can be modeled mathematically as the step activation function takes the value of 0 if V is less than 0 and 1 when V is equal or more than 0.

$$F(V) = \begin{cases} 0, & V < 0 \\ 1, & V \geq 0 \end{cases}$$

The Piecewise-Linear function below is capable of recalling values of 0 or 1 and also takes values equal to V in a specified range between 0 and 1.

$$F(V) \begin{cases} 0, & V \leq 0 \\ V, & 1 > V > 0 \\ 1, & V \geq 1 \end{cases}$$

The Sigmoid function uses the following relation in the range of -1 to 1. All these functions are shown in Figure 2-23.

$$F(V) = \tanh\left(\frac{V}{2}\right) = \frac{1-\exp(-V)}{1+\exp(-V)}$$

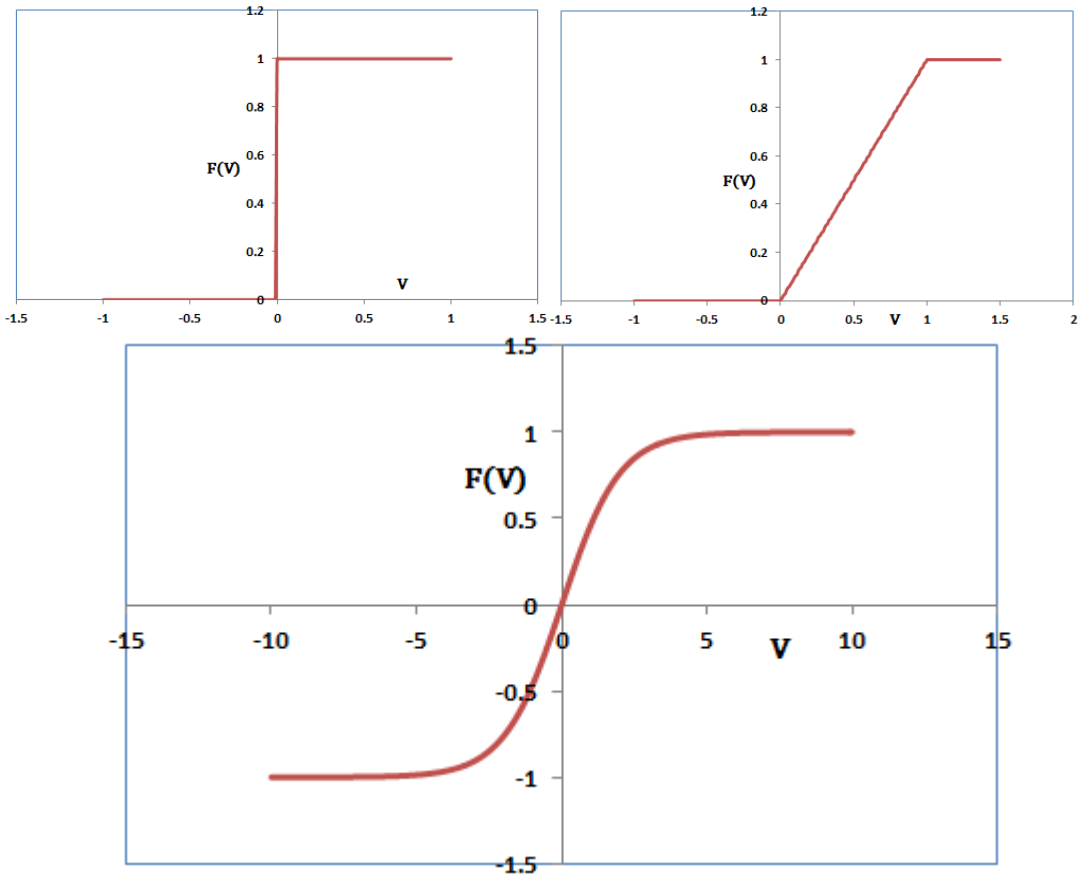

Figure 2-23: Three type of activation functions (top left: step, top right: Piecewise-Linear, bottom: Sigmoid function)

Neural network topologies are determined by connection patterns between neurons and propagation of data. In "Feed-forward" neural networks, there is no feed-back from the output results into the layers and units. In contrast, "Recurrent" neural networks receive feedback from predicted outputs dynamically. For example in unstable situations, activation functions' values for specific neurons do not change and experience relaxation until getting to stable conditions [31].

2-4-1-3 Back-propagation Neural Networks

The training procedure in neural networks is based on updating the weights in order to correct the output results. In the back-propagation training method, weight updating is enhanced by use of errors, the difference between the desired value and actual value, which are filtered back through the network. The objective is minimization of errors subject to

changes in the weights. The gradient descent method is used for calculation of the weight changes and the steepest path is taken to minimize the error function. By minimizing the error function, the output error may be modified by multiplying it by the activation function gradient. Depending on whether the error is positive or negative, the gradient of the activation function may move up or down [32].

Error gradient at each neuron k and hidden layer J is calculated by following formulas:

$$\delta_k = y_k(1 - y_k)(d_k - y_k)$$

$$\delta_j = y_j(1 - y_j)\sum_{k=1}^{n} w_{jk}\delta_k$$

Where y_k and d_k are output and desired values at neuron k. The weights are then manipulated into the following formula:

$$w_{jk} = w_{jk} + \Delta w_{jk} \quad , \quad w_{jk} = \alpha.\delta_k$$

Where α represents learning rate and takes the value between 0 and 1; this value determines the rate of weight adjustments and learning speed. Small values of α cause low learning rates and high values may lead to network instability or stuck in local optima.

2-4-2 Neural Network Applications

Applications of neural networks have gained support and practicality in different fields. Due to their successful applications in addition to ongoing research and development, a promising path for the future is projected. Different usages of neural networks are discussed briefly in the following.

One of the first and most extensive applications of neural networks is referred to as "Signal Processing," which specifically removes noise from telephone lines. Noise cancelation technique uses the Adaline neural network, which is trained to remove the noise from the output signal. Conventional echo suppression systems fail to filter high speed transmission signals from satellites or wire based telephones [32].

The other usage of neural network is in the "Control" process. A fairly popular example in this area is providing backward steering for a trailer truck to the loading dock position. Due to the complexity of solving multiple differential equations, it is not possible to use

conventional control procedures. However, a solution was developed by neural networks which were able to predict new position of the truck by knowing its current location, angle and speed or emulator. Additionally, neural networks act as controller to provide adjusting signals for the truck to get into its final position [32].

Pattern Recognition is a general area with variety of complicated problems. The most common one was recognition of handwriting characters in the post industry. The problem was entirely too complex for traditional methods due to the disparity in style, size, and positions of handwritings. Initially, Back-propagation neural networks have been used for recognition of handwritten zip codes and were advanced for more complex problems.

Medicine is another example of a field which has benefited from neural networks significantly as portrayed through the "Instant Physician," which is able to receive set of symptoms and find the best diagnoses and treatment. The "Instant Physician" was created by turning an auto associative neural network with an extensive diagnostic data and medical records such as symptoms, diagnoses, and treatment of a disease. The performance of the neural network was remarkably precise in diagnosing illnesses and recommending treatment for specific symptoms [32].

Besides of mentioned applications, neural networks also have been used in speech recognition, business, robotics, game predictions, security, image processing, data mining, and even quantum chemistry [33]

2-4-3 Neural Network Applications in E&P Industry

Neural networks have shown wide variety of application in different E&P disciplines, but the implementation of neural networks is not recommended in the cases where the conventional method provides firm solutions. Neural networks have been able to perform accurate analysis for large historical data bases which cannot reveal explicit information by conventional modeling [30].

The early usages of neural networks in the oil industry go back to reservoir characterization, specifically porosity, permeability, and fluid saturation from well logs. Well logs generally were used as the inputs for neural networks while core results such as porosity and permeability were considered as outputs. It was possible to predict reservoir characteristics by well logs where core data was not available [30]. Additionally, it was

possible to train neural networks for generating synthetic Magnetic Resonance logs by use of conventional wireline logs such as SP, gamma ray, density, and induction logs [34].

Another well-known implication of neural networks is the oil and gas PVT property estimation. There are many empirical correlations that estimate some PVT properties. Ridha *et al* [35] trained a universal neural network using 5200 PVT data points gathered from all around the world to predict bubble point pressure (Pb) and oil formation volume factor(Bob) as function of solution gas ration(Rs), gas specific gravity(γg), oil specific gravity(γo) and reservoir temperature. The results were more accurate than existed PVT correlations.

Neural networks also were used to predict conditions for wax precipitation in the pipelines. One important parameter that determines wax formations is temperature. A neural network was trained by Adeymi *et al* [36] by having combination of data including molecular weight, density, and activation energy provided very good estimation for wax appearance temperature (WAT).

Forecasting post-fracture deliverability of wells in Clinton Sandston gas storage field was done by Mohaghegh *et al* [37] using back-propagation neural network. The input parameters in this work included well data(date of completion, well type, sand thickness, flow test values…),flow fracture deliverability and hydraulic fracture data(number of times well was fractured, fracturing fluid, total water used, total sand used ,acid volume, injection rate and pressure,…) while maximum flow rate after fracture was selected as an output. Post fracture well deliverability was forecasted by neural networks with very high accuracy. Additionally, neural networks were used with the Genetic Algorithm to optimize fracturing operation and select the best candidate for well re-stimulation.

The other application of neural networks is in development of the Surrogate Reservoir Model, SRM- a replica of the reservoir simulation models which reproduce simulation results with high accuracy and in very short time. SRM can be a good substitute for a reservoir simulation model especially when numerous simulation runs are needed. Risk assessment, uncertainty analysis, optimization, and history matching are typical analyses which required many simulation runs. Amini *et al* [38] developed a SRM for the reservoir simulation model of the CO_2 storage site in Australia which included 100,000 grid blocks. The grid-based SRM was developed by 12 simulation runs to generate an inclusive data

base for the neural network including well data, static, and dynamic data for all grid blocks in the reservoir.

The Top-Down Model (TDM), which was invented by Mohaghegh [39] is another neural network application which incorporates field measurements such as drilling data, well logs, cores, well tests, production history, etc., to build a comprehensive full field reservoir model. Haghighat *et al* [40] analyzed production behavior of 145 wells located in an unconventional asset in Wattenberg Field-Niobrara using wells' static (reservoir properties, well completion information) and dynamic data (operational information like days of production per month).

Besides of mentioned applications , neural networks were used in the oil and gas industry for drill-bit diagnoses [41], inversion of seismic waveforms [42], seismic attribute calibration [43], lithology prediction from well logs [44], pitting potential prediction [45], reservoir facies classification [46], EOR method evaluation and screening [47], stuck pipe prediction [48] , assessment of formation damage [49] , water flooding analysis [50], conductive fracture identification [51], bit bounce detection [52] and calibration of quarts transducers [53].

2.5: Discussion of Pervious Works

CO_2 leakage detection in storage sites using pressure data from PDGs is a fairly new topic in CO_2 sequestration research area. Several authors [54] [55] [56] [57] [58] [59] tried to investigate this topic with different methodologies. Generally, most of the presented methods attempted to use analytical solutions to find pressure behavior subject to CO_2 leakage characteristic and solve the inverse problem to find leakage components [57] [58]. The other methodology which was introduced by Jalali *et al* [59], considered neural networks to find seepage in a CO_2 sequestration model in coal bed with multiple sensors (PDGs). All mentioned studies used synthetic models which were completely homogenous with at most two reservoir layers. The significance of the current study over previous works is usage of a history matched reservoir simulation model developed for real CO_2 sequestration project (Citronelle Field). Additionally, CO_2 leakage was detected based on a novel data processing method, implemented for analysis of real time pressure data. Finally, the robustness of our proposed method and workflow was evaluated by considering various

reservoir and CO_2 leakage characteristics. Two different CO_2 leakage detection techniques based on Smart Well technology are discussed briefly as follow.

2-5-1 Leakage detection-Leakage Test with Analytical Model

Hydraulic or water injection test can be applied for underground saline aquifers in order to examine if the reservoir has the proper confinement capacity for CO_2 storage. For this case study [57], water is injected into the aquifer and the pressure is monitored at the observation well in an upper aquifer for a specific period of time (Figure 2-24).

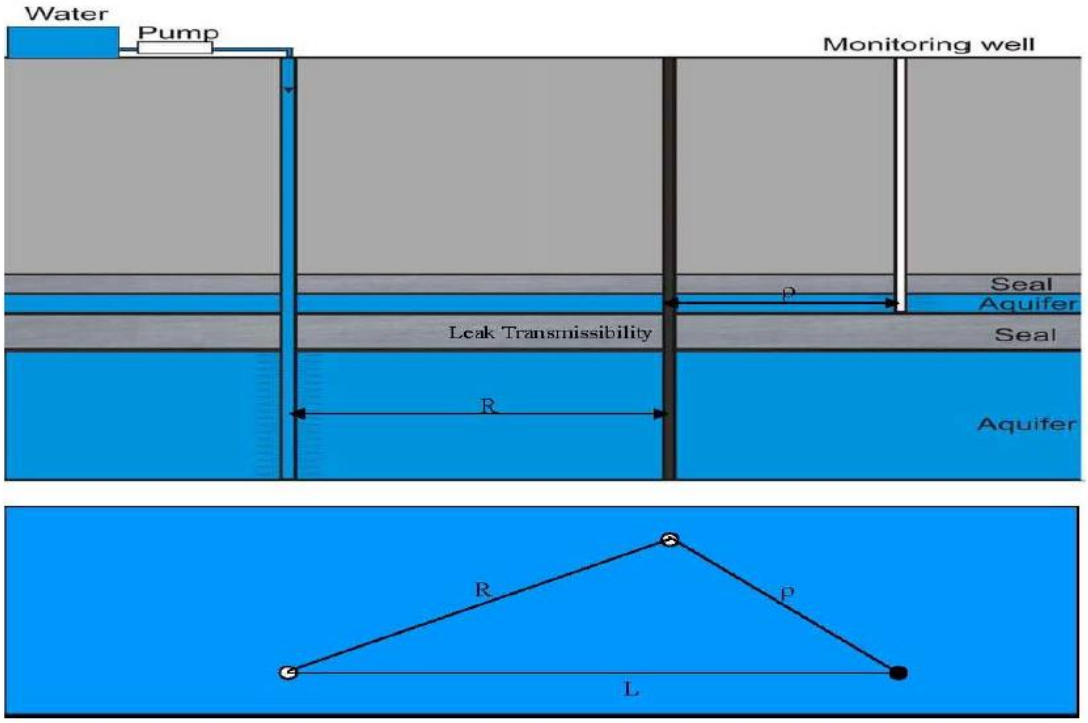

Figure 2-24: Leakage test configuration [57]

The objective here is to determine leakage placement and transmissibility based on pressure data. This test is somehow similar to pressure interference well test which is widely used in petroleum industry to determine directional permeability and other major reservoir properties like skin factor, and average reservoir pressure. The leakage problem in this case is an inverse problem since the leakage parameters are manipulated so that the

modeled pressure matches the measured data. In this test, the analytical solution which is the dimensionless pressure response at the monitoring well can be expressed as (the bar sign means the equation is given in Laplace domain [57]):

$$\bar{P}_{mD} = \frac{\bar{q}_{lD}(s) K_0\left(\sqrt{\frac{s}{\eta_D}}\rho_D\right)}{T_D r_{ID}\sqrt{\frac{s}{\eta_D}} K_1\left(\sqrt{\frac{s}{\eta_D}} r_{lD}\right)}$$

q=flow rate (m3/s), K0=Zero order Bessel function, s=Laplace transform, ρ=leak monitor distance (m), T=transmissibility (m3), η=diffusivity (m2/s), K1=first order Bessel function, r=radius (m)

When the transient pressure measurement at the monitoring well is given, the inverse problem would be finding the leakage characteristics (Cartesian coordinates, leak radius and permeability) in a way that the difference between measured pressure(Y) and predicted pressure ($\overline{P_{md}}$) is minimzed: $f(x) = Y - \overline{P_{md}}$

This method can provide little information about the leakage location (the solution of the objective function respect to leak location is not unique) but the leak transmissibility can be evaluated within a narrower confidence interval. Different test strategies can enhance the leak characterization capability. These strategies include increasing pressure sampling frequency, use of pulsing in the water injection, increasing the number of monitoring and/or injection wells and using a pressure derivative respect to time analysis.

2-5-2 Leakage Detection with Neural Network- Reservoir Simulation Model

In this case study [59] a horizontal, single-layer, homogeneous coal bed CO_2 storage model with constant reservoir properties, such as permeability, porosity, and thickness is considered. Sixteen pressure sensors are located at equal spacing throughout the reservoir (Figure 2-25).

Daily pressure data was recorded from all sixteen sensors along with the location of each pressure sensor. Leakage was introduced to the reservoir by creating a small pressure difference, ΔP, between the reservoir pressure and bottom-hole pressure of an imaginary

well as the source for CO_2 seepage. In this homogeneous model, 92 simulation cases were generated (Figure 2-25).

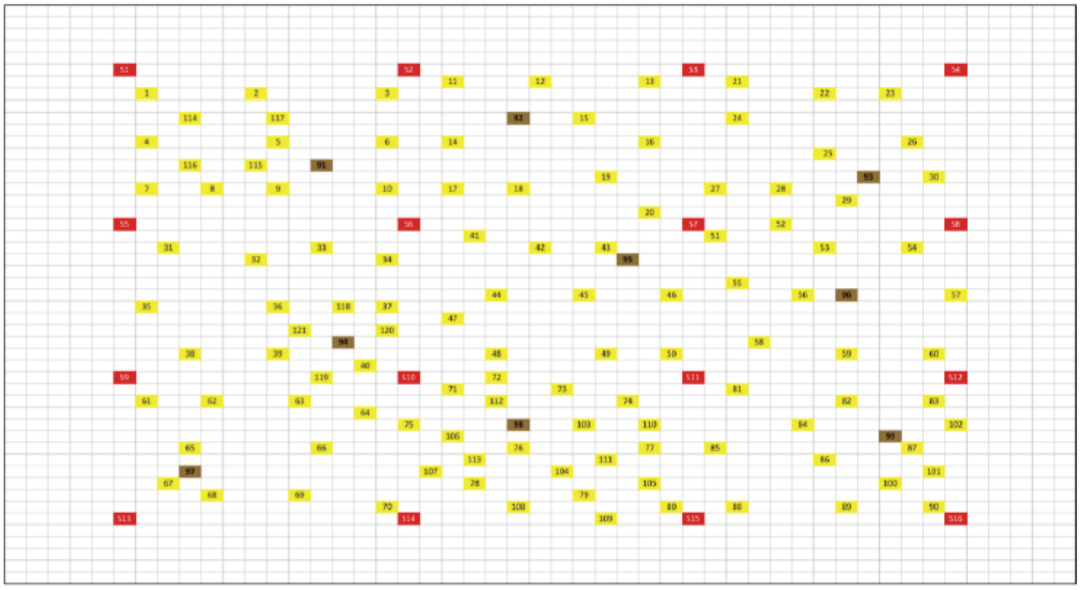

Figure 2-25: Leakage location for training and test cases [59]

In each case, a specific location for CO_2 seepage was selected. In order to avoid high reservoir simulation run time, the Surrogate Reservoir Model (SRM) was used in this case. A Surrogate Reservoir Model (SRM) is a prototype of full-field reservoir simulation models and are essentially artificial neural networks, which once trained can mimic the behavior of the reservoir with change in selected input parameters. An important feature of SRMs is their fast analysis and generation of outputs in a very short time.

For each run, pressure data was collected on a daily basis. The results of these models would generate a large dataset. The pressure difference between the actual field pressure distributions, recorded by the pressure sensors, and the SRM predictions at pressure sensors' locations (with no leakage) are then sent to the ANN trained for CO_2 seepage location detection. The network looks for changes in pressure measurements at the sensors. Once the pressure change exceeds a threshold, it starts searching for the possible location of the seepage. In the case of CO_2 seepage, the ANN provides an approximate location and the amount of the CO_2 seepage (Figure 2-26).

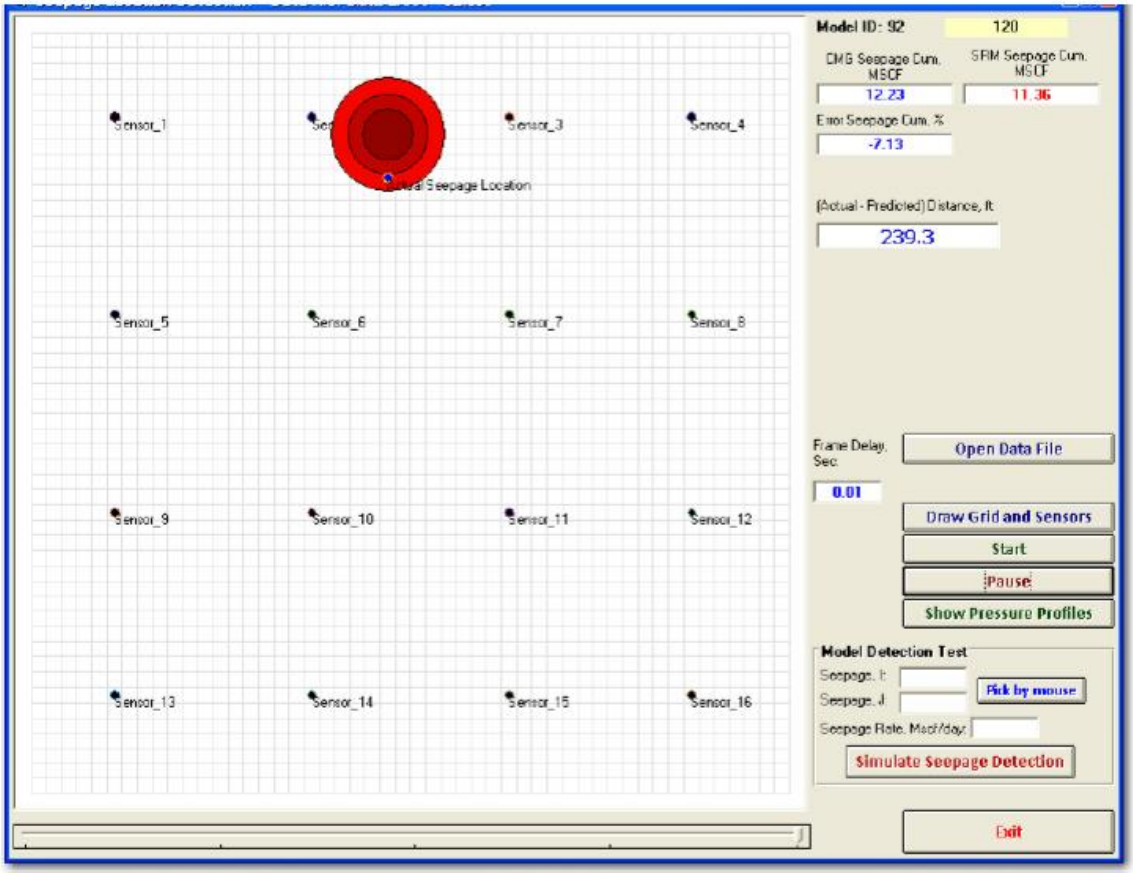

Figure 2-26: Network prediction of leakage location

An ANN trained for a heterogeneous reservoir (heterogeneity in porosity and permeability) could detect the location of the seepage with reasonable accuracy, as low as an area of 0.6 acres in a reservoir with a total area of around 579 acres. The seepage rate in such a reservoir was around 0.3% of the total stored gas per year, which was slightly above the 0.1% per year limit found in the literature.

Chapter 3 Reservoir Simulation Model

Injection and storage of CO_2 in Citronelle, AL is the phase III of South Eastern Carbon Sequestration Partnership and it aims to demonstrate commercial-scale storage of CO_2 captured from an existing coal-fired power plant. Alabama Power Company's Plant Barry is the source of CO_2 which is approximately 12 miles from the Southeast Citronelle Unit (Figure 3-1). The project will be capable of capturing approximately 125,000 metric tons of anthropogenic CO_2 per year. A pipeline was constructed from Plant Barry to Denbury's Southeast Citronelle Unit, and the CO_2 is injected into saline Paluxy sandstones at depths of approximately 10,000 feet. Injection will continue for three years at a rate of 185,000 tons per year. After finishing of injection, the sequestered CO_2 will be monitored for additional four years in order to determine how well the CO_2 has been contained [60].

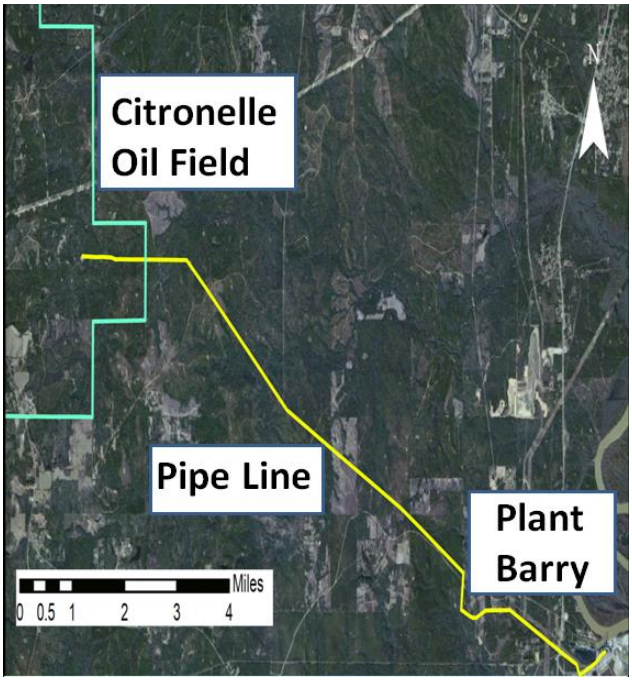

Figure 3-1: CCS project in the Citronelle field [60]

3-1 Geology of the Storage Formation

CO_2 injection site is located inside the Citronelle oilfield boundaries on the southeast flank of Citronelle Dome, three miles far from Mobile County in Alabama. Citronelle oil field (discovered in 1955) covers more than 16,400 acres including about 500 wells. Water flooding which started since 1961 has resulted in 1701 MMbl of cumulative oil production. The current average oil production is about 1670 bbl/day [61].

The Paluxy formation (proposed injection zone) is located at the depth of about 9400 to 10500ft; this formation represents a coarsening-upward succession of variegated shale and sandstone [60]. Based on the logs from the injection well, twenty seven individual sandstones in the Paluxy formation were identified as potential storage reservoirs for CO_2. Seventeen sand layers which are the thickest and most extensive ones were selected for the injection. Citronelle Dome, a broad, gently dipping anticline, provides Citronelle field with structural closure at all stratigraphic horizons of Jurassic through Tertiary age including the Paluxy formation [61]. Moreover, there is an apparent lack of faulting at the Citronelle dome structure. The proposed confining zone for this CO_2 injection test is the basal shale of the Washita-Fredericksburg interval and has an average thickness of 150 ft (Figure 3-2). The aquifers on top and bottom of this confining unit (including Paluxy) represent exhibit extremely low groundwater velocities. Sands layers in the Paluxy formation represent satisfactory reservoir properties (porosity, permeability and extension) for CO_2 storage.

Paluxy formation in the injection zone can be divided into 3 sub layers based on thickness of sand and shale layers. The middle section is mainly dominated by carbonate or lime stone while the other ones consist of thicker sand layers.

Cretaceous	Upper	Selma Group			Confining Unit
		Eutaw Formation			Minor Saline Reservoir
		Tuscaloosa Group	Upper Tusc.		Minor Saline Reservoir
			Mid. Tusc	Marine Shale	Confining Unit
			Lower Tusc.	Pilot Sand Massive sand	Saline Reservoir
Cretaceous	Lower	Washita-Fredericksburg Interval		Dantzler sand	Saline Reservoir
				Basal Shale	Primary Confining Unit
		Paluxy Formation		'Upper' 'Middle' 'Lower'	Proposed Injection Zone
		Mooringsport Formation			Confining Unit
		Ferry Lake Anhydrite			Confining Unit

Formation Tops	Depth (ft bgs)	Interval Thickness (ft)
Bottom of Fresh Water (<1,000 mg/l)	~1,000	
Base of USDW (<10,000 mg/l)	~1,200	
Selma Chalk Group (seal)	4,560	1,310
Eutaw	5,870	150
Tuscaloosa Group		
Upper Tuscaloosa	6,020	720
Middle Tuscaloosa (seal)	6,740	210
Lower Tuscaloosa	6,950	410
Washita-Fredericksburg (seal)	7,360	2,040
Paluxy Formation (target)	9,400	1,110
Mooringsport Formation	10,510	240
Ferry Lake Anhydrite	10,750	190
Rodessa Formation (oil reservoir)	10,940	-

Figure 3-2 Stratigraphic Column for Citronelle Field [60]

The geological model of the Paluxy formation is based the interpretation of 16 well logs in three cross sections (Figure 3-3). The injection well D-9-7 is the well which was considered as a reference well in three cross sections. Seventeen sand layers are picked and correlated (Figure 3-4) based on the highest resistivity and highest SP values. Areal dimensions of some of the thicker sandstones are on the order of 6 square miles or 3,840 acres. The total thickness of sand layers is about 470ft ranging from 10 to 80 ft. Structural and Iso-pach maps of the sand layers would be used to make reservoir simulation model.

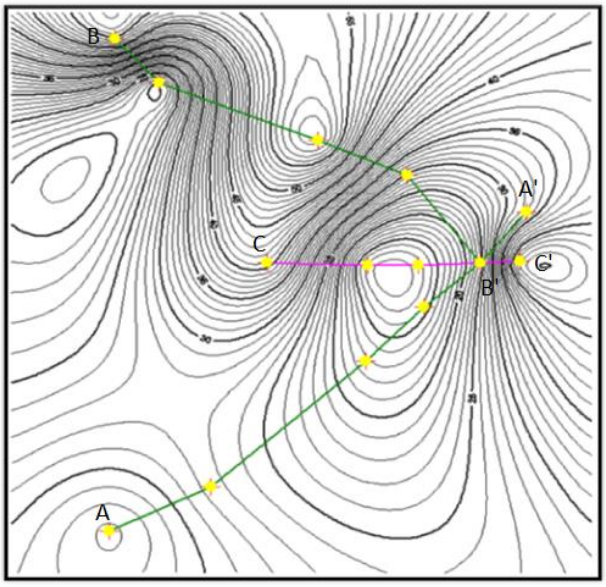

Figure 3-3: Location of three cross sections in the Citronelle Dome

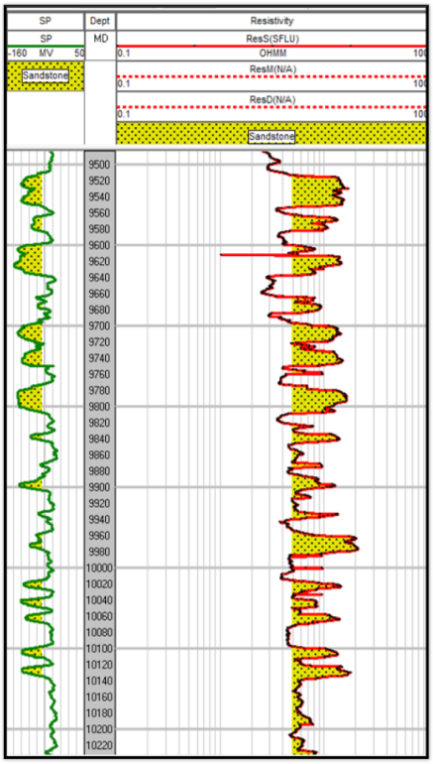

Figure 3-4: sand layers in Injection well (D-9-7)

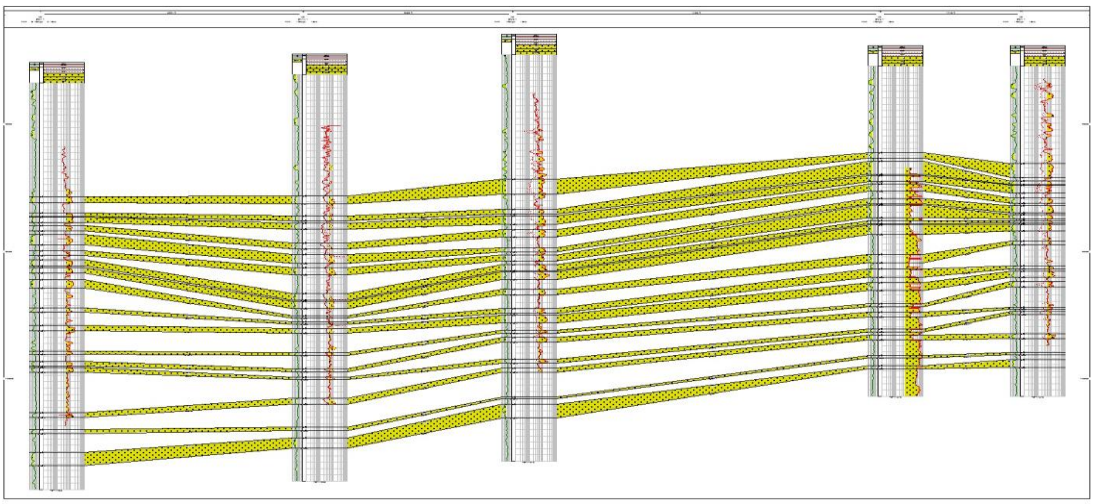

Figure 3-5: Correlated sand layers of cross section B-B'

The final structure maps for top and thickness of 17 sand layers after importing into the reservoir simulator are depicted in Figure 3-6 and Figure 3-7.

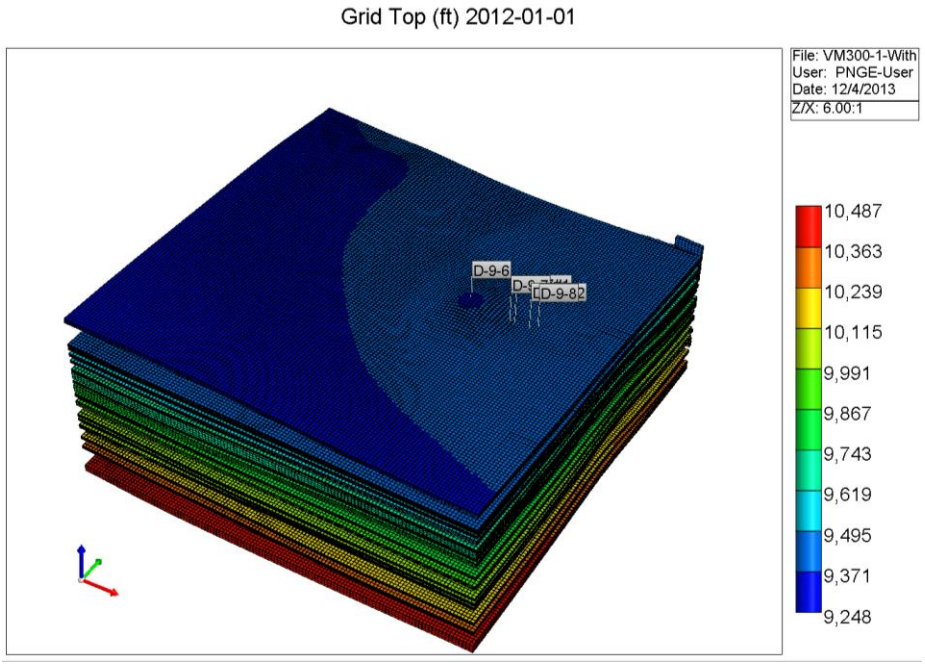

Figure 3-6: Top maps for Sand layers

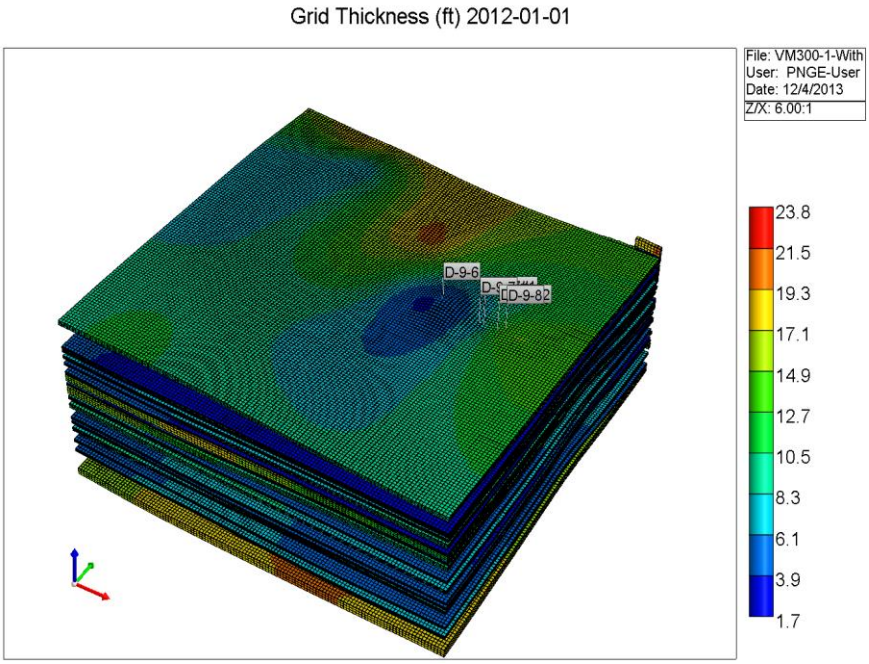

Figure 3-7: Thickness maps for sand layers

3-2 Reservoir Simulation Model

Based upon interpretation and evaluation of geophysical well logs, a comprehensive picture of the subsurface geology has been developed for the reservoir simulation modeling. The reservoir models were built in Computer Modeling Group (CMG) software. Geological structure of the model includes 17 sand layers representing 51 simulation layers. The Cartesian grid coordination has been used with dimension of 50*50*51 grids (Δx and Δy equal to 400 ft). Well logs from 40 offset wells that are within the area of study has been acquired and interpreted in order to generate porosity maps. The resistivity logs are used in the injection depth which is from about 9400ft to about 10500ft. The Archie equation was used [61] to calculate the porosity values using the resistivity logs.

$$\emptyset = \left(\frac{a}{\left(\frac{Rt}{Rw}\right) * Sw^{n}} \right)^{1/m}$$

Where

a = tortousity factor = 1; default value

m = cementation factor = 2.25; best match to Citronelle oilfield porosity logs

n = saturation exponent = 2; common default value

Rw = resistivity of the formation water = 0.045; best match to Citronelle oilfield porosity logs

Sw = Water saturation =0.95; assuming only residual gas saturation

φ = porosity

Rt = True formation resistivity = obtained from logs.

The weighted average for porosity values were calculated by taking the thickness of each layer into account: $\emptyset ave = \frac{\sum \emptyset h}{\sum h}$

The porosity map for the first simulation layer is shown in Figure 3-8. Also, porosity-permeability cross plots that were obtained from core analysis provide reasonable estimates for the permeability distribution within the reservoir.

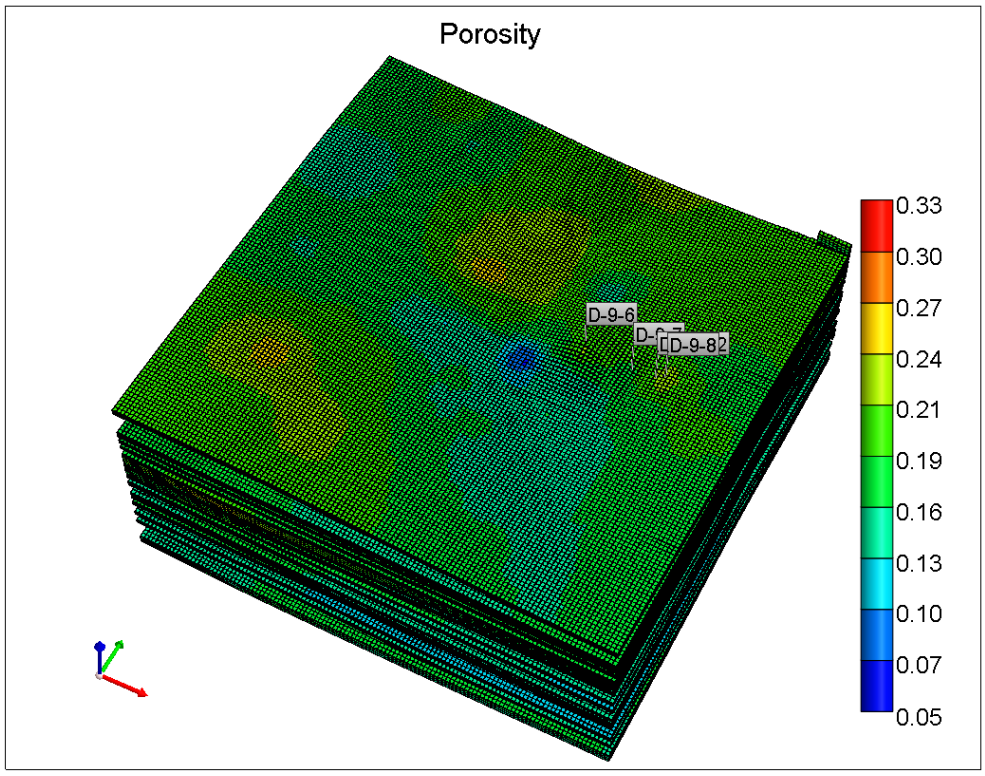

Figure 3-8: Porosity map for the first layer generated by 40 well logs

Relative permeability curves (Figure 3-9) from the history-match of the injection pilot test at the Mississippi Test Site were used in this simulation [61] .Trapped gas saturation was considered value of 7.5 percent; this value determines how much gas is trapped residually due to hysteresis effects. For the reservoir simulation, the injection well was operated with maximum bottom-hole pressure limit of 6,300 psi (based on conservative fracture pressure gradient of 0.772 psi per foot [61]) and injection rate constraint of 9.45 million standard cubic feet per day (500 tons/day). The injection started at the beginning of 2012 and takes 3 years. The saline formation was assumed to be a close reservoir (no-flow boundary condition). Other reservoir properties are summarized in Table 3-1. This is considered as a base case model in the following sections.

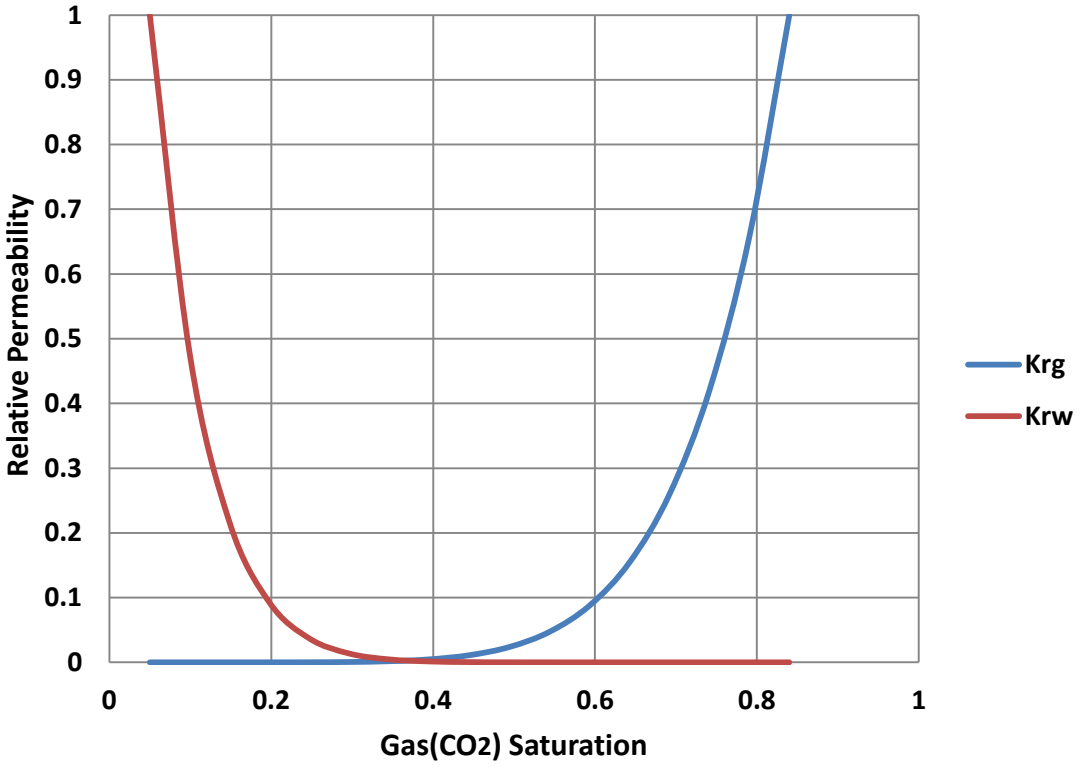

Figure 3-9: Relative permeability curves used in reservoir simulation model

Table 3-1: Reservoir parameters and properties (base case model)

Parameter	**Value**	**Parameter**	**Value**
Permeability(md)	$0.824e^{28.18\varphi}$	Water density(lb/ft^3)	62
Temperature(◦F)	230	Water viscosity(cp)	0.26
Salinity(ppm)	100000	Water compressibility(1/psi)	3.2E-6
Residual gas saturation	0.35	K_v/K_h(permeability ratio)	0.1
Residual water saturation	0.6	Pressure reference@9415ft(psi)	4393

3-2-1Reservoir Model Gridding Analysis

Three different grid geometries were considered in order to examine the effect of the number or size of the grid blocks on the accuracy of the Citronelle numerical model results. The first case is consisted of 50 grid blocks in each i and j direction and 51 layers in k direction. The size of each coarse grid block is 400ft by 400ft. The second case consists of 2419 coarse grids and 729 fine girds in the Area of Investigation (AoI). The size of the each fine grid in the second case is 133ft by 133 ft (Figure 3-10). In the 3rd case (Figure 3-11) the model includes 4 different grid types where the size of grids changes from totally coarse (400 * 400 ft) totally fine (66.7*66.7ft). Table 3-2 lists the total number of each grid type.

Table 3-2: Number of grid blocks in case 3

Grid Type	Coarse	1	2	Fine	Total
Number of Grids	2305	384	666	900	4255

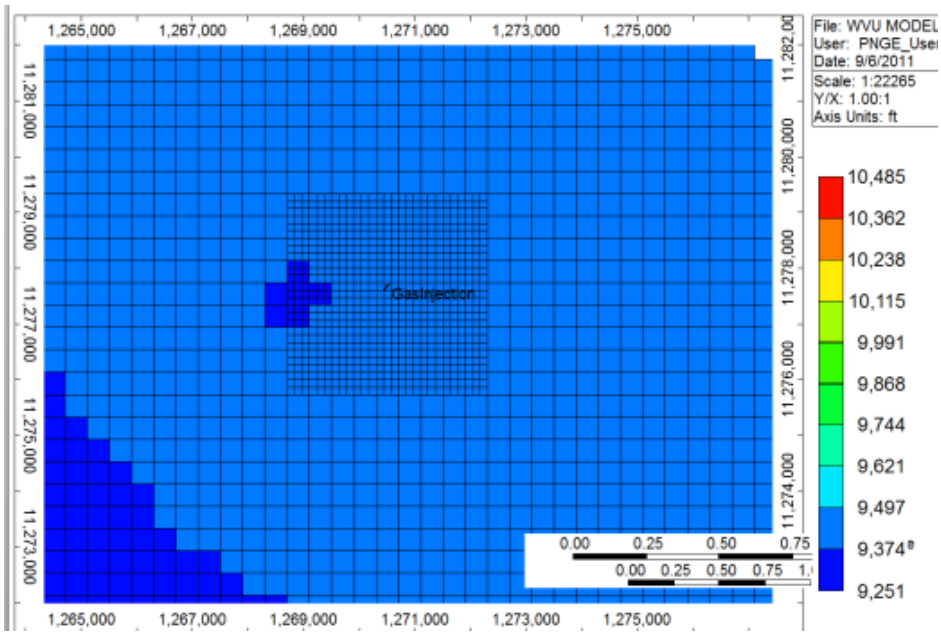

Figure 3-10: Citronelle model with coarse and fine grid-blocks (case 2)

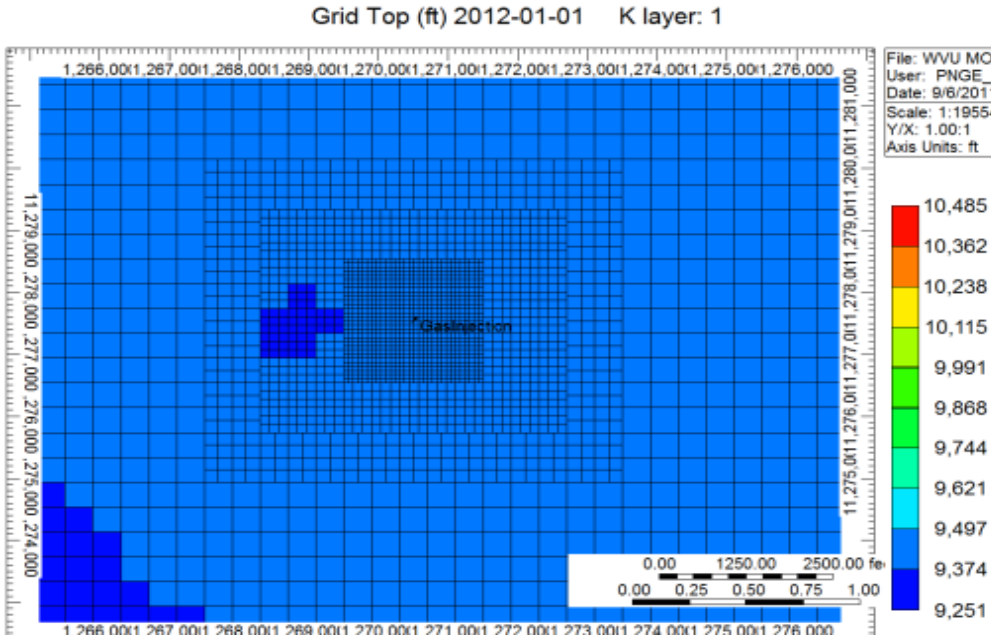

Figure 3-11: Citronelle model having 4 types of grid-blocks (case 3)

As the number of grid blocks increases, the resolution increases which leads the model to deliver more accurate results. It should be mentioned that the run time for case 1(coarse grids) is much less than the case with 4 types of grid blocks. Figure 3-12 illustrates the

effect of number of grids in CO_2 saturation profile in at the location of observation well. As the number of grid blocks increases, significant changes in the gas saturation values are observed. Local Grid Refinement (LGR) in two steps and three steps represent the same accuracy for the gas saturation. Therefore, a reservoir simulation model with fine grids including 150 by 150 grid blocks (in x-y direction) would be used for simulation analysis.

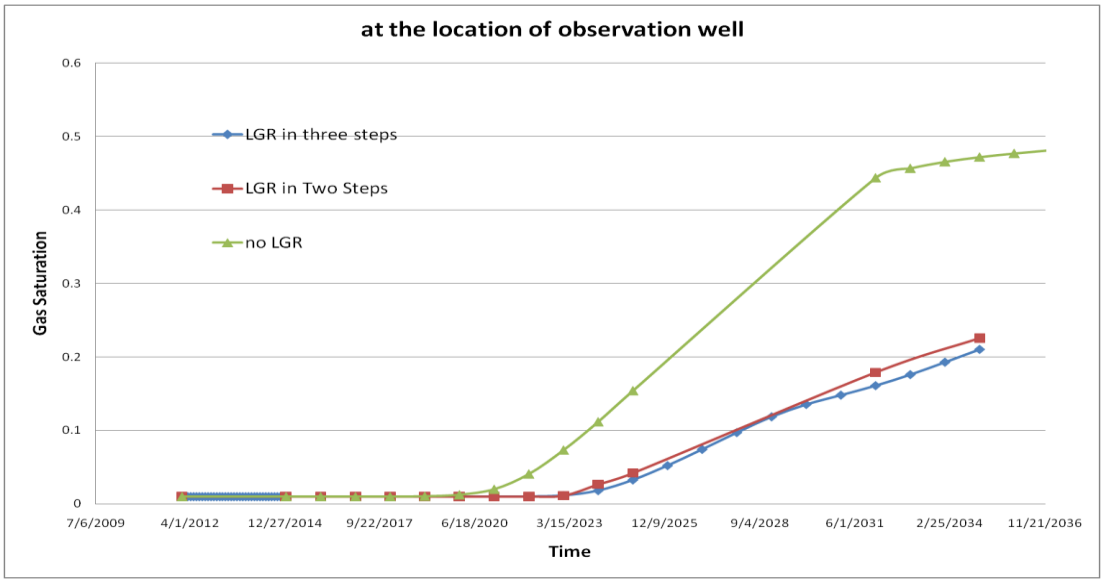

Figure 3-12: CO_2 Saturation at the location of the observation well

3-2-2 Reservoir Simulation Results

Initial reservoir simulation runs showed that maximum extension of the CO_2 plume takes place in the first (top) layer and sixth layer. It is mainly due to the fact that these layers represent sands with the higher permeability, which causes CO_2 to migrate further from the injection well. As it is shown in Figure 3-13, the plume area has the approximate major diameter of 4,933 ft, 500 years after the end of injection [62]. CO_2 plume extension in all the target layers (vertically) is shown in Figure 3-14.

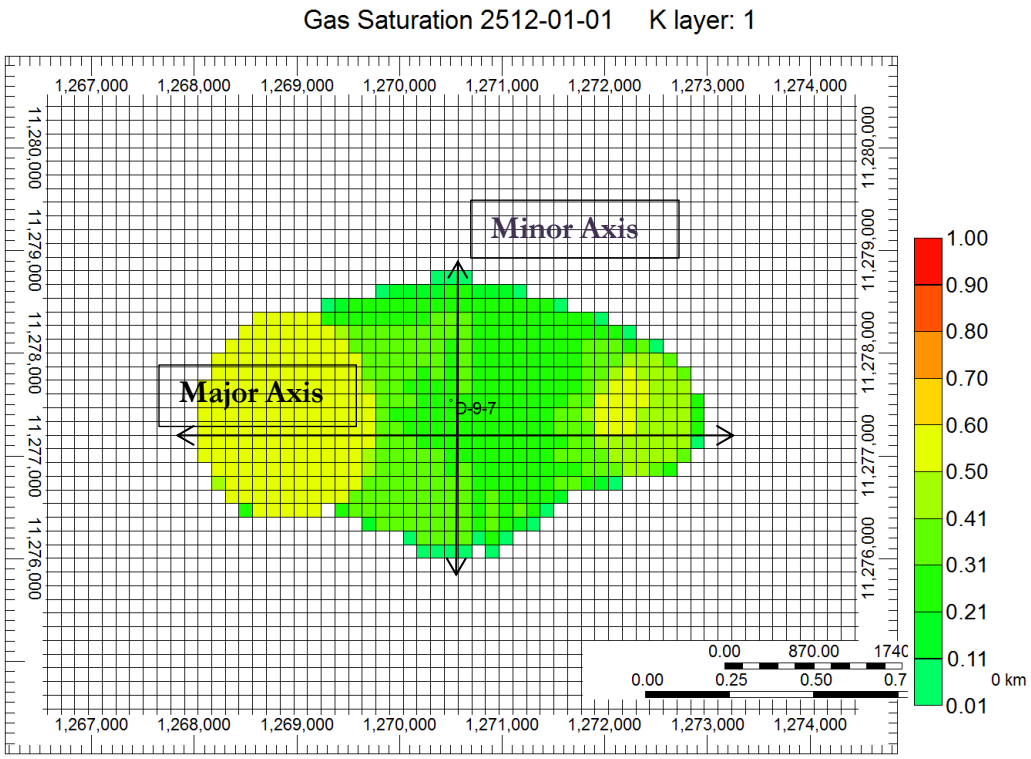

Figure 3-13: CO_2 Plume extension in the first layer 500 years after injection

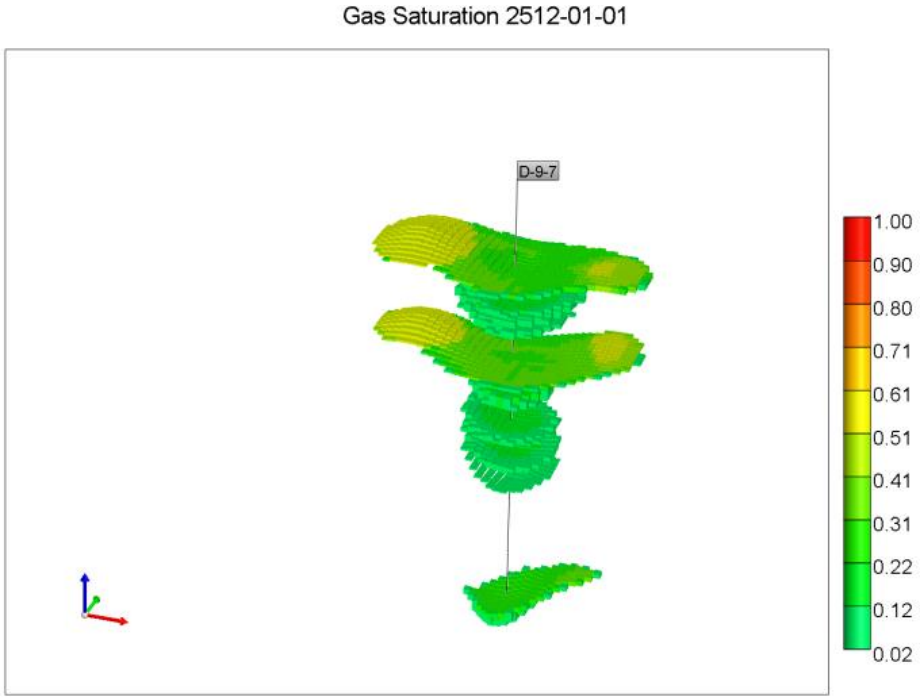

Figure 3-14: CO_2 Plume extension in all layers 500 years after injection

Two Pressure Down-hole Gauges (PDG) are installed in the project's observation well (D-9-8#2), which is located 820 ft at the east side of the injection well. These PDGs can provide real time pressure and temperature measurements. The actual pressure data can be used for reservoir monitoring (especially CO_2 leakage detection) in addition to history matching. Therefore, the main focus of this study is to analyze the reservoir simulation pressure behavior at the grid block that corresponds to the exact location of the PDG in the observation well. Pressure in the observation well rises from 4,400 psi to 4,727 psi (maximum pressure) during the 3 years of injection from 2012 to 2015. After the injection is stopped, the pressure decreases gradually to 4,660 psi after 1 year (stabilized pressure). Finally the reservoir pressure in the observation well follows a very gentle decline and stable trend from 4,660 to 4,653 psi over 500 years (Figure 3-15).

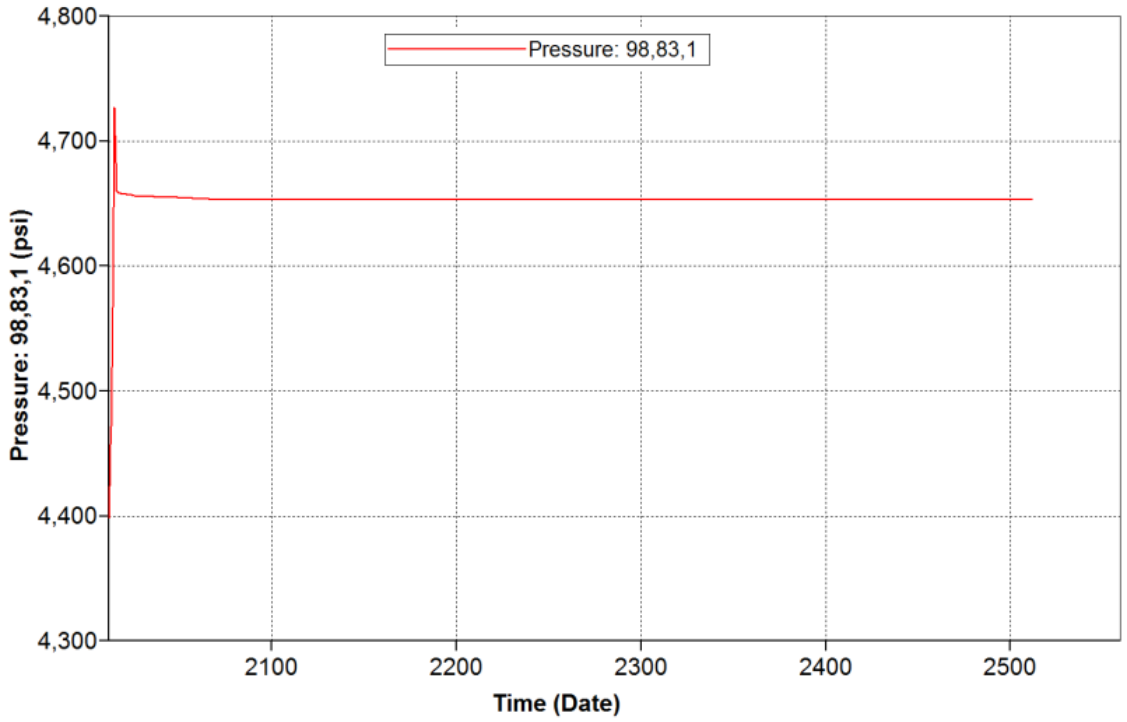

Figure 3-15: Pressure behavior in the observation well (base case model)

3-2-3 Sensitivity Analysis

In this section, simulation model predictions are presented considering uncertainty in some reservoir properties. The sensitivity analysis procedure was to change one parameter at a time (within the uncertainty range) to investigate the corresponding effects on the reservoir pressure (at the observation well) and CO_2 plume extension [63] [64]. The reservoir parameters that we analyzed in this study are permeability (rock type), gas relative permeability, maximum residual gas saturation (hysteresis), vertical to horizontal permeability ratio, boundary condition, brine compressibility, and density. Since the CO_2 plume extension shape is elliptical, the magnitude of the major and minor axis (Figure 3-13) can characterize the underground CO_2 distribution 5, 50 or 500 years after the injection. Additionally, to analyze the reservoir pressure behavior, we focused on maximum (at the end of injection) and stabilized pressures.

3-2-3-1 Permeability

From here on, the contribution of each parameter to the reservoir pressure and plume extension would be identified. In the Citronelle reservoir model, porosity originates from maps that are generated by the interpretation of 40 well logs. Figure 3-16 shows porosity-permeability cross-plots of the Geological Survey of Alabama's southwestern Dataset [61]. In order to have reliable porosity-permeability correlation, the data points are clustered into 5 different rock types, ranging from very tight to very conductive. The initial porosity-permeability data gathered from well D-9-8 (observation well) core analysis, represents a conductive rock type (this is used in the base model). Average ($K = 0.64e^{21.87\varphi}$)) and Very Conductive ($K = 9.964e^{21.74\varphi}$) rock types are introduced to the reservoir simulation model.

For the Average rock type, due to the lower permeability values, CO_2 injectivity decreases. Thus, it is not possible to store the all the CO_2 according to planned target (Figure 3-17). Injectivity of CO_2 is the same for both Conductive and Very Conductive rock types equal to the target values. We can see the results for pressure in Figure 3-18.since the stabilized

reservoir pressure changes very gently during 500 years; we show the results for 20 years after the injection to be able to see more detail. By decreasing the permeability (use of average rock type), CO_2 injectivity decreases to 60% of target value, resulting in reduced reservoir pressure compared with base case. For higher permeability (Very Conductive), stabilized reservoir pressure is 42 psi less than the base case, due to the higher conductivity that prevents more pressure build up. Additionally, an increase in the permeability enhances CO_2 and brine displacement, which leads to larger CO_2 plume extensions, according to Table 3-3.

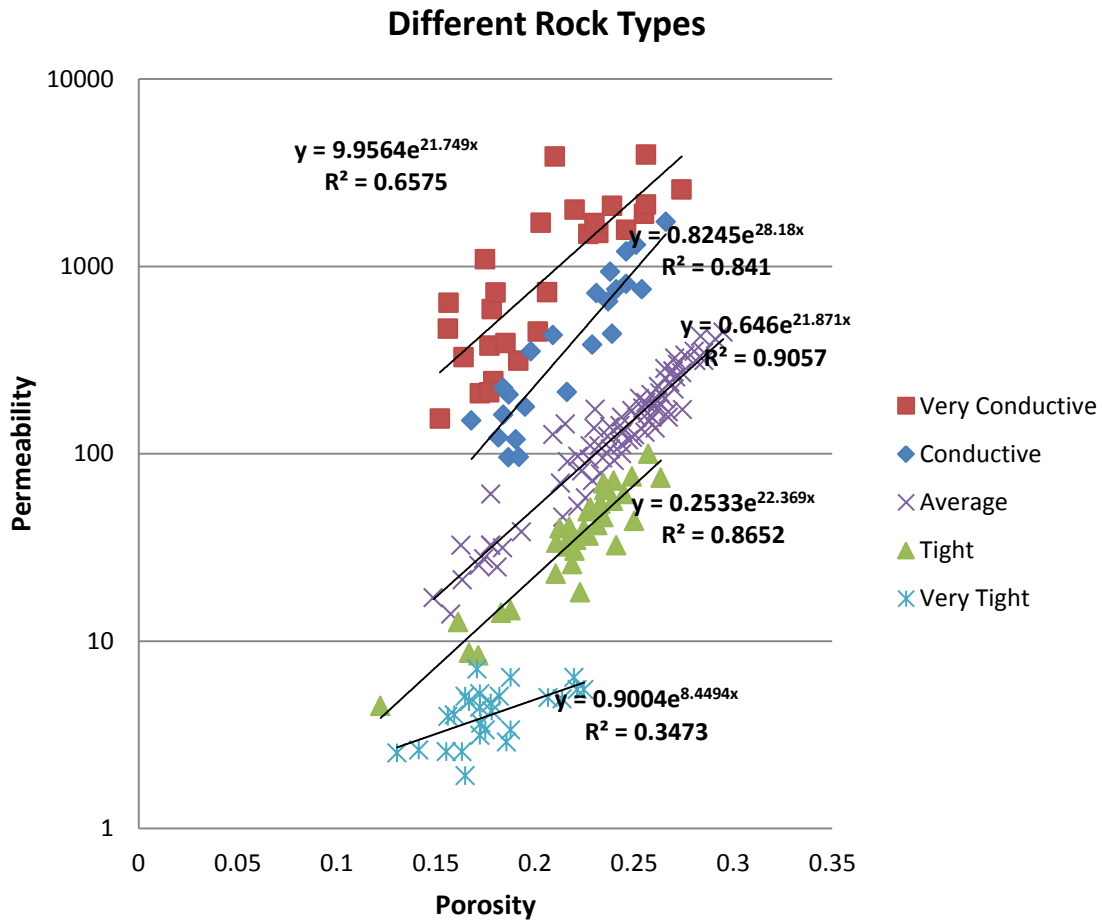

Figure 3-16: Porosity-permeability cross-plot

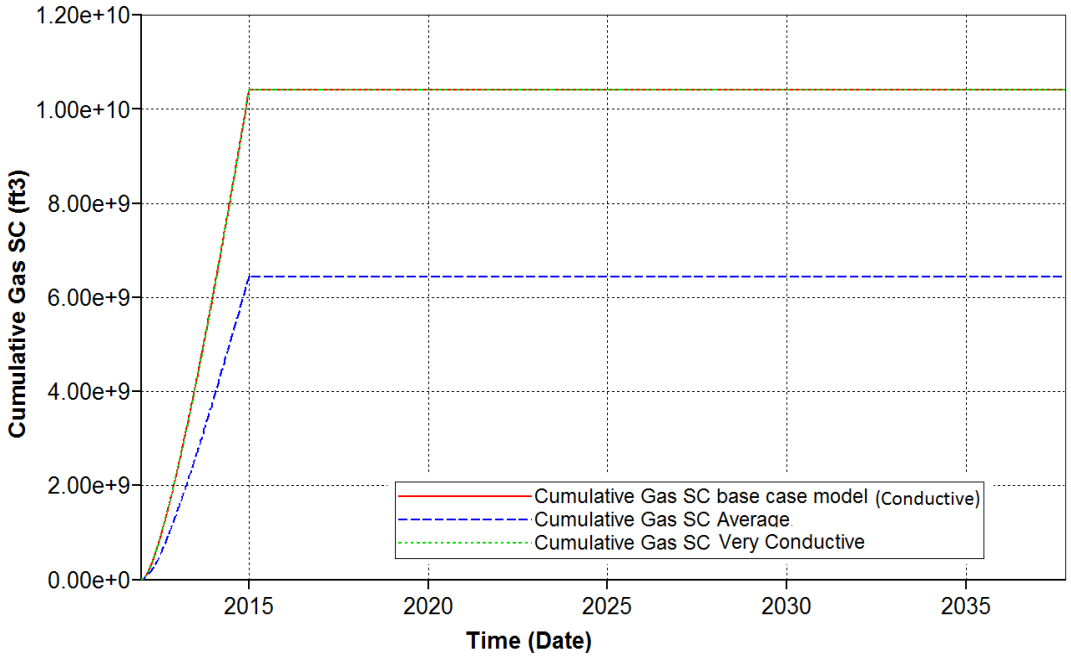

Figure 3-17: CO_2 injectivity for different rock types

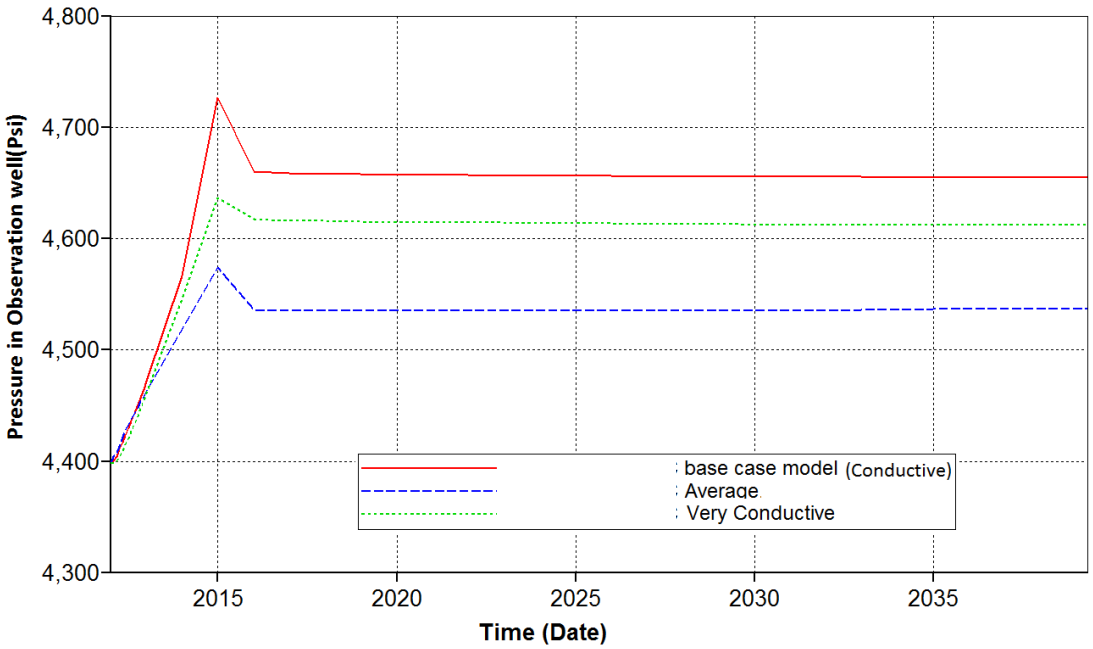

Figure 3-18: Reservoir pressure in observation well for different rock types

Table 3-3: CO_2 Plume extension size over time (in the first layer) for different rock types

			Permeability		
			Base Case (K=0.824e^28.18 φ)	Average (K=0.64e^21.87 φ)	Very Conductive (K=9.964e^21.74φ)
CO_2 Plume Extension	5 Years after Injection	Minor Axis(ft)	2133	1600	2533
		Major Axis(ft)	2400	1733	3200
	50 Years after Injection	Minor Axis(ft)	2533	1867	2800
		Major Axis(ft)	4000	2133	4667
	500 Years after Injection	Minor Axis(ft)	2667	2133	2667
		Major Axis(ft)	4933	3733	5067

3-2-3-2 Permeability

Typically, vertical permeability is determined as a ratio to horizontal permeability. In this study, for the base case model, Kv/Kh is considered to be 0.1. For the sensitivity analysis; we assigned values of 0.3, 0.5, and 0.7 to the Kv/Kh. As shown in Figure 3-19, an increase in the Kv/Kh generates less pressure build up during the injection. However, after the transition time, the higher vertical to horizontal permeability ratio, the higher the stabilized pressure value is. Also, the size of the CO_2 plume slightly increases for higher Kv/Kh, especially for 5 and 50 years after injection (Table 3-4).

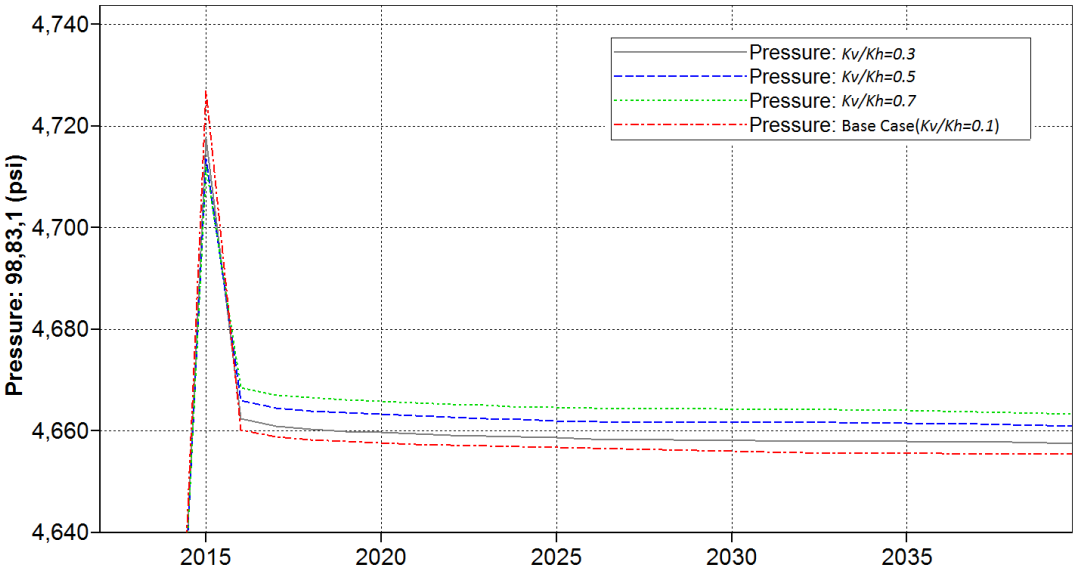

Figure 3-19: Reservoir pressure in observation well for different permeability ratios

Table 3-4: CO_2 Plume extension size over time (in the first layer) for different permeability ratios

			Vertical to Horizontal Permeability Ratio			
			Base Case	Kv/Kh=0.3	Kv/Kh=0.5	Kv/Kh=0.7
CO_2 Plume Extension	5 Years after Injection	Minor Axis(ft)	2133	2133	2133	2267
		Major Axis(ft)	2400	2533	2667	2800
	50 Years after Injection	Minor Axis(ft)	2533	2667	2667	2667
		Major Axis(ft)	4000	4133	4267	4400
	500 Years after Injection	Minor Axis(ft)	2667	2667	2800	2800
		Major Axis(ft)	4933	4933	5067	5067

3-2-3-3 Gas Relative Permeability Curves

Four different gas relative permeability curves were generated so that two of them represent higher at any given gas saturation and two represent lower values of relative permeability, compared with the base case (Figure 3-20). It is worth mentioning that the curves with the higher gas relative permeability values have lower residual gas saturations and vice versa. The results are shown in Table 3-5 and Figure 3-21. Higher gas relative permeability curves represent lower residual gas saturation that can mobilize CO_2 phase earlier (at lower gas saturations). Therefore, CO_2 moves further resulting in larger CO_2 plume extension. Additionally, higher gas relative permeability increases the stabilized reservoir pressure. Reversely, lower gas relative permeability leads to less extensive plume and lower stabilized reservoir pressure

Table 3-5 Plume extension size over time in the first layer for different gas relative permeability curves

			Gas Relative Permeability				
			Base Case	Krg Low 2	Krg Low 1	Krg High1	Krg High2
CO_2 Plume Extension	5 Years after Injection	Minor Axis(ft)	2133	1867	2000	2133	2400
		Major Axis(ft)	2400	2133	2266	2533	2800
	50 Years after Injection	Minor Axis(ft)	2533	2133	2267	2667	2933
		Major Axis(ft)	4000	2800	3467	4267	4533
	500 Years after Injection	Minor Axis(ft)	2667	2400	2533	2800	2933
		Major Axis(ft)	4933	4133	4533	5067	5467

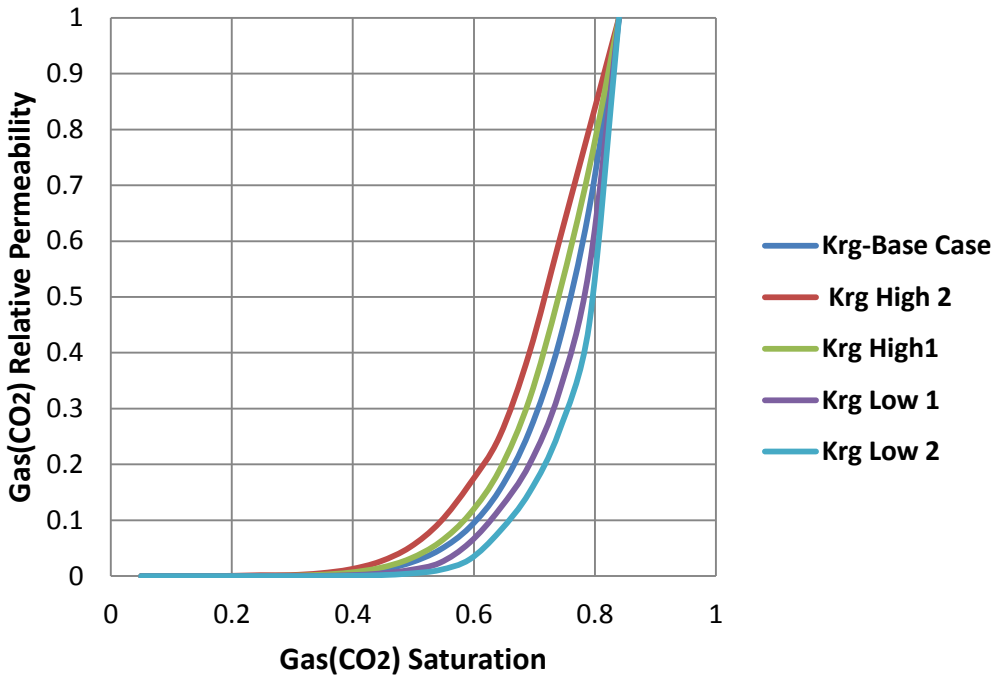

Figure 3-20: Different gas relative permeability curves

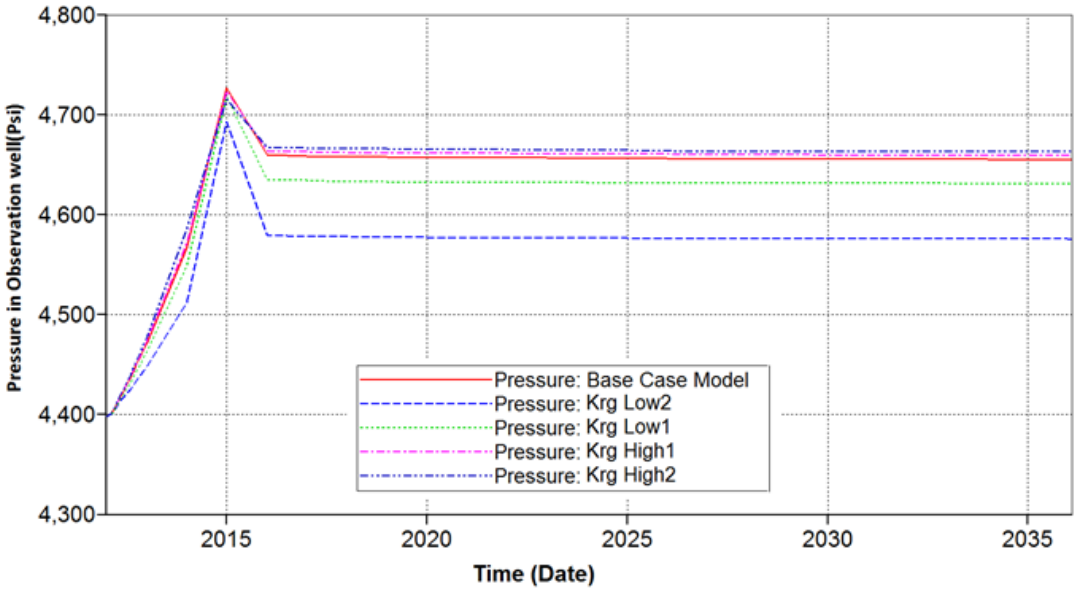

Figure 3-21: Reservoir pressure in observation well for different gas relative permeability curves

3-2-3-4 Maximum Residual Gas Saturation

Generally, drainage relative permeability curves are provided for the reservoir simulation model. When the maximum residual gas saturation is introduced, the imbibition gas relative permeability curve can be determined based on the drainage curve [21]. During CO_2 movement in the reservoir, water imbibition causes a portion of gas phase to be trapped in the pores (residual trapping). Therefore, when the maximum residual gas saturation increases, more gas is trapped, resulting in less mobile CO_2 and consequently a smaller CO_2 plume extension (Table 3-6). Changing maximum residual gas saturation has no significant impact on the reservoir pressure.

Table 3-6: CO_2 Plume extension size over time in the first layer for different maximum residual gas saturations

			Maximum Residual Gas Saturation(Hysteresis)			
			Base Case	0.05	0.1	0.2
CO_2 Plume Extension	5 Years after Injection	Minor Axis(ft)	2133	2133	2133	2133
		Major Axis(ft)	2400	2400	2400	2400
	50 Years after Injection	Minor Axis(ft)	2533	2533	2533	2400
		Major Axis(ft)	4000	4000	3867	3733
	500 Years after Injection	Minor Axis(ft)	2667	2800	2533	2533
		Major Axis(ft)	4933	4933	4800	4533

3-2-3-5 Brine Compressibility

In a closed geologic system, the amount of CO_2 that can be injected into the saline reservoir is mostly dependent on the availability of the additional pore space that can be provided due to brine compressibility [64]. Additionally, compressibility determines how much injected fluid contributes to reservoir pressure build up or brine volume change (also can be referred to as a change in brine density). As observed in Figure 3-22, an increase in brine compressibility results in lowering the maximum and stabilized reservoir pressures. For higher brine compressibility, injected CO_2 results in more changes in brine density rather than generating pressure build up in the reservoir. Changing brine compressibility shows no considerable influence on the CO_2 plume extension.

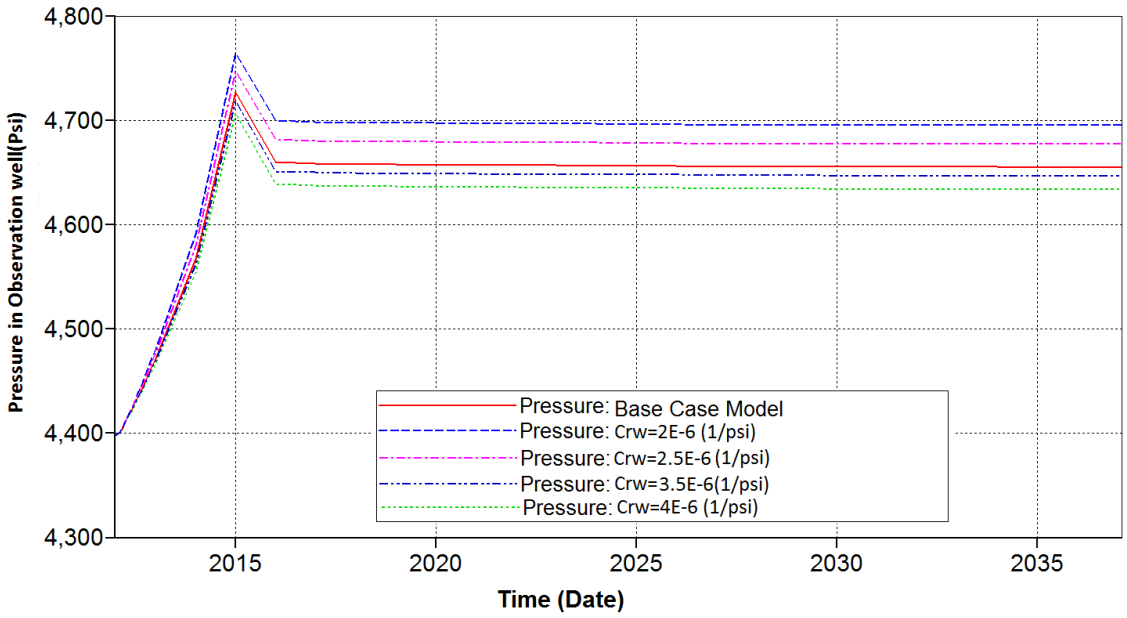

Figure 3-22: Reservoir pressure in observation well for different brine compressibility

3-2-3-6 Brine Density

The impact of a change in brine density on the reservoir pressure can be analyzed by considering the fact that denser the brine is, the less compressible it is, allowing more pressure build up during and after CO_2 injection. As it is illustrated in Figure 9, the higher brine density contributes to more pressure gain for the reservoir (both maximum and stabilized pressures). The influence of the brine density on CO_2 plume extension is addressed by the driving mechanism that governs fluid movement in the reservoir. During CO_2 injection, viscous forces makes the CO_2 move forward, and after injection, buoyancy would be the dominant driving force. The density difference between brine and CO_2 determines the magnitude of the buoyant force [23]. Higher brine density results greater density differential and consequently, more buoyance force. Therefore an increase in brine density accounts for more buoyant force to be exerted to the CO_2 plume resulting in larger extensions (Table 3-7).

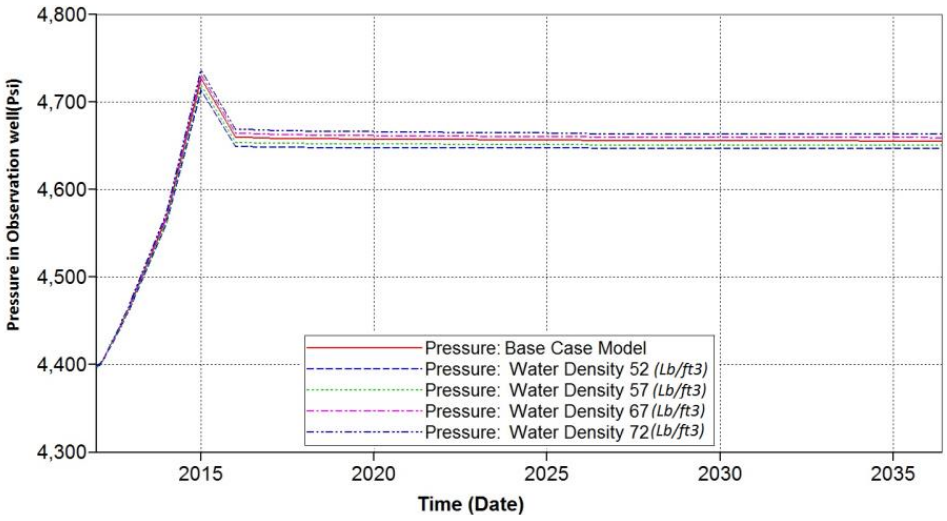

Figure 3-23: Reservoir pressure in observation well for different brine densities

Table 3-7: CO_2 Plume extension size over time (in the first layer) for different brine densities

			Brine Density(lb/ft3)				
			Base Case	52	57	67	72
CO_2 Plume Extension	5 Years after Injection	Minor Axis(ft)	2133	2133	2133	2133	2133
		Major Axis(ft)	2400	2267	2400	2533	2667
	50 Years after Injection	Minor Axis(ft)	2533	2533	2533	2533	2667
		Major Axis(ft)	4000	3467	3733	4133	4133
	500 Years after Injection	Minor Axis(ft)	2667	2533	2667	2800	2800
		Major Axis(ft)	4933	4667	4933	4933	5066

3-2-3-6 Boundary Condition

In this section, we assume that the saline reservoir in the Paluxy formation is not a closed system. A Fetkovich aquifer which keeps the reservoir pressure constant at the reservoir boundaries is assigned to the East, East- South and East-South-West edges of the reservoir (Figure 3-24). As shown in Figure 3-25, reservoir pressure behavior in the open system is significantly different compared to what was observed in the previous sections. First of all, maximum reservoir pressure at the end of injection is much less (almost 200 psi) in the open systems. Secondly, the stabilized pressure reaches initial or native reservoir pressure after particular moment of time.

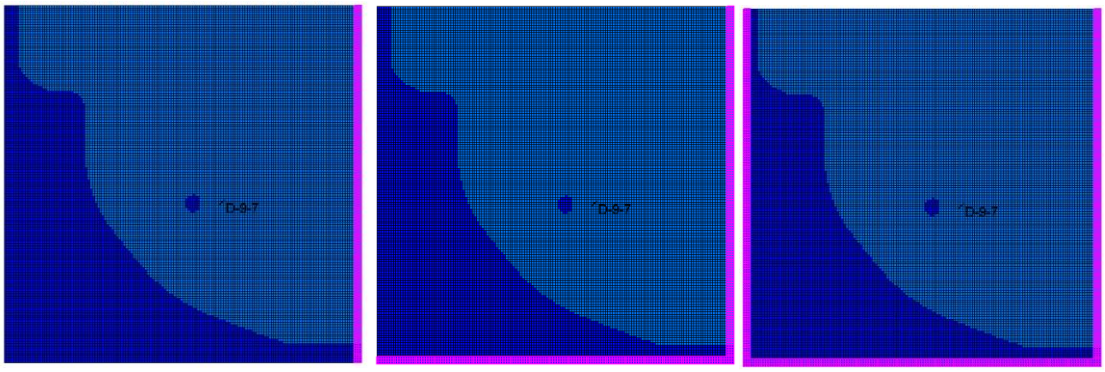

Figure 3-24: Different locations for constant pressure boundary (Fetkovich aquifer)

As the portion of reservoir boundary that is exposed to the constant pressure (Fetkovich aquifer) increases, less pressure build up is observed at the end of injection. Additionally, when more edges of the reservoir are connected to open aquifer, it takes less time that reservoir pressure reaches to the native conditions. Changing reservoir boundary conditions represents an insignificant effect on the CO_2 plume size (Table 3-8).

Table 3-8: Plume extension size over time (in the first layer) for different boundary conditions

			Reservoir Boundary(Fetkovich Aquifer)			
			Base Case	East	East+ South	East+ South+ West
CO_2 Plume Extension	5 Years after Injection	Minor Axis(ft)	2133	2133	2267	2267
		Major Axis(ft)	2400	2400	2667	2800
	50 Years after Injection	Minor Axis(ft)	2533	2533	2667	2667
		Major Axis(ft)	4000	4000	4133	4133
	500 Years after Injection	Minor Axis(ft)	2667	2800	2800	2800
		Major Axis(ft)	4933	5066	5066	5066

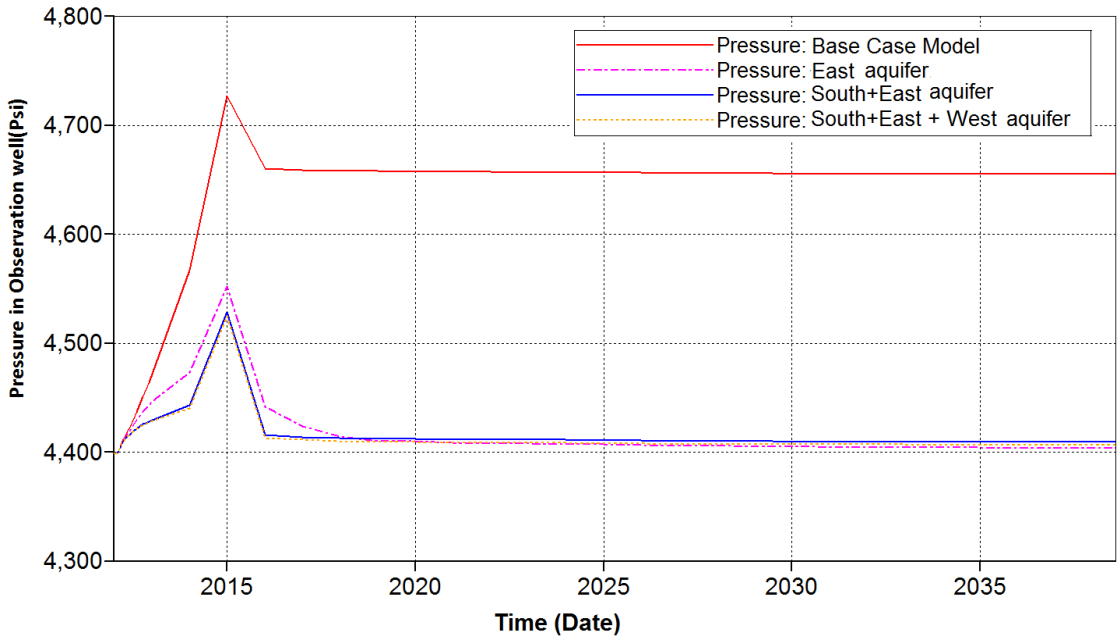

Figure 3-25: Reservoir pressure in observation well for different boundary conditions

3-3: Conclusions

In this chapter, all the steps for reservoir simulation model development for CO_2 injection in the Paluxy saline reservoir of the Citronelle Dome were explained. The model was used to predict storage performance behavior. Sensitivity analyses was performed to study the impacts of reservoir uncertainty on the reservoir pressure in the observation well and CO_2 plume extension. The results of sensitivity analysis can be considered for risk assessment in addition to history matching the reservoir simulation model while actual field measurements (pressure data) are available. The main findings can be summarized as:

- Rock type (permeability) contributes to CO_2 injectivity, reservoir pressure and CO_2 plume extension significantly. Higher permeability represents more extensive CO_2 plume and less reservoir pressure gain. Also an increase in vertical to horizontal ratio leads to higher stabilized pressure and CO_2 plume extension.
- It is observed that an increase in gas relative permeability results in a higher stabilized pressure and a larger CO_2 plume extension. Additionally, the higher maximum residual gas saturation ends up with more residual trapping, accounting for a lower CO_2 plume extension.

- Brine compressibility plays a role in reservoir pressure build up, especially in a closed geologic system. When brine compressibility rises, we observe a decrease in stabilized reservoir pressure.
- Density of brine is the parameter that affects both reservoir pressure and CO_2 plume extension. Denser brine causes more buoyancy force, which drives CO_2 to move further and distributes in more area. Also higher brine density values contribute to more reservoir pressure build up.
- Changing the boundary condition of the reservoir from closed to constant pressure, affects reservoir pressure behavior significantly. When Fetkovich aquifers are placed at the edges of the reservoir, maximum pressure build up decreases notably. In addition, stabilized reservoir pressure comes back to native reservoir pressure after a while when injection is ceased.

Chapter 4 Model's History Match

All the steps for development of Reservoir Simulation model for CO_2 injection into the Citronelle saline aquifer with commercially available software (CMG-GEM) were explained in Chapter 3. Field measurements of CO_2 injection rates are assigned as the operational constraint to the model. In addition to the Injection rates, high frequency, real-time pressure data from two down-hole pressure gauges imbedded in an observation well (833 ft away from the injection well) is also provided. Several uncertain reservoir properties were tuned within reasonable ranges in order to find proper match between simulated pressure results and actual field measurements [65].

4-1 Introduction

Different types of potential risks, like leakage of CO_2 or brine from the target zone, are generally associated with geological storage of CO_2. Reservoir simulation and modeling in addition to implementation of appropriate monitoring techniques are considered to be expedient tools for CO_2-risk management.

Reservoir pressure/temperature measurement by down-hole gauge has been widely used in the oil and gas industry for reservoir monitoring, well test analysis and history matching. In CO_2 sequestration projects, real time reservoir pressure can deliver CO_2 migration/leakage indications. Meckel *et al* [66] interpreted permanent down-hole gauges (PDGs) data collected from single well at injection and above zone monitoring interval for CO_2 injection at Cranfield field. They suggested almost no inter-formational communication (vertical) at the site based on analysis of pressure changes that were due to seven injection and nine production wells' activities. Tao *et al* [67] analyzed the same pressure and temperature data (collected from the monitoring well at Cranfield) and concluded a very small leakage had occurred from the injection interval to the overlying formation. PDG data can also provide valuable information for reservoir simulation models.

Reservoir models can be used for assessment of CO_2 storage capacity, well injectivity; CO_2 trapping mechanisms, CO_2 plume extension, and reservoir pressure build up. Sifuentes *et al* [63] studied the effect of different physical parameters on the CO_2 trapping in Stuggart formation in Germany. In order to determine the contribution of each parameter on CO_2 trapping, they used reservoir simulation coupled with experimental design to perform

sensitivity analysis. Torn *et al* [68] carried out almost the same sensitivity analysis on Mt. Simon sandstone model to assess storage capacity and safety issues. Senel *et al* [69] performed a reservoir simulation and uncertainty analysis study on CO_2 injection in the same formation (Mt. Simon sandstone -USA) incorporating more geophysical and petro-physical data. They investigated the effect of uncertainty on trapping mechanisms and CO_2 area of extension by providing probabilistic estimates. Masoudi *et al* [70] coupled a geo-mechanical and simulation model in order to study feasibility and risks associated with CO_2 injection in M4 Field (East Malaysia).They determined maximum allowed reservoir pressure considering cap rock integrity for different CO_2 injection scenarios.

Reservoir simulation performance must be validated by checking if the model is able to regenerate the past behavior of a reservoir. History matching of oil and gas reservoir models are much more applied (compared to CO_2 storage models) due to availability of large amount of production or/and injection data. For CO_2 storage projects especially in saline formations, reservoir history data are limited to injection rate in addition to down-hole injection/observation well pressure. Mantilla *et al.* [71] used probabilistic history matching software known as Pro-HMS which incorporated injection data from active injection and inactive observation wells. They implemented Pro-HMS to a synthetic model, CO2 storage in aquifer with one/three injection and one observation wells, to obtain high permeability streaks by use of only injection and pressure data. In another history matching attempt, Krause *et al.* [72] conducted core flooding (brine/CO_2) followed by numerical simulation of the experiment. They matched Simulation results with experimental data by calculation of permeability, using porosity and capillary pressure data. Xiao *et al* [73] studied numerical simulation of CO_2 /EOR and storage in a pilot-5spot pattern unit of SACROC field. Since the target storage field had long term production/injection history, they performed history matching for five wells' gas, oil and water production. They also predicted reservoir performance for three enhanced oil recovery (EOR) injection schemes and analyzed CO_2 storage capacity considering different CO_2 trapping mechanisms.

This chapter explains one of the very few of its kind that aims to history match reservoir simulation model of CO_2 injection in Citronelle Dome (saline formation). The available field data for history matching are ten months of CO_2 injection rate as wells as pressure data coming from two gauges installed in the observation well.

4-2 History Match

Locations of injection and observation wells are shown in Figure 4-1.CO_2 injection started on August 20th, 2012 with the rate of 918 Mcf/day. After that time, the injection rate increased with an oscillating trend (because of operative difficulties) until the end of September 2012 when it reached 9 Bcf/day (targeted rate). Then, the injection continued until August 2013 with a stable rate although periodic shut downs occurred. The daily injection rate from the beginning up to August 2013 is shown in Figure 4-2. These injection rates were used in the reservoir simulation model as operational constraints.

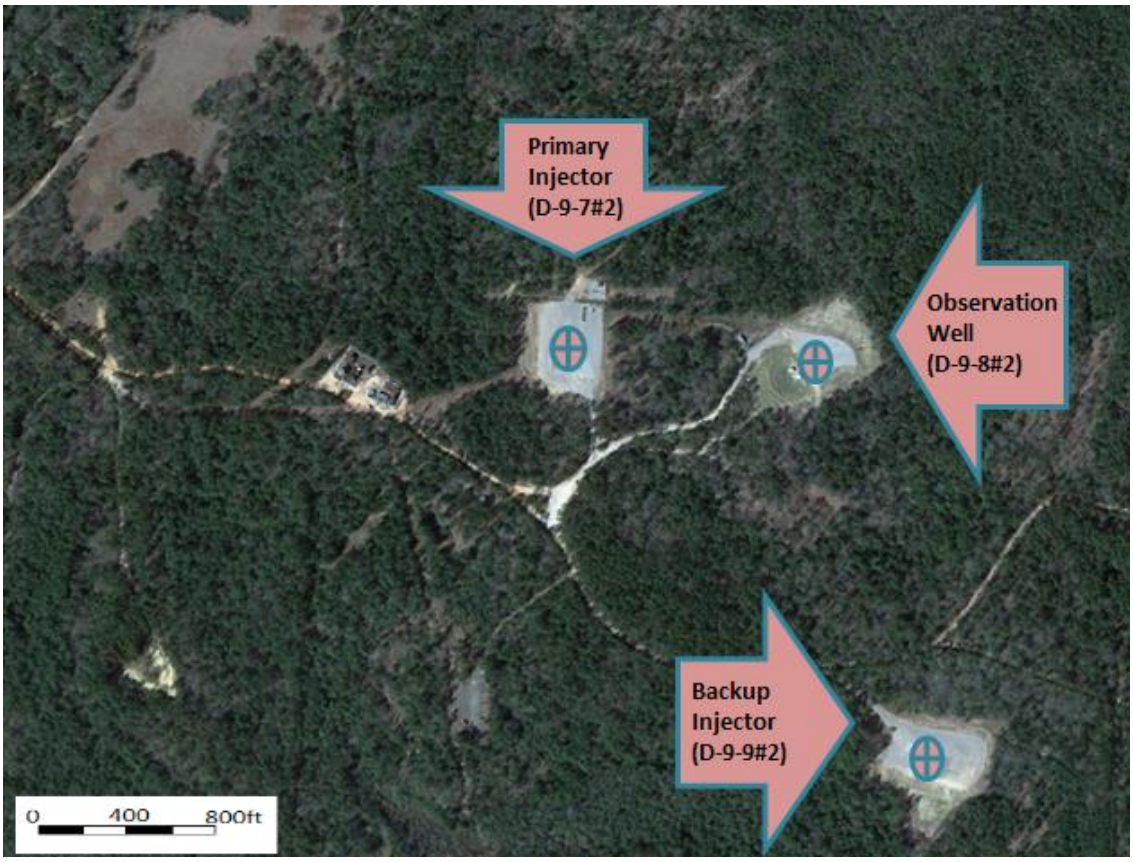

Figure 4-1: Locations of the CO_2 injection, observation and backup injection wells in Citronelle Dome

In the observation well (D-9-8#2) at Citronelle field (Figure 4-1), two Pressure Down-hole Gauges PDG-5108/5109 are installed at different depths of 9416 and 9441 ft TVD in order to provide real time pressure and temperature readings during and after injection period. The pressure data is available from Mid-August of 2012 until August 1st 2013, recorded at

every minute, listed in 1440 records daily. There were some gaps in the pressure records due to onsite computer failure. Since history matching the data on a minute basis was computationally expensive and time consuming, the pressure data was summarized by averaging over each day. The results of actual pressure data on a daily basis are illustrated in Figure 4-3.

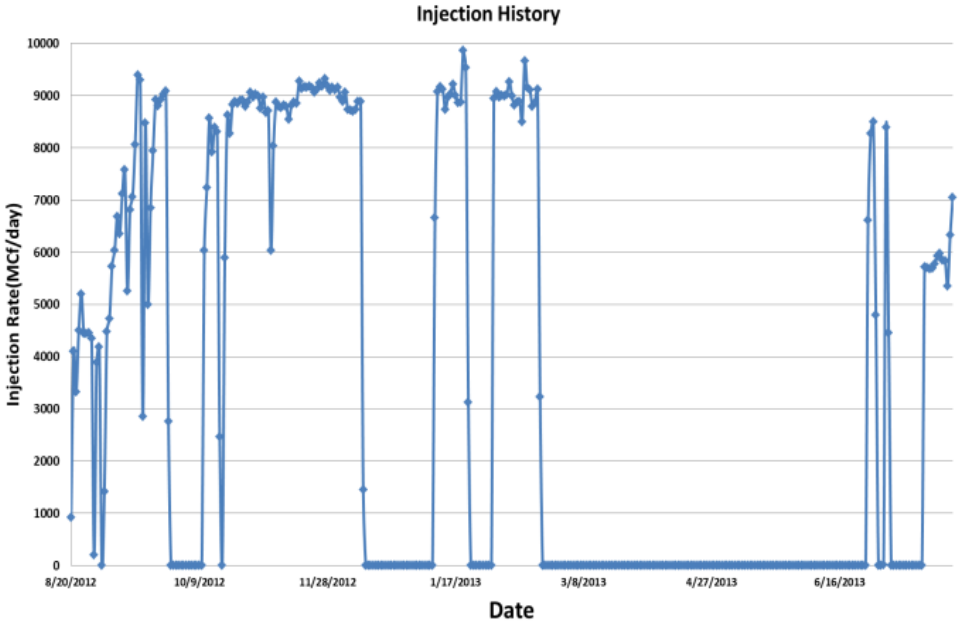

Figure 4-2:CO_2 injection rate history

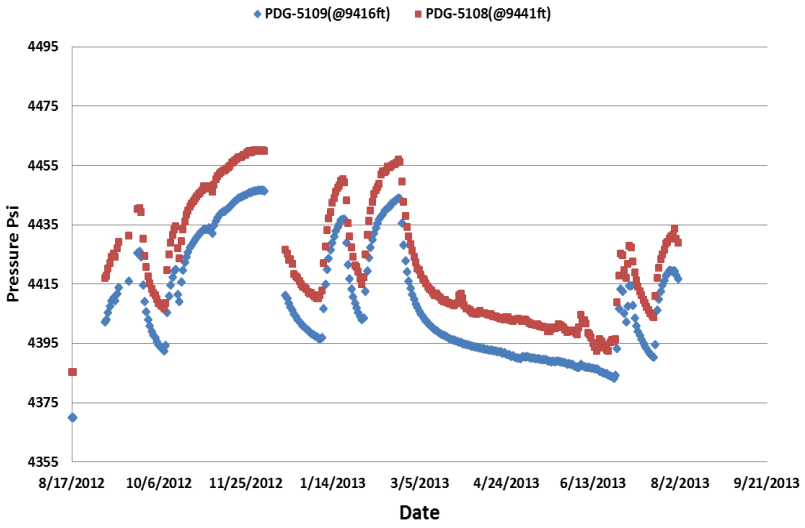

Figure 4-3: Daily pressure data from PDGs at observation well

Initially a base case reservoir model was developed considering reservoir properties that are summarized in Table 4-1. Porosity maps for each simulation layer were acquired by interpretation of 40 well logs. In this model, operational constraints were the actual CO_2 injection rates in addition to maximum bottom-hole pressure limit of 6,300 psi. The solubility of CO_2 in the brine was not considered in the base model. Block pressure for the grids corresponding to the PDGs were compared with the actual data. Simulated pressure data using the base model are plotted against actual pressure history in Figure 4-4.

Table 4-1: Reservoir parameters and properties (base model)

Parameter	**Value**	**Parameter**	**Value**
Permeability (md)	460	Water density (lb/ft^3)	62
Temperature (◦F)	230	Water viscosity (cp)	0.26
Salinity (ppm)	100,000	Water compressibility (1/psi)	3.2E-6
Residual gas saturation	0.35	Kv/Kh (permeability ratio)	0.1
Residual water saturation	0.6	Pressure reference@9415 ft (psi)	4393

The simulation data were matching neither at the start point, nor the difference between the values of two gauges. Initial reservoir pressure was adjusted by changing the reference pressure to 4370 psi at the datum depth of 9416 ft. Pressure gradient between the PDGs was 0.62 psi/ft while between the simulation grids was 0.43 psi/ft. Therefore, it was concluded that the brine density should be set at a higher value in order to mimic the same pressure gradient Brine density at the reservoir conditions can be calculated using the following equation:

$$\tilde{\rho}_{br} = \tilde{\rho}^{0}_{br}\left[1 + c_{br}\left(p - p^{0}\right)\right]$$

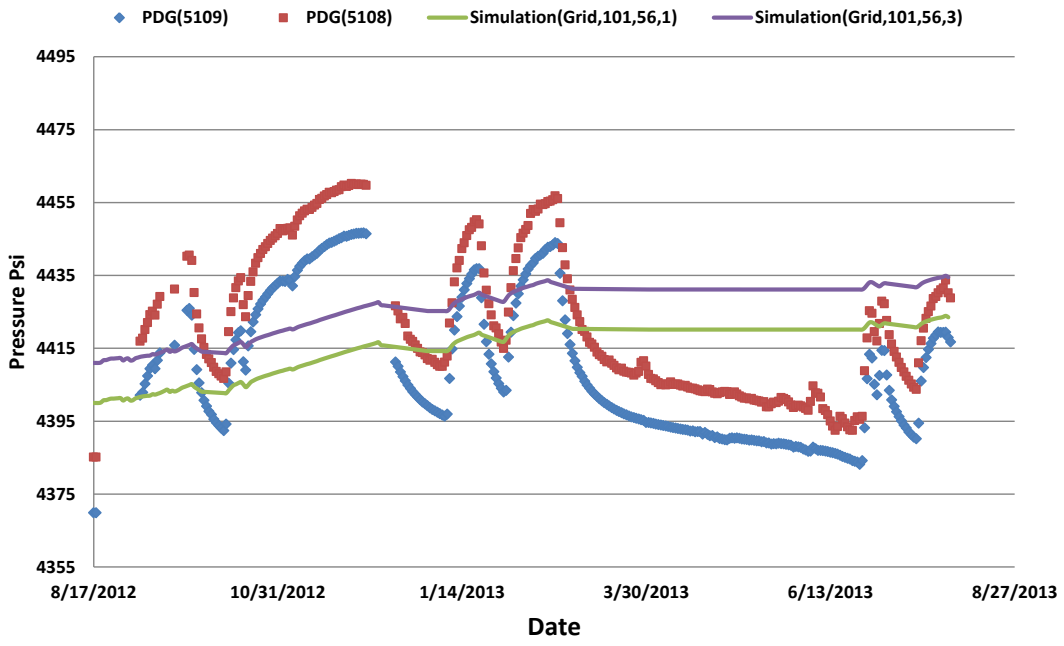

Figure 4-4: Actual pressure vs. simulated pressure in the base model.

Keeping the brine compressibility unchanged, density of brine should be altered to 87 lb/ft^3.

As mentioned in Chapter 3, a thorough sensitivity analysis was performed to study the effect of several uncertain reservoir parameters on pressure behavior in the observation well. The results of sensitivity analysis showed that permeability significantly contributed to injectivity, CO_2 plume extension and reservoir pressure. Using available core data (not taken from Citronelle field) porosity-permeability cross-plot was generated for the Paluxy formation (Figure 3-16). Available data from the core samples taken from injection well demonstrated the dominancy of conductive rock type in the vicinity of the injection area [60]. Also, vertical to horizontal permeability ratio was calculated to be 0.58 using core data analysis. Modification of pressure reference, brine density and permeability in addition to setting zero transmissibility between the sand and shale layers resulted in pressure predictions illustrated in Figure 4-5.

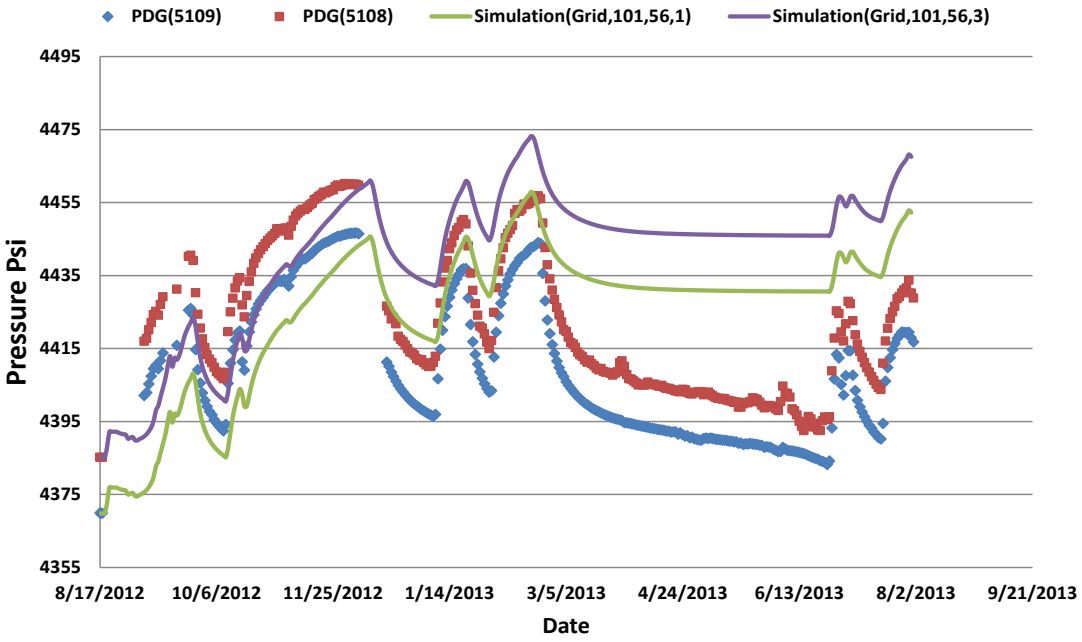

Figure 4-5: Model's pressure results and actual history; modified pressure reference, brine density and permeability

By Implementation of modified parameters in the model, prediction results resembled initial pressure and pressure gradient similar to the actual data. However, model pressure predictions didn't follow PDGs pressure trend correctly. As shown in Figure 4-5, reservoir simulation results underestimated actual data during first four months after the injection, and overestimated the rest of pressure history. Additionally, simulation pressure drawdowns reached a stable trend much faster, compared with actual data. This behavior can be explained by the fact that higher permeability (in the model) resulted in lowering the time for pressure drawdown to reach a steady trend. Therefore, it was necessary to decrease the permeability in the model to adjust pressure drawdown behavior. On the other hand, lowering the permeability led to CO_2 injectivity reduction (as shown in chapter 3). As a result, reservoir model was divided into two regions: (a) grids in the vicinity of the injection zone (20*20 grids around the injection well) and (b) grids outside the injection zone (Figure 4-6). To correct model's pressure drawdown trend, dual modification in reservoir permeability was done by decreasing permeability in region "a" and increasing permeability in region "b".

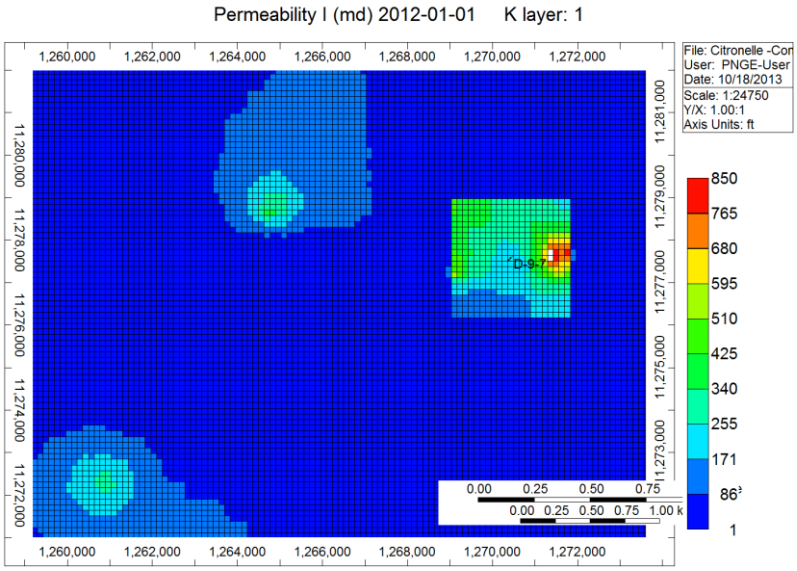

Figure 4-6: Two permeability regions in the reservoir

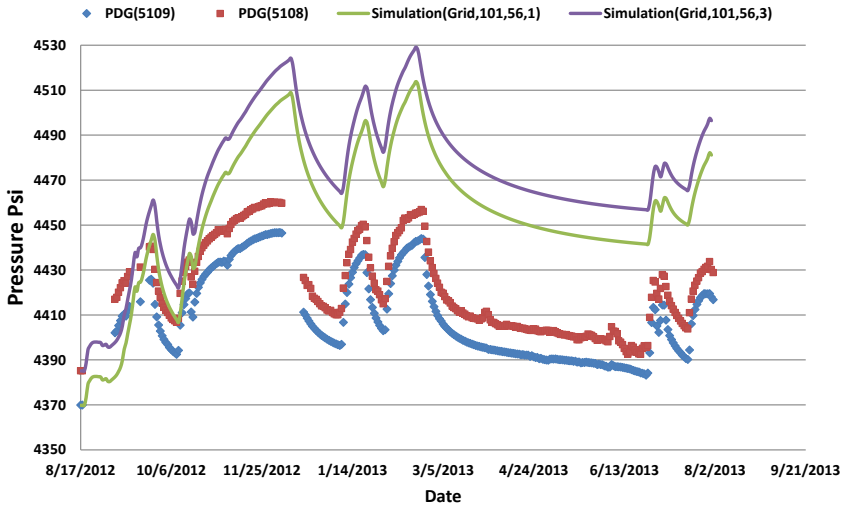

Figure 4-7: Model's pressure results and actual history; modified permeability in different reservoir regions

As shown in Figure 4-7, although modifications in the model's permeability improved pressure drawdown behavior, pressure predictions were overestimated considerably compare with the actual PDG data. To lower pressure results, solubility of CO_2 in the brine (aqueous phase) was incorporated in the model [21]. More importantly, volume modifier was assigned to the grids at the east boundary of the reservoir (Figure 4-8). This accounted for the fact that reservoir boundary and volume might be bigger than what was assigned to

the model. To develop the geological model, top and thickness of sand layers were picked for log data of 14 wells crossing at injection well and then correlated (Figure 4-8).

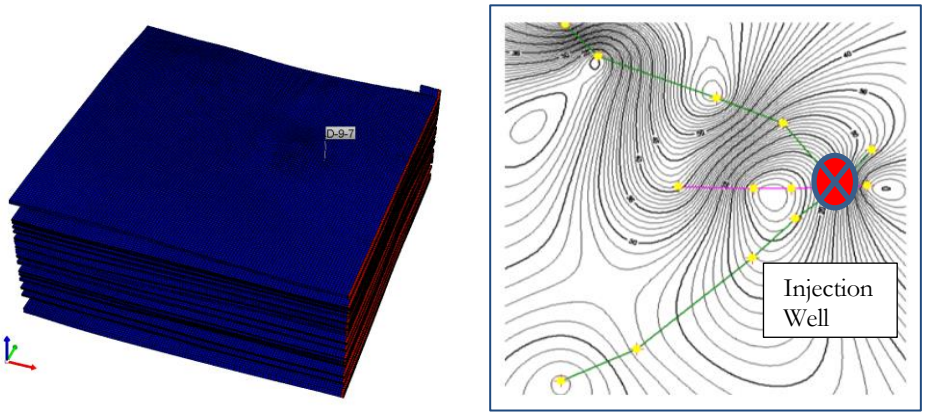

Figure 4-8: Left: Increased volume modifier at the east boundary, Right: well cross sections

Due to the limited amount of information (just two well logs) at east side of the injection well, it was not possible to estimate the extension of the sand layer on that area. Therefore it was probable that more reservoir volume existed outside the boundary of the geological model. Adding more volume to the reservoir (sand layers) resulted in lowering the pressure prediction. After activating CO_2 solubility in the brine phase and tuning "volume modifier'" a good match between model results and actual pressure data with less than 0.001% average error was achieved (Figure 4-9).

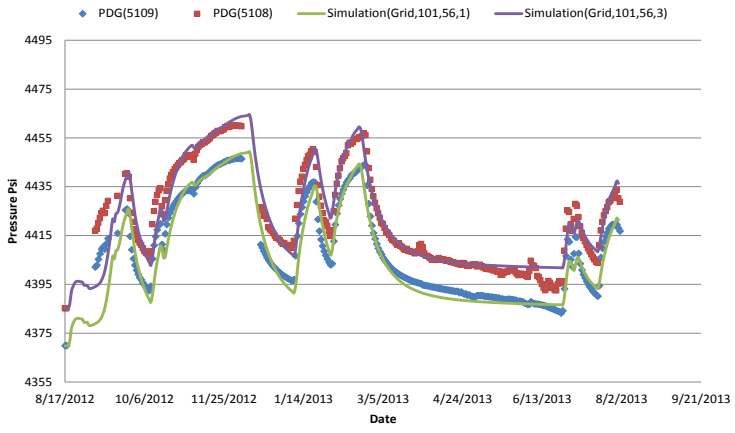

Figure 4-9: Model's pressure results and actual history; final history match

4-3 Model Validation

History matched model showed very good precision in generating ten months of pressure results which resembled the actual field measurements. In order to study predictability of reservoir model, last three months, from August 1st to October 30th, 2013 of actual injection/pressure was unused in history matching and set aside for forecast validation (Figure 4-10). During these three months, CO_2 was injected steadily according to targeted rate 9.48 Bcf/day. Injection experienced few shutdowns resulted in average rate to be 7.98 Bcf/day. Consequently, reservoir pressure increased during August 2013, followed by some drawdowns due to no injection in September 2013 and gentle buildup during the last month.

Considering the last three months of injection rate profile as the model's operational constraints, simulation pressure predictions were obtained. Pressure prediction result has been plotted versus actual data in Figure 4-11. The prediction has precisely captured actual data trend such that the average errors for gauges 5109 and 5108 are 0.12% and 0.073% respectively which is quite satisfactory.

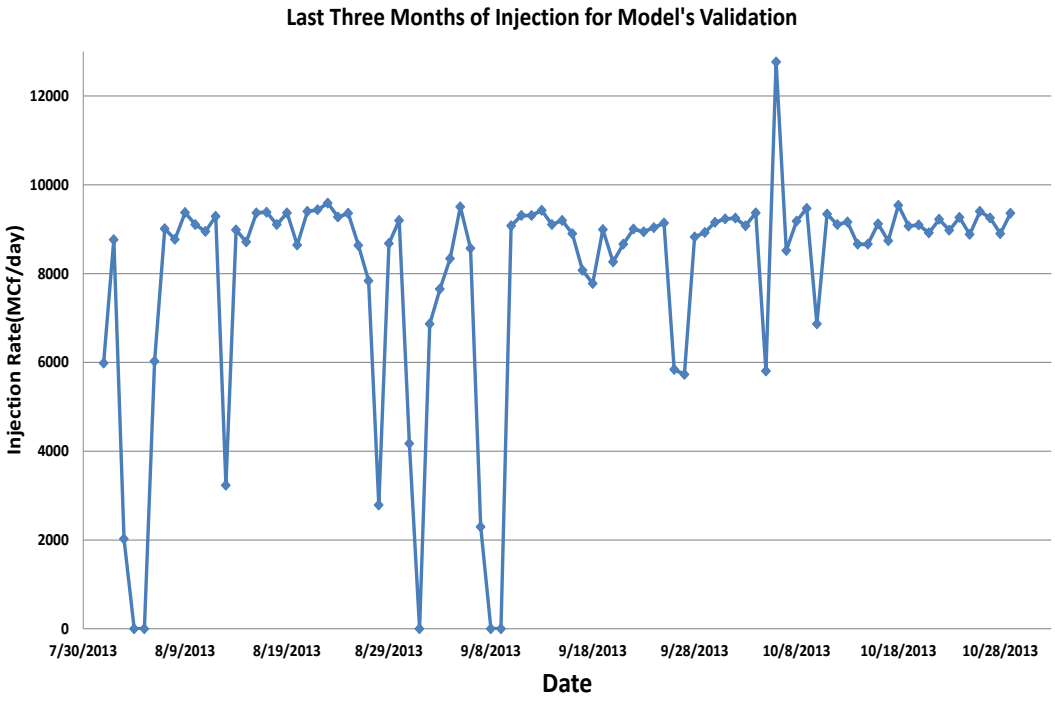

Figure 4-10: Last three months of injection rate

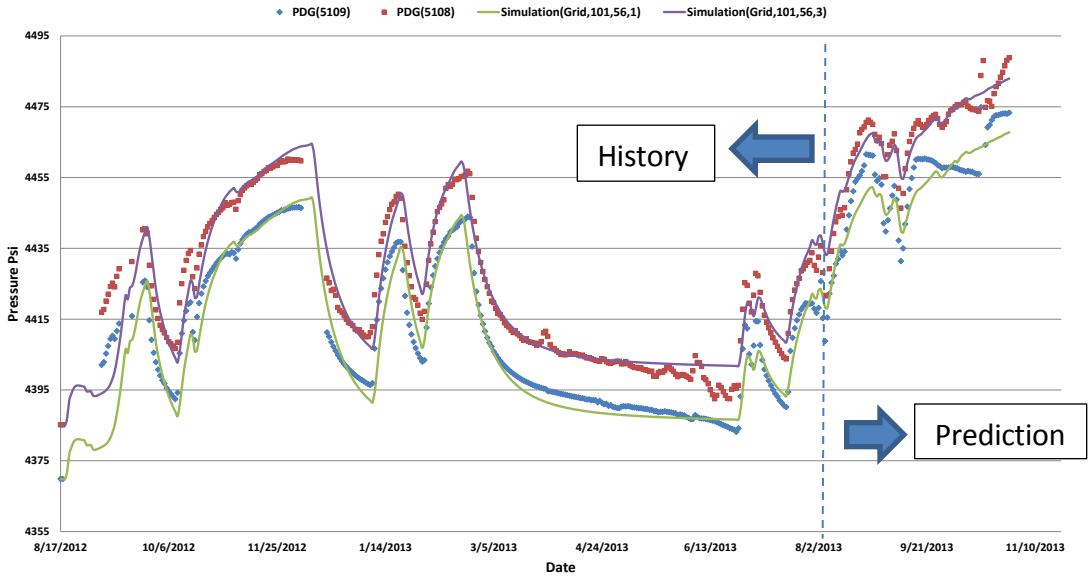

Figure 4-11: Model's pressure result and actual data for prediction and history

4-4 Conclusion

Ten months of CO_2 injection in the Citronelle's Dome saline formation (Paluxy) was modeled by numerical reservoir simulation. The presence of two PDGs (Pressure Down-hole Gauge) at the observation (monitoring) well was considered in the model. A comprehensive sensitivity analysis was performed to assess the effect of uncertainty of several reservoir parameters on model's pressure (at observation well) behavior. The analysis was used to match the history of actual field pressure data with model's prediction by tuning reservoir parameters. By modification of brine density, permeability (in two reservoir regions), vertical to horizontal permeability ratio,CO_2 solubility in brine and reservoir volume , a reasonable match (less than .001% error) between actual and model's pressure data was achieved. This model was validated using the last three months pressure-injection profiles and showed acceptable predictability. However, history matching of the numerical model is a non-unique solution to a complex problem; other combinations of reservoir parameter modification may possibly result in the same match between actual and model's data.

Chapter 5 Intelligent Leakage Detection System (ILDS) Development

To assure the cap rock integrity, CO_2 storage sites must have active monitoring systems to detect CO_2 leakage and be prepared to take remedial action in the event that leakage occurs. Industry has much experience with a combination of monitoring techniques for underground geological sites, selected primarily based on accessibility and geological characteristics. The monitoring methods can be classified into two different categories: surface and underground measurements. In surface monitoring activities, the presence of CO_2 emitted from the ground can be directly assessed [74]. Also, CO_2 related parameters like change in ground level or high frequency Electromagnetic (EM) waves [75] are subject to frequent measurements. Satellite –based optical methods, gas sampling, EM and gravity survey are considered to be types of surface or near surface monitoring. For Subsurface monitoring, the main focus is on tracking the CO_2 plume at the reservoir level. Well logs (Pulsed Neutron, RST), 4D seismic, borehole gravity, cross-well seismic, brine-gas composition sampling and introduced tracers have been applied to monitor the underground movement of CO_2 [60]. Although these methods have been deployed in the field, there are still some drawbacks associated with the practical application of CO_2 monitoring systems. In the surface monitoring method, the main concern is that it remains essential for the CO_2 to be detectable at surface. Before that time, even though the leakage could have occurred, it would not be possible yet to detect it [76].Regarding the underground monitoring systems, it is worthy to mention that since most of these methods are implemented periodically, it is not possible to detect any leakage during the time interval that no test or monitoring is offered. Therefore the remediation activity and response to the leakage is considered to be reactive with some time lag. This fact points out the need to have a real time or online monitoring system in order to detect the CO_2 leakage as fast as possible that leads to much more efficient CO_2 leakage risk management. Permanent Down-hole Gauges (PDG) and valves have been used for continuous monitoring of pressure, temperature, flow rates, and automatic flow controls [29]. This technology can be used in the underground CO_2 reservoirs to monitor the pressure in real time. To help accommodate CO_2 leak detection; two PDGs have been installed in the observation well. A reservoir simulation model for CO_2 sequestration at Citronelle Dome

was developed. Multiple scenarios of CO_2 leakage are modeled and high frequency pressure data from the PDGs in the observation well are collected. The complexity of the pressure signal behavior and the reservoir model makes the use of inverse solution of analytical models impractical. Therefore an alternate solution is developed for the Intelligent Leakage Detection System (ILDS), based on Machine Learning.

In order to investigate proof the concept for ILDS, initially a simple reservoir simulation model of CO_2 injection in the Citronelle field was used for CO_2 leakage modeling. This model represented homogenous porosity and permeability in every sand layer. After successful deployment of ILDS with simple and homogenous reservoir model, history matched reservoir model which was explained in chapter 4, was used to build and test an upgraded ILDS. Chapter 5 covers all the steps required for development of ILDS with homogenous and heterogeneous reservoir simulation model.

5-1 ILDS Development based on Homogenous Model

5-1-1 Reservoir Simulation Model

A reservoir model was built using a commercial numerical reservoir simulator using the results obtained from the interpreted geophysical well logs. The geological model of the Paluxy formation in homogenous model consists of 51 simulation layers. This model is divided to 50*50*51 Cartesian grids (Δx and Δy equal to 400 ft; local grid refinement was applied around the injection well). Based on an initial core study taken from the characterization and monitoring well, constant values for porosity and permeability were assigned to each layer (Table 5-1). The temperature of the reservoir is 230◦ F. The brine salinity and density values are 100,000 ppm and 62lb/ft^3, respectively. The pressure reference in this model is 4,393 psi at 9,415 feet (TVD).

Table 5-1: Porosity and Permeability values for different layers in Citronelle reservoir simulation model

Layer	1	2	3	4	5	6	7	8	9	10	11	12	13	14	15	16	17
Porosity (%)	19.8	18	18	19.3	21.8	19.3	18.2	17	18.	16	15.5	19.3	19.3	19.3	19.3	19.3	17.5
Permeability(md)	436	168	168	88	1234	88	191	100	211	59	46	88	88	88	88	88	132

Initial reservoir simulation runs showed that maximum extension of the CO_2 plume takes place in the first (top) layer. This is mainly due to the fact that the top layer represents sand with the higher permeability, which causes CO_2 to migrate further from the injection well. As it is shown in Figure 5-1, the approximate diameter of the plume area in the first layer, reaches to 3,900 feet, 25 years after the injection has stopped.

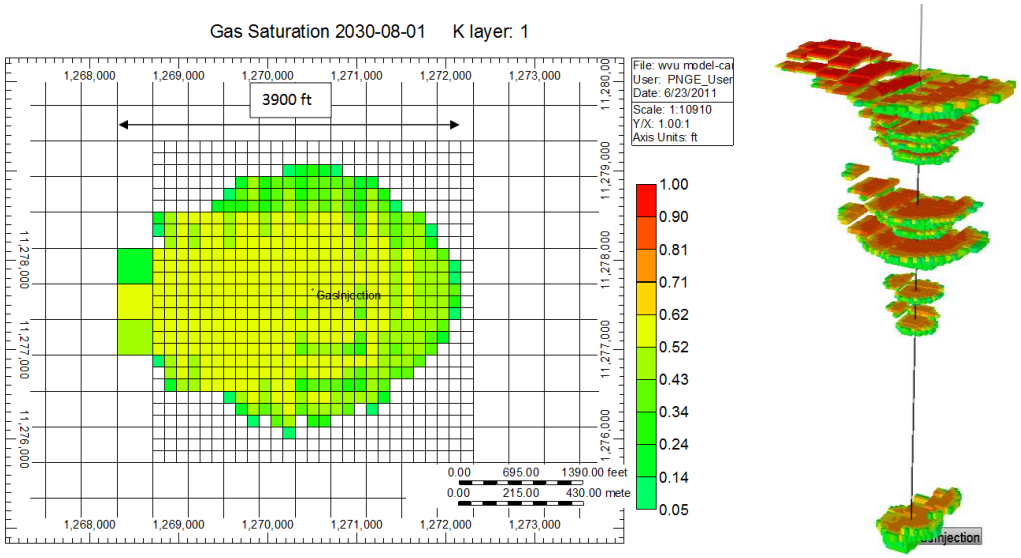

Figure 5-1: Plume extension in the first layer (left) and all layers 25 years after injection

5-1-2CO_2 Leakage Modelling

In order to make and develop Intelligent Leakage Detection System(ILDS) by use of pressure data that are received in high frequency streams from Permanent Down-hole Gauges (PDG), it is required to design set of simulation runs that provide pressure behavior in the observation wells (D-9-8) with respect to leakage rates and locations(synthetic or artificial leakage). Nine wells are located (D9-7 or injection well, D-9-1, D-9-2, D-9-3, D-9-6, D-9-8, D-9-9, D-9-10 and D-9-11) in the Area of Investigation. There are two pressure gauges in the well D-9-8. The maximum CO_2 plume extension (3800 to 4000 ft) is in the first layer. Therefore leakage from these wells can be initiated by perforating them in the first layer. The focus has been on the different leakage rates (Table 5-2) that were observed in the real cases all around the world [76]. Based on the analysis of data from leaked wells, the majority of leaks from the wellbore are negligible with limited consequences. These

leakage rates were assigned to the existing wellbores to see what would be the pressure behavior in the observation well.

Table 5-2: Leakage rates observed in real cases [76]

Ton/year	ft^3/day
35	1,837.5
100	5,250
210	11,025
800	42,000
1400	73,500
1900	99,750
2300	120,750
2500	131,250
10000	525,000
100000	5,250,000

Based on the above-mentioned study, the leakage rates of the order of 35-100 tons/year are considered as small leakages. The rates that range from 100 to 800 tons/year are the ones that typically happen in the underground CO_2 storage projects. About 93% of the wells have a leak rate smaller than 1,400 ton/year. A major event which may result in fatalities and extreme damages requires the leak rate of the order of 10,000 to 100,000 ton/year.

In order to generate high frequency pressure data in observation and injection well, twenty different CO_2 leakage rates, in the range of real leakage rates observed in actual cases, were assigned to the wells D-9-2, D-9-6 and D-9-10(Figure 5-2). These CO_2 leakage rates are shown in Table 5-3.

Table 5-3: Leakage rates assigned for the wells D-9-2, D-9-6 and D-9-10

Leakage rate			
Ton/year	**ft^3/day**	**Ton/year**	**ft^3/day**
286	15000	1333	70000
381	20000	1429	75000
476	25000	1524	80000
571	30000	1619	85000
667	35000	1714	90000
762	40000	1810	95000
857	45000	1905	100000
952	50000	2000	105000
1048	55000	2095	110000
1143	60000		
1238	65000		

At each CO_2 leakage scenario it is assumed that leakage starts 2 years after the end of injection (1/1/2017). For each CO_2 leakage rate, reservoir simulation run was performed in hourly basis (each time step is considered one hour). The duration of leakage is 6 months. We also performed a simulation with no leakage. In this case the bottom-hole pressure in the observation well starts increasing during the injection until it reaches to its maximum at the end. After end of injection, the pressure drops until reservoir reaches the equilibrium. The typical time for this period is about 4 to 5 months. After that, the bottom-hole pressure becomes almost constant.

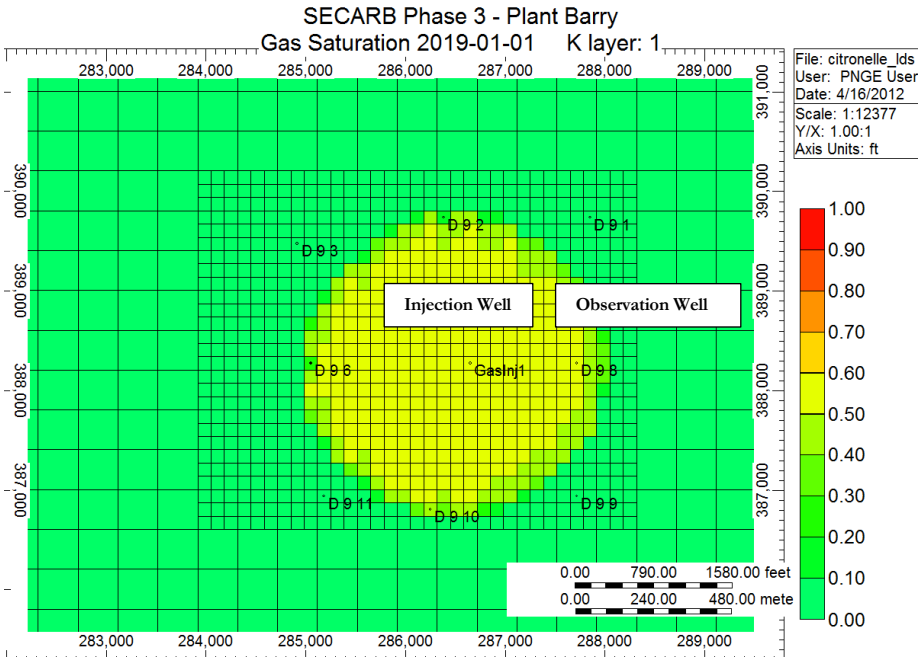

Figure 5-2: Location of the wells in the plume extension

When a CO_2 leakage occurs in one of the wells, it creates a pressure change in the reservoir. This pressure change can be observed in the observation well. The difference between pressure in the observation well, in the case that no leakage exists and when a leakage happens, is considered as the leakage indicator (Figure 5-3).

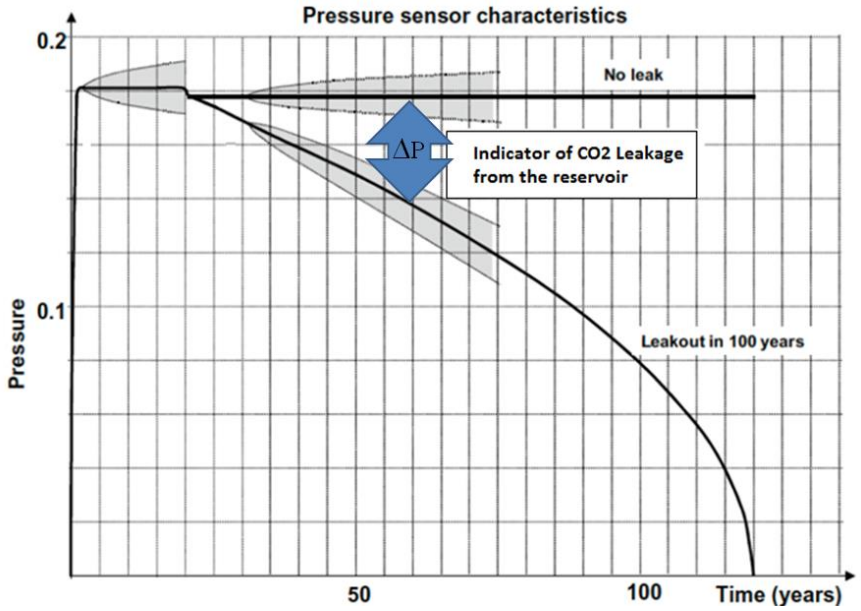

Figure 5-3: Reservoir pressure behavior during leakage [59]

This pressure difference (or Δp) behavior can characterize the specifications of the leakage specifically the location and the amount of CO_2 seepage. For example the magnitude of Δp is directly proportional to the amount of the CO_2 leakage rate. Also the trend of the Δp as the function of time is related to the location of the leakage. As an example Δp trend (high frequency-hourly basis) in the observation well, for the case that well D-9-6 leaks with the rate of 30,000ft^3/day is depicted in Figure 5-4. For all the leakage rate scenarios in Table 5-3(3 wells leak individually) high frequency Δp values were generated for observation well.

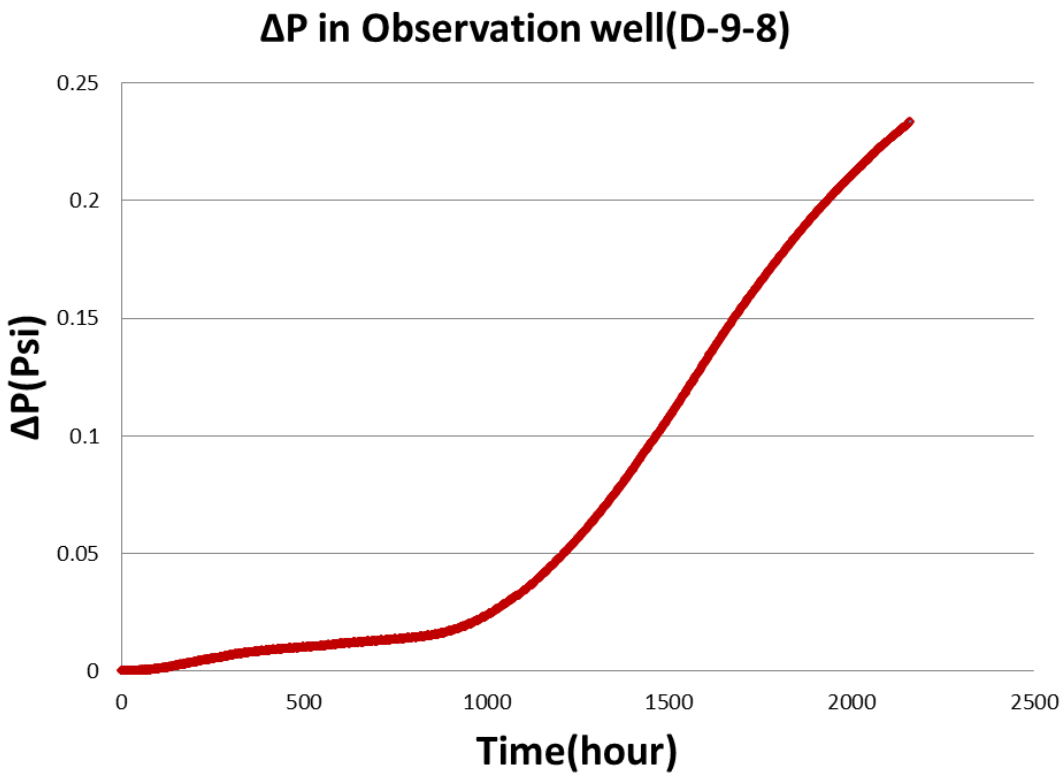

Figure 5-4: ΔP in injection well in the case that well D-9-6 leakage rate is 30,000ft^3/day

5-1-3 Data Summarization

Normally the data transmitted from the PDG sensors can be categorized in noisy-high frequency data streams. The first step in processing such data streams is removing the noise associated with the data. The process of de-noising will be explained comprehensively in

"Chapter 6". The high frequency PDG data should be summarized and transformed into a format that can be used by the pattern recognition technology.

Based on the characteristics of the Δp (high frequency data streams), "Descriptive Statistics" was used for data summarization. Descriptive Statistics quantitatively describes the main features of a collection of data and provides simple summaries about the sample and about the observations that have been made [77]. These summaries may form the basis of the initial description of the data that will be used by the pattern recognition technology.

The parameters that can represent and summarize a large amount of data can be listed as: Mean, Standard Error, Median, Mode, Standard Deviation, Sample Variance, Kurtosis, Skewness, Range, Maximum, Minimum and Sum. For example the descriptive statistics and summarization of 504 hourly Δp data points in the observation well(D-9-8) for the case that well D-9-6 leaks with the rate of 110,000ft^3/day is listed in Table 5-4.

Table 5-4: Descriptive statistics and summarization of 504 hourly Δp data points in the observation well (D-9-8)

Descriptive statistics	
Mean	0.053
Standard Error	0.0034
Median	0.012
Mode	0
Standard Deviation	0.077
Sample Variance	0.0059
Kurtosis	1.088
Skewness	1.52
Range	0.28
Minimum	-0.00048
Maximum	0.28
Sum	26.70
Count	504

Another way to represent large numbers of data points that can also be implemented in the neural network training and pattern recognition is Curve Fitting. In this process a curve is constructed, providing a mathematical function that has the best fit to a series of data points. Trend of Δp history curve is different respect to the location of the leakage.

Therefore it is not possible to determine a typical curve (linear, exponential…) to fit all the data points. The only curve that can provide a good fit for Δp points is "Polynomial" curve. In this study 4th degree polynomial curve was used to fit Δp points for different leakage rates and leakage locations. For instance for the case that well D-9-6 leaks with the rate of 30,000 ft^3/day (Figure 5-4), the following polynomial mathematical function represents the best fit with the R^2=0.9992:

$\Delta p = -7E\text{-}14t^4 + 3E\text{-}10t^3 - 3E\text{-}07t^2 + 0.0001t - 0.0085$

The coefficients and intercept of the mentioned mathematical relation can be used for pattern recognition and neural network training. Based on neural network training results, using descriptive statistics parameters leads to much more accurate predictions compare with network which was trained with coefficients of the fitted curve. Therefore descriptive statistics would be used from now on for data summarization.

5-1-4 Data Partitioning for Neural Network Modeling

In order to make neural network model, first of all it is necessary to prepare a data set including input and output features. In this study, the aim is to determine the location and amount of leakage based on the data that is provided by PDGs reading. Therefore latitude and longitude (X, Y) of the leaking well (D-9-2, D-9-6 and D-9-10) and the CO_2 leakage rate are the output features of the neural network. The CO_2 leakage rates are shown in Table 5-3.

The actual input data received directly from PDGs are pressure readings from observation well or in another word, the difference between pressure reading during the leakage and no leaking condition (Δp). As explained in the previous section, the Δp readings at different times (hourly basis) are summarized into the descriptive statistics parameters. For initial study, the pressure information (PDG readings) in observation after 1 week of leakage in hourly basis was selected.

Prior to the input data selection, KPI or Key Performance Indicator analysis should be completed in order to determine which parameters are more influential to be considered as the inputs. The first KPI test was performed on the location of leakage or coordinates of the possible leaking wells; to see which parameters are more effective. The results of the

key performance indicator analysis for the location of the leakage are shown in Figure 5-5 and Figure 5-6.

Rank	Feature	% Degree of Influence
1	Skewness	100
2	Kurtosis	89
3	Range	12
4	Standard Deviation	11
5	Standard Error	11
6	Sum	11
7	Sample Variance	9
8	Maximum	8
9	Mean	6
10	Median	1

Figure 5-5: Key performance indicator analysis results for the latitude of the leakage

Rank	Feature	% Degree of Influence
1	Skewness	100
2	Kurtosis	44
3	Standard Error	15
4	Range	15
5	Maximum	15
6	Standard Deviation	14
7	Sum	14
8	Sample Variance	9
9	Mean	2
10	Median	1

Figure 5-6: Key performance indicator analysis results for the longitude of the leakage

Based on the key performance indicator results, skewness, kurtosis and range (or maximum) have the most influence on the location of the leakage and mean and median are in the least degree of importance. Therefore the median was not selected as the input data for neural network training.

The same analysis was done to see the effect of each parameter on the CO_2 leakage rate. According to the results of the KPI (Figure 5-7), skewness, kurtosis and maximum have the most effects on the CO_2 leakage rate and the median has the least effect on the leakage rate.

Rank	Feature	% Degree of Influence
1	Skewness	100
2	Kurtosis	57
3	Maximum	19
4	Standard Deviation	19
5	Mean	18
6	Sum	18
7	Range	18
8	Sample Variance	15
9	Standard Error	15
10	Median	1

Figure 5-7: Key performance indicator analysis results for the CO_2 leakage rate

According to the key performance indicator analysis results, we decided to select 10 inputs (mean, standard error, mode, standard deviation, sample variance, kurtosis, skewness, range, maximum, and sum) for neural network training. In this case we assigned 20 different CO_2 leakage rates to 3 leakage locations(wells D-9-2,D-9-6 and D-9-10).As a result, totally 60 different records including 10 input parameters for each scenario were considered for neural network training. For this data set, intelligent data partition was used for the segmentation of the records in which 80% of data were allocated for neural network training, 10% for network calibration and 10% for verification. Therefore 48 records will be used for training, 6 for calibration and 6 for verification.

5-1-5 Neural Network Architecture Design

Error Back-propagation is one of the popular learning algorithms used in this study. For this algorithm, just one hidden layer was provided. Based on the 10 inputs and 3 outputs, 12 neurons in the hidden layer and one random seed number were allocated for the neural network (Figure 5-8). The random numbers initialize the weights on the neural network prior to the training.

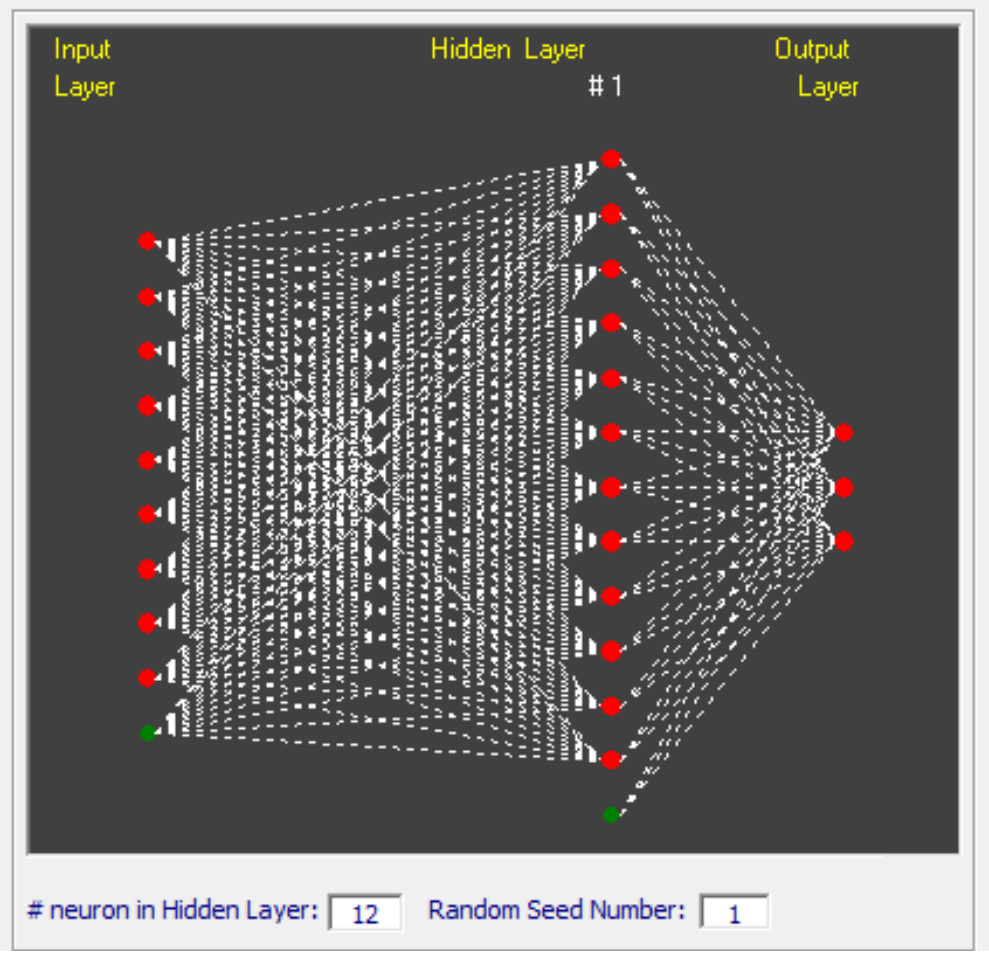

Figure 5-8: Neural Network architecture

As shown in Figure 5-8 , there are two sets of synaptic connections in the network. First is the synaptic connections between the input layer and the hidden layer, and the second set of connections are those between the hidden layer and the output layer. Since we used "Vanila " and "Enhance " network, for each connection set, 2 parameters as momentum and learning rate are assigned. "Learning rate" which is an indication of how fast the network learns the information presented. This is usually a moderate to low number (between 0 and 1). Small learning rate value may prolong the learning process and slow it down. Momentum is an extra push to the learning process that serves two purposes. First, it may accelerate the learning process, and second, it has the potential to kick the solution out of the local minima, that usually exists in the search space and causes the solutions to converge pre-maturely [78]. In this project learning rate and momentum are considered 0.3

and 0.8 respectively. Also Logistic activation function was used to connect input layers to the hidden layers.

The next step is to identify how and when to save the trained network. It is recommended to save the network that has achieved the best training set, or the calibration set. Also the network can be saved after 1 epoch or more of training. Each epoch of training is completed when all the records in the training set have been visited by the network once.

5-1-6 Results (Homogenous Model)

The initial results of the neural network training are illustrated in Figure 5-9 and Figure 5-10. These figures compare actual data (leakage rate and location) with neural network predictions. The neural network quantifies the location of the leaking well with precise accuracy (R^2 =1). For leakage rates, the neural network results cannot predict a few of the actual data correctly (R^2=0.92), specifically the rates belonging to well D-9-6. In order to improve the results for CO_2 leakage rates predictions, we developed a neural network for each leaking well individually. This approach was successful in enhancing the prediction performance of the neural network model for the leakage rate, which is shown in Figure 5-11 (R^2=0.96).

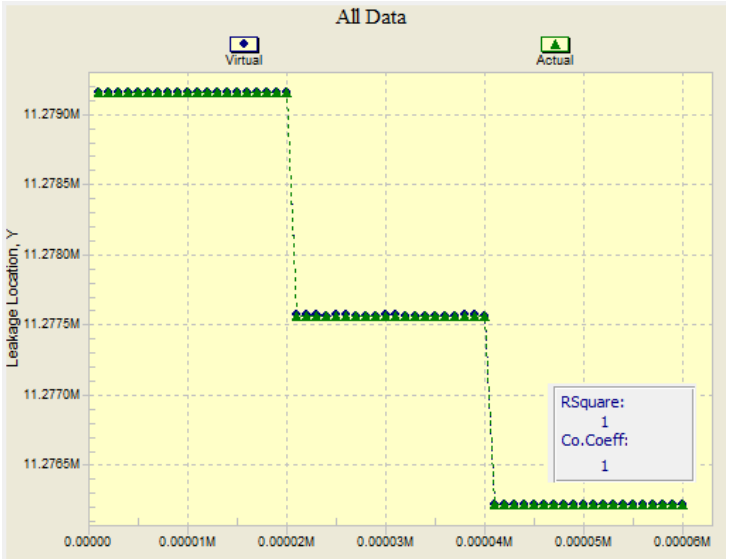

Figure 5-9 Actual leakage locations and the corresponding NN predictions

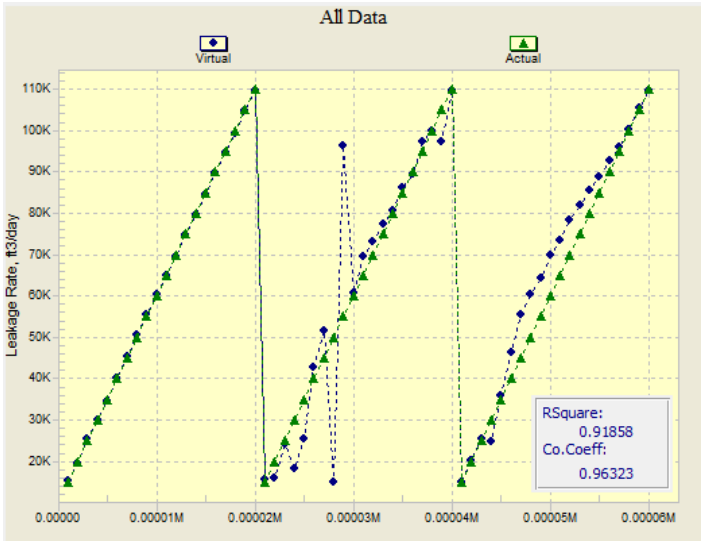

Figure 5-10: Actual leakage rates and the corresponding NN predictions

Based on the neural network modeling results, ILDS is designed in the following manner. Initially, the high-frequency pressure data is summarized by descriptive statistics then summarized features of pressure data are fed to the main neural network that predicts the location of the CO_2 leakage. Afterwards when the location is determined, the pressure data would be fed into the corresponding neural network that was designed for that specific location(Figure 5-12).

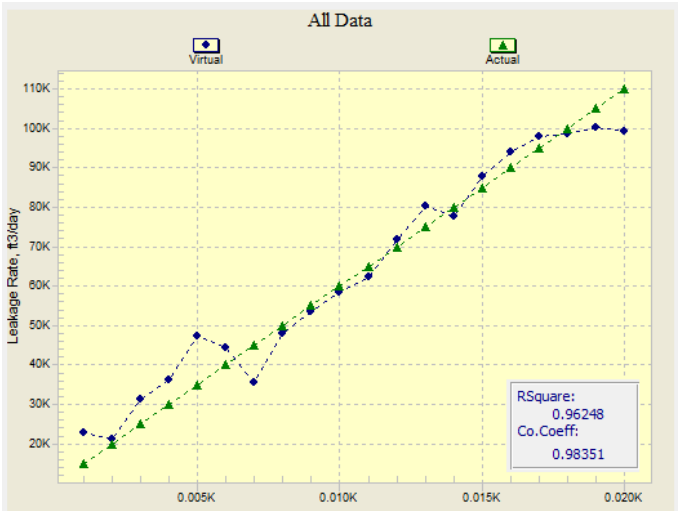

Figure 5-11: Neural network prediction for Leakage rate (network trained for each well individually)

In order to validate the performance of the ILDS, three different CO_2 leakage rates not seen by the neural network before (25,52,and 88 Mcf/day) were assigned to a possible leakage location (wells D-9-2, D-9-6, D-9-10) as blind runs.

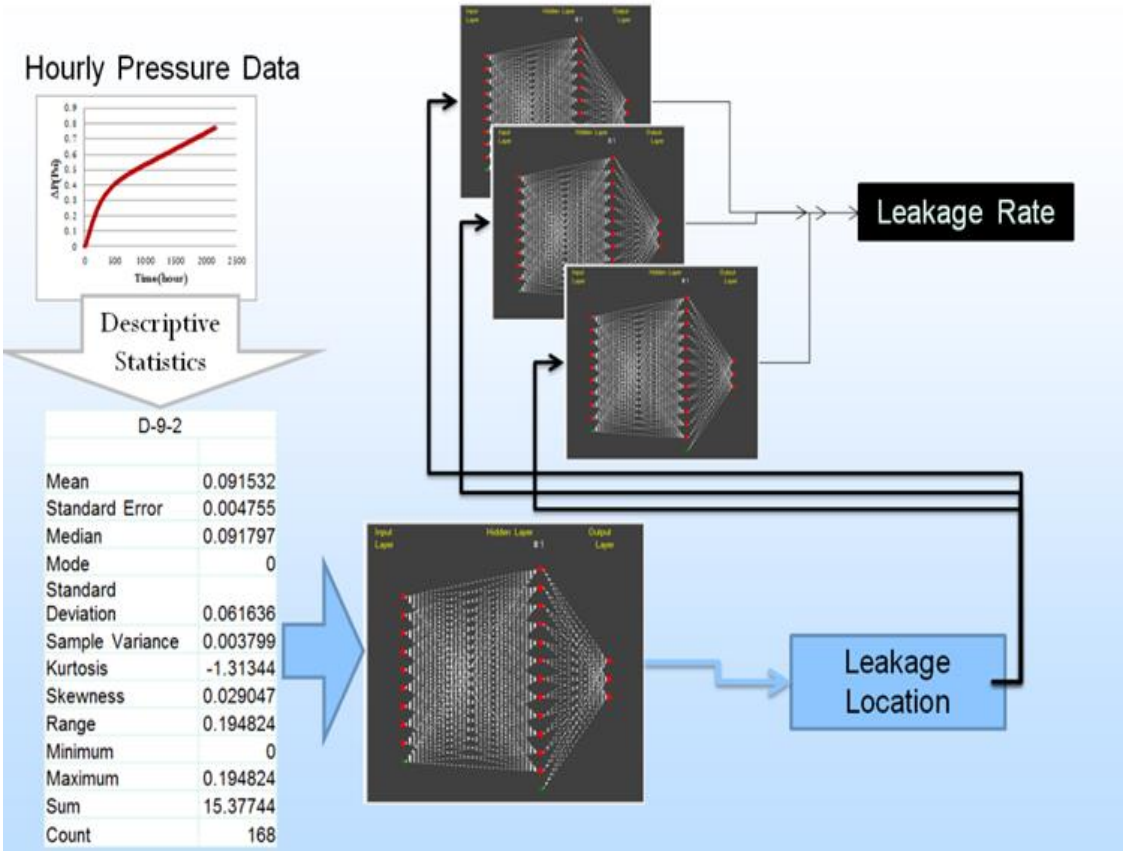

Figure 5-12: The workflow for ILDS

Pressure data from these runs were summarized by descriptive statistics and fed into the ILDS. The ILDS predications for CO_2 leakage location and rate are shown in Table 5-5 and Figure 5-13, respectively. The prediction of the ILDS for the leakage location is highly accurate in a way that the results are almost the same as actual values. For leakage rate predictions, the results are similar to actual values as well, although for the low leakage rate (26Mcf/day), they differ minimally with the actual values, but the range of predicted rates is reasonably correct.

Table 5-5: The actual Leakage locations and the ILDS predictions

Run	Leakage Location(X) Actual	Leakage Location(X) ILDS	Leakage Location(Y) Actual	Leakage Location(Y) ILDS
1	1268902.53	1268903.05	11277566.74	11277569.97
2	1268902.53	1268902.78	11277566.74	11277565.13
3	1268902.53	1268902.55	11277566.74	11277567.57
4	1270359.37	1270359.03	11279158.24	11279157.46
5	1270359.37	1270359.11	11279158.24	11279157.51
6	1270359.37	1270359.17	11279158.24	11279157.44
7	1270184.29	1270184.53	11276221.98	11276223.47
8	1270184.29	1270185.16	11276221.98	11276224.14
9	1270184.29	1270183.81	11276221.98	11276222.66

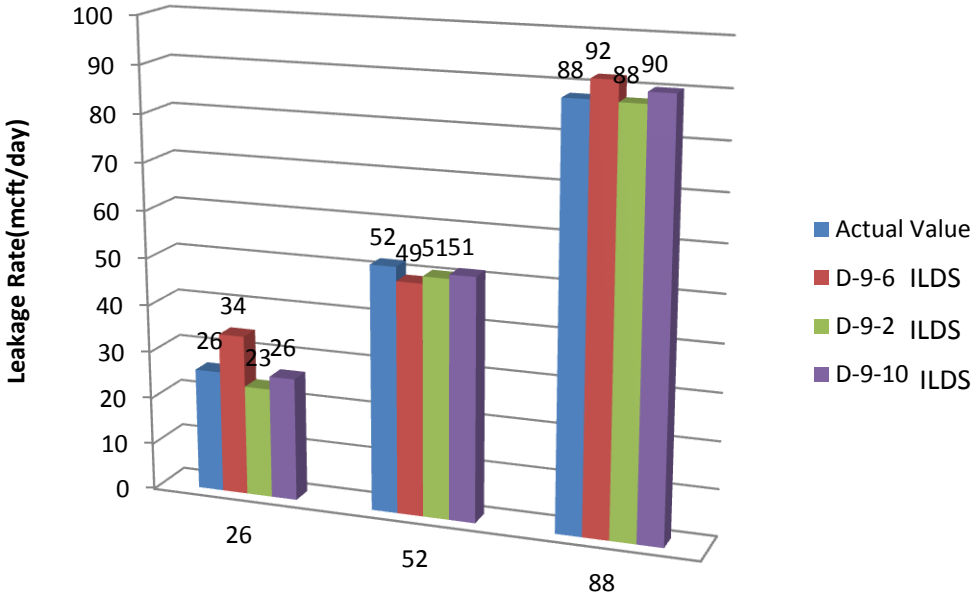

Figure 5-13: ILDS leakage rate predications

5-2 ILDS Development based on Heterogeneous Model

An Intelligent Leakage Detection System (ILDS) system was developed using heterogeneous- history matched model. Availability of additional actual field data resulted in updating the reservoir simulation model which was explained in Chapter 4 .The history matched model represented more realistic data in comparison to the homogeneous model by considering the porosity data which was obtained by comprehensive well log interpretation and permeability-porosity correlation. Additionally, assimilation of real field data led to modification of some reservoir parameters to simulate a closer pressure value to actual measurements. The updated reservoir simulation was used for modeling high frequency pressure signal behavior subject to various CO_2 leakage scenarios.

5-2-1 CO_2 Leakage Modelling

In the area of interest which is the extension of the CO_2 plume (Figure 5-14), five different wells are located. Each well can be a possible leakage path if the proper well integrity is not available. Since wells D-9-7#2 (injection well) and D-9-8#2 (observation well) were drilled recently specifically for CO_2 storage purposes, probability of CO_2 leakage through these wells was neglected. Wells D-9-6, D-9-7 and D-9-8 may experience some kind of leakage. When a leakage occurs, a pressure change (Δp) signal can be observed in the observation well. The pressure change signal in the observation well for the leakage rate of 65,000ft^3/day, at well D-9-7 is illustrated in Figure 5-15.

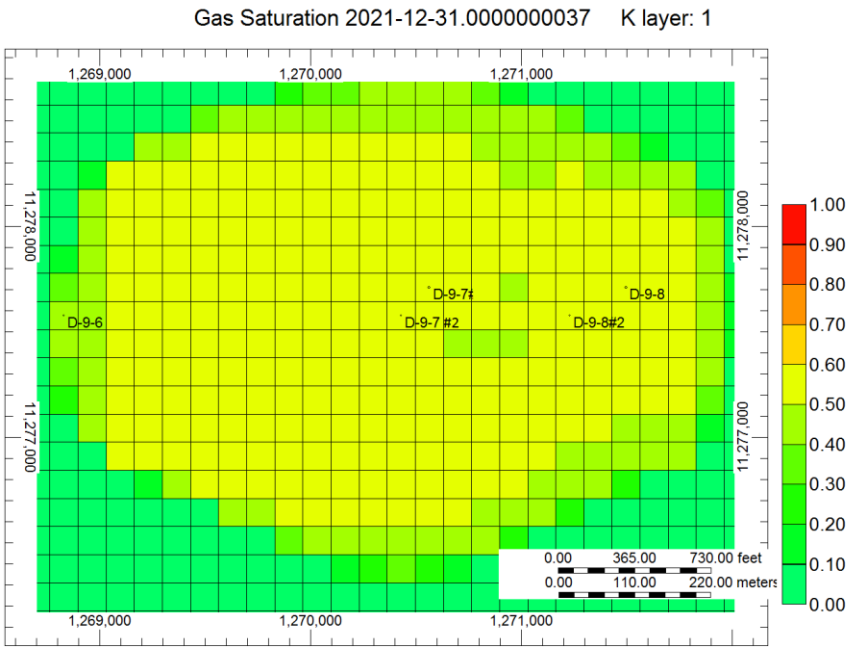

Figure 5-14:CO_2 Plume extension in history matched model

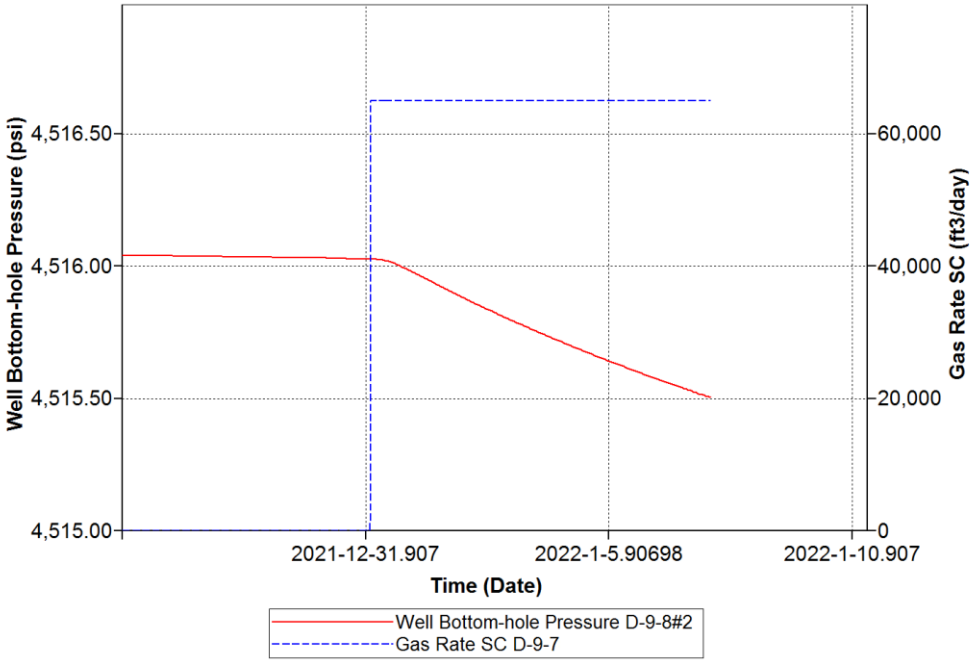

Figure 5-15: Reservoir Pressure in the observation Well (D-9-8)

5-2-2 Neural Network Data Preparation

Intelligent Leakage Detection System (ILDS) consisted of a neural network which learned patterns that related the leakage characteristics (location and rate) to the corresponding pressure signal. In order to train the neural network, it was necessary to have pressure signals corresponding to each leakage scenario. Reservoir simulation was used to generate mentioned pressure signals. Each well that was prone to the leakage (wells D-9-6, D-9-7 and D-9-8) experienced different leakage rates (in the range of 15,000 - 105,000 ft^3/day with 10,000 ft^3/day increments). The synthetic leakage will initiate at 1/1/2022 and 168 pressure signals in hour basis are recorded from the observation well (D-9-8#2).Descriptive statistics was used to summarize the pressure signals to develop the data set for neural network training. Intelligent data partitioning was used to divide the data set into training (80%), calibration (10%) and verification (10%) portions. Then, data set was analyzed by Key Performance Indicator (KPI) in order to identify the relative impact of each input parameter of summarized pressure data on the output features. The results of KPI analysis are shown in Figure 5-16 and Figure 5-17.

Rank	Feature	% Degree of Influence
1	Skewness	100
2	Kurtosis	76
3	Standard Error	21
4	Range	20
5	Maximum	18
6	Sum	16
7	Standard Deviation	16
8	Mean	15
9	Sample Variance	12
10	Median	1

Figure 5-16: Key performance indicator for Leakage location

Rank	Feature	% Degree of Influence
1	Kurtosis	100
2	Skewness	45
3	Sample Variance	7
4	Standard Error	6
5	Sum	6
6	Mean	6
7	Maximum	5
8	Median	2
9	Range	2
10	Standard Deviation	1

Figure 5-17: Key performance indicator for Leakage rate

5-2-3 Neural Network Architecture Design

Back-propagation method was used for training the networks using all the parameters that were analyzed in key performance indicator as the inputs. Leakage location (X coordinate) and rate were set as the output parameters. Based on input-output selection, 10 neurons with one hidden layer formed the structure of the neural network (Figure 5-18). Input layers were connected to the hidden layers by logistic activation function. Also one random seed number was used to start initialization of neural network weights.

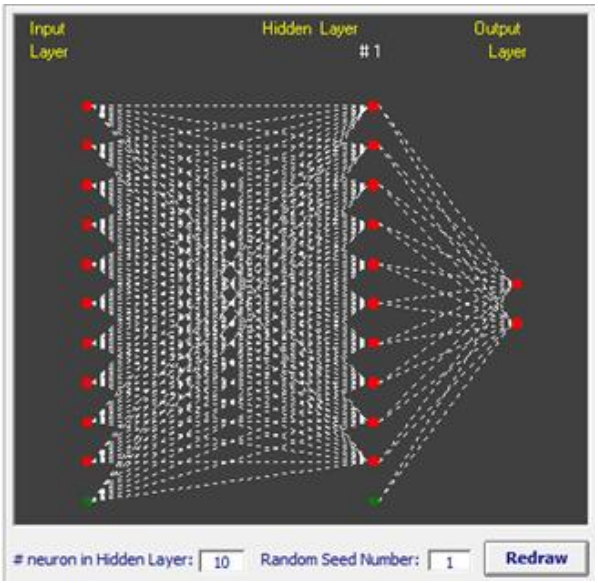

Figure 5-18: Neural network architecture

5-2-4 ILDS Validation

In order to validate the ILDS that was developed by heterogeneous and history-matched model, 9 different simulation runs were performed to generate pressure signals corresponding to the leakage rates that were not seen by the neural network during the training process. Three different leakage rates were assigned to each well (Table 5-6) and the pressure signals were collected and summarized by descriptive statistics. The results of neural network were compared to the actual data to investigate the predictability of ILDS (Figure 5-19 and Figure 5-20).

Table 5-6: leakage rates and locations for ILDS validation

Run Number	Leakage Rate(ft^3/day)	Leakage Location(ft)	Well
1	23000	1268829	D-9-6
2	72000	1268829	
3	93000	1268829	
4	32000	1270562	D-9-7
5	61000	1270562	
6	87000	1270562	
7	27000	1271495	D-9-8
8	48000	1271495	
9	101000	1271495	

5-2-5 Neural Network Model Analysis

The neural network prediction's precision can be analyzed by looking at the error plots and R^2. As it is shown in Figure 5-21, the R^2 for leakage location predictions is 0.99 which shows high precision in neural network predictions. Additionally the error for leakage location prediction ranges between -5 to 7 ft (actual leakage locations are: 1268829, 1270562, 1271495ft).For leakage rate results (Figure 5-22); the R^2 is equal to 0.98 which portray promising predictions. The maximum errors for leakage rate predictions range from -5 to 9 Mcf/day which is less than 10 % of actual rates.

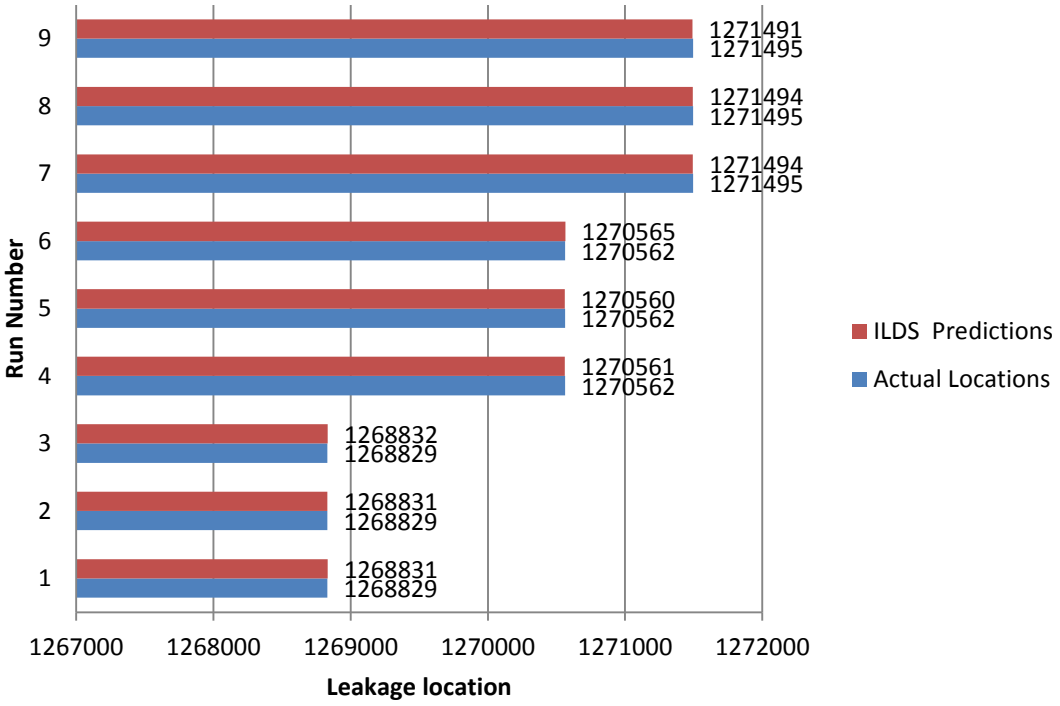

Figure 5-19: Results for neural network validation-leakage locations

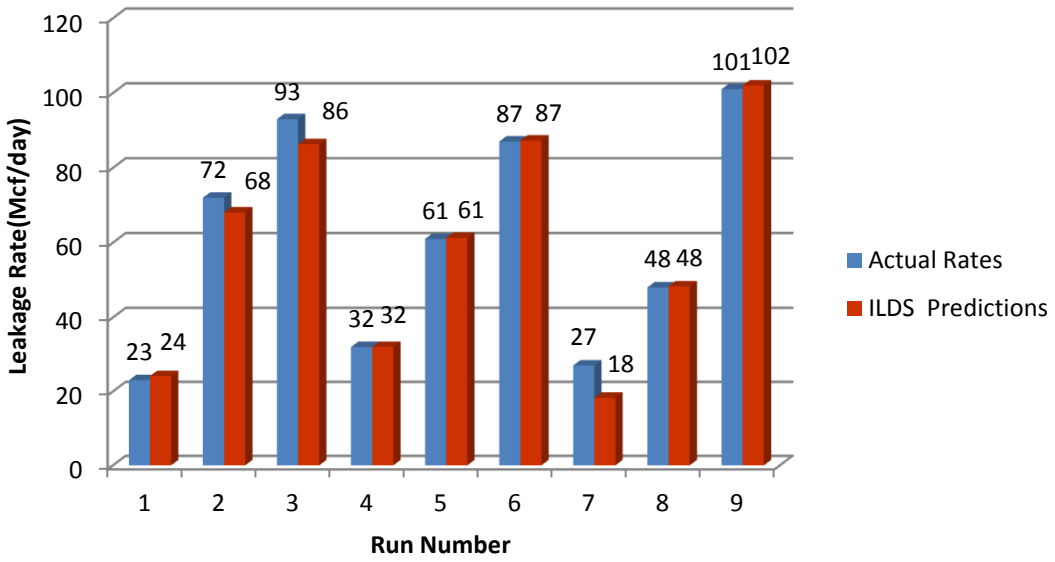

Figure 5-20: Results for neural network validation-leakage rate

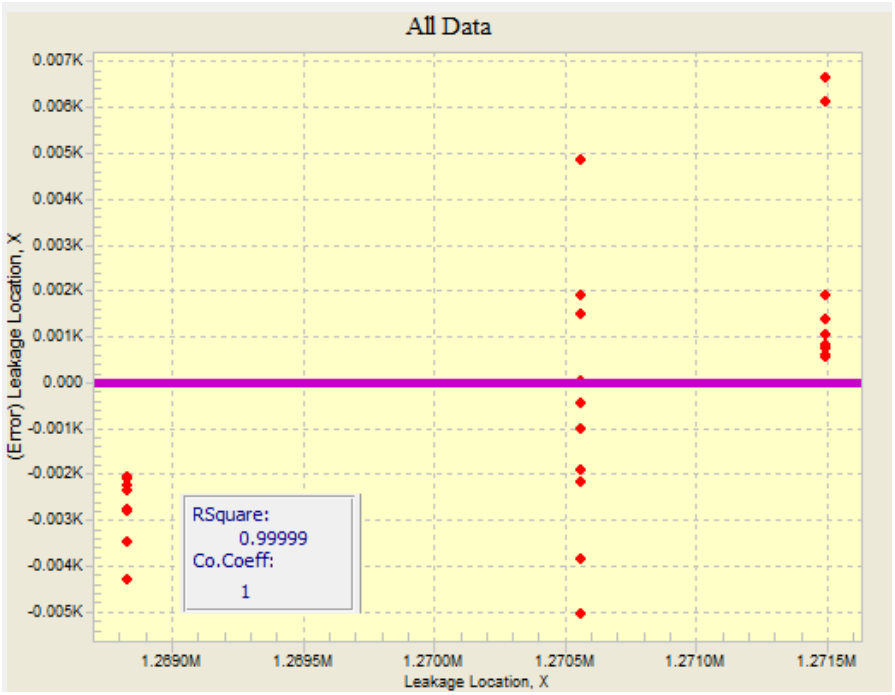

Figure 5-21: Neural network prediction errors for leakage location

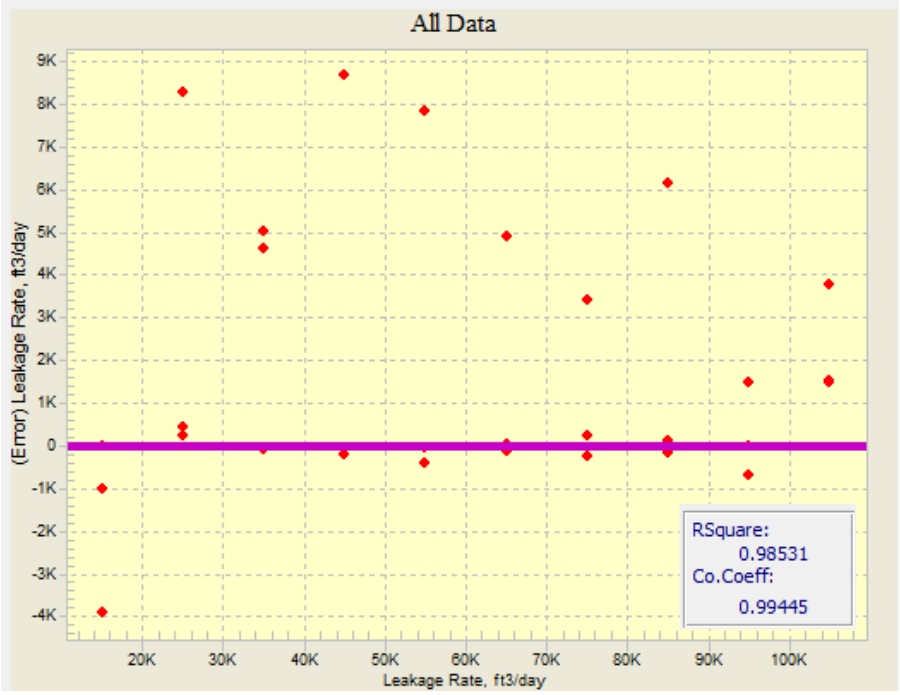

Figure 5-22: Neural network prediction errors for leakage rates

5-3 Conclusion

This chapter explained developing the next generation of intelligent technique that takes maximum advantage of the data collected using "Smart Field" technology to continuously and autonomously monitor and verify CO_2 sequestration in geologic formations. This technology will provide the means for in-situ detection and quantification of CO_2 leakage in the reservoir.

Injection of CO_2 in a saline reservoir (Citronelle Dome) was modeled and studied in order to predict reservoir performance, specifically under a variety of modeled CO_2 leakage scenarios. CO_2 leakage was modeled considering the existence of PDGs in the observation well. High frequency pressure data was processed and summarized by descriptive statistics. Finally, an Intelligent Leakage Detection System (ILDS) was designed, developed, and tested with simple-homogenous and history matched-heterogeneous model.

The main findings can be summarized as:

- Pattern recognition capabilities of Artificial Intelligence and Data Mining (AI&DM) may be used as a powerful de-convolution tool.
- Locating and quantifying CO_2 leakage rates in storage sites, using "Smart Field" technology, is a technologically feasible concept.
- ILDS attempts to identify the location and amount of the CO_2 leakage at the reservoir level (long before it reaches the surface). By providing such information to the monitoring team at the surface, ample time is provided for pro-active intervention rather than reactive responses.

Chapter 6 : ILDS Enhancement and Evaluation

As part of a monitoring technique, an Intelligent CO_2 Leakage Detection System (ILDS) was developed for CO_2 storage project at Citronelle Dome. This system, which was designed based on Pattern Recognition Technology and Smart Wells, is able to identify the location and amount of the CO_2 leakage at the reservoir level using real-time pressure data from PDGs.

In this chapter, history matched reservoir simulation model (based on 11 months of actual injection/pressure data) was used for CO_2 leakage modeling studies. High frequency real time pressure streams were processed with a novel technique to form a new data driven Real-time ILDS(R-ILDS) which was able to detect leakage characteristics in a short time(less than a day). R-ILDS also demonstrated high precision in quantifying leakage characteristics subject to complex rate behaviors. The performance of R-ILDS was examined under different conditions as multiple well leakage, availability of additional monitoring well, uncertainty in the reservoir model, leakage at different vertical locations along the well and cap-rock leakage. At the end the noise behavior in the pressure data and different data cleansing methods are discussed.

6-1 Real-time Intelligent Leakage Detection System (R-ILDS)

Intelligent Leakage Detection System (ILDS) is a data driven monitoring package which receives real time pressure data and determines occurrence of a CO_2 leakage, and consequently predicts location and amount of the leak. This system previously was designed(Chapter 5) in a way that it received pressure signals for a time interval ,one week of hourly signals-168 records after the leakage . Summarized pressure data obtained by descriptive statistics was fed into trained neural networks to find leakage characteristics. In that system, it was necessary to wait till the end of the time interval to find leakage characteristics. A new method of data processing is proposed in this Chapter for development of Real-time Intelligent Leakage Detection System(R-ILDS). In this method the pressure data is analyzed in real time considering the previous trend of the signals. By this method it is possible to determine leakage characteristics much faster in less than a day.

In order to process the data and convert it to a format which is appropriate for pattern recognition technology, pressure signal based on thirty different CO_2 leakage scenarios were used. Each scenario was corresponded to a simulation run that modeled specific CO_2 leakage rate (ranging from 15 to 105 Mcf/day with 10Mcf/day increments) at one of the three leakage location (wells D-9-6,D-9-7 and D-9-8). The specifications of the simulation runs and behavior of the pressure signal for each scenario was explained in Chapter 5. First of all, a threshold was assigned as .01 psi for the Δp ($P_{\text{No leakage}} - P_{\text{Leakage}}$) as the leakage indicator. This threshold is actually equal to precision of the actual PDG which is located in the observation well D-9-8#2. When this threshold is achieved, data processing starts by considering values of Δp, pressure derivative, Δp average, Δp summation, Δp standard deviation, Δp skewness and kurtosis for the past history of the data. The hourly pressure data for one week for each CO_2 leakage scenario was used to generate the whole data set for the neural network training, calibration and verification. The first 12 hours of the data after beginning of the leakage ($\Delta p > 0.01$ psi) were neglected for the data processing.

6-1-1 Neural Network Data Preparation

Development of the R-ILDS is mainly based on the training, calibration and verification of neural networks that received processed real time pressure data for each CO_2 leakage

scenario as the input and the corresponding leak rate and location as the output. Initially, a neural network was trained to find a pattern between leakage location (output) and the corresponding processed pressure signals. The whole data set for leakage location neural network consisted of 3527 data records which were partitioned to 2821,353 and 353 records for training, calibration and verification respectively. The influence of each input parameter on the output results (leakage location) was determined by Key Performance Indicator analysis. As it is illustrated in the Figure 6-1, skewness, standard deviation and average of the Δp show to have the most impact on the output (leakage location). It is worth mentioning that descriptive statistics for ΔP (Deltp in Figure 6-1and Figure 6-2) data at each time step is calculated in cumulative basis after pressure threshold of 0.01 psi (leakage indicator) was observed. For example, at time step 24 (after pressure threshold was detected), average, summation, standard deviation, skewness and kurtosis were calculated for 24 Δp records (Cumulative). Derivative and Δp are point values at time step 24. The last 12 data records and corresponding calculated parameters will be used in neural network training.

Rank	Feature	% Degree of Influence
1	Cum Skewness(DeltP)	100
2	Cum ST Dev(DeltP)	61
3	Cum Avereage(DeltP)	59
4	Delp	58
5	Cum Kurtosis(DeltP)	50
6	Cum Sum(DeltP)	26
7	Derivitive	2
8	Time(New)	1

Figure 6-1: Key performance Indicator for the Leakage Location

For leakage rate determination, one neural network was trained for each well separately. The number of input data records for each well is different due to implementing 0.01 psi threshold as the leakage indicator. For instance, 1553 records were used to train leakage

rate neural network for Well D-9-8. That data records were partitioned to 1243,155 and 155 for training, calibration and verification. The results for Key Performance Indicator analysis for well D-9-8 which shows the impact of the input parameters on the CO_2 leakage rate are shown in Figure 6-2.

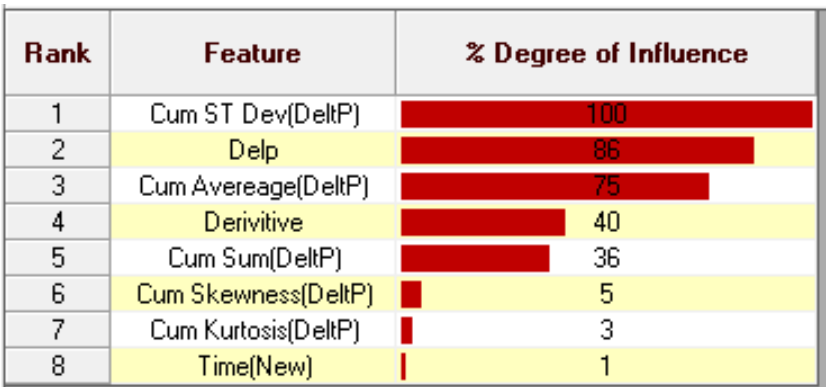

Rank	Feature	% Degree of Influence
1	Cum ST Dev(DeltP)	100
2	Delp	86
3	Cum Avereage(DeltP)	75
4	Derivitive	40
5	Cum Sum(DeltP)	36
6	Cum Skewness(DeltP)	5
7	Cum Kurtosis(DeltP)	3
8	Time(New)	1

Figure 6-2: Key performance Indicator for the leakage rate at well D-9-8

6-1-2 Results and Validation

Neural network training process attempted to calculate most proper weights that described a pattern between leakage locations and the specified input data (pressure signals). The whole process consisted of number of epochs that attempted to minimize the difference or error between actual and predicted results. It was necessary to calibrate the training process by looking over the training results and finding the best training outcomes. When the error in the calibration reached to the minimum value, the training process was completed. The results for all the training processes (training, calibration and validation) are shown in Figure 6-3(CO_2 leakage location) and Figure 6-4(CO_2 leakage rate in well D-9-8). For both leakage location and results, R-square is more than 0.99 which represents high precision.

For verifying the performance of the R-ILDS, a set of blind runs (not used for neural network training) were designed. As it is shown in Table 5-6,nine total simulation runs were performed considering assignment of three CO_2 leakage rates to the possible locations of the leakage (wells: D-9-6, D-9-7, and D-9-8). Pressure signals which corresponded to each CO_2 leakage scenario were processed by applying the leakage threshold (0.01 psi) and generating Δp, pressure derivative, Δp average, Δp summation, Δp standard deviation, Δp

skewness, Δp kurtosis at each time step. For each leakage scenario, all the calculated parameters were fed to R-ILDS to get the prediction for leakage location and leakage rate. All the results for R-ILDS prediction for each blind run are shown in Figure 6-5 , Figure 6-6 and Appendix 1.

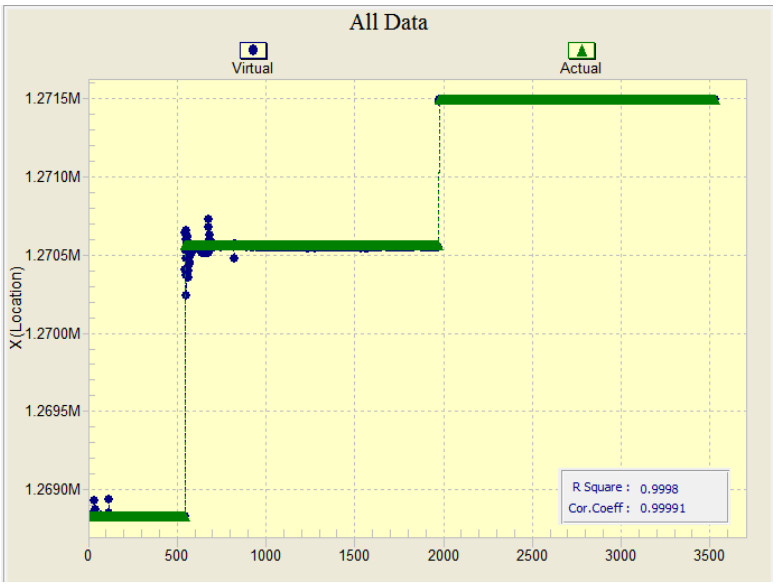

Figure 6-3: Neural network results for leakage location

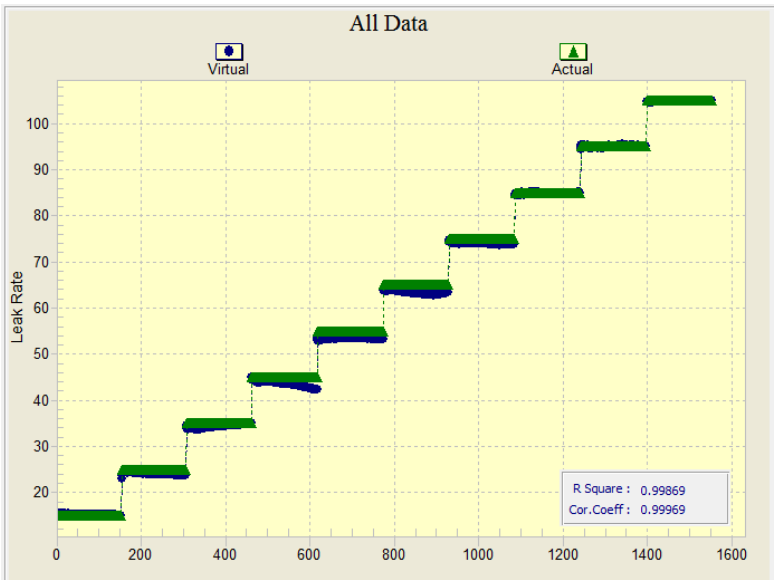

Figure 6-4: Neural network results for leakage rate in well D-9-8

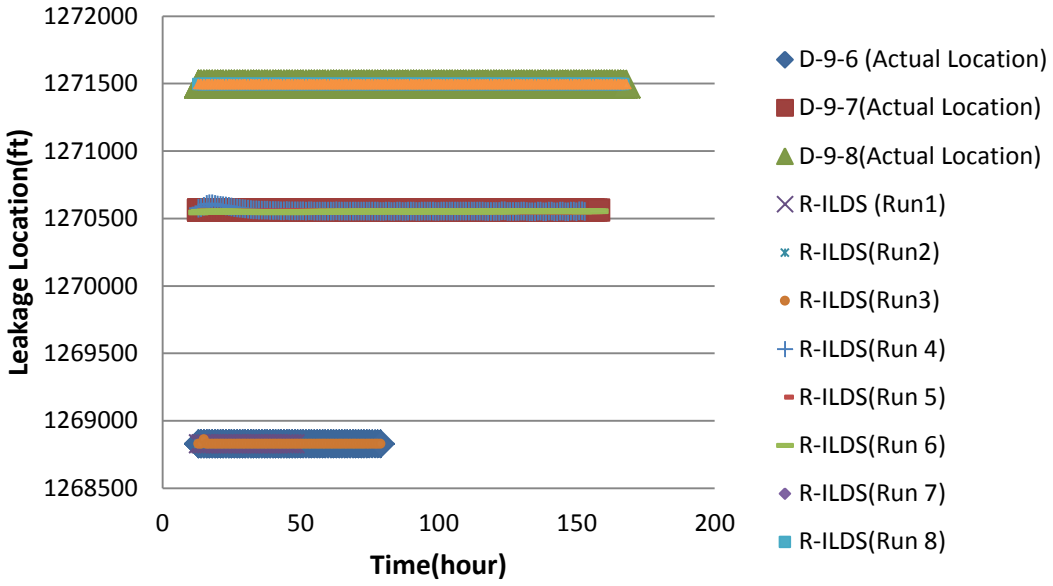

Figure 6-5: R-ILDS Leakage Location prediction, all blind runs

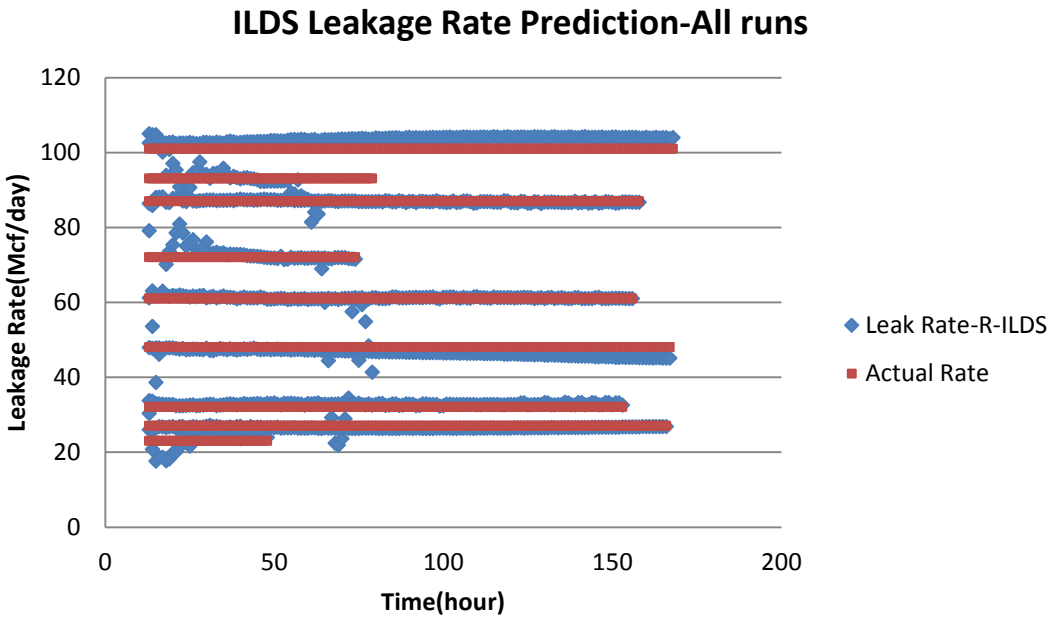

Figure 6-6: R-ILDS Leakage rate prediction, all blind runs

The precision of the neural network predictions can be quantified by R^2 parameter and the distribution of the errors. The neural network that was trained for leakage location represents the R^2 which is almost equal to 1. The prediction's error histogram for locations of wells is shown in Figure 6-7. The average error for the leakage location is 3 ft with

maximum error of 46 ft. The R square for CO_2 leakage rate predictions is 0.998 which represents a good precision. The percentage error plot for leak rate at well D-9-8 is shown in Figure 6-8. The maximum error for the leakage rate is less than 9 %. The average error for CO_2 leakage rate predictions is less than 4% at well D-9-8.

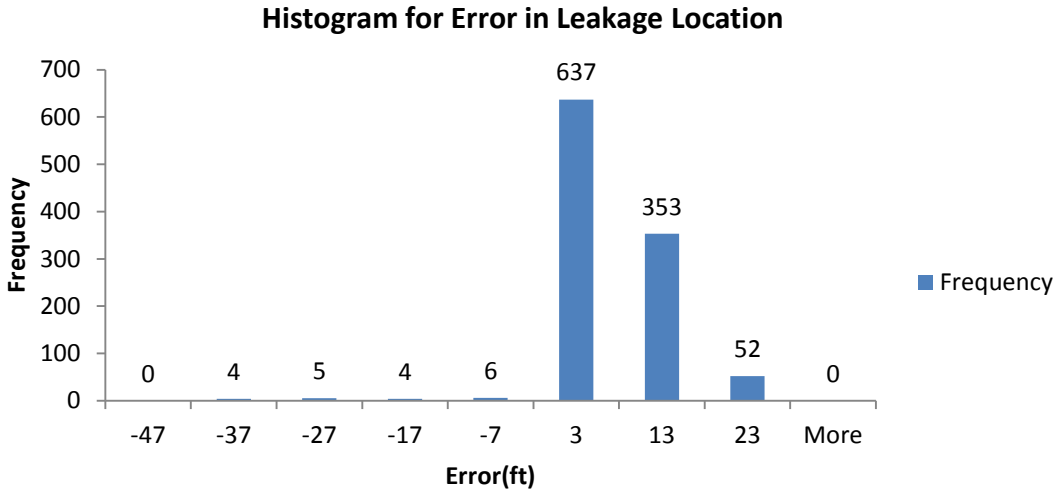

Figure 6-7: Histogram for the error in neural network's location prediction

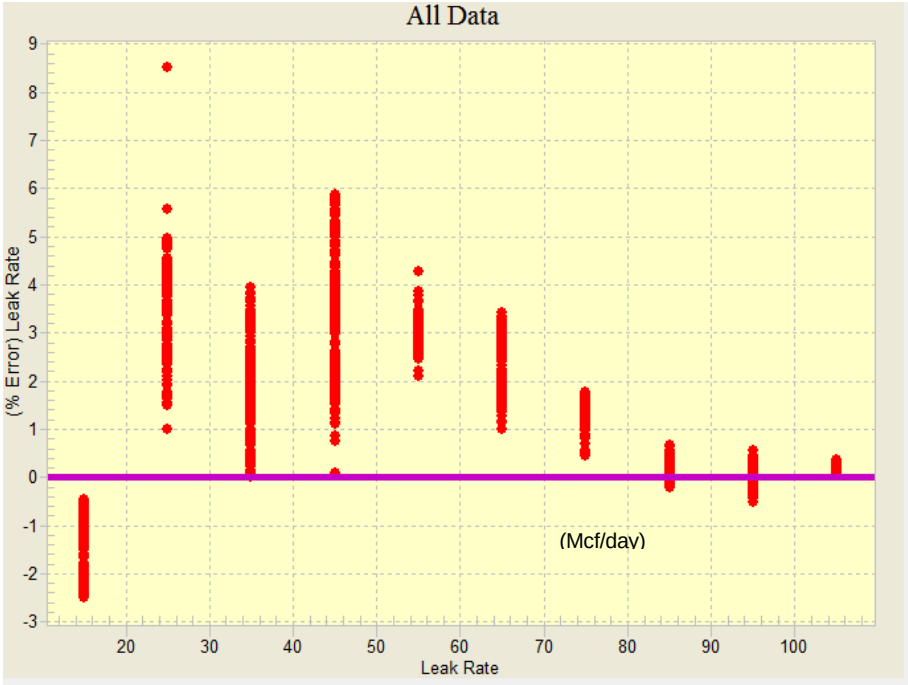

Figure 6-8: Neural network prediction errors for Leakage rates in well D-9-8

6-2 Detection Time

When CO_2 leakage occurs in the reservoir (from the existing wells, D-9-6, D-9-7 and D-9-8), there is a delay until Pressure Down-hole Gauge receives the generated pressure signal. The time that takes to detect CO_2 leakage depends on the Pressure Down-hole Gauge resolution and amplitude of the pressure signals. Resolution of the PDGs that were installed in observation well is 0.01 psi. Therefore, if the amplitude of an induced pressure signal due to CO_2 leakage is less than PDG resolution, it wouldn't be possible to detect the leak. The other important parameter in leakage detection timing is the amplitude of the pressure signal. The signal amplitude is proportional to the inverse distance of the leakage location to the observation well. The distances of each possible leakage location (wells D-9-6,D-9-7,D-9-8) to the observation well are shown in the Figure 6-9. The induced pressure signal for the cases that each of three wells leaked 55Mcf/day is shown in Figure 6-10. As the leakage location gets closer to observation well the amplitude of the pressure signal increases. R-ILDS was developed based on the fact that pressure change threshold of 0.01 psi can be detected by PDG. Also the first 12 pressure data records (after reaching to Δp=0.01psi) were not included in R-ILDS development. Based on mentioned criteria, detection times for different CO_2 leakage rates at each leakage location are plotted versus CO_2 leakage rate in Figure 6-11. As the distance between leakage source and observation well decreases, pressure signal amplitudes increase and it takes less time to detect the leakage and provide valid results.

Figure 6-9: Distance of possible leakage locations to the observation well

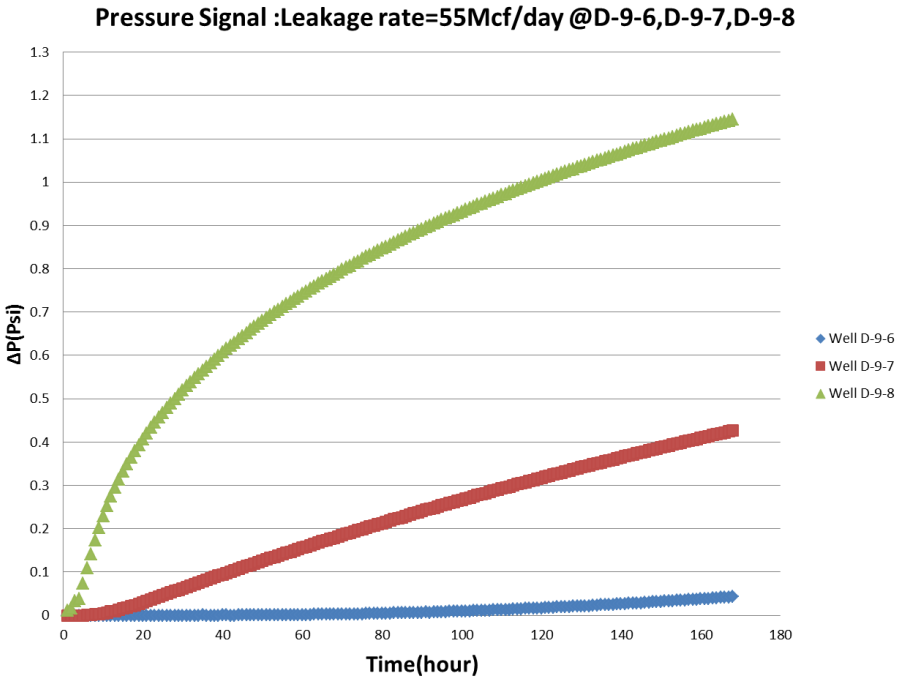

Figure 6-10: Comparison of pressure signal amplitude when wells leaked with the same rate

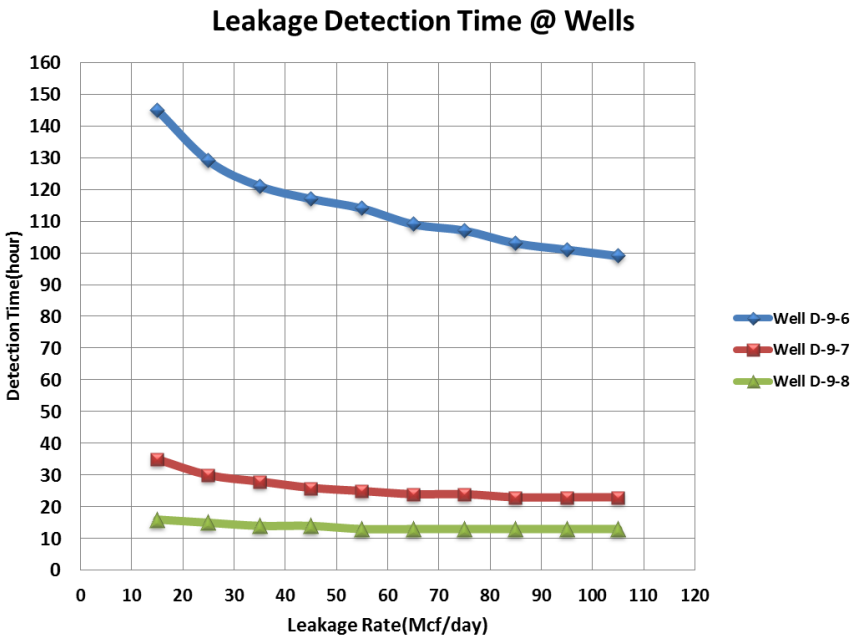

Figure 6-11: Detection time for each rate at different locations

6-3 Testing R-ILDS for Multiple Geologic Realization

Reservoir simulation model for CO_2 injection at Citronelle saline aquifer was developed and history matched with real field data. This model acknowledged "Lateral Heterogeneity" in different ways. The first reservoir characteristics that played important role in making the reservoir model heterogeneous was top of sand layers. Top maps for 17 sand layers (most extensive ones that were targeted for CO_2 injection) were generated by interpretation and correlation of 14 well logs. The location of the well logs and three cross sections for correlating the wells are shown in Figure 3-3. Based on well correlation, 17 top maps were generated representing lateral heterogeneity in the reservoir. The top map for the first sand layer is shown in Figure 3-6. The same well logs were used to generate thickness maps for all the layers. The example for grid thickness map (first sand layer) depicted in Figure 3-7. In order to make porosity maps, 40 well logs were analyzed and interpreted. Three different porosity maps were generated for each sand layer (51 total porosity maps for the entire reservoir). The lateral heterogeneity for porosity is depicted in Figure 3-8. In this model, permeability of the reservoir was obtained using porosity-permeability correlations from core analysis. This means that there are lateral heterogeneities for the permeability as well.

Multiple realizations were generated aimed at changing the parameters that control lateral heterogeneity characteristics. Reservoir porosity, sand layer top/thickness and vertical to horizontal permeability ratio were the main parameters to be modified for generating lateral heterogeneity realizations. All these parameters varied compared with the original value according to Table 6-1. For each realization, leakage rates equal to 70, 60 and 50 Mcf /day were assigned to wells D-9-6, D-9-7 and D-9-8 respectively

Table 6-1: Changes in reservoir Property Parameter

Variation / Reservoir Parameter	2% UP	2% low	5% low	10% up	10% low
Porosity				X	X
Sand Layer Top	X	X			
Sand Layer Thickness			X		
Vertical to Horizontal Permeability Ratio				X	

The corresponding pressure signal at the observation well, were collected, processed and fed to the R-ILDS. It should be mentioned that after changing reservoir characteristics (like porosity or thickness), initial reservoir pressure and stabilization pressure after end of injection varied (compare with the initial history matched). It means that $P_{\text{No leakage}}$ and consequently Δp represents unreasonable value. This Δp is called Δp –Original. In order to represent corrected Δp values, for each realization, No-Leakage scenario was simulated. Reservoir pressure signals at the observation well were collected for each realization. At this point, new Δp was calculated for each realization, having No-Leakage pressure data for all the cases. As an example, Δp –Original and Δp –New for the realization that porosity of the reservoir lowered 10% and CO_2 leakage rate equal to 60Mcf/day was assigned to well D-9-7, are shown in Figure 6-12.

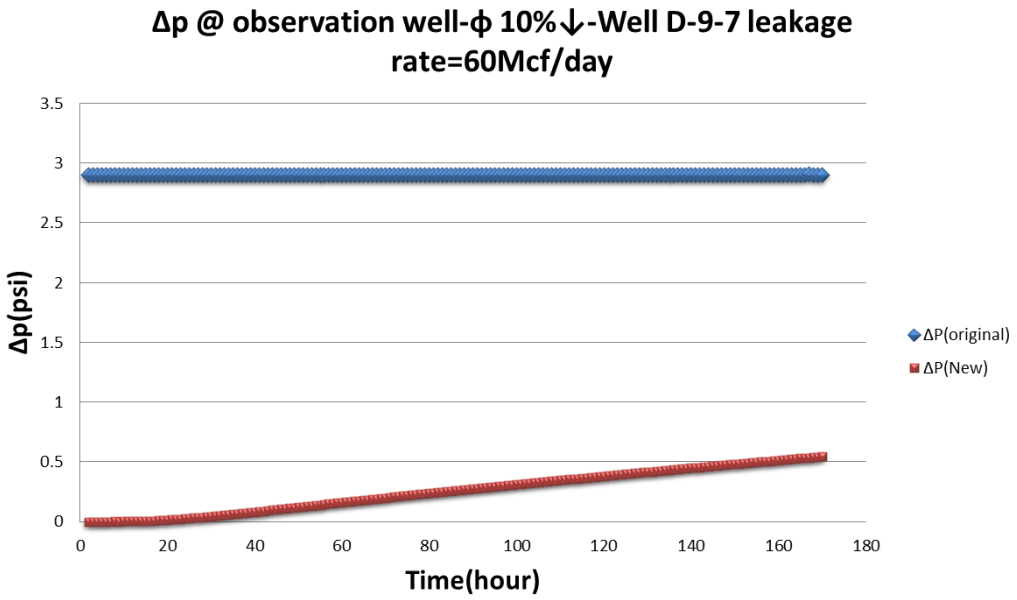

Figure 6-12: Original and new Δp at observation well subject to lowering reservoir porosity

Pressure signals from different CO_2 leakage rate scenarios and reservoir characteristic realizations were collected, processed and fed into the R-ILDS. The results were shown in Appendix 2.

First the effect of each specific parameter on the R-ILDS predictions for leakage location is explained. When the leakage (rate=70Mcf/day) took place at well D-9-6,R- ILDS predicted the location for all the realization correctly except for the case that reservoir porosity decreased 10%. In this case, R-ILDS prediction started deviating from the actual value (1268829ft) almost 35 hours after detecting the leakage. The location prediction from that time showed 1000 ft deviation from the actual value and then it gradually moved back to the actual value.

For the case that well D-9-7 leaked (rate=60Mcf/day), R-ILDS location prediction represented almost 20ft error .In the situation that reservoir porosity decreased 10%, prediction values showed 20ft error early after leakage detection. Then, the error for R-ILDS location prediction slightly increased to 80 ft. This error is acceptable since the predicted location is still in the vicinity of the target leaking well (D-9-7).

When well D-9-8 was leaking with the rate of 50 Mcf /day, changing the reservoir characteristics showed no effect in R-ILDS location prediction apart from the case that reservoir porosity increased 10%. In this case, R-ILDS predicted the leakage location to be at well D-9-6.

The impact of model's specific parameters on R-ILDS's prediction for leakage rate is as follow. R-ILDS's predictions for CO_2 leakage rate at well D-9-6 were almost precise excluding the cases that reservoir porosity varied. The R-ILDS's results for CO_2 leakage rate were 105 Mcf/day (actual value=70 Mcf/day) while reservoir porosity was changed ±10%.

Once well D-9-7 was leaking, change of main reservoir parameters showed very little impact of R-ILDS's results for CO_2 leakage rate. The maximum error of 10Mcf/day in the results was caused by decreasing reservoir porosity for 10%. It should be mentioned that CO_2 leakage rate for this well was 60 Mcf/day.

Finally, for the case that well D-9-8 was leaking 50 Mcf/day, R-ILDS's results for CO_2 leakage rate were consistent with the actual value with the exception of the realizations with reservoir porosity change. Lowering reservoir porosity for 10% led to R-ILDS prediction to be 15Mcf/day while increasing reservoir porosity resulted in 70 Mcf/day predictions.

All in all, the impact of models specific parameters was studied on the performance of R-ILDS. For most of the cases, changes in the model's parameter did not show significant impact on R-ILDS's results. The only parameter that impacted considerably R-ILDS's predictions for both CO_2 leakage rate and location was reservoir porosity. In reservoir simulation model that was developed for CO_2 injection at Citronelle filed, reservoir permeability was calculated by porosity-permeability correlation. Therefore, variation of reservoir porosity indirectly changes reservoir permeability. In other words, any change in reservoir porosity leaded to change in permeability as well. Reservoir permeability plays very important role in fluid flow in the reservoir and consequently pressure signals coming from the observation well. Porosity change caused different fluid flow behavior and consequently different pressure signal behavior. As a result, R-ILDS's results were impacted by variation of reservoir porosity.

6-4 Detection of Leaks at Different Vertical Locations along the Wells

A reservoir simulation model for CO_2 sequestration in Citronelle field was built and history matched. Based on the reservoir simulation results for CO_2 distribution and extension, it was observed that CO_2 plume reached to existing wells in reservoir mainly in layer 1(Figure 6-13). Therefore all the synthetic leakages were assigned to the wells at layer 1(the well was perforated just in that layer). More investigation showed that CO_2 Plume was in contact with Well D-9-7 through 9 layers and Well D-9-8 in two layers. This means that CO_2 leakage could take place at different vertical locations along the well D-9-7. For that reason, the changes in the vertical leakage location were applied to investigate if the system was capable of detecting the leak and the rate regardless of where (vertically) the leak was initiated within a well. It should be mentioned that two Pressure Down-hole Gauges were installed at well D-9-8#2 in the first layer of the reservoir. During the history matching process, based the reservoir pressure behavior in the observation well, it was concluded that the transmissibility of the shale layers that were inter-bedded in the sand layers was zero (Figure 6-14). This resulted in no communication between sand layers vertically. Therefore, if a leakage took place at well D-9-7 in layer 5, it would not be possible to observe the pressure change by the sensors located in layer 1. The pressure change in PDG located in

well D-9-8#2 when well D-9-7 was leaking from layer 5 (50Mcf/day) is shown in Figure 6-15.

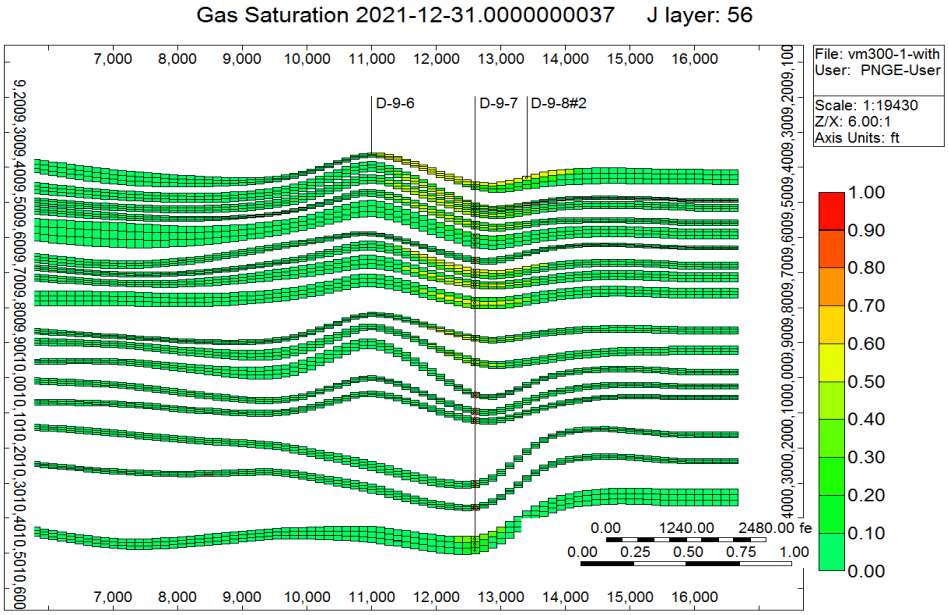

Figure 6-13: CO_2 plume extension in different layers

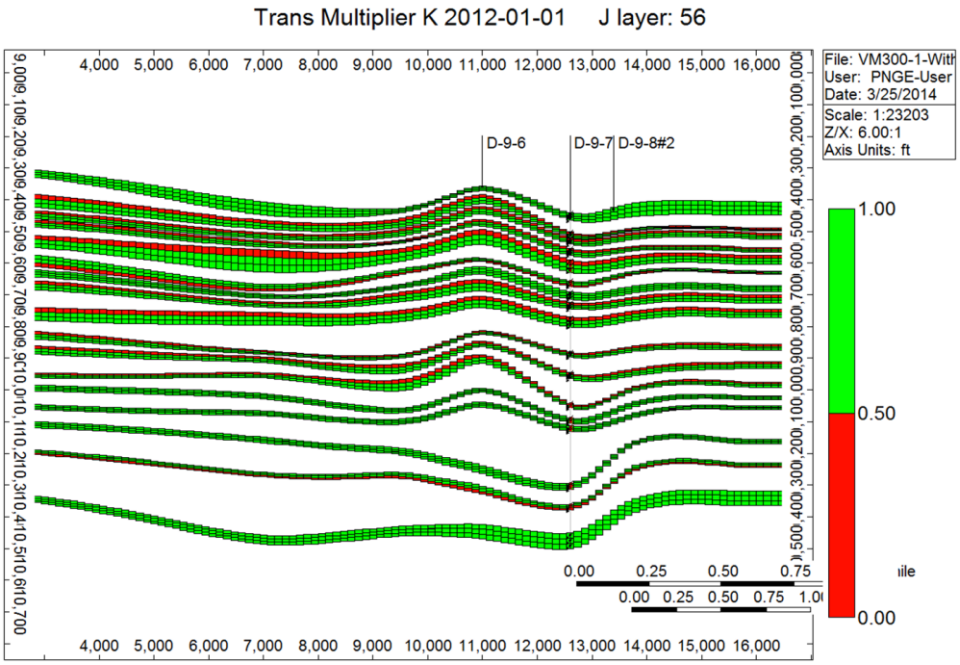

Figure 6-14: Transmissibility multiplier for shale layers

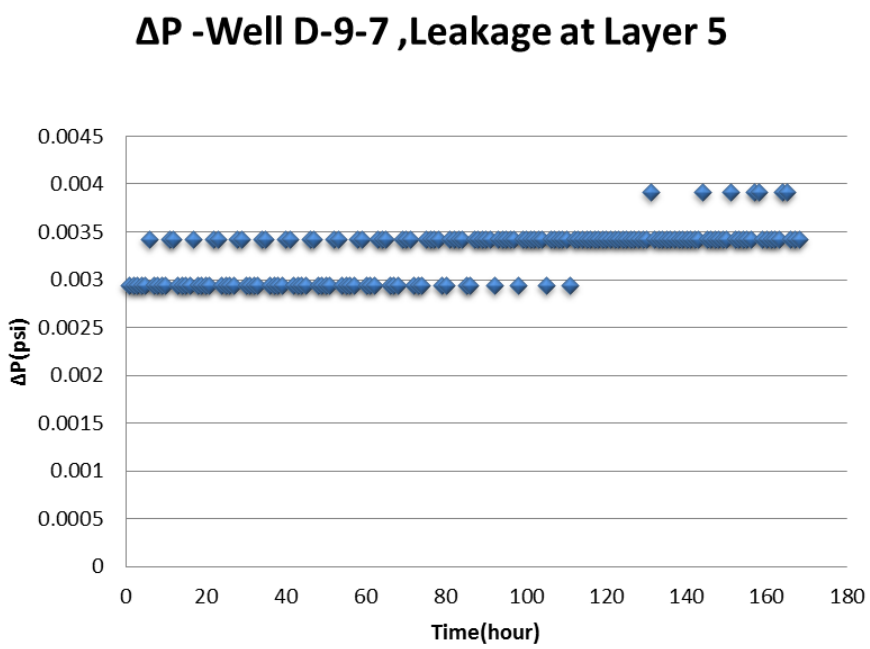

Figure 6-15: Pressure change in observation well when leakage initiated at layer 5

It was assumed that several Pressure Down-hole Gauges were installed at the observation well, exposing to every sand layer in the reservoir. By making this assumption, it would be possible to measure pressure change due to CO_2 leakage at every layer. Therefore the corresponding pressure changes (Δp), while well D-9-7 and D-9-8 were leaking from different vertical locations, were recorded, processed and provided to R-ILDS. The R-ILDS's results for CO_2 leakage location and rate are shown In Figure 6-16, Figure 6-17 and Figure 6-18.

Based on the results for leakage location (Figure 6-16), it can be concluded that R-ILDS is able to detect CO_2 location correctly when CO_2 leakage took place in well D-9-8 at different vertical locations (assuming existence of PDG in every layer). When CO_2 leakage took place at well D-9-7, R-ILDS predicted the leakage location correctly specially till 80 hours after the leakage (except the cases that well leaked form layer 5 and layer 29). Then after 80 hours from the detection time, the results started deviating from actual location of well D-9-7.

CO_2 leakage rate equal to 50Mcf/day was assigned to each leakage scenario (different vertical locations along the well). For the case that well D-9-7 was leaking (Figure 6-17); R-ILDS's leakage rate predictions were around 100 Mcf/day. When the leakage was from well D-9-8(at different layers), R-ILDS predicted the rate for case that CO_2 leakage was from layer 19 correctly (Figure 6-18). However the results for CO_2 leakage rate when leak was initiated from layer 5, was not satisfactory. The main reason for not having correct prediction for the cases that CO_2 leakage initiated at different vertical locations is that pressure signals are coming from different layers with completely different reservoir characteristics. Therefore, these pressure signals cannot be exactly the same as the case the CO_2 leakage initiated from layer 1(the R-ILDS was developed based on pressure signals for different CO_2 leakage scenarios at layer 1).

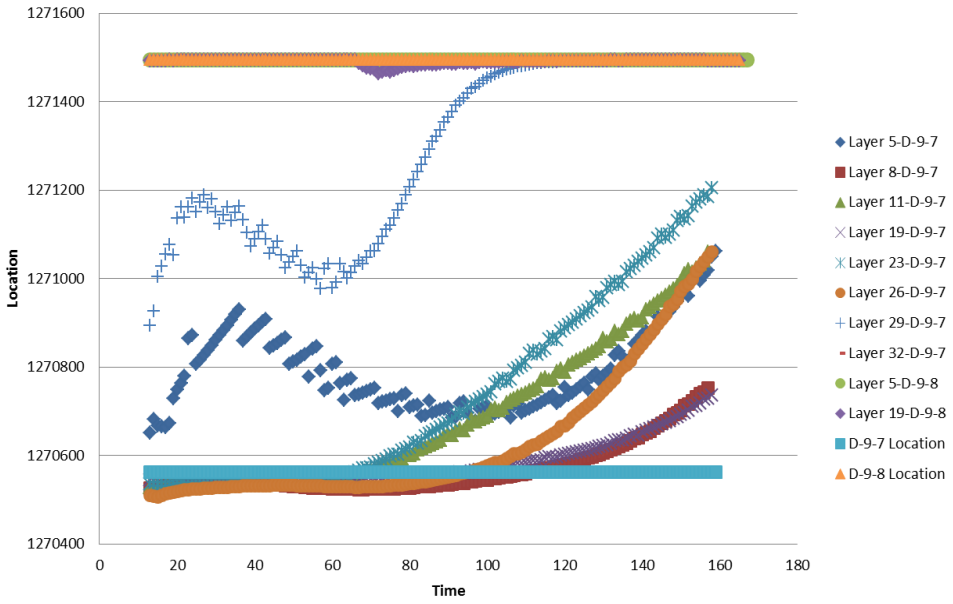

Figure 6-16: Leakage location prediction; leakage took place at different vertical locations

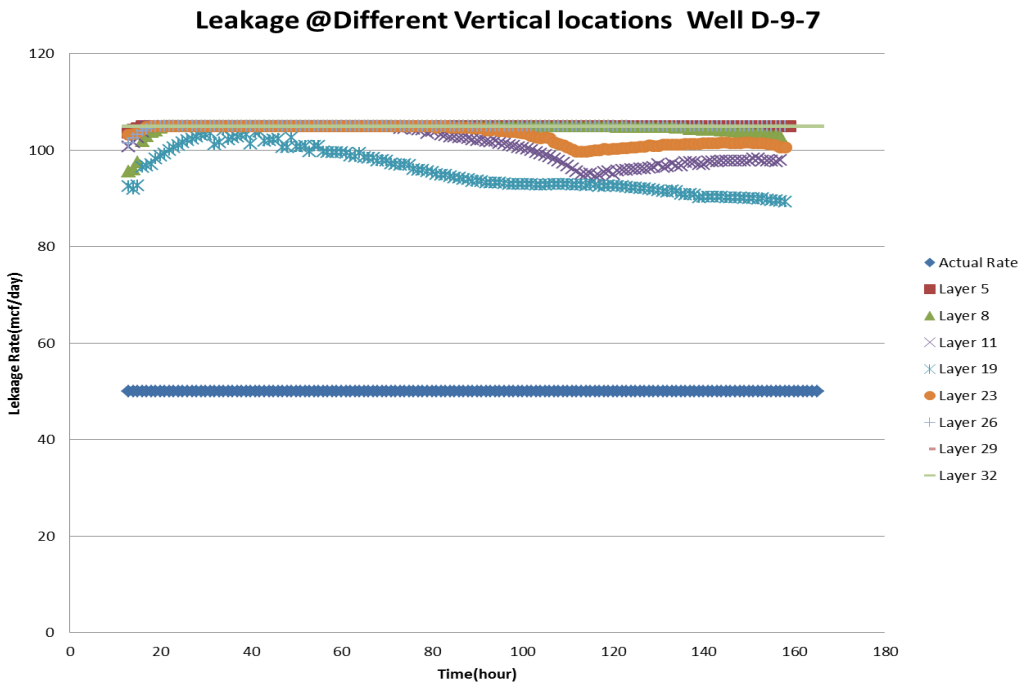

Figure 6-17: Leakage rate prediction at well D-9-7 when leakage took place at different vertical locations

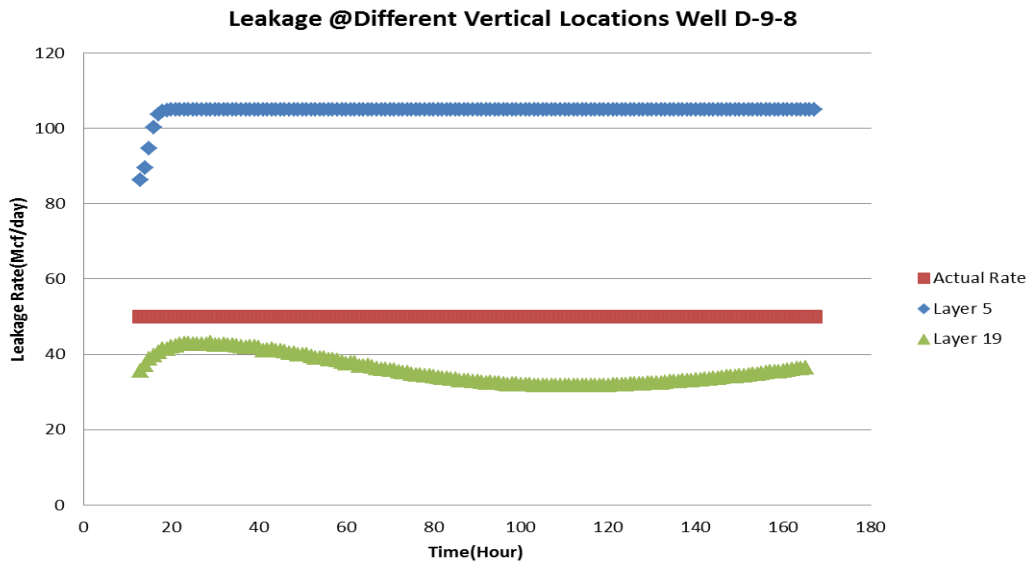

Figure 6-18: Leakage rate prediction at well D-9-8 when leakage took place at different vertical locations

6-5 Effect of Gauge Accuracy or Pressure Drift on R-ILDS Results

One of the important parameters that affect the accuracy of the pressure measurements is Pressure Sensor Drift (PSD). Most of the Pressure Down-hole Gauges (PDGs) experience PSD over their life time. PSD can be defined as gradual malfunction of the sensor that may create offsets in pressure readings from the original calibrated form [79]. The changes in the reservoir temperature or pressure make the PDGs to respond differently depending on manufacturing characteristics. The scale of PSD changes according to working conditions and manufacturing specifications.

PSD can be measured as how much pressure readings deviated from the original value in a year (psi/year). Distributions of different PSD values [80] are shown in Figure 6-19.For R-ILDS, Pressure Sensor Drift (PSD) can act as a CO_2 leakage indicator. When $\Delta p=0.01$ is recorded by the pressure sensor, R- ILDS reports a leakage and starts processing the data to quantify leakage characteristics. For example PSD equal to 1 psi/year generates $\Delta p=0.01$, almost 88 hours after the initiation of the drift.

Based on the different values of reported PSDs (Figure 6-19), the times that R-ILDS reports a leakage mistakenly are shown in Figure 6-20. This leakage is due to pressure gauge drift not actual induced pressure change. As mentioned earlier, PSD can be considered a CO_2 leakage indicator for the ILDS. Therefore, PSD trends (are substitute for Δp for actual leakage) over 168 hours were proceed and fed to R-ILDS. The R-ILDS prediction results for CO_2 leakage location and rate are shown in Figure 6-21. ILDS results for the leakage location at early times oscillate between wells D-9-6 and D-9-7. After 80 hours, all the results converge to Well D-9-6. This means that PSD makes ILDS to reports inaccurately that well D-9-6 is leaking.

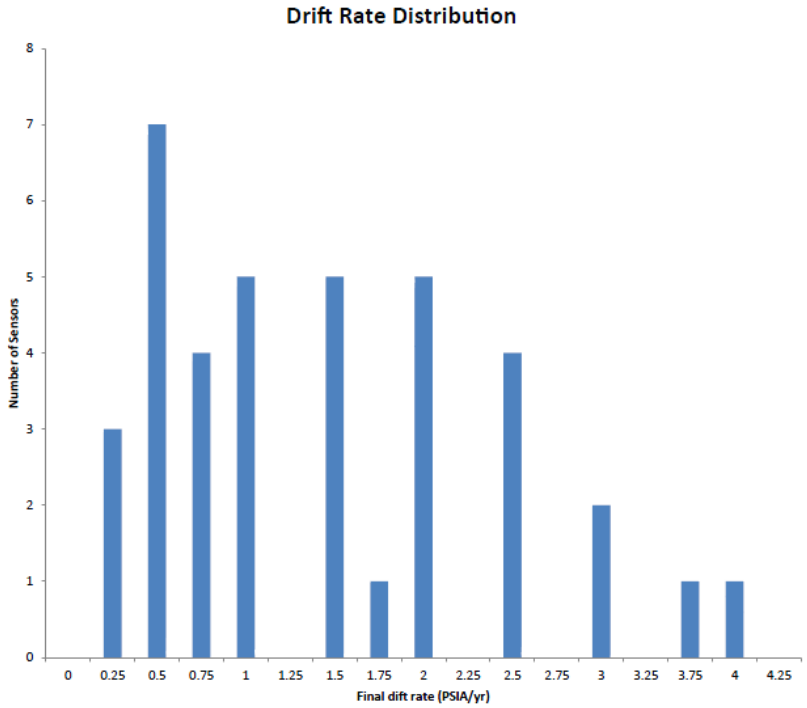

Figure 6-19: PSD distribution for the sensors

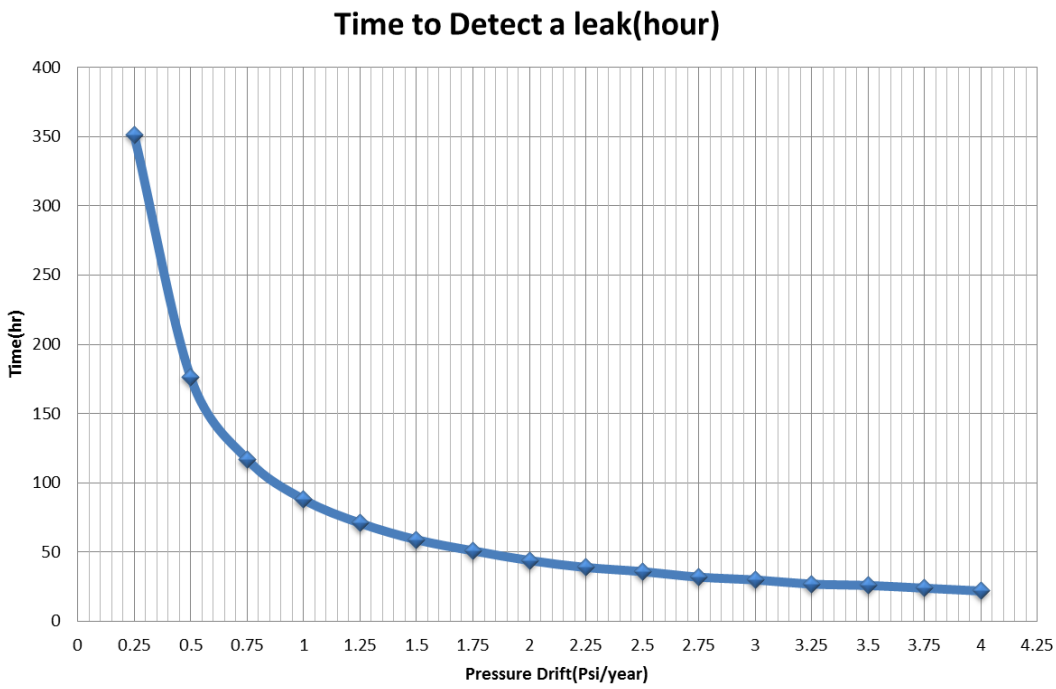

Figure 6-20: Time to report a leak based on different PSD values

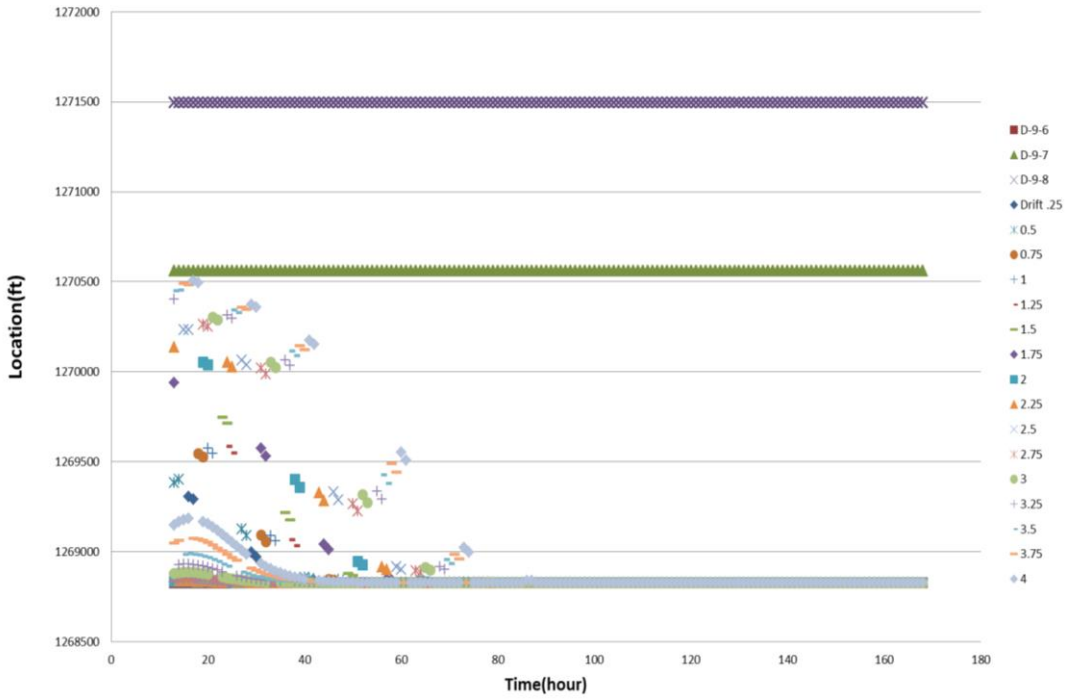

Figure 6-21: R-ILDS prediction for leakage location based on different drift values

6-6 Use of Well Head Pressure at Injection Well

Typically, there are 3 different reservoir pressure regimes during the injection and post injection. The first period refers to the start of the CO_2 injection until it ends (t1). At this period, reservoir pressure proportionally increases to the amount of injection and it reaches to a maximum value at the end of injection. When the CO_2 injection ends, there would be a transition time (t2) when the reservoir pressure decreases until the brine and injected CO_2 reaches to semi-equilibrium. At the end of the transition time (t2), reservoir pressure remains almost constant (or decrease with a slow trend) which can be referred to a steady state period (t3). These three time cycles are shown in Figure 6-22.The objective of this study was to develop R- ILDS for time cycle t3 when there had been no injection in the field and reservoir pressure reached to steady state trend. During this time period, since CO_2 injection stopped, there is no fluid flow in the well and well head pressure would not change (it is possible to have well head pressure during the injection-t1). Therefore it is not possible to use well head pressure at the injection well for leakage detection in this study.

The wells can be equipped with a pressure gauge [81] that measures casing pressure (Figure 6-23). When there is only steady state production from tubing and no leakage occurs, the casing gauge shows zero. Sometimes due to heating of casing and completion fluids, casing gauge does not read zero. By closing a needle valve, casing pressure should get back to zero. Otherwise, the casing represents Sustained Casing Pressure (SCP) which is an indicator for leakage; analysis of SCP can lead to determination of leakage pathway characterization on the same well (no other wells in that area). This is out of scope for this Study.

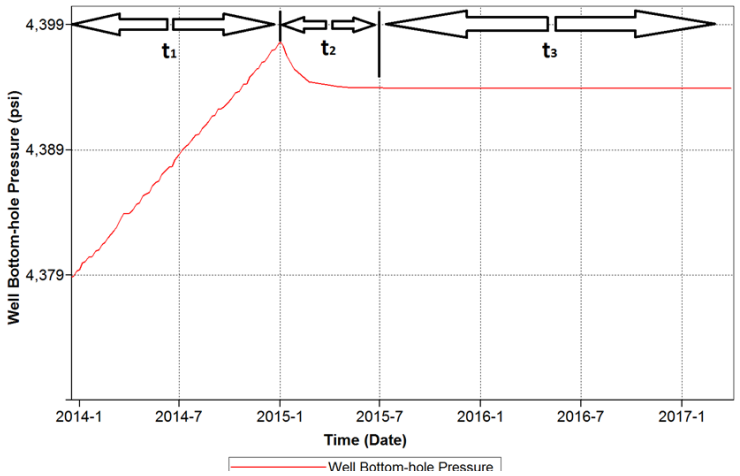

Figure 6-22: Different time cycles during and after CO_2 injection

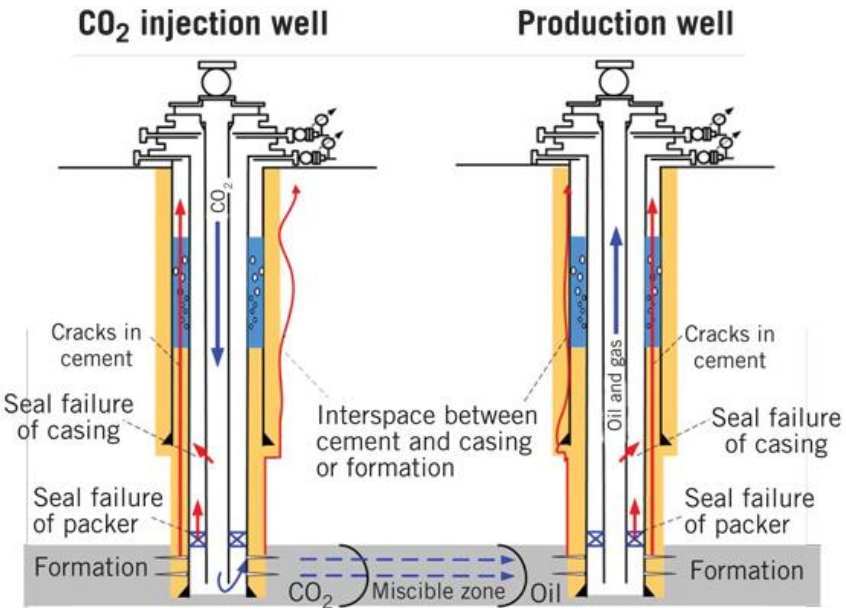

Figure 6-23: Sustained Casing Pressure [82]

6-7 R-ILDS for Variable CO_2 Leakage Rates

In previous sections, R-ILDS was developed by incorporating pressure signals that were generated by CO_2 leakage rates with step function behavior (Figure 6-24). CO_2 leakages were initiated with a specific rate that remained constant as the time passed. In order to investigate the effect of the CO_2 leakage function on the performance of R-ILDS, a set of simulation runs was designed to assimilate different CO_2 leakage rate behaviors such as linear, exponential and logarithmic. The corresponding pressure signals for each rate function should be included in leakage detection system development. Exponential and logarithmic CO_2 leakage rate functions are shown in Figure 6-25. Additionally, 20 different linear CO_2 leakage rates were assigned to each possible leakage locations (well D-9-6, D-9-7, and D-9-8) in the reservoir simulation model (60 total simulation runs). Linear CO_2 leakage rates are shown in the Figure 6-26. The corresponding pressure signals for each CO_2 leakage scenario were collected, processed and sorted to form a data set which is appropriate for pattern recognition technology.

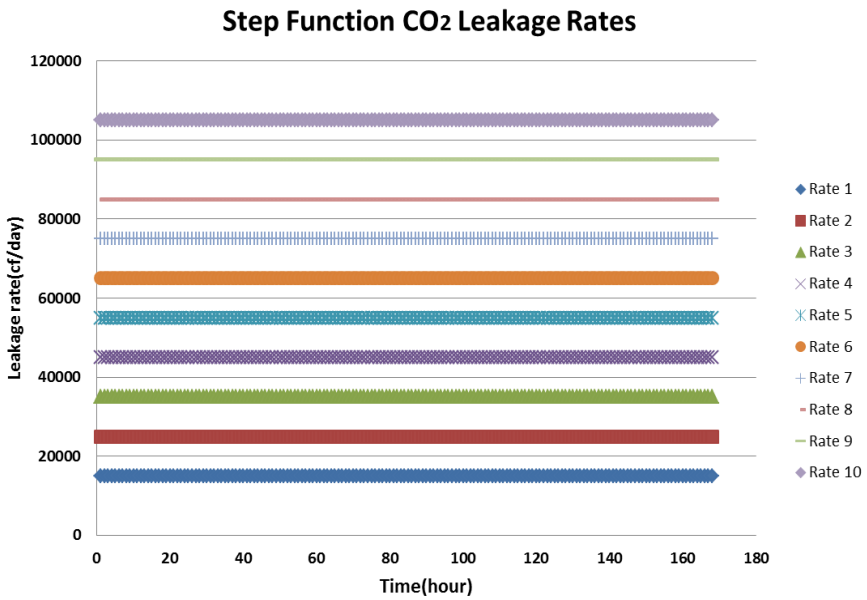

Figure 6-24: Step function CO_2 leakage rate

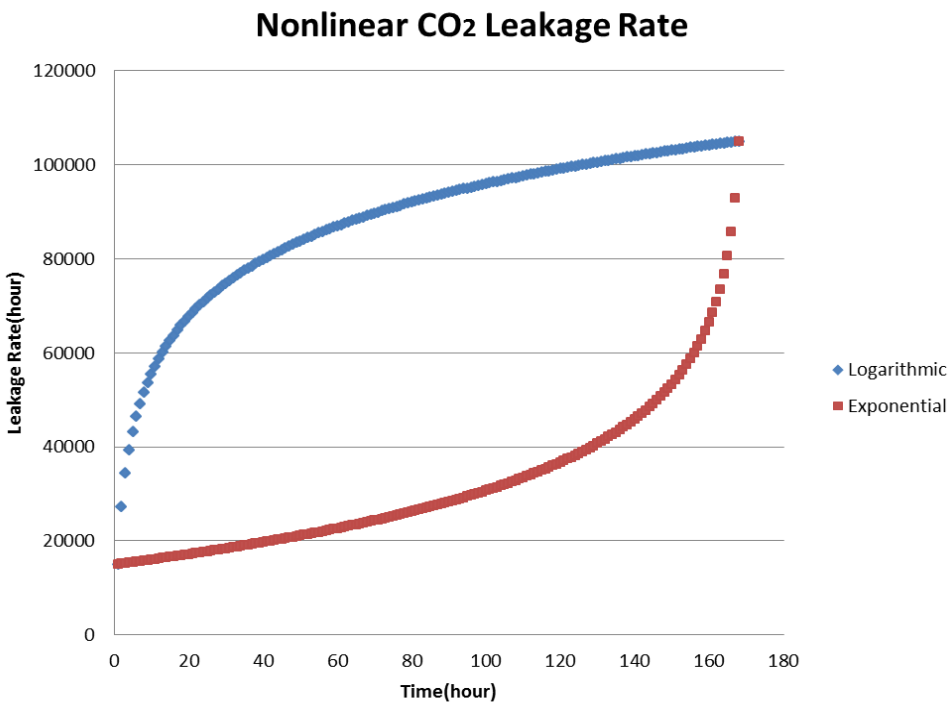

Figure 6-25: Logarithmic and exponential CO_2 leakage rates

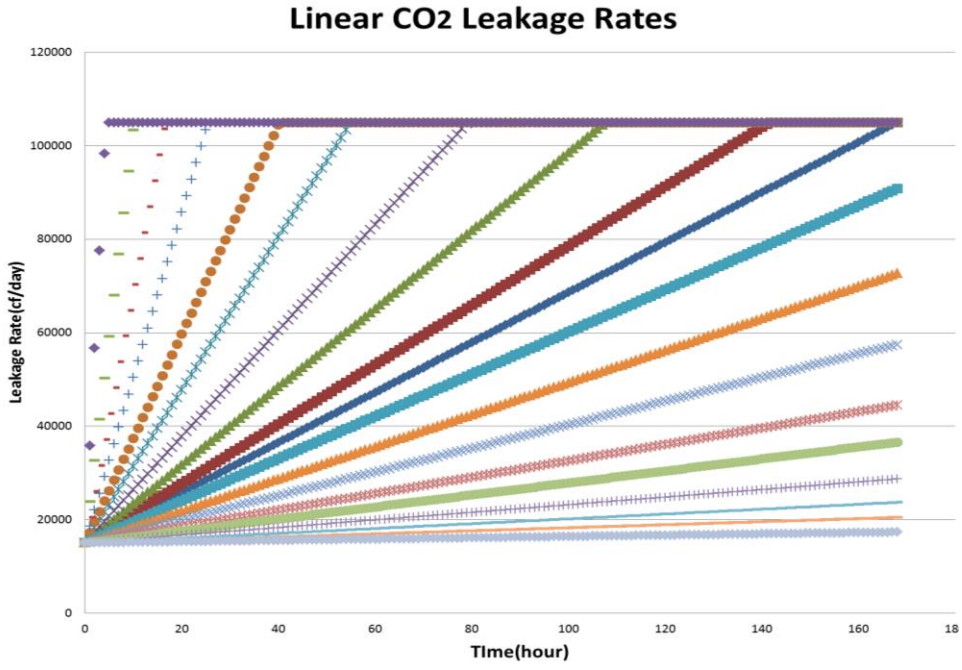

Figure 6-26: Linear CO_2 leakage rates

For CO_2 leakage location detection (with different leakage rate functions) all the pressure signals (coming from 60 simulation runs) as function of time and their calculated time-based descriptive statistics were lumped together to form input data set. Therefore input data set included 10950 data records that were partitioned into training, calibration and verification sets (80 %, 10% and 10% respectively). The outputs for this network were three leakage locations (wells D-9-6,D-9-7 and D-9-8).

Back-propagation neural network with 50 neurons in hidden layers was selected for training process. Neural network results (virtual versus actual) for CO_2 leakage location are shown in Figure 6-27. Neural network was able to find the pattern between leakage location and pressure signals with high precision(R-Square: 0.9985)

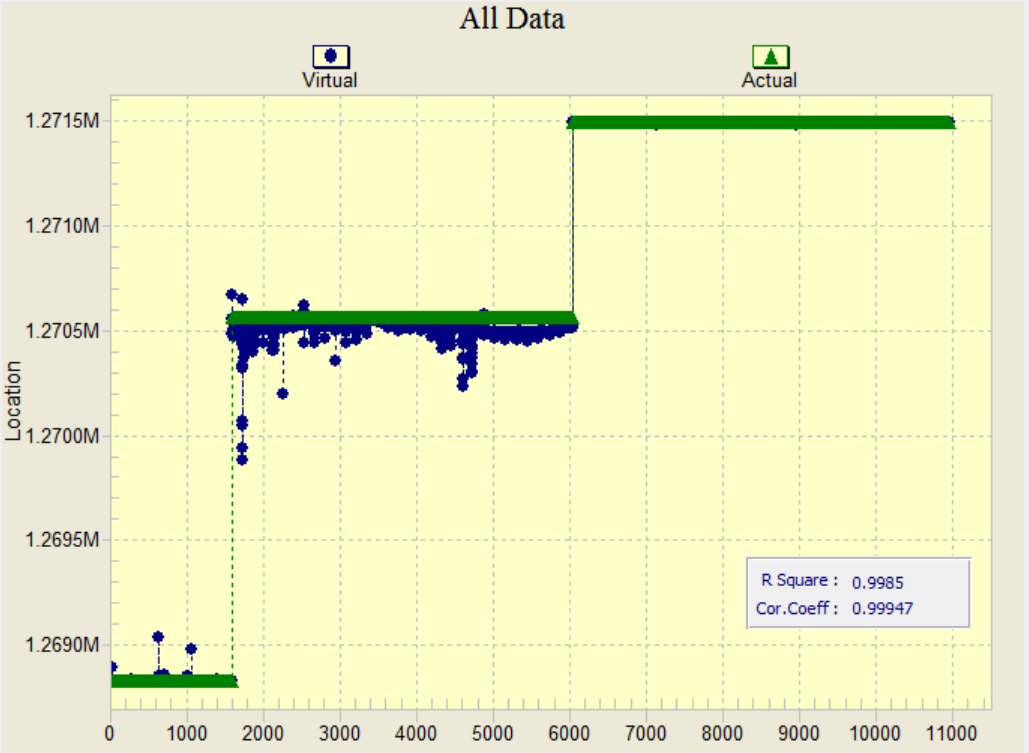

Figure 6-27: Neural network results for leakage location

Three neural networks were trained for each well individually to detect the leakage rate. The input data was the same as what was used for the leakage location training. However the output is CO_2 leakage rate at each specific time. It is different from that case the leakage rate remained constant as function on time.

The neural network architecture was almost the same as previous ones except the number of neurons in hidden layers. The results for CO_2 leakage rate (well D-9-8) are shown in Figure 6-28(results for other wells are in Appendix 3). Neural networks were able to determines a pattern between 32 different CO_2 leakage rate functions (as function of time) and corresponding pressure signals very accurately(R^2 : 0.9999).

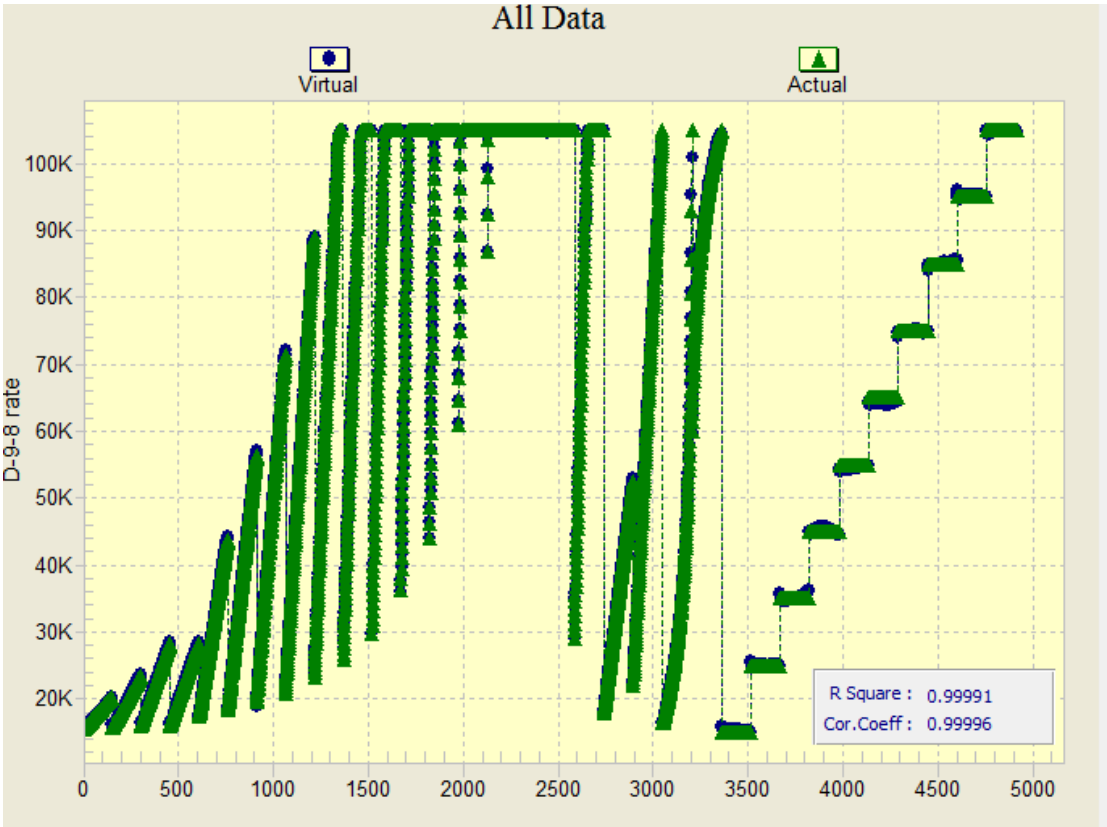

Figure 6-28: Neural network results for leakage rates at well D-9-8

In order to validate the performance of newly developed R-ILDS, a complex CO_2 leakage rate as function of time was considered for the blind run. This rate function represented logarithmic behavior at the beginning followed by a linear trend. The end part of the rate function showed exponential characteristic.

The rate function for the blind run is shown in Figure 6-29. This rate function was assigned to each of the leakage locations (D-9-6, D-9-7 and D-9-8) as the rate constraints and corresponding pressure signal from observation well (D-9-8#2) was collected. The pressure signals were processed to get real time Δp and calculated descriptive statistics values to be fed into the R-ILDS and find CO_2 leakage location and rate. R-ILDS predictions for

leakage location and rate (at well D-9-8) are shown in Figure 6-30and Figure 6-31. (All the results are shown in Appendix 3).

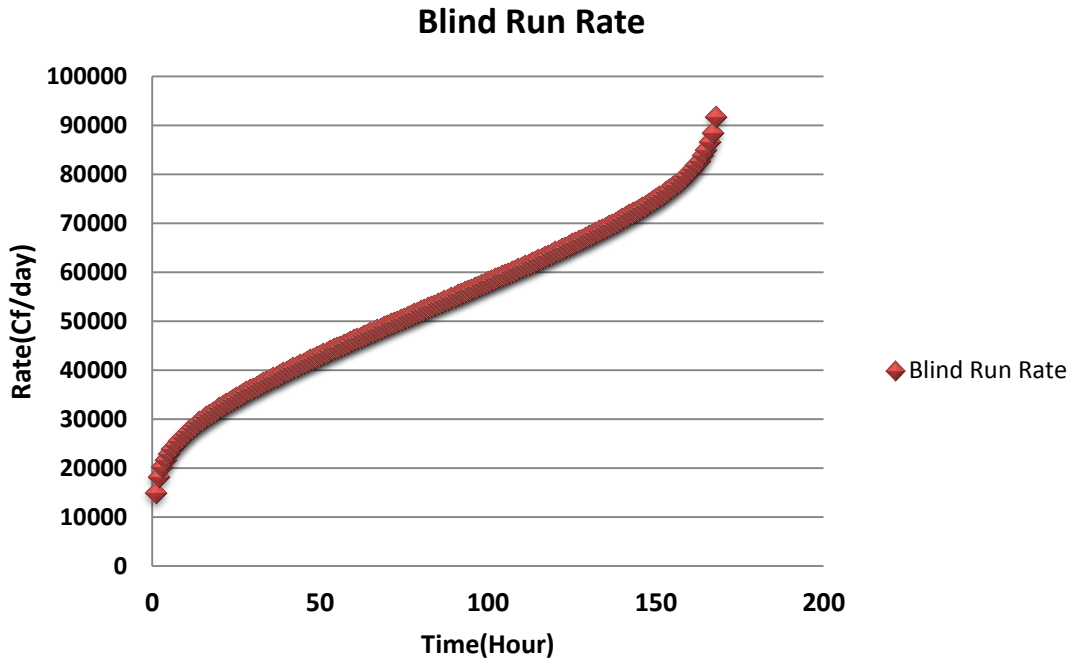

Figure 6-29: Rate function for the blind run

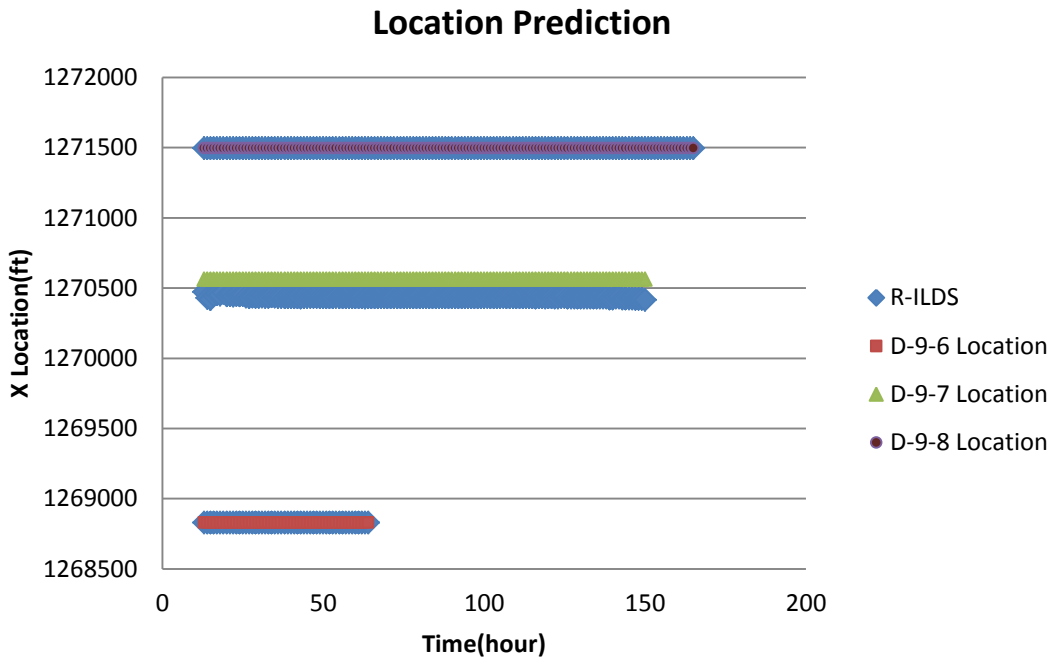

Figure 6-30: R-ILDS prediction for leakage location (variable rate)

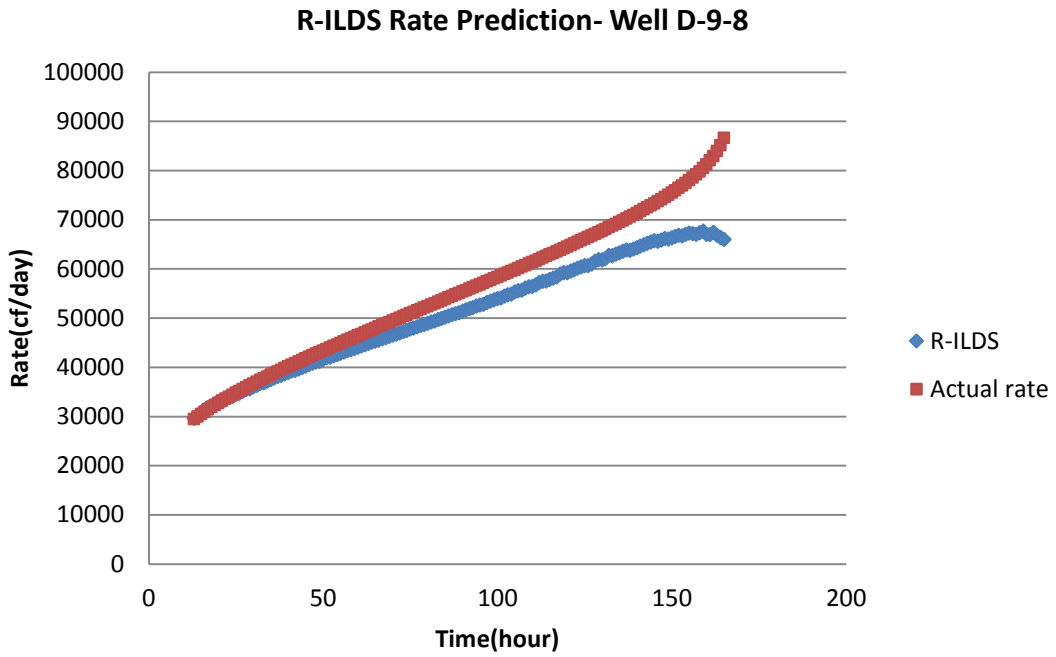

Figure 6-31: R-ILDS prediction for leakage rate in well D-9-8 (variable rate)

R-ILDS predictions for CO_2 leakage locations were reasonably accurate. Additionally, R-ILDS was able to predict the location of each well correctly. For CO_2 leakage rate in well D-9-8, R-ILDS prediction represented the actual rate especially at the early times.

R-ILDS predicted just one value for rate at each time. In order to have range of rates rather than a single value, "Monte Carlo" simulation was used. Monte Carlo method is a computerized mathematical technique designed for explanation of risk in quantitative analysis and decision making, [83].

Monte Carlo simulation tends to have the following pattern:

1. Identification a range for possible inputs.
2. Generate random inputs from a probability distribution over the range.
3. Perform a large number of computations with determined inputs
4. Collect, combine and analyses the results

The domain of the input parameters was defined by having Key Performance Indicator (KPI) analysis for leakage rate in Well D-9-8(Figure 6-32).

Rank	Feature	% Degree of Influence
1	Cum Sum(DeltP)	100
2	Cum Avereage(DeltP)	80
3	Cum ST Dev(DeltP)	64
4	Cum Skewness(DeltP)	56
5	Derivative	51
6	Delta P	48
7	Time(New)	3
8	Cum Kurtosis(DeltP)	1

Figure 6-32: KPI for CO_2 leakage rate in well D-9-8

As it is shown in in Figure 6-32, cumulative summation(Δp), average(Δp),standard deviation(Δp) and skewness indicated the most impact on CO_2 leakage rate in well D-9-8. Based on the "±20%" rectangular probability distribution, 1000 random variables for each mentioned parameter were generated. Then, trained neural network computed CO_2 leakage rate 1000 times based on combinations of the generated input variables. Calculated leakage rates were sorted according to their relative frequency and cumulative probability. As an example at time 162hr after leakage, the actual rate was 83Mcf/day while R-ILDS prediction showed 67.4Mcf/day. Monte Carlo results provided a leakage rate range (Figure 6-33) that includes the actual rate.

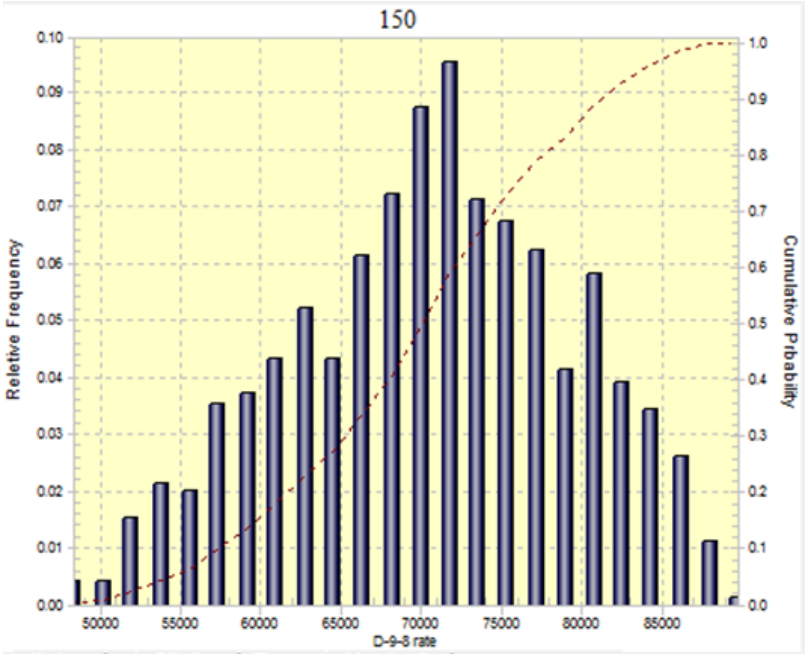

Figure 6-33: Relative Frequency and cumulative probability for leakage rate (well D-9-8) at time 162hr

6-8 Use of Pressure Down-hole Gauge (PDG) in Injection Well

Two Pressure Down-hole Gauges were installed in the well D-9-8#2 to transduce real time pressure data (Figure 6-34). All the studies were performed based on the presence of PDG at observation well. At this section, it is assumed that a pressure down-hole gauge is installed in the Injection well (D-9-7#2) rather than observation well. This may reduce the need for drilling an observation well in the system. All the reservoir simulations runs that addressed 30 different CO_2 leakage scenarios (explained in section 6-1) were used to generate high frequency pressure data at the injection well. The same procedure was used to develop R-ILDS based on high frequency pressure data collected at the injection well. The results for the R-ILDS development based on the presence of the PDG at the injection well are in Appendix 4(The results included neural network and blind runs based on Table 5-6.

Figure 6-34: Location of the injection and observation well in the area of interest

According to training results R-ILDS was able to predict the CO_2 leakage rates with very good precision (CO_2 leakage rate R^2 were more than 0.99 for all three wells, D-9-6, D-9-7 and D-9-8). For CO_2 leakage location, the R-ILDS results were not representing the actual locations (CO_2 leakage location R^2 was 0.49). The reason for not having good results is that injection well is located approximately in the middle of wells D-9-6 and D-9-8

(Figure 6-34). This symmetric characterization of well locations, led to having the same pressure signals, when well D-9-6 or D-9-8 leaked (Figure 6-35). Since the injection well is located in the middle of CO_2 plume (based on reservoir characterization), it receives the same pressure signals from different leakages that are at the same distance to the well. Therefore it is not possible to detect the exact location correctly. PDG should be installed in location that represents distinct pressure signals from different leakage location. Otherwise the presence of second monitoring well is necessary to be able to detect CO_2 leakage location correctly.

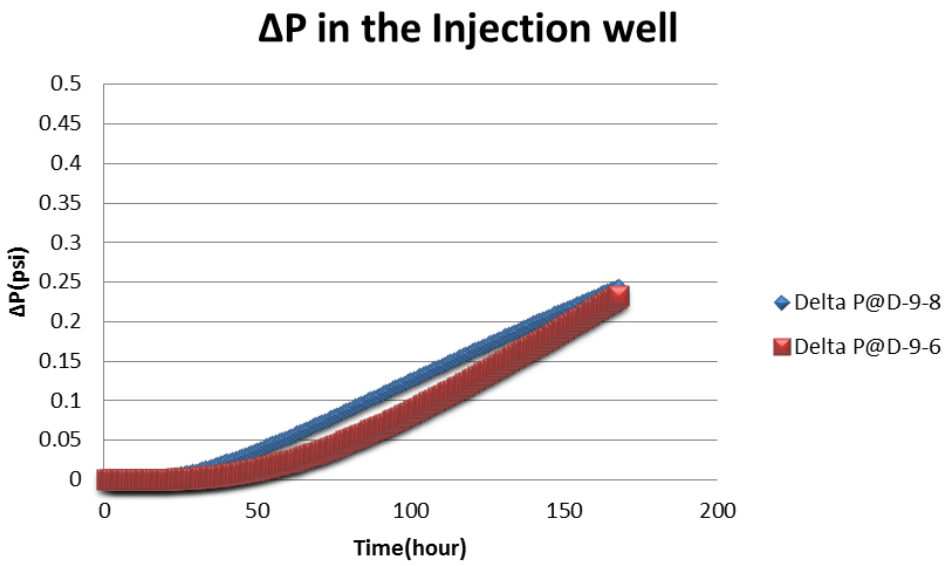

Figure 6-35: Pressure signals subject to leakages at well D-9-6 and D-9-8

6-9 Cap-rock Leakage

Initially, the reservoir was assumed to have a continuous sealing cap-rock that prevented any communication between the layers. After the injection period, pressure on one side of the seal (in the target zone) would increase leading to a pressure difference across the cap-rock. As explained in section 2-2-1-2, when the pressure difference exceeds the fracture pressure, the seal layer breaches and provides a path for CO_2 to migrate to the other layer. In order to model cap-rock leakage in the reservoir simulator, the pressure in the Dantzler

sand located on top of the seal (Figure 3-2) was estimated by having the pressure gradient in the formation and its average depth. This pressure was assigned as the constraint for the cap rock leakage in the model. The pressure difference between two layers is the main driving force for CO_2 flow through the leakage path. As an example, the reservoir pressure (in the observation well) and CO_2 leakage rate behavior for the case that cap rock leakage occurs (at 01/01/2022) in the North direction of injection well (Figure 6-36) is shown in Figure 6-37. When the cap-rock fracture is initiated, large amount of CO_2 is released and leaked to the upper layer in very short time(less than a day). This high flow rate of CO_2 leakage causes sharp decline in the reservoir pressure. As the reservoir pressure decreases, the driving force (pressure difference between reservoir and top sand layer) declines and less CO_2 leakage rate is observed. Typically ,the pressure signal that is created due to cap rock leakage represents higher amplitudes compare with the well leakages signals (that were studied in previous sections). Therefore a different R-ILDS was developed to be able to detect and quantify the characteristics of cap rock leakage.

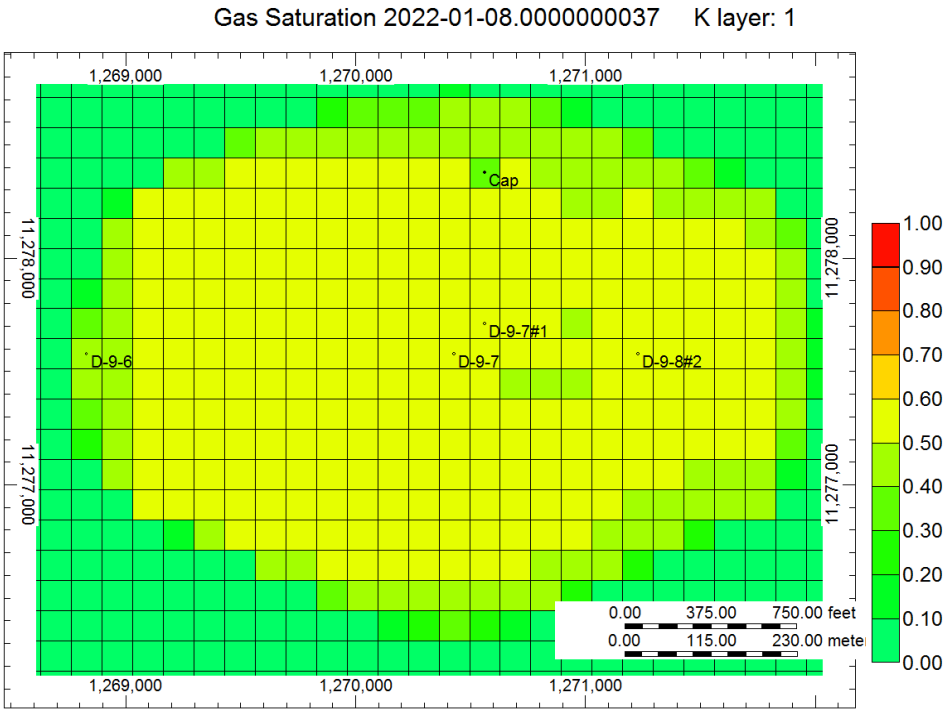

Figure 6-36: Cap-rock leakage location

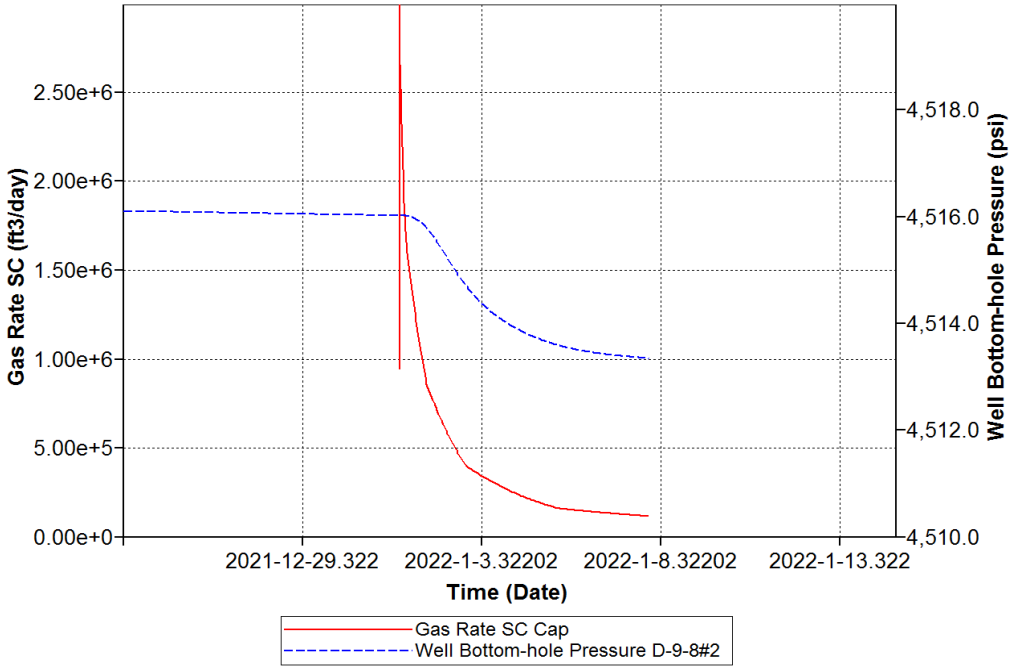

Figure 6-37: Pressure behavior in the observation well and CO_2 rate due to cap rock leakage

In order to develop R-ILDS for detecting the cap-rock leakage, 9 different simulation runs were designed based on the location of the leakage (Figure 6-38). The only constrain for cap-rock leakage was pressure in the upper layer (Dantzler sand) which was assigned as the bottom–hole pressure for the synthetic well that was drilled in the leakage location. As mentioned earlier, there is a sharp pick in the CO_2 leakage rate. To eliminate this pick in the CO_2 leakage rate behavior, cumulative amount of leaked CO_2 was used instead of rate. The training process is exactly the same as what was explained in this chapter. For each leakage scenario, the corresponding pressure signals were processed in real time by descriptive statistics to be used as the input for neural network. The outputs for the neural network were leakage location(x and y) and cumulative leaked CO_2. The results for neural network training are shown in Appendix 5. The neural network results for cumulative leaked gas and x coordinate of leakage location were precise with R^2 equal to 0.97 and 0.99 respectively. For leakage location "y" coordinate the neural network predictions were not as accurate as the other ones (cumulative leaked gas and x coordinate). It might be due to the symmetric locations of cap-rock leakages respect of observation well in "y" direction.

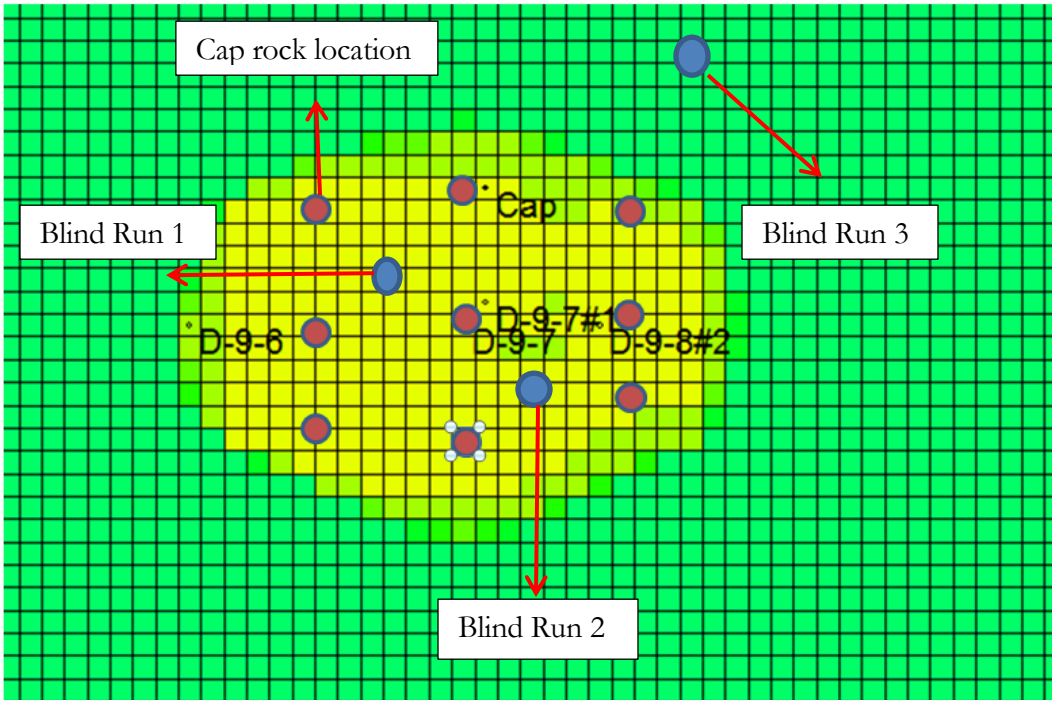

Figure 6-38: 9 different locations for cap-rock leakages and 3 blind runs

The final part for verification of cap-rock R-ILDS was to design set of blind runs that were unused in neural network training process. Three cap-rock leakage locations were considered in the reservoir simulation model (Figure 6-38). Two cap-rock leakage locations (out of three) were inside the range of the locations used for neural network training. The results for blind run verification are shown in Appendix 5. It can be observed that for cumulative leaked gas, R-ILDS results are almost the same as actual values for the first two blind run cases (were located in the range of locations). For the third blind run which was located outside the range, R-ILDS results overestimated the actual value considerably. X-coordinate results were almost the same as actual locations except blind runs 2. For the Y coordinate results there were noticeable difference between actual values and R-ILDS prediction. Overall, location of cap-rock leakage can be predicted as accurate as well-leakage due to symmetry of the location and impulsive and uncertain behavior of the leakage.

6-10 Multi-Well Leakage

In the previous sections, a single well leakage was studied and analyzed. The remaining question and concern is if it would be possible to detect multi-well leakages .To investigate multi-well leakage, combination of rates for two and three well leakages were assigned to the wells in the reservoir model according to Table 6-2.

Table 6-2:CO_2 leakage rates for multi-well leakage

Two Well			Three Well		
Leakage Rate(Mcf/day)			Leakage rate(Mcf/day)		
D-9-6	D-9-7	D-9-8	D-9-6	D-9-7	D-9-8
15	15	0	15	15	15
15	60	0	15	15	60
15	105	0	15	15	105
60	15	0	15	60	15
60	60	0	15	60	60
60	105	0	15	60	105
105	15	0	15	105	15
105	60	0	15	105	60
105	105	0	15	105	105
15	0	15	60	15	15
15	0	60	60	15	60
15	0	105	60	15	105
60	0	15	60	60	15
60	0	60	60	60	60
60	0	105	60	60	105
105	0	15	60	105	15
105	0	60	60	105	60
105	0	105	60	105	105
0	15	15	105	15	15
0	15	60	105	15	60
0	15	105	105	15	105
0	60	15	105	60	15
0	60	60	105	60	60
0	60	105	105	60	105
0	105	15	105	105	15
0	105	60	105	105	60
0	105	105	105	105	105

After performing simulation runs (start of leakage was at 1/1/2022) based multi-well leakage scenarios and processing all the corresponding pressure signals, it was required to train a neural network to differentiate between various combinations of well leakages. In this regard, a "Leakage Index" was defined based on the distance of each well from the observation well. Longer distances from the observation well resulted in selecting lower values for leakage index. The index values ranged from 1 to 7(higher values represent higher pressure signal amplitudes) according to distance to observation well and number of the leaking wells. All the scenarios can be divided into three classes as :single well leakage(indexes:1,2,3), two well leakage(indexes 4,5,6) and three well leakage(index:7) Leakage index values are shown in Table 6-3.

Table 6-3: Leakage Index for different single and multi-well leakage scenarios

Leaking Well	Leakage Index
D-9-6	1
D-9-7	2
D-9-8	3
D-9-6 & D-9-7	4
D-9-6 & D-9-8	5
D-9-7 & D-9-8	6
D-9-6 & D-9-7 & D-9-8	7

Several neural networks were trained considering different leakage indexes as the output and processed pressure signals (Δp) as the input. The results are shown in Appendix 6. As it can be seen, it was not possible to get reasonable results for the neural networks. The main reason for not getting acceptable neural network training is that convolution of several pressure signals (generated by different combinations of well leakages) makes it impossible for networks to catch specific patterns out of final pressure signals.

In order to de-convolve mixed pressure signals (generated by multi-well leakages), existence of a pressure down-hole gauge was considered in the injection well (in addition to the observation well). The problem also was simplified in a way where only two well leakages were subject to investigation (leakage index values of 4, 5, and 6). Addition of one

more pressure down-hole gauge brought in more information about pressure signals and the time that signals were observed by the gauges. For this case, a neural network was trained by Generalized Regression Neural Network GRNN, algorithm. The results for neural network training are shown in Figure 6-39.

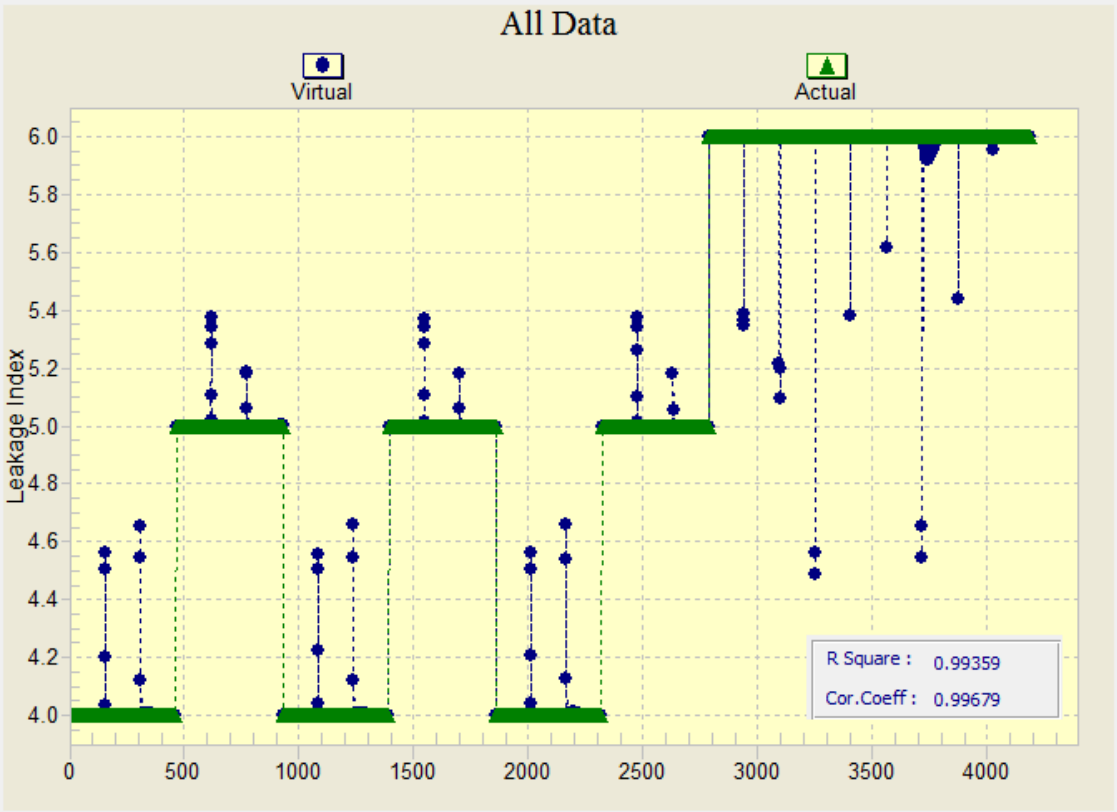

Figure 6-39: Neural network results for two-well leakage

By use of new approach (adding more pressure gauge in the injection well), the results for neural network training improved significantly (R^2 equal to 0.9935). As a result, it became possible to differentiate which two wells were leaking by having pressure signals coming from two pressure down-hole gauges. The final step was to verity the practicality of the R-ILDS which was devolved for multi well leakage. To do so, six simulation runs considering combinations of two-well leakages (Table 6-4) were performed.

Table 6-4:CO_2 leakage rates for the blind runs-two well leakages

Run	Two Well Leakage Rate(Mcf/day)		
	D-9-6	D-9-7	D-9-8
1	40	80	0
2	80	40	0
3	40	0	80
4	80	0	40
5	0	40	80
6	0	80	40

The results for blind run verifications are shown in Figure 6-40. R-ILDS was able to predict the leakage index correctly except for few hours at the early times after the leakages. Although the probability of two wells leak simultaneously is very low, but with use of two pressure gauges installed in two distinct wells, it was possible to say which wells leak at the same time.

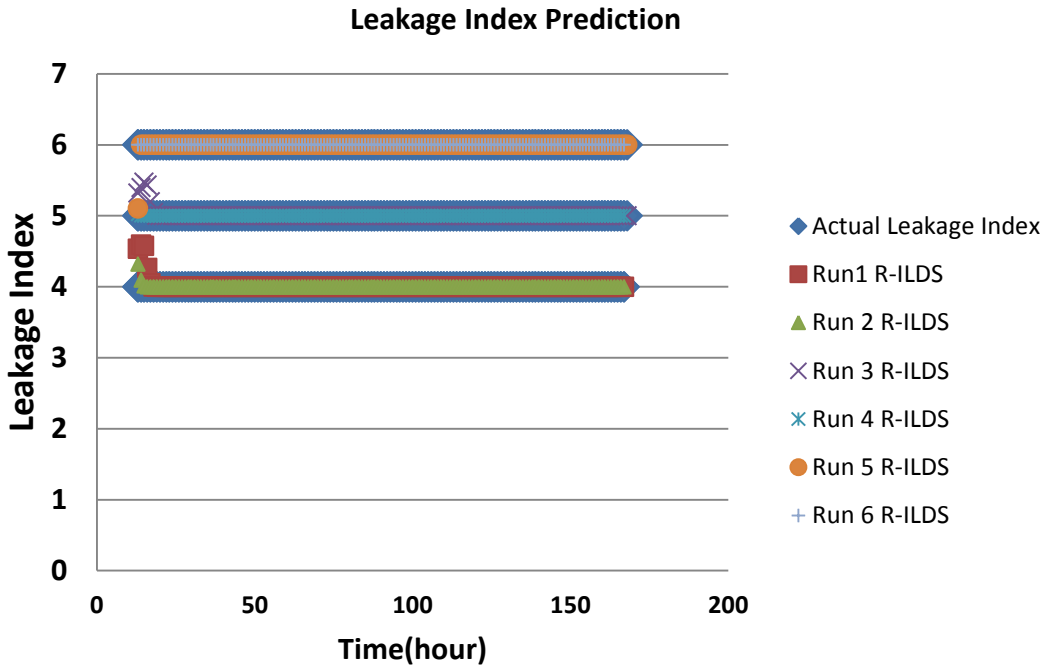

Figure 6-40: R-ILDS predictions for two-well leakages

6-11 Data Cleansing

Interpretation of the PDG data can be challenging due to disturbances like noise and outliers. Noise is a group of data points that scatter around the trend of the overall data but lie in the same neighborhood as the true data. Outliers are data points that lie away from the trend of data. Both can be identified from their misalignment with the rest of the data. The real field pressure data that are gathered from pressure down-hole gauges represent some type of noise. In this section, associated noise with pressure data would be analyzed. Additionally, two de-noising methods for cleansing the noisy data are discussed.

6-11-1 Determination of noise level and distribution

In the observation well (D-9-8#2) at Citronelle field, two Pressure Down-hole Gauges (PDG) are installed at different depths (9416 and 9441 ft) in order to provide real time pressure and temperature readings during and after injection period. The pressure data is available from 8/17/2012 to 11/29/2013 almost at every minute. It should be mentioned that there are some gaps in the pressure records due to onsite computer failure. The pressure trends from the PDGs are illustrated in Figure 6-41.

In order to prepare high frequency data for pattern recognition (and also de-noising process) it is necessary to evaluate the noise behavior. There are 2 main features in the noisy pressure data that are required to be analyzed in more detail as: noise distribution and noise level.

The noise level [84] can be determined by knowing the difference between actual data and the fitted curve of the same data over a predefined time interval (with no fluctuation in the data).

$$NL = P_{actual} - P_{fitted} \rightarrow Noise\ Level = \left(\frac{1}{n-1}\sum_{i=1}^{n} N_i^2\right)^{1/2}$$

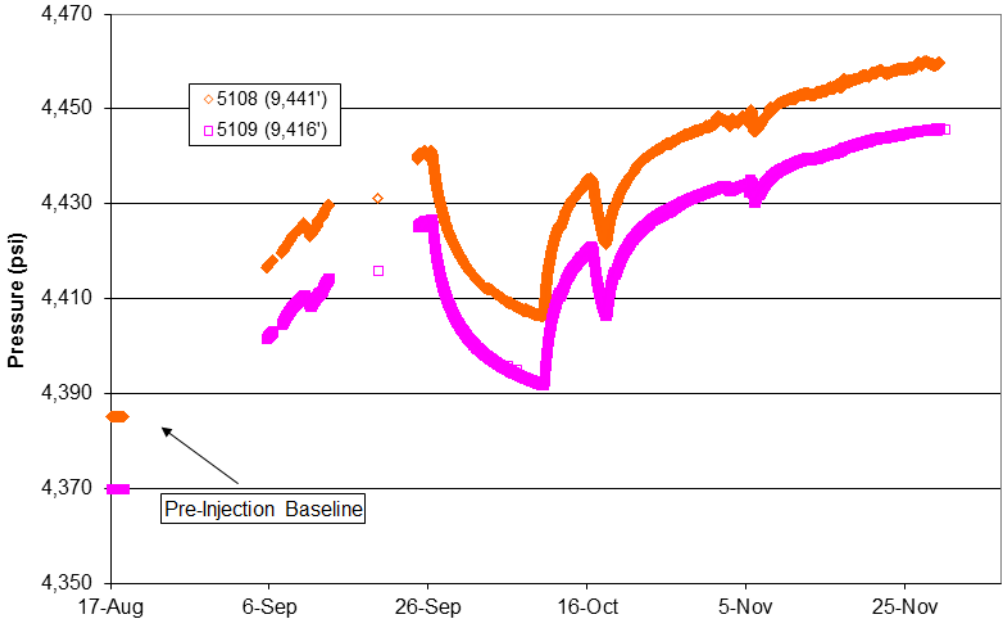

Figure 6-41 Monitoring Well (D-9-8#2) PDG data

Six thousand five hundred pressure records were selected in the interval from 26th to 29th of September 2012 when the pressure trend had no sharp transients. Generalized Regression Neural Network (GRNN) was used to determine the fitted curve of the selected data. The results of curve fitting are shown in Figure 6-42.

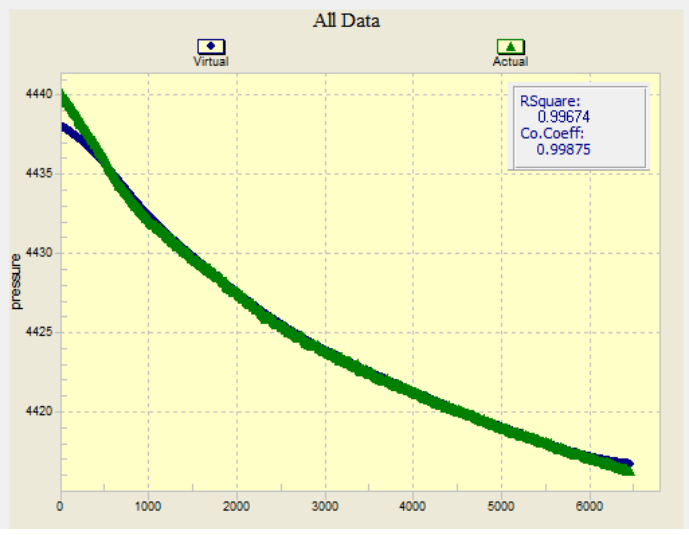

Figure 6-42: GRNN results for fitted pressure curve

Based on the mentioned formula the noise level is 0.08 psi. The maximum and minimum of the Noise Levels are equal to 0.185 and -0.282 psi respectively. Also the frequency distribution of the noises was generated. Based on the results it can be concluded that the noises represents Normal or Gaussian distribution (Figure 6-43). Therefore the noise with the mentioned characteristics will be added to the reservoir simulation pressure scenarios. The noisy and de-noised data would be preprocessed to be transformed into a format that is suitable for pattern recognition analysis.

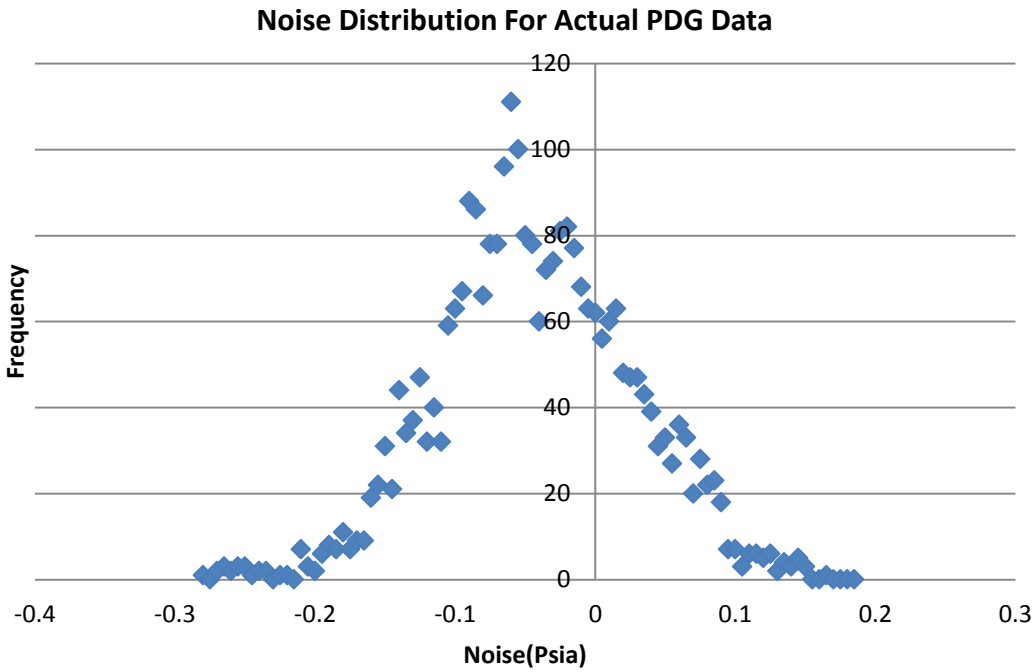

Figure 6-43: Noise distribution for actual PDG data (6500 records, Normal Distribution)

6-11-2 De-noising the Pressure reading

In order to extract the most representative features from the data and reduce fluctuations, a procedure called de-noising is commonly applied. Most of the de-noising methods tend to smear out sharp features in the data. The method being used in this project is denominated the Wavelet Thresholding Method [85] which generally preserves most of these features.

Wavelets are mathematical functions that divide or separate data into different frequency components, and then study each component with a resolution matched to its scale, basically provides a multi-resolution framework for data representation. They have

advantages over traditional Fourier methods in analyzing physical situations where the data contains discontinuities and sharp features [85].

The general de-noising procedure consists of 3 different steps. Initially, the noisy data should be divided to N levels, following with decomposition of the data at level N. After that for each level from 1 to N, a threshold should be considered and then soft thresholding should be applied to the detail coefficients. Finally the data is reconstructed using the original approximation coefficients of level N and the modified detail coefficients of levels from 1 to N. The important step in de-noising data is threshold selection method for each level. Three threshold selection rules can be implemented as: Rigorous SURE, Heuristics SURE and Fixed form threshold [86]. Threshold selection is mainly subjective to the noisy data characteristics. Also several methods have been developed regarding wavelet shrinkage and thresholding. The main two thresholding methods are the soft-thresholding and hard-thresholding method. The main difference between them is that the soft-thresholding method consists on analyzing the difference between the wavelet coefficients and the chosen threshold smoothing the data once the wavelet transform is applied. In the hard-thresholding method, wavelet coefficients whose absolute values are less than the threshold are set to zero. Depending on the scale and particular characteristics of the data both method can be used and the result is a cleaned-up data which will still show important details [86].

The pressure data from reservoir simulation model was considered to be clean with no noise or outlier. For further analysis, it was necessary to add noise with the same characteristic (mentioned earlier) to the pressure data. After adding the noise data cleansing methods should be applied to the noisy record (generated by adding noise to the clean data). In this study Daubechies wavelet 10 in five levels were used to decompose the noisy data. After decomposition to 5 levels, a threshold assigned to each level to remove the data that lies outside the specified level. Then the processed data from each level were combined to reconstruct the de-noised data. An example of pressure data from simulator, the same data with normal distributed noise and cleansed data (De-noised with Wavelet threshold method) when well D-9-6 leaked CO_2 with the rate of 30 Mcf/day are shown in Figure 6-44.

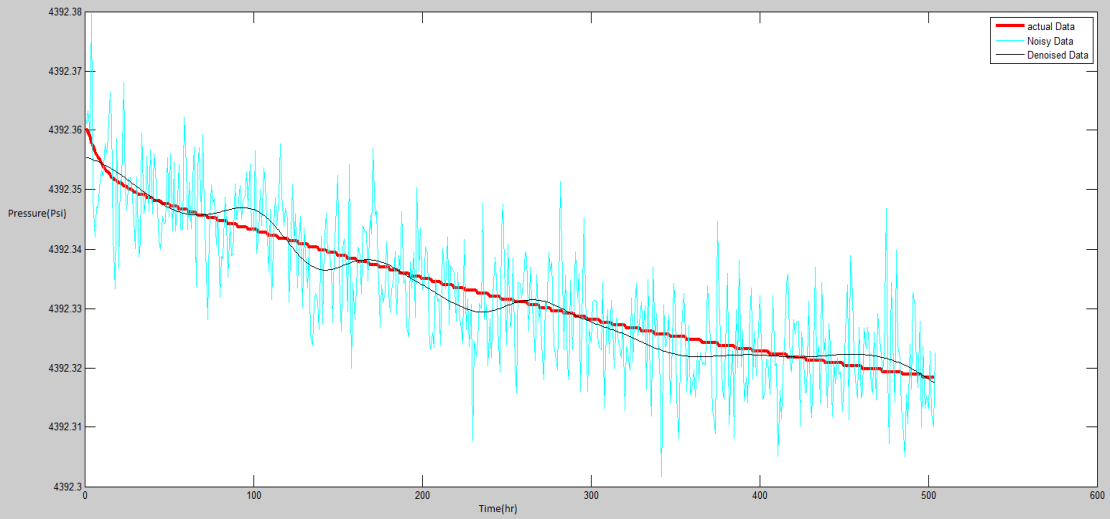

Figure 6-44: Pressure data from simulator(red),added noise(green) and de-noised (black) when well D-9-6 leaks with the rate of 30Mcf

The main concern for using Wavelet threshold method for data cleansing is the de-noised data generally follows the trend of noisy data. This is mostly the case when leakages rates are low and corresponding real time pressure signal changes in the observation well are in a narrow range. This oscillating pattern of de-noised data changes the parameters that were obtained by data summarization of clean data. In order to alleviate the effect of noise and clean the data in a way that represent behavior of pressure trend, GRNN (General Regression Neural Networks) was used. GRNN is a type of probabilistic neural networks that requires just some small portion of data records for training [59]. That specification of GRNN is advantageous since it would be able to capture the underlining trend and functionality of the large amount of data with few samples. When high frequency noisy pressure data should be processed for leakage detection, it would be better to use GRNN rather than the Wavelet threshold method. Because the GRNN uses smaller portion of data, the presence of the noise cannot generally affect the calculated trend. This would be the case especially when the frequency of data increases. Therefore GRNN can be considered to be a very useful tool to de-noise high frequency pressure data. The results for de-noising pressure records by GRNN are shown in Figure 6-45. By comparing the resulted trends from Wavelet threshold de-noising method and GRNN with the original clear data, it can be concluded that GRNN method performs better.

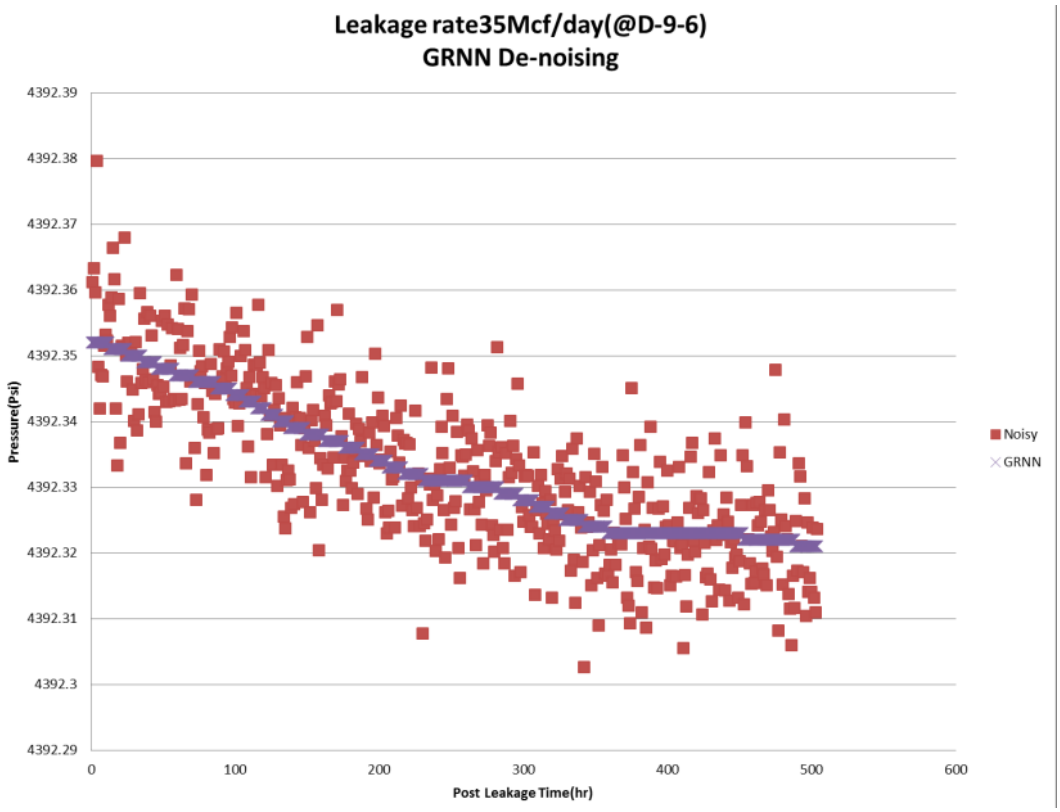

Figure 6-45: Noisy and De-noised pressure data using GRNN

6-12 Conclusion

In this chapter, a comprehensive study was performed to improve ILDS capabilities and test it over different uncertain parameters. Verified and history matched model was used for CO_2 leakage modeling.

At the beginning a new data processing method was proposed to make ILDS to a fast responsive and real time detection tool(R-ILDS). CO_2 leakage characteristics (amount and location) were determined much faster that what was proposed in Chapter 5 by R-ILDS. Additionally, minimum detection times for R-ILDS subject to various leakage locations and rates were determined by considering pressure behavior at observation well and resolution of the PDG. Closer the leaking well to the observation well and higher the leakage rates represented shorter time for leakage detection.

4 different reservoir parameters (porosity, sand layer top, sand layer thickness and vertical to horizontal permeability ratio) were varied to investigate their effect on the R-ILDS predictions. Change of reservoir porosity showed to have higher impacts on R-ILDS results

especially for CO_2 leakage location and some cases leakage rate predictions. Sand layer top was the other important parameter that impacted R-ILDS results.

The ability of ILDS was tested to see if it was possible to detect leakages that took place at different vertical locations along the wells. It was observed that with current locations of the PDGs (first sand layer) it would not be possible to sense any pressure changes due to leakage in other layers. Due to presence of impermeable shale layers between the sands that caused no inter communications between layers; PDG should be installed at each layer specifically, to be able to detect leakages at different vertical locations.

The effect of Pressure Sensor Drifts (PSD) was studied on performance of the R-ILDS. According to different reported values for PSDs, the time that R-ILDS reported a leakage (false leakage) and predicted leakage locations were determined. Within the range of pressure drifts (0.25 to 4 psi/year), it took from 20 to 350 hours that R-ILDS report a leakage. Additionally, R-ILDS predicted that leakage took place mostly at well D-0-6.

The use of well-head pressure instead of PDG data was studied in this chapter. Well-head pressure during the injection time or t1 would be available. This study's objective was to use pressure data during stabilization time or t3. Therefore it was not possible to use well head pressure for leakage detection purposes. Instead, analysis of Sustained Casing Pressure (SCP) was proposed as an alternative solution.

The ability of detecting leakages with variable CO_2 leakage rates was added to R-ILDS. To do so, multiple CO_2 leakage rates with linear, exponential and logarithmic behavior were assigned to leakage locations. Corresponding pressure signals were used to train a new neural network. R-ILDS represented good results and was tested successfully with a blind run. Besides that, R-ILDS demonstrated distribution (by use of Monte Carlo simulation) for predicted CO_2 leakage rates.

The possibility of using injection well as the monitoring well was investigated as part of this chapter. The procedure of developing R-ILDS based on presence on PDG in the injection well was almost the same as what mentioned at the beginning of this chapter. Injection well R-ILDS predicted the leakage rates with high accuracy but failed to predict the location of leaking wells due to the symmetric locations of leaking wells respect to injection well.

Cap-rock fractures provide a conduit for CO_2 to leak of the target formations. Cap-rock leakage behavior (release high amount of CO_2 in very short time) was different from well – leakage and was modeled separately in the simulation model considering the cap-rock thickness and reservoir pressure in the overlaying sand layer. Nine possible locations of Cap-rock leakage were proposed within the CO_2 plume extension. R-ILDS was re-developed and verified based on pressure signals coming from 9 simulation and 3 blind runs. R-ILDS predictions were within a reasonable range for cumulative leaked gas and x-coordinate of leakage location.

The other concern for R-ILDS was the ability of detecting multi-well leakages. Fifty four simulation runs were performed with two-well and three-well leaking scenarios. With just one observation well, it was not possible to distinguish different leakage scenarios. Addition of one more observation well in the location of injection well, enabled R-ILDS to find which two wells leak simultaneously.

The last part of the chapter studied the behavior of the noise associated with PDG pressure readings. The noise behavior was analyzed based on standard methods (fitted curve analysis). Noise with the same characteristics was added to clean pressure data coming from reservoir simulation model. Two different de-noising methods (Wavelet Threshold and GRNN) were implemented to clean the high frequency noisy data. GRNN showed better de-noising results compare with the other method.

Chapter 7 Conclusions and Recommendations

7-1 Conclusions:

The objective of this study was proof the concept and feasibility of using real time pressure data from PDGs in order to notice occurrence of leakage and identify its characteristics (location and rate) in a real CO_2 storage project by utilizing AI & DM techniques.

1- A reservoir simulation was developed to model CO_2 injection in the Paluxy saline reservoir of the Citronelle Dome. This model was built based on comprehensive geological study by interpretation of more than 40 well logs. Initially, the reservoir simulation model was used to perform a sensitivity analysis to examine the impact of uncertain reservoir parameters on CO_2 plume extension and reservoir pressure in the observation well. Based on the sensitivity analysis, it was concluded that higher reservoir permeability contributed to more extensive CO_2 plume and less reservoir pressure build up. The same behavior was observed when gas relative permeability increased however; higher values for residual gas saturation had no effect of reservoir pressure gain and reduced the CO_2 plume extension. Higher brine compressibility resulted in less reservoir pressure build up while increasing brine density led to higher reservoir pressure gain and CO_2 plume extension. Moreover, changing the reservoir boundary condition from closed to constant boundary caused the reservoir pressure to return to initial pressure after end of injection.

2-The reservoir simulation model was history matched by use of data from ten months of CO_2 injection in the Citronelle's saline formation (Paluxy). The history match process was based on setting the actual daily injection rates as the well operational constraint in the model and tune some reservoir parameters to minimize the mismatch between simulation results and actual pressure data coming from two PDGs in the observation well. A reasonable pressure history match with less than 0.001% error was achieved by modification of brine density, permeability (in two reservoir regions), vertical to horizontal permeability ratio, CO_2 solubility in brine and reservoir volume. At the end of history match process, the predictability of the model was validated by comparing the reservoir simulation results with the last three months of actual pressure which was not used during

the history match process. The history matched reservoir simulation model was main foundation to prove the feasibility of Intelligent Leakage Detection System (ILDS).

3-Reservoir simulation was used to model variety of different CO_2 leakage scenarios specifically for obtaining pressure signals in the observation well with respect to various leakage locations and rates. A Set of simulation runs were performed covering all the available leakage locations (existing wells) and rates (observed in the real cases). Corresponding high frequency pressure signals (hourly) were processed by descriptive statistics over one week time period after the leakage. Several neural networks (form the core of ILDS) were trained to find a pattern between CO_2 leakage location/rate and summarized pressure data. Based on verification tests that used both simple-homogenous and history matched-heterogeneous model, it was concluded that locating and quantifying CO_2 leakage rate in storage sites, using "Smart Field" technology, was possible.

4-ILSD was redeveloped to reduce the detection time from one week to less than a day or almost real time(R-ILDS) by introducing new data processing technique that look at the real time pressure and its statistical parameters' history. Blind runs verifications showed very high accuracy for R-ILDS performance.

5-Detection time was also determined based on leakage rate, distance of the leaking well to the observation well and PDG resolution.

6-The effects of changing 4 different uncertain parameters (porosity, sand layer top, sand layer thickness and vertical to horizontal permeability ratio) were studied on the R-ILDS predictions. It was concluded that reservoir porosity and top impacted R-ILDS results especially for CO_2 leakage locations.

7-With current locations of PDGs (layer one), it was not possible to sense pressure changes due to leakage at different vertical locations along the wells (in other layers). Installation of PDGs in all the layers with extended CO_2 plume was suggested as a solution.

8-Pressure Sensor Drift (PSD) made R-ILDS to report false CO_2 leakages. According to different values for PSD (0.25 to 4 psi/year), detection time and location of the false reported leak were determined to be from 20 to 35 hours and well D-9-6 respectively.

9-Based on the objective of this study which was leakage detection by use of pressure signals during stabilization time (t3), well-head pressure at injection well could not be used for leakage detection. As an alternative, use of Sustained Casing Pressure (SCP) was recommended.

10-R-ILDS was facilitated and tested successfully with the ability to detect variable leakage rates (linear, exponential and logarithmic). Additionally, Monte Carlo simulation was used to provide range of values as the leakage rates prediction.

11-Instalment of PDG in the injection well (rather than observation well) resulted in correct predictions for leakage rates. However, it was not possible to detect CO_2 leakage location. Symmetric locations of leaking wells generated almost the same pressure signal due to the leakage.

12-Cap-rock leakage was modeled and the corresponding R-ILDS was developed. Behavior of pressure signal due to cap-rock leakage was considerably different from well leakage due to sudden release of large volume of CO_2. Developed R-ILDS provided reasonable predictions for range for cumulative leaked gas and X coordinate of leakage location.

13-Several neural networks were trained to detect multi-well leakages based on 54 simulation runs that were designed to cover different combinations of two-well and three-well leakages. It was noticed that with just one observation well, it was possible to detect multiwall leakage. However, two-well leakages were differentiated by R-ILDS considering presence of one more PDG in the location of the injection well.

14-Behavior of the associated noise with actual pressure data coming from PDGs was determined by fitted curve analysis. Wavelet Threshold and GRNN method were used to clean the noisy data. Smoother de-nosed data was achieved by using GRNN method.

7-2 Future work

- In this study, descriptive statistics was used for feature selection of high frequency pressure signals. It is recommended to test other feature extraction or dimension reduction methods in order to use high frequency pressure data for neural network training.

- The presence of Pressure Sensor Drift (PSD) and its effect on R-ILDS results was studied in this work with linear behavior. It is worthy to evaluate the effect of PSD with different mathematical behaviors (logarithmic or exponential) on R-ILDS results. Additionally, PSD values should be considered in pressure signals form blind runs to see their impact on the final results.

- The initiation of the CO_2 leakage was assumed to be at the approximate time that CO_2 plume reached to the location of the wells. Initiation of leakage at different times can be considered for future studies.

- Development of a SRM with the capability of generating pressure signals with respect to various leakage scenarios would be praiseworthy for further investigation. SRM will be a verification tool to generate pressure signals based on R-ILDS results. If the SRM signal is the same as actual signal due to the leakage, the R-ILDS prediction is correct, otherwise the process of leakage quantification should be repeated iteratively in a way that SRM results matches the actual pressure data.

Chapter 8 Works Cited

[1] "National Climate Data Center," [Online]. Available: http://www.ncdc.noaa.gov/indicators/.

[2] C. Cooper, A Technical Basis for Carbon Dioxide Storage, CO2 Capture Project, 2009.

[3] M. L. Szulczewski, "The Subsurface Fluid Mechanics of Geologic Carbon Dioxide Storage," MASSACHUSETTS INSTITUTE OF TECHNOLOGY, MASSACHUSETTS, 2013.

[4] A. Yamasaki, "An Overview of CO2 Mitigation Options for Global Warming—Emphasizing CO2 Sequestration Options," *JOURNAL OF CHEMICAL ENGINEERING OF JAPAN,* vol. 36, no. 4, pp. 361-375, 2003.

[5] L. (. v. d. Meer and P. (. Egberts, "A General Method for Calculating Subsurface CO2 Storage Capacity," in *Offshore Technology Conference*, Houston, 2008.

[6] S. Bachu, "Comparison between Methodologies Recommended for Estimation of CO2 Storage Capacity in Geological Media," Carbon Sequestration Leadership Forum, 2008.

[7] B. Metz, O. Davidson, H. d. Coninck, M. Loos and L. Meyer, "Carbon Dioxide Capture and Storage," Cambridge University Press, New York, 2005.

[8] D. C. W. M. D. R. Dooleya J.J., "Accelerated Adoption of Carbon Dioxide Capture and Storage Within the United States Utility Industry," in *7th International Conference on Greenhouse Gas Control Technologies*, Vancouver, 2004.

[9] NETL, "Carbon Sequestration Atlas of the United States and Canada (Atlas III).," DOE, Morgantown, 2010.

[10] N. Kumar, "CO2 Sequestration: Understanding The Plume Dynamics and Estimating Risk," The University of Texas at Austin, Austin, 2008.

[11] CO2CRC, "Cooperative Research Centre for Greenhouse Gas Technologies," Australian Government's Cooperative Research Centres program, [Online]. Available: http://www.co2crc.com.au.

[12] P. McGrail, Artist, [Art]. Pacific Northwest National Laboratory, 2010.

[13] M. E. Initiative, "Carbon Capture & Sequestration Technologies," Massachusetts Institute of Technology, [Online]. Available: https://sequestration.mit.edu/tools/projects/sleipner.html.

[14] GTM, "Greentech Media," Greentech Media, [Online]. Available: http://www.greentechmedia.com.

[15] T. Simmenes, O. R. Hansen, O. Eiken, G. M. G. Teige, C. Hermanrud, S. Johansen, H. M. Nordgaard Bolaas and H. Hansen, "Importance of Pressure Management in CO2 Storage," in *Offshore Technology Conference*, Houston, 2013.

[16] D. E. Riestenberg, G. J. Koperna, V. A. Kuuskraa, R. A. Esposito, K. E. Harrison, C. R. Berry, J. Sparks and R. Rhudy, "CO2 Sequestration Permitting at the SECARB Mississippi Test Site," in *Society of Petroleum Engineers*, San Antonio, 2009.

[17] BP, "BP," [Online]. Available: http://www.bp.com/.

[18] R. P. Hepple and S. M. Benson, "Implications of Surface Leakage on the Effectiveness of Geologic Storage of Carbon Dioxide as a Climate Change Mitigation Strategy," in *Sixth International Conference on Greenhouse Gas Control Technologies*, Kyoto, 2003.

[19] T. L. Watson and S. Bachu, "Evaluation of the Potential for Gas and CO2 Leakage Along Wellbores," in *E&P Environmental and Safety Conference*, Galveston, 2007.

[20] N. J. Huerta, "Studying Fluid Leakage along a Cemented Wellbore," The University of Texas at Austin, Austin, 2009.

[21] C. M. Group, "CMG Software Manual," Computer Modelling Group, 2011.

[22] D. Tran, V. K. Shrivastava, L. X. Nghiem and B. F. Kohse, "Geomechanical Risk Mitigation for CO2 Sequestration in Saline Aquifers," in *SPE Annual Technical Conference and Exhibition*, New Orleans, 2009.

[23] C. R. Nelson, J. M. Evans, E. N. Steadman and J. A. Harju, "Factors Affecting The Potential For Co2 Leakage From Geologic Sinks," NETL, 2005.

[24] W. C. Chang, "A Simulation Study of Injected CO2 Migration in The Faulted Reservoir," The University of Texas at Austin, Austin, 2007.

[25] B. McMillan, "Surface Dissolution:Adressing Technical Challenges of CO2 Injection and Storage in Brine Aquifers," The University of Austin at Texas, Austin, 2008.

[26] V. A. Kuuskraa, "Cost-Effective Remediation Strategies for Storing CO2 in Geologic Formations," in *SPE International Conference on CO2 Capture, Storage, and Utilization*, San Diego, 2009.

[27] D. R. Brouwer, "Dynamic Water Flood Optimization with Smart Wells Using Optimal Contro lTheory," Deflt University of Technology, Delft, 2004.

[28] A. A. Al Omair, "Economic Evaluation of Smart Well Technology," Texas A&M University, College Station, 2007.

[29] J. Jansen, S. Douma, D. Brouwer, P. Van den Hof, O. Bosgra and A. Heemink, "Closed Loop Reservoir Management," in *SPE Reservoir Simulation Symposium*, Woodlands, 2009.

[30] S. Mohaghegh, "Virtual-Intelligence Applications in Petroleum Engineering: Part 1—Artificial Neural Networks," *Journal of Petroleum Technology,* vol. 52, no. 09, pp. 64-73, 2000.

[31] D. Kriesel, A Brief Introduction to Neural Networks, Bonn: www.dkriesel.com, 2005.

[32] L. V. Fausett, Fundamentals of Neural Networks: Architectures, Algorithms and Applications, Pearson , 1993.

[33] C. Clabaugh, D. Myszewski and J. Pang, "Neural Networks," The Intellectual Excitement of Computer Science,Stanford University, 2000. [Online]. Available: http://cs.stanford.edu/people/eroberts/courses/soco/projects/2000-01/neural-networks/index.html.

[34] S. D. Mohaghegh, C. Goddard, A. Popa, A. S. and M. Bhuiyan, "Reservoir Characterization Through Synthetic Logs," in *SPE Eastern Regional Meeting*, Morgantown, 2000.

[35] R. B. Gharbi and A. M. Elsharkawy, "Universal Neural Network Based Model for Estimating The PVT Properties of Crude Oil Systems," in *SPE Asia Pacific Oil and Gas Conference and Exhibition*, Kuala Lumpur, 1997.

[36] B. Adeyemi and A. Sulaimon, "Predicting Wax Formation Using Artificial Neural Network," in *Nigeria Annual International Conference and Exhibition*, Lagos, 2012.

[37] S. Mohaghegh, D. McVey, K. Aminian and S. Ameri, "Predicting Well Stimulation Results in a Gas Storage Field in the Absence of Reservoir," *SPE Reservoir Engineering,* vol. 11, no. 04, pp. 268 - 272, 1995.

[38] S. Amini, S. D. Mohaghegh, R. Gaskari and G. Bromhal, "Uncertainty Analysis of a CO2 Sequestration Project Using Surrogate Reservoir Modeling Technique," in *SPE Western Regional Meeting*, Bakersfield, 2012.

[39] S. Mohaghegh, G. O, Z. S, K. A and B. G, "Top Down, Intelligent Reservoir Modeling of Oil and Gas Producing Shale Reservoirs; Case Studies," *International Journal of Oil, Gas and Coal Technology,* vol. 5, no. 1, 2012.

[40] S. A. Haghighat, S. D. Mohaghegh, V. Gholami and D. Moreno, "Production Analysis of a Niobrara Field Using Intelligent Top-Down Modeling," in *SPE Western North American and Rocky Mountain Joint Meeting*, Denver, 2014.

[41] R. Arehart, "Drill-Bit Diagnosis With Neural Networks," *SPE Computer Applications,* vol. 2, no. 04, pp. 24 - 28, 1990.

[42] R. Gunter and T. Albert, "Inversion of Seismic Waveforms Using Neural Networks," in *1992 SEG Annual Meeting*, New Orleans, 1992.

[43] D. H. Johnston, "Seismic Attribute Calibration Using Neural Networks," in *SEG Annual Meeting*, Washington, 1993.

[44] D. A. Ford and M. C. Kelly, "Using Neural Networks to Predict Lithology From Well Logs," in *SEG Annual Meeting*, San Antonio, 2001.

[45] S. Gartland, G. Owen, R. Cottis and M. Turega, "Neural Network Methods for the Prediction of Pitting Potentials," in *CORROSION 99*, San Antonio, 1999.

[46] H. Tang, "Improved Carbonate Reservoir Facies Classification Using Artificial Neural Network Method," in *Canadian International Petroleum Conference*, Calgary, 2008.

[47] L. Surguchev and L. Li, "IOR Evaluation and Applicability Screening Using Artificial Neural Networks," in *SPE/DOE Improved Oil Recovery Symposium*, Tulsa, 2000.

[48] C. Siruvuri, S. Nagarakanti and R. Samuel, "Stuck Pipe Prediction and Avoidance: A Convolutional Neural Network Approach," in *IADC/SPE Drilling Conference*, Miami, 2006.

[49] M. Kalam, S. Al-Alawi and M. Al-Mukheini, "Assessment of Formation Damage Using Artificial Neural Networks," in *SPE Formation Damage Control Symposium*, Lafayette, 1996.

[50] P. Nakutnyy, K. Asghari and A. Torn, "Analysis of Waterflooding Through Application of Neural Networks," in *Canadian International Petroleum Conference*, Calgary, 2008.

[51] A. L. Thomas and P. R. La Pointe, "Conductive fracture identification using neural networks," in *The 35th U.S. Symposium on Rock Mechanics (USRMS)*, Reno, 1995.

[52] M. Vassallo and G. Bernasconi, "Bit Bounce Detection Using Neural Networks," in *SEG Annual Meeting*, Denver, 2004.

[53] R. Schultz and D. Chen, "Dynamic Neural Network Calibration of Quartz Transducers," in *SPE Annual Technical Conference and Exhibition*, Denver, 2003.

[54] J. Birkholzer, J. Nicot, C. Oldenburg, Q. Zhou, S. Kraemer and K. Bandilla, "Brine flow up a well caused by pressure perturbation from geologic car-bon sequestration: static and dynamic evaluations," *Int. J. Greenh. Gas Con,* no. 5, pp. 850-861, 2011.

[55] M. Celia, J. Nordbotten, B. Court, M. Dobossy and S. Bachu, "Field-scale appli-cation of a semi-analytical model for estimation of CO2and brine leakage alongold wells," *Int. J. Greenh. Gas Con,* no. 5, pp. 257-269, 2011.

[56] Y. Z. Jung and B. J. Q., "Early detection of brine and CO2leakagethrough abandoned wells using pressure and surface-deformation monitoringdata: concept and demonstration.," Adv. Water Resources, 2011.

[57] M. Zeidouni and M. Pooladi-Darvish, "Characterization of Leakage through Cap-Rock with Application to CO2 Storage in Aquifers - Single Injector and Single Monitoring Well," in *Canadian Unconventional Resources and International Petroleum Conference*, Calgary, 2010.

[58] A. Sun and N. J.P, "Inversion of pressure anomaly data for detecting leakage at geologic carbon sequestration sites," *Advances in Water Resources,* vol. 56, pp. 49-60, 2013.

[59] J. Jalali, "Artificial Neural Networks for Reservoir Level Detection of CO2 Seepage Location Using Permanent Down-Hole Pressure Data," West Virginia University, Morgantown, 2010.

[60] G. Koperna, V. Kuuskraa, D. Reistenberg, R. Rhudy, R. Trautz, G. Hill and R. Esposito, "The SECARB Anthropogenic Test: The First US Integrated Capture, Transportation, and Storage Test," in *Carbon Management Technology Conference*, Orlando, 2012.

[61] I. P. Denbury Resources, "SECARB PHASE III ANTHROPOGENIC TEST Volume 1 of 2," Alabama Department of Environmental Management, 2010.

[62] S. Haghighat, S. D. Mohaghegh, N. Borzouie, D. Moreno and A. Shahkarami, "Reservoir Simulation of CO2 Sequestration in Deep Saline Reservoir, Citronelle Dome, USA," in *Twelfth Annual Conference on Carbon Capture, Utilization and Sequestration.*, Pittsburgh, 2013.

[63] W. Sifuentes, t. M. Blun and M. Giddins, "Modeling CO2 Storage in Aquifers: Assessing the key contributors to uncertainty," in *Offshore Europe*, Aberdeen, 2009.

[64] Q. Zhou, J. Birkholzer, J. Rutqvist and C. Tsang, "Sensitivity study of CO2 storage capacity in brine aquifers with closed boundaries: Dependence on hydrogeologic properties," U.S. Department of Energy, 2008.

[65] S. A. Haghighat, S. D. Mohaghegh, V. Gholami and A. Shahkarami, "Pressure History Matching for CO2 Storage in Saline Aquifers: Case Study for Citronelle Dome," in *Carbon Management Technology Conference*, Alexandria, 2013.

[66] T. Meckel and S. Hovorka, "Above-Zone Pressure Monitoring as a Surveillance Tool for Carbon-Sequestration Projects," in *SPE International Conference on CO2 Capture, Storage, and Utilization*, New Orleans, 2010.

[67] Q. Tao, S. Bryant, M. T.A and Z. Luo, "Wellbore Leakage Model for Above-Zone Monitoring at Cranfield," in *Carbon Management Technology Conference*, Orlando, 2012.

[68] A. Torn, F. Torabi and K. M. M. Asghari, "Effects of Aquifer Parameters on Long-Term Storage of Carbon Dioxide in Saline Aquifers," in *Carbon Management Technology Conference*, Florida, 2012.

[69] O. Senel and N. Nikita Chugunov, "CO2 Injection in a Saline Formation: How Do Additional Data Change Uncertainties in Our Reservoir Simulation Predictions," in *Carbon Management Technology Conference*, Orlando, 2012.

[70] R. Masoudi, l. M. Jali, D. Press, K. Lee, C. Tan, L. Anis, N. Darman and M. Othman, "An Integrated Reservoir Simulation-Geomechanical Study on Feasibility of CO2 Storage in M4 Carbonate Reservoir, Malaysia," in *International Petroleum Technology Conference*, Bangkok, 2012.

[71] C. A. Mantilla, S. Srinivasan, E. A. Cross and S. L. Bryant, "Inexpensive Assessment of Plume Migration During CO2 Sequestration," in *SPE International Conference on CO2*

Capture, Storage, and Utilization, San Diego, 2009.

[72] M. Krause, J. Perrin and S. M. Benson, "Modeling Permeability Distributions in a Sandstone Core for History Matching Coreflood Experiments," in *SPE International Conference on CO2 Capture, Storage*, San Diego, 2009.

[73] C. Xiao, M. Harris, F. Wang and R. Grigg, "Field Testing and Numerical Simulation of Combined CO2 Enhanced Oil Recovery and Storage in the SACROC Field," in *Canadian Unconventional Resources Conference*, Alberta, 2011.

[74] S. A. Haghighat, S. Mohaghegh, V. Gholami, A. Shahkarami and D. Moreno, "Using Big Data and Smart Field Technology for Detecting Leakage in a CO2 Storage Project," in *SPE Annual Technical Conference and Exhibition*, New Orleans, 2013.

[75] T. Wilson and A. Wells, "Multi-frequency EM surveys help identify possible near-surface migration pathways in areas surrounding a CO2 injection well: San Juan Basin, New Mexico, USA," *Environmental and Engineering Geophysical Society, Fast Times,* vol. 15, no. 3, pp. 43-53, 2010.

[76] M. Lozzio, O. Akemu, L. James, J. Desroches, S. Lombardi and A. Annunziatellis, "Quantifying the Risk of CO2 Leakage Through Wellbores," in *SPE*, New Orleans, 2010.

[77] Wikipedia, " Wikipedia, the free encyclopedia," [Online]. Available: http://en.wikipedia.org/wiki/Descriptive_statistics.

[78] I. Intelligent Solutions, "IDEA User Manual," Intelligent Solutions, Inc., Morgantown, 2014.

[79] Solinst, "Solinst Canada Ltd," Solinst Canada Ltd, [Online]. Available: http://www.solinst.com/products/dataloggers-and-telemetry/3001-levelogger-series/technical-bulletins/understanding-pressure-sensor-drift.php. [Accessed 2013].

[80] J. Reiter, D. Murphy and N. Larson, "Drift Measurements in Pressure Sensors," in *Ocean Sciences Meeting*, Salt Lake City, 2012.

[81] Q. Tao, D. Checkai and S. Bryant, "Permeability Estimation for Large-Scale Potential CO2 Leakage Paths in Wells Using a Sustained-Casing-Pressure Model," in *SPE International Conference on CO2 Capture, Storage, and Utilization*, New Orleans, 2010.

[82] H. Zhu, Y. Lin and D. Zeng, "Oil and Gas Journal," [Online]. Available: http://www.ogj.com/articles/print/volume-111/issue-12/drilling-production/study-addresses-scp-causes-in-co-2-injection-production-wells.html. [Accessed 2 12 2013].

[83] Wikipedia, "Wikipedia," Wikipedia, the free encyclopedia, [Online]. Available: http://en.wikipedia.org/wiki/Monte_Carlo_method.

[84] K. Kin, "Permanent Down-hole Gauge Data Interpretation," Stanford University, Stanford, 2001.

[85] A. Graps, "An Introduction to Wavelets," *IEEE Computational Science & Engineering,* vol. 2, no. 2, pp. 50-61, 1995.

[86] Mathworks, "Mathworks," MathWorks , 1994. [Online]. Available: http://www.mathworks.com/. [Accessed 1994].

Chapter 9 Appendix

Appendix 1 Blind run verification for R-ILDS (section 6-1)

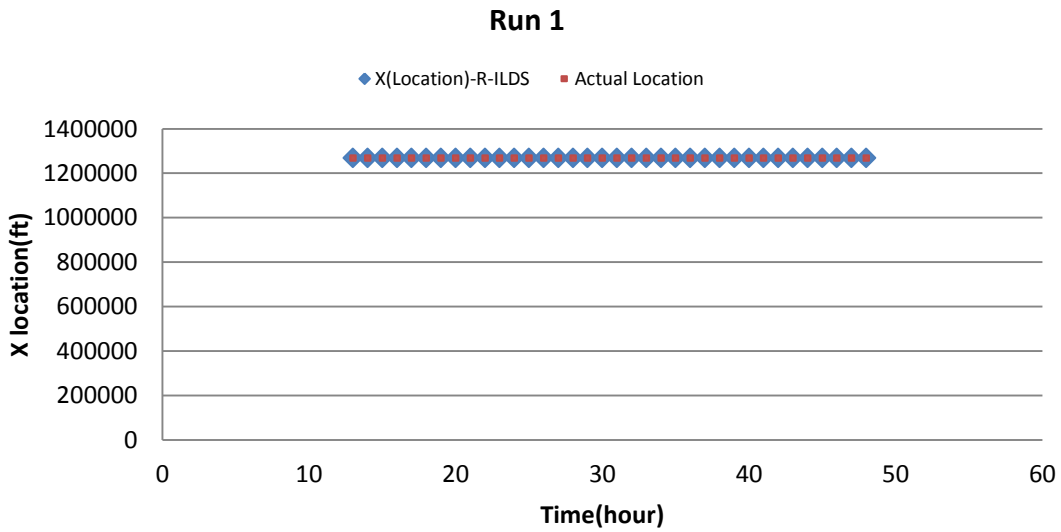

Figure 9-1: R-ILDS leakage location prediction, run1: well D-9-6 leaks 23 Mcf/day

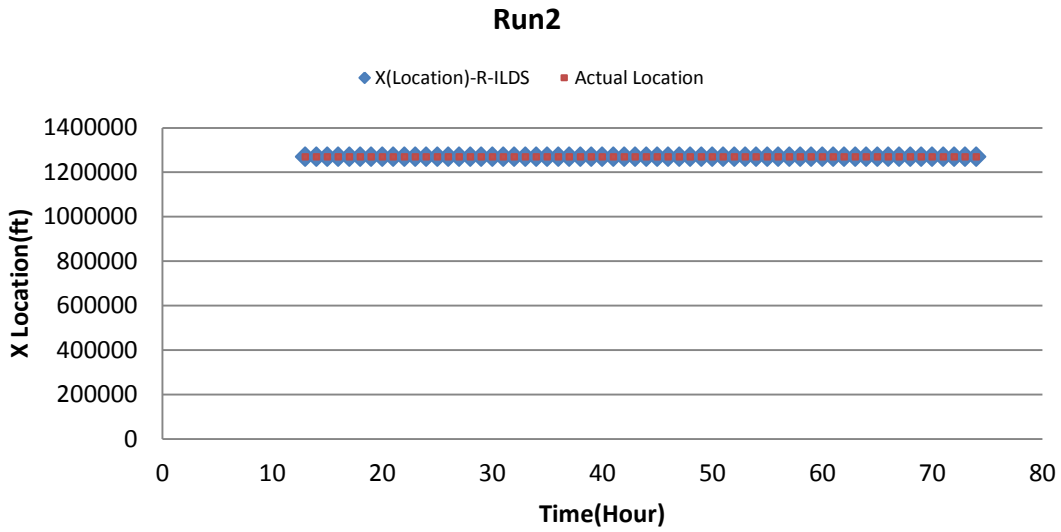

Figure 9-2: R-ILDS leakage location prediction, run2: well D-9-6 leaks 72 Mcf/day

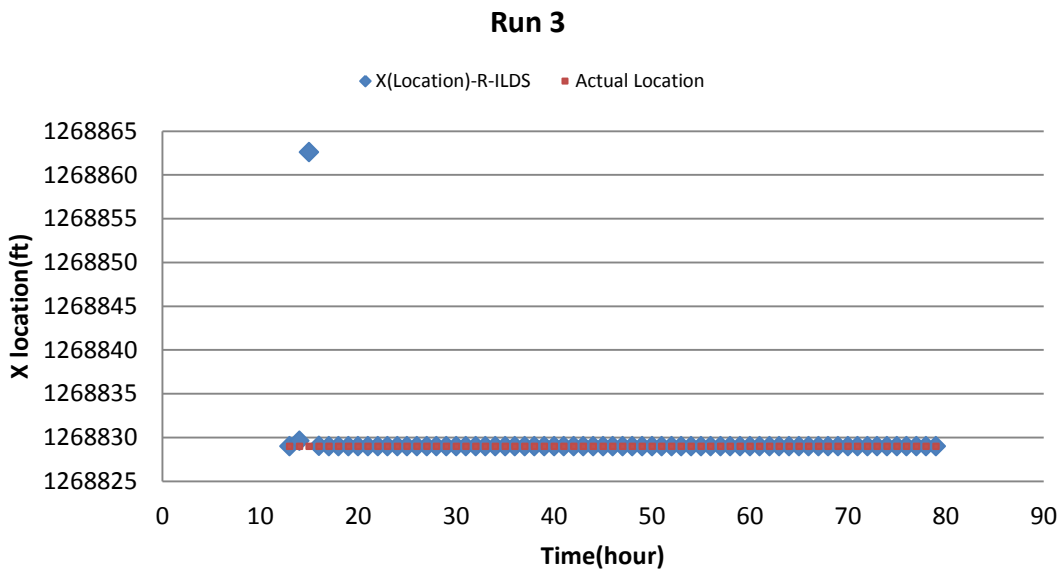

Figure 9-3: R-ILDS leakage location prediction, run3: well D-9-6 leaks 93 Mcf/day

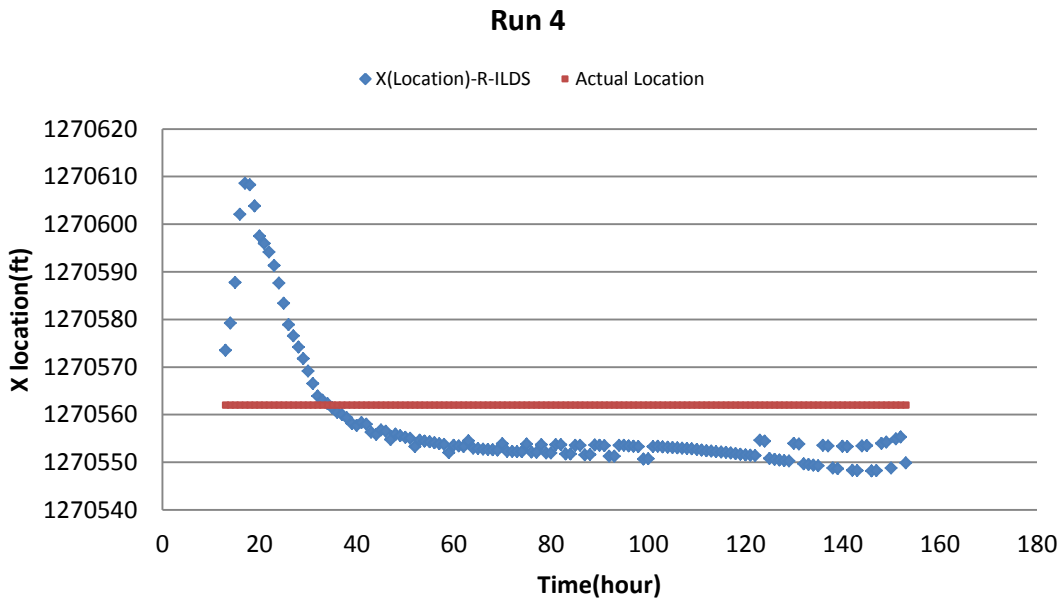

Figure 9-4: R-ILDS leakage location prediction, run4: well D-9-7 leaks 32 Mcf/day

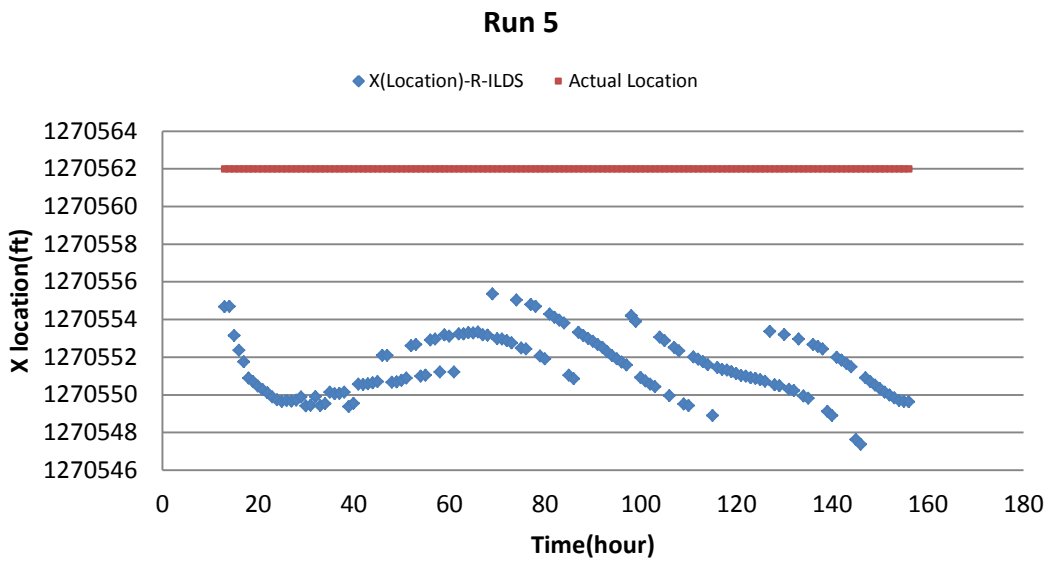

Figure 9-5: R-ILDS leakage location prediction, run5: well D-9-7 leaks 61 Mcf/day

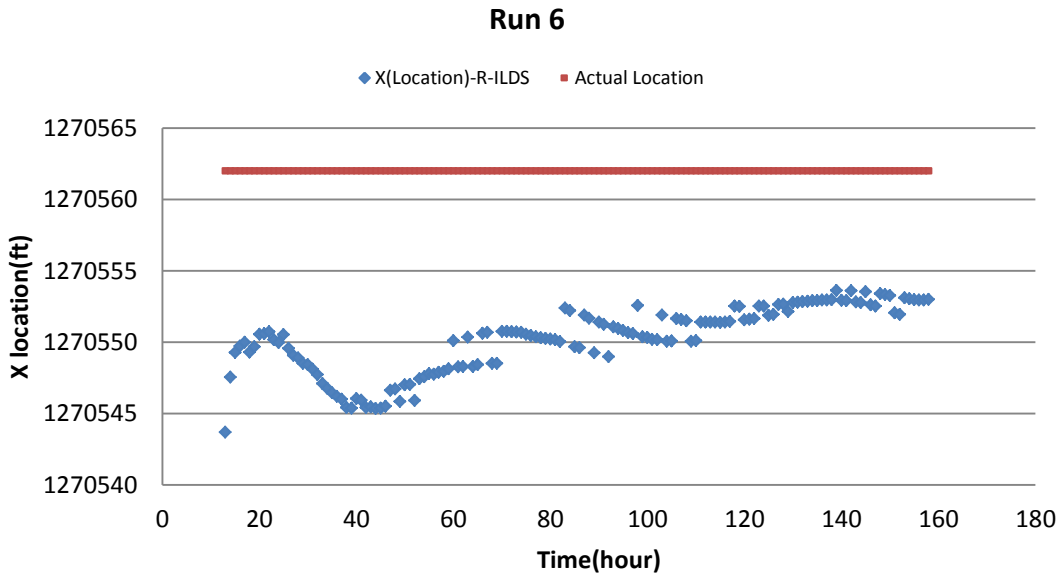

Figure 9-6: R-ILDS leakage location prediction, run6: well D-9-7 leaks 87 Mcf/day

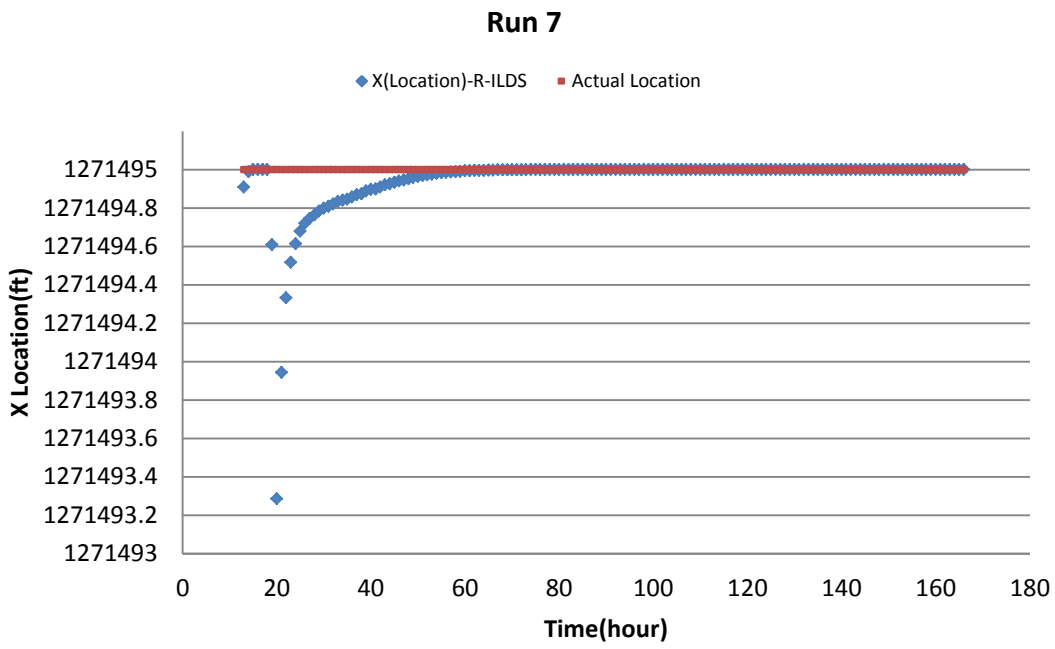

Figure 9-7: R-ILDS leakage location prediction, run7: well D-9-8 leaks 27 Mcf/day

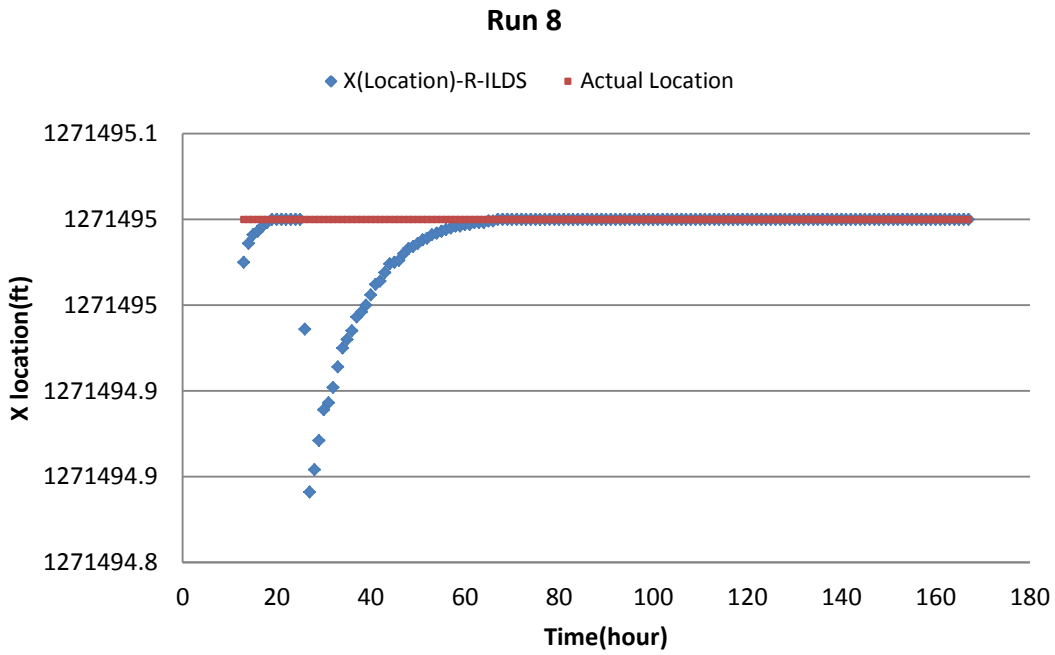

Figure 9-8: R-ILDS leakage location prediction, run9: well D-9-8 leaks 101 Mcf/day

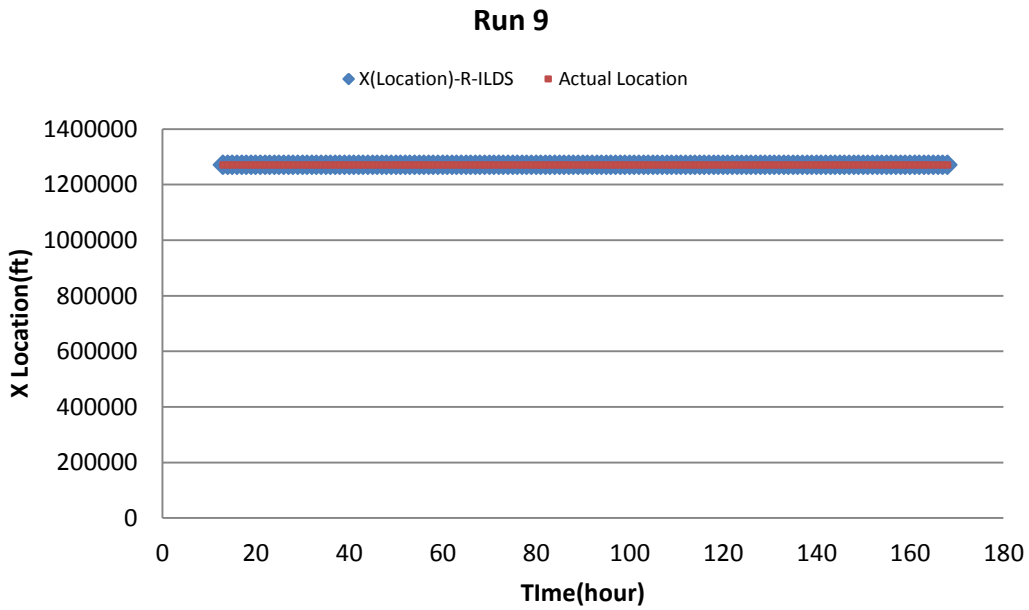

Figure 9-9: R-ILDS leakage location prediction, run9: well D-9-8 leaks 101 Mcf/day

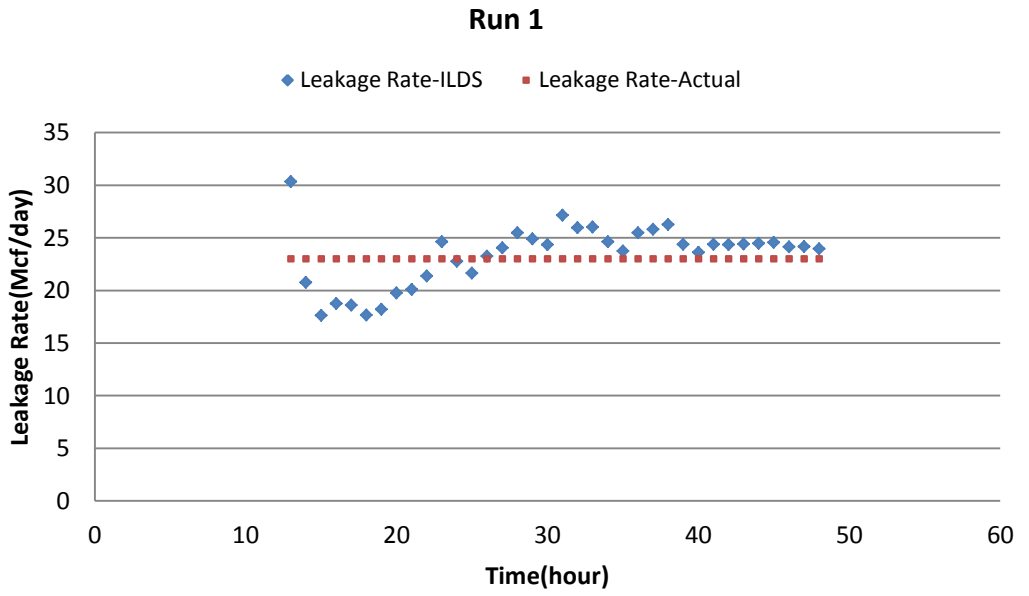

Figure 9-10: R-ILDS leakage rate prediction, run1: well D-9-6 leaks 23 Mcf/day

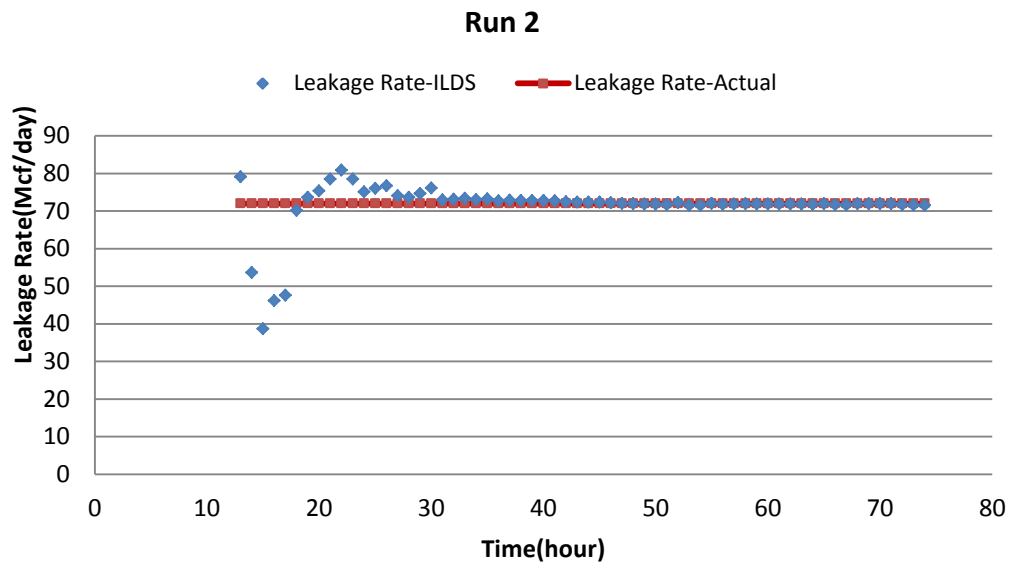

Figure 9-11: R-ILDS leakage rate prediction, run2: well D-9-6 leaks 72 Mcf/day

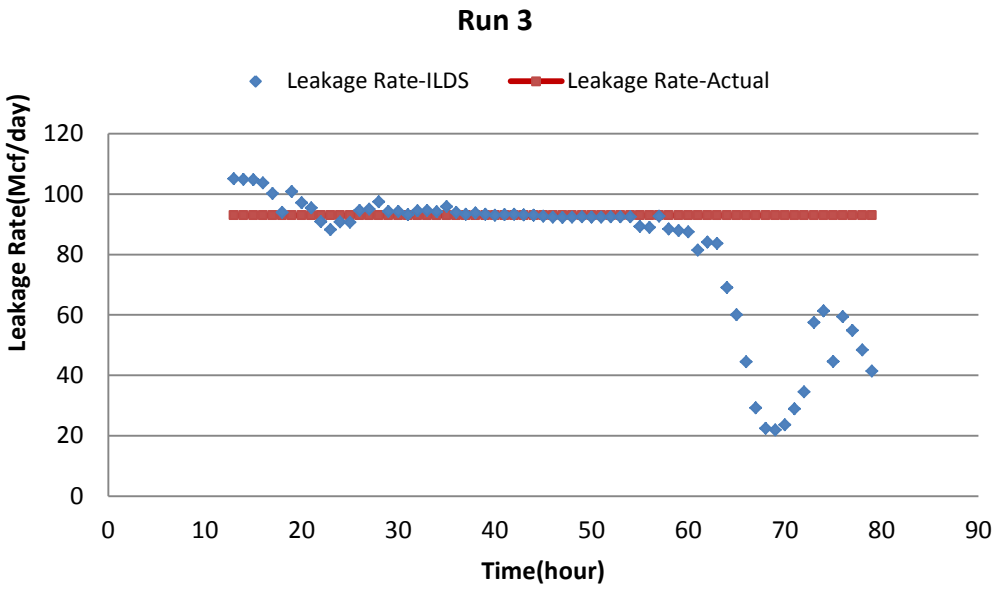

Figure 9-12: R-ILDS leakage rate prediction, run3: well D-9-6 leaks 93 Mcf/day

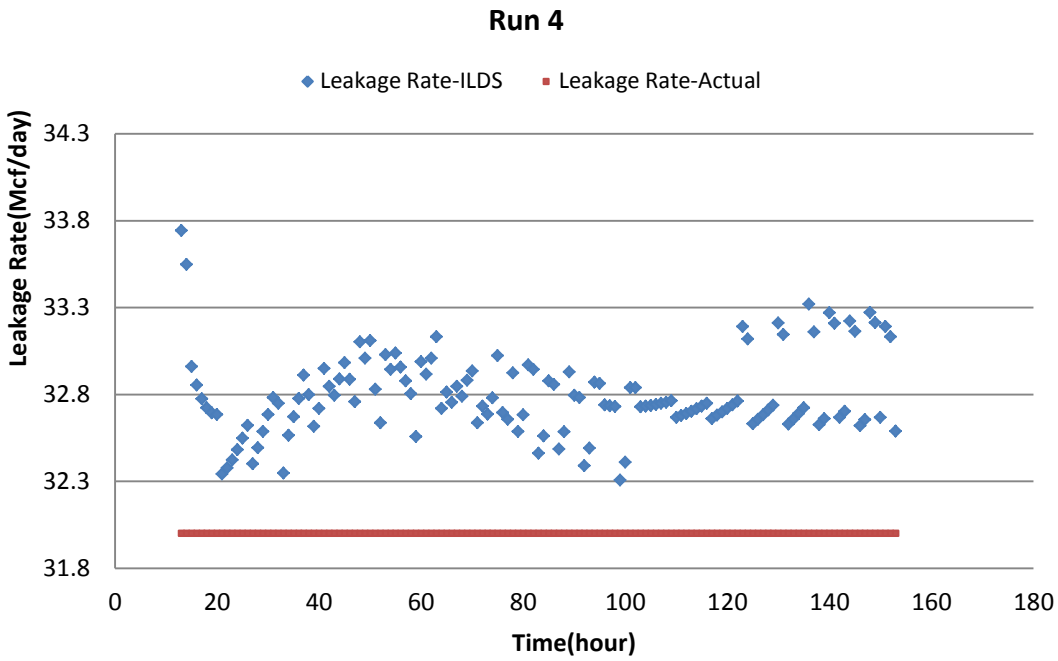

Figure 9-13: R-ILDS leakage rate prediction, run4: well D-9-7 leaks 32 Mcf/day

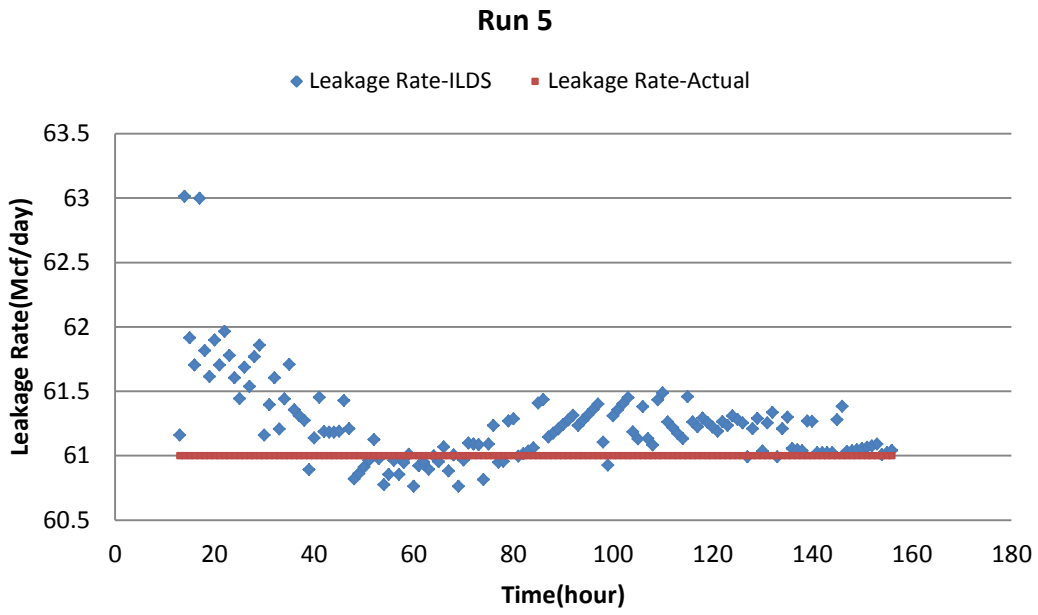

Figure 9-14: R-ILDS leakage rate prediction, run5: well D-9-7 leaks 61 Mcf/day

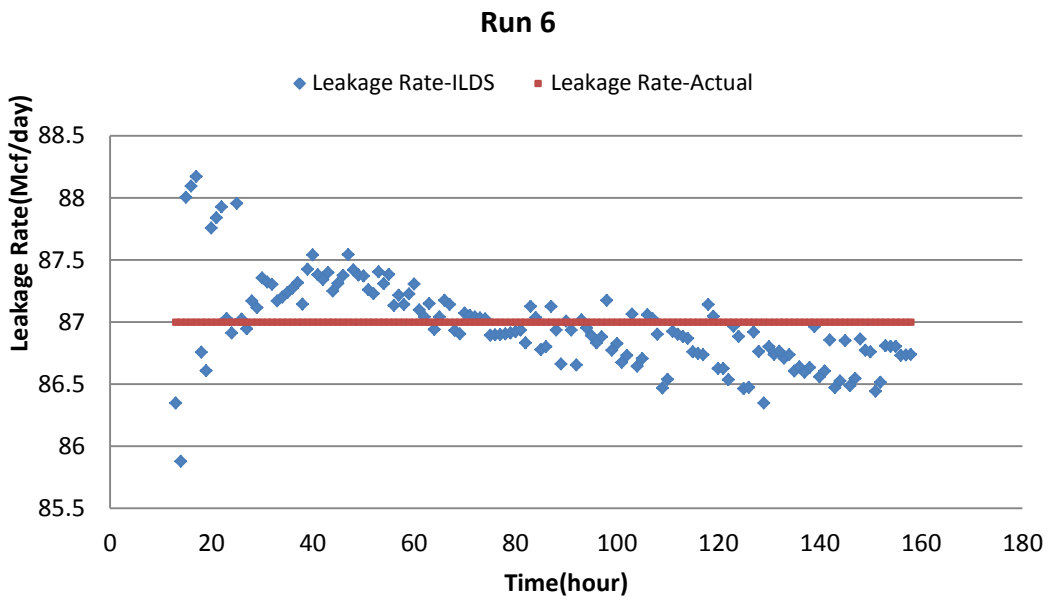

Figure 9-15: R-ILDS leakage rate prediction, run6: well D-9-7 leaks 87 Mcf/day

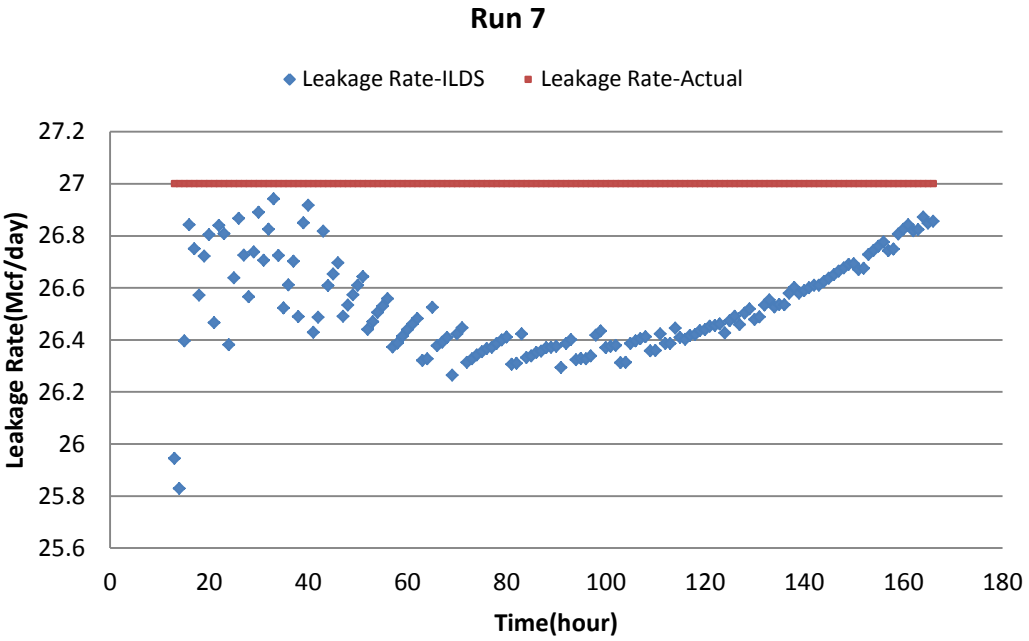

Figure 9-16: R-ILDS leakage rate prediction, run7: well D-9-8 leaks 27 Mcf/day

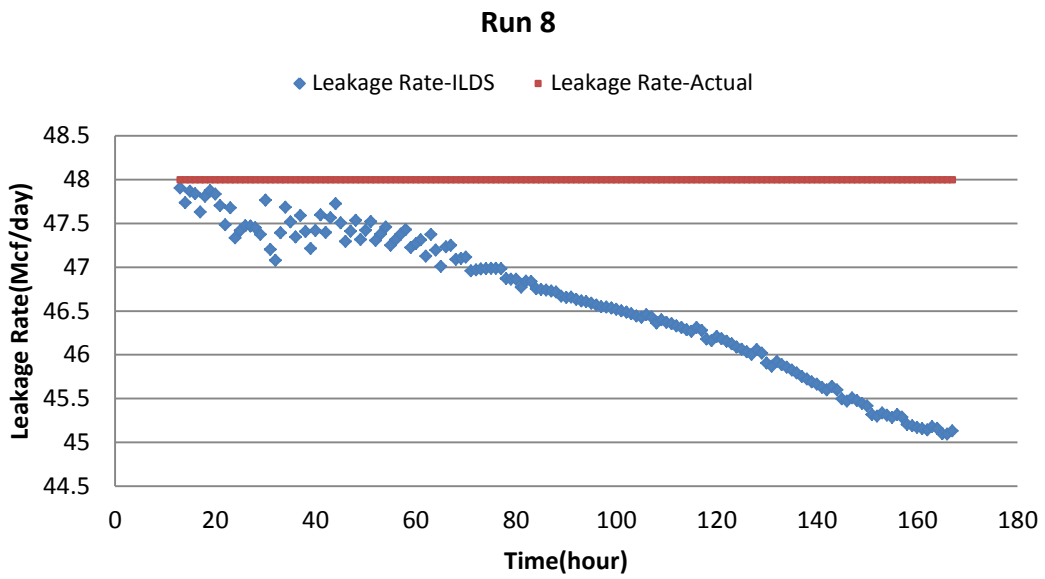

Figure 9-17: R-ILDS leakage rate prediction, run8:well D-9-8 leaks 48 Mcf/day

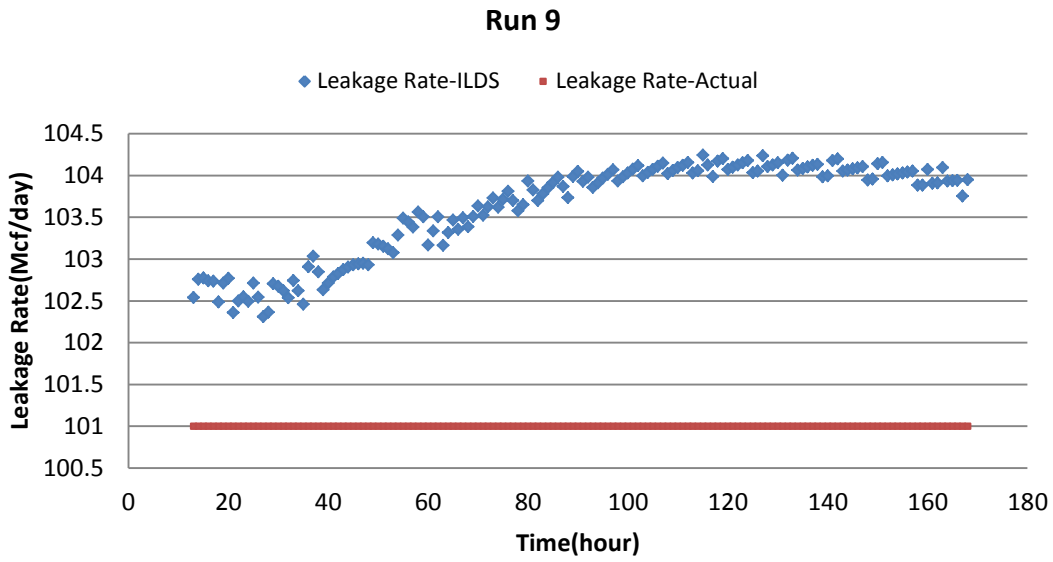

Figure 9-18: R-ILDS leakage rate prediction, run9: well D-9-8 leaks 101 Mcf/day

Appendix 2 Impact of reservoir parameters on R-ILDS Results (Section 6-3)

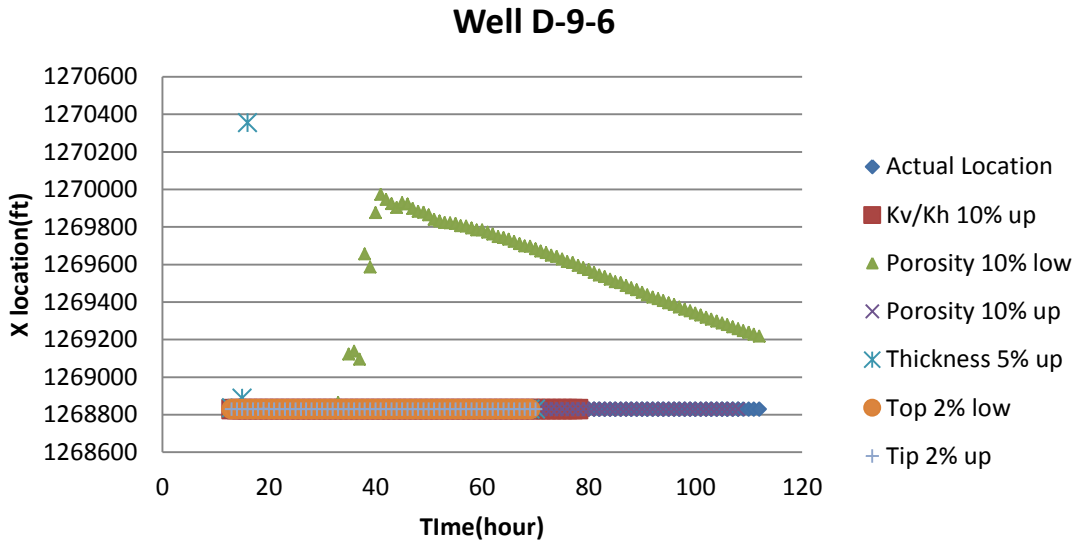

Figure 9-19: Sensitivity analysis of the reservoir parameters on R-ILDS leakage location prediction Well D-9-6

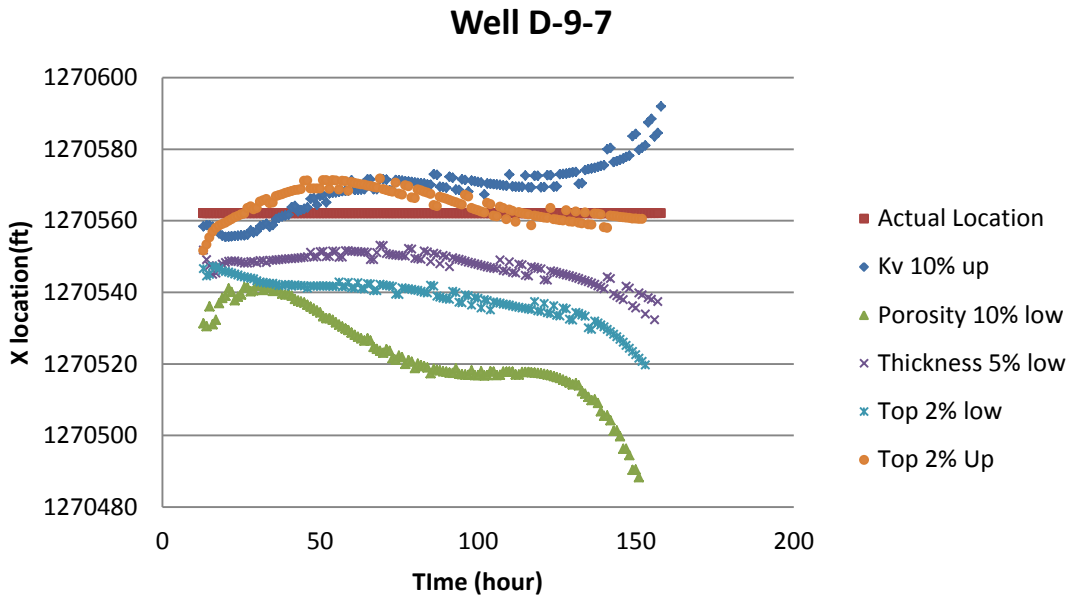

Figure 9-20: Sensitivity analysis of the reservoir parameters on R-ILDS leakage location prediction Well D-9-7

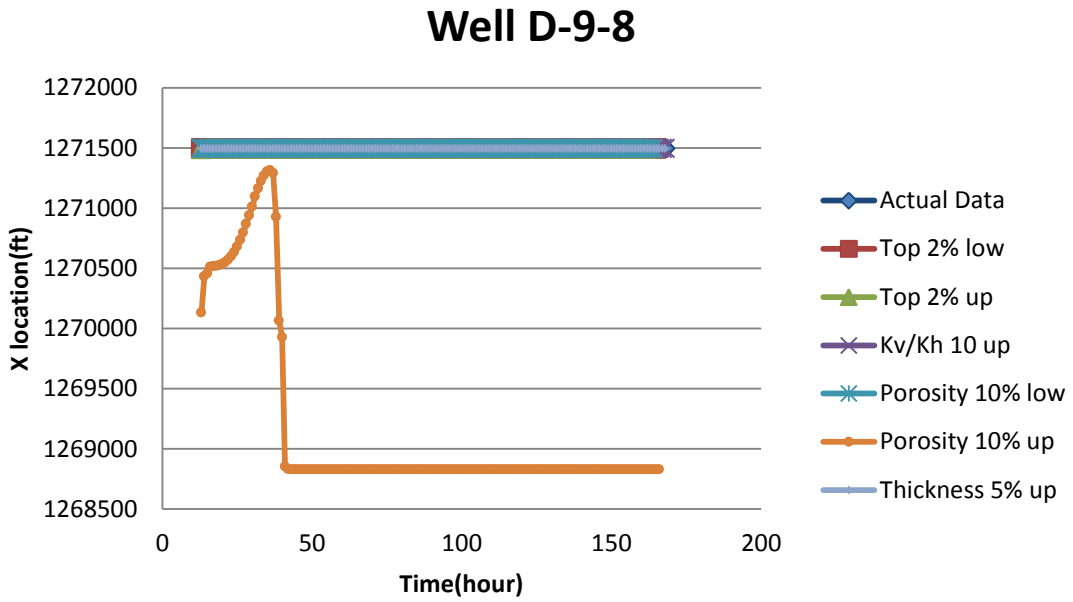

Figure 9-21: Sensitivity analysis of the reservoir parameters on R-ILDS leakage location prediction Well D-9-8

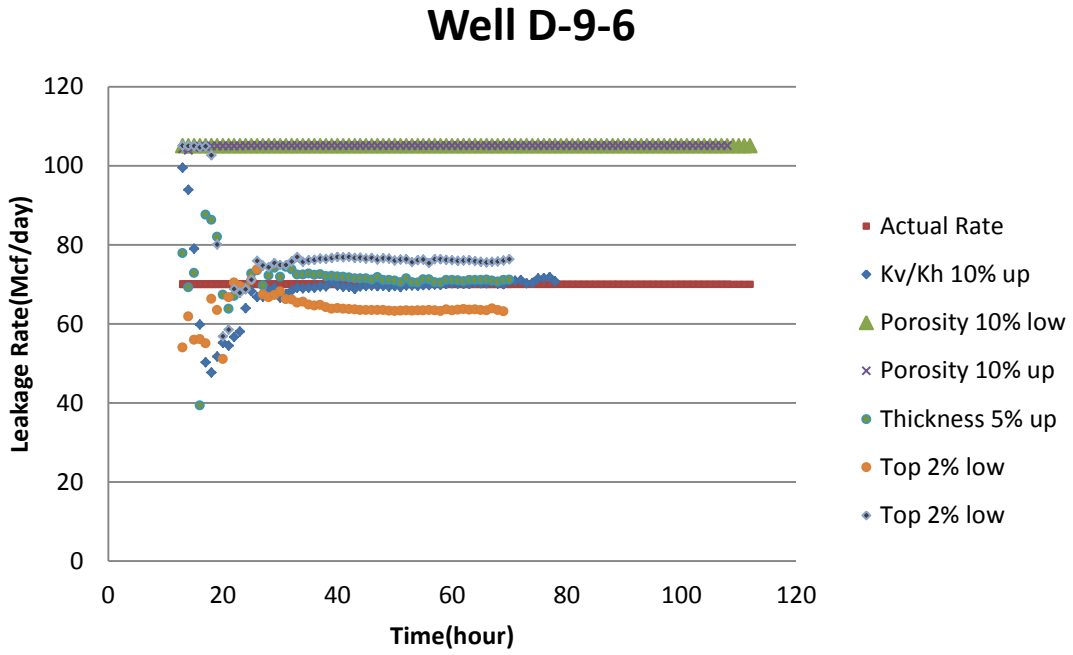

Figure 9-22: Sensitivity analysis of the reservoir parameters on R-ILDS leakage rate prediction Well D-9-6

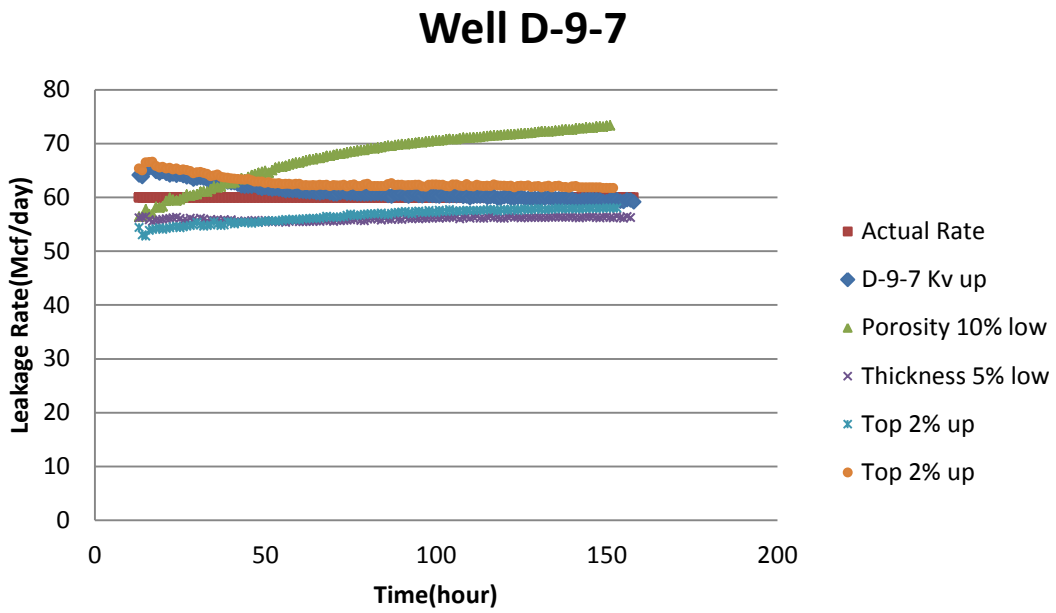

Figure 9-23: Sensitivity analysis of the reservoir parameters on R-ILDS leakage rate prediction Well D-9-7

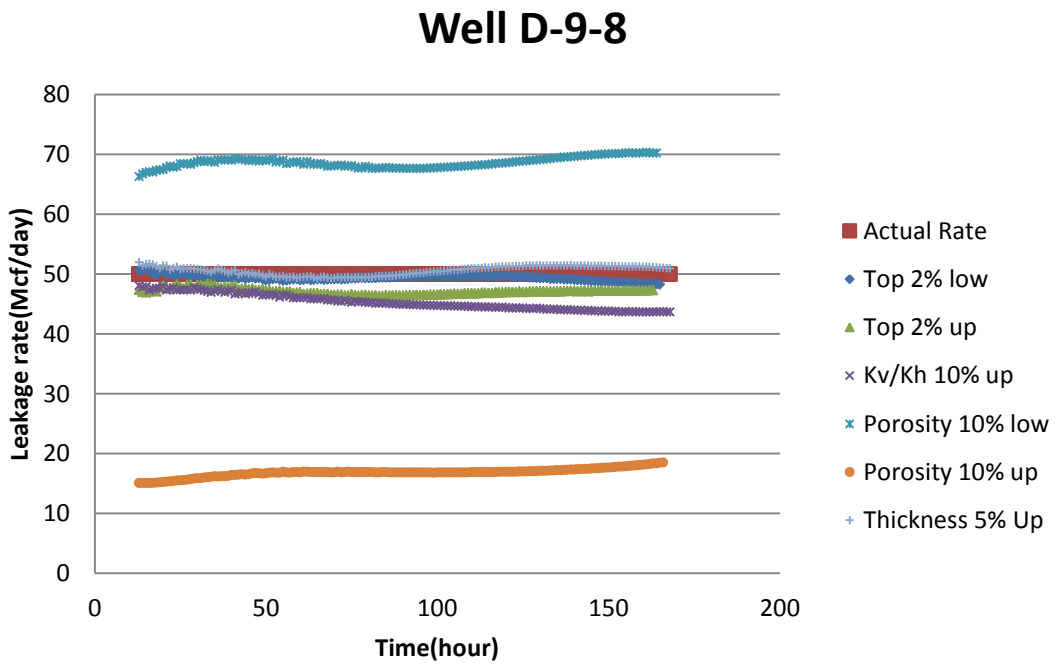

Figure 9-24: Sensitivity analysis of the reservoir parameters on R-ILDS leakage rate prediction Well D-9-7

Appendix 3 R-ILDS results for variable rates (Section 6-7)

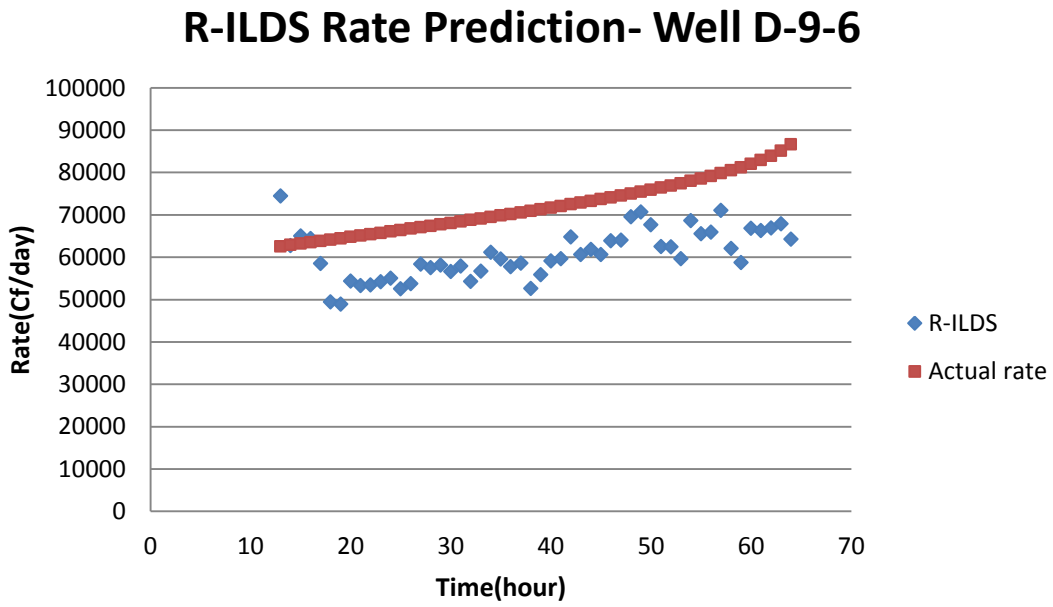

Figure 9-25: R-ILDS prediction for leakage rate in well D-9-6 (variable rate)

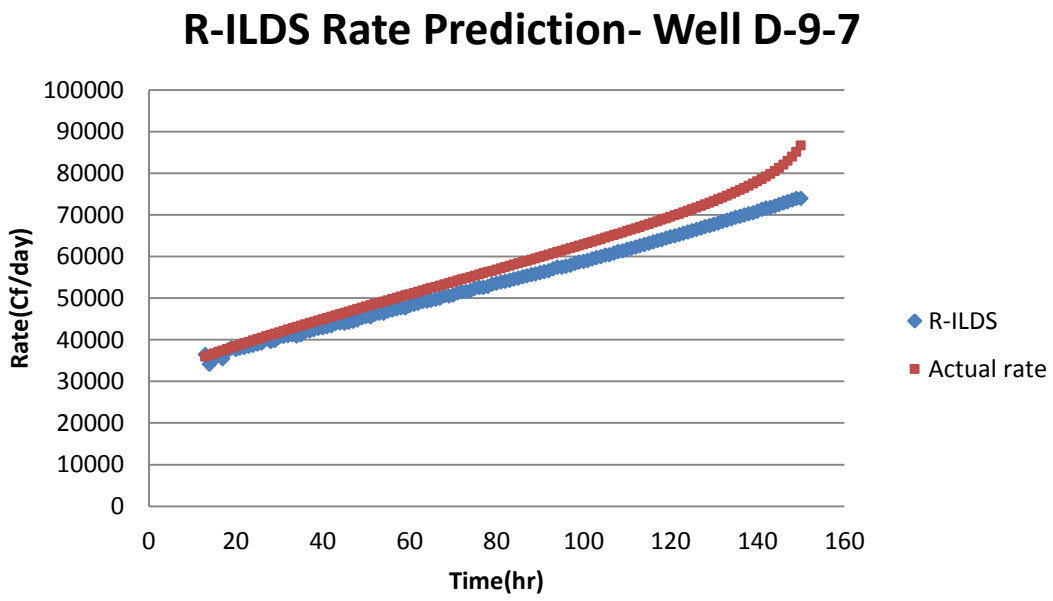

Figure 9-26: R-ILDS prediction for leakage rate in well D-9-7 (variable rate)

Appendix 4 Results for R-ILDS neural network and blind runs-PDG in injection well (Section 6-8)

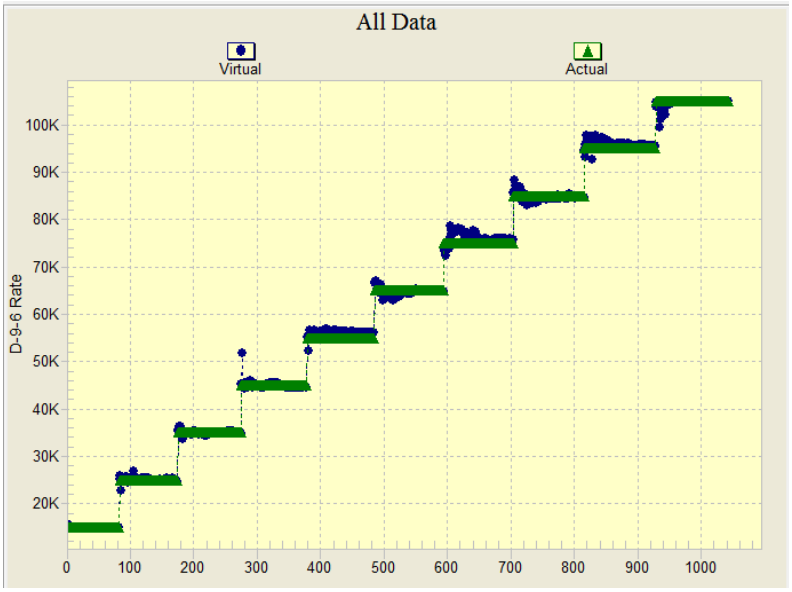

Figure 9-27: Neural network predictions for the leakage rate for the case that PDG is in Injection well, D-9-6 results

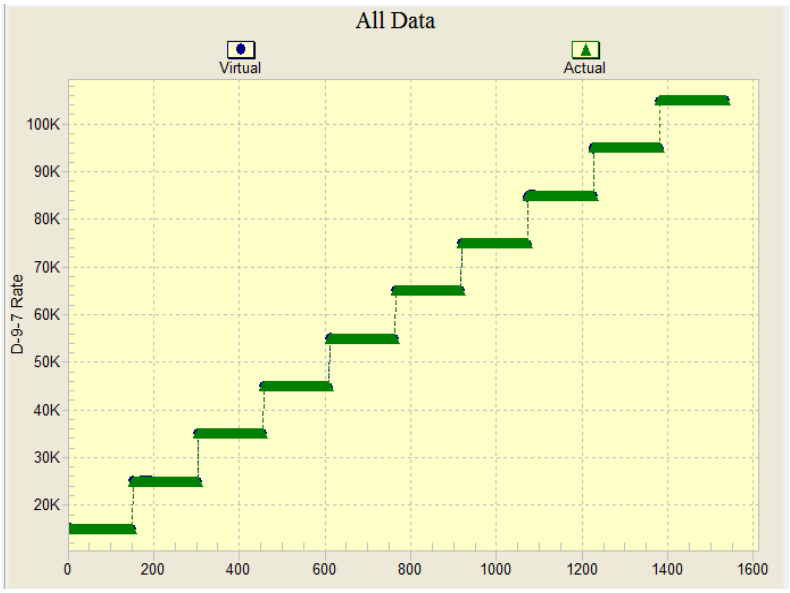

Figure 9-28: Neural network predictions for the leakage rate for the case that PDG is in Injection well, D-9-7 results

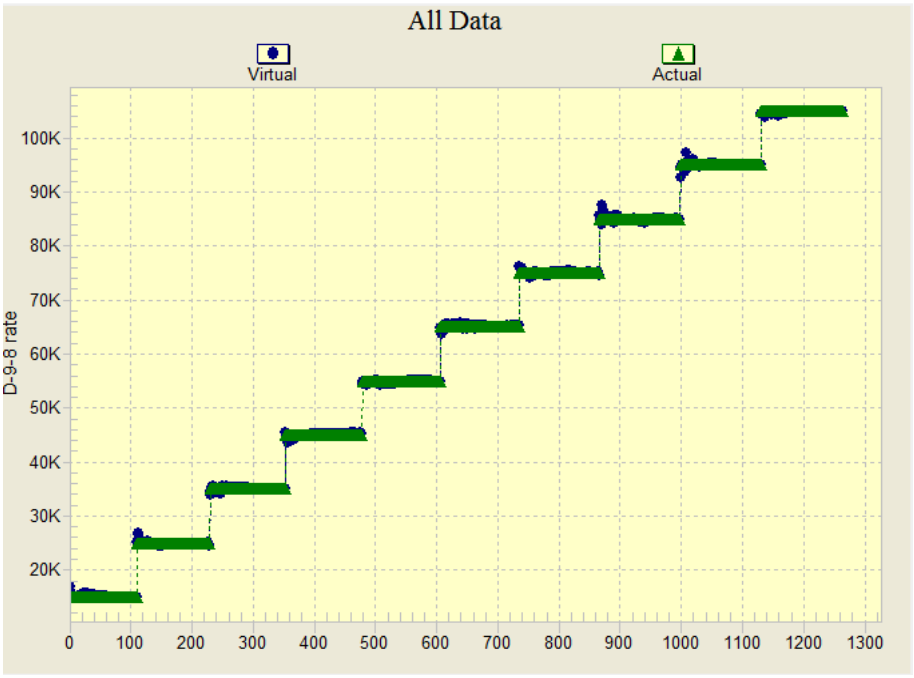

Figure 9-29: Neural network predictions for the leakage rate for the case that PDG is in Injection well, D-9-8 results

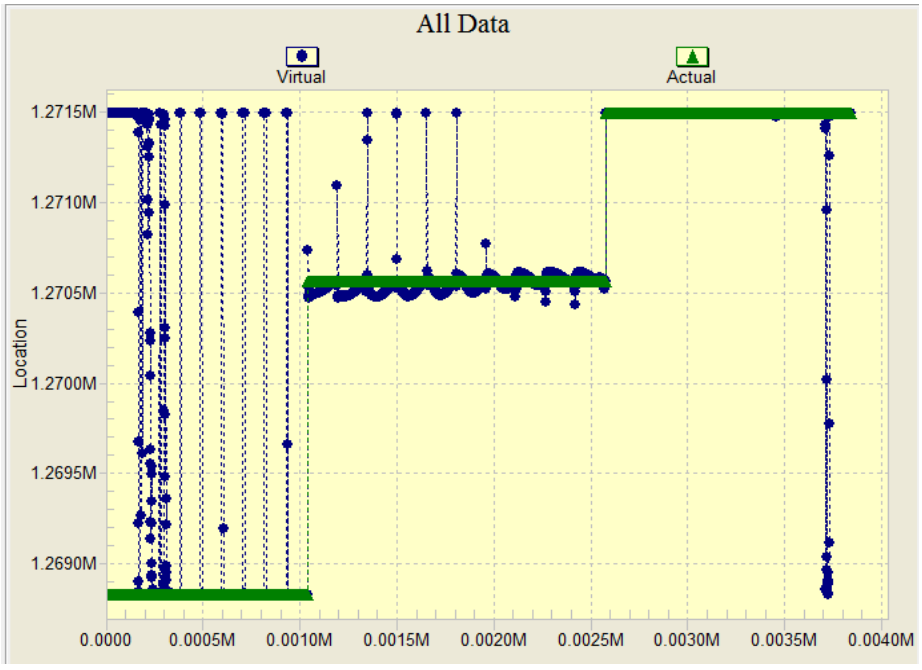

Figure 9-30: 45: Neural network predictions for the leakage location for the case that PDG is in Injection well

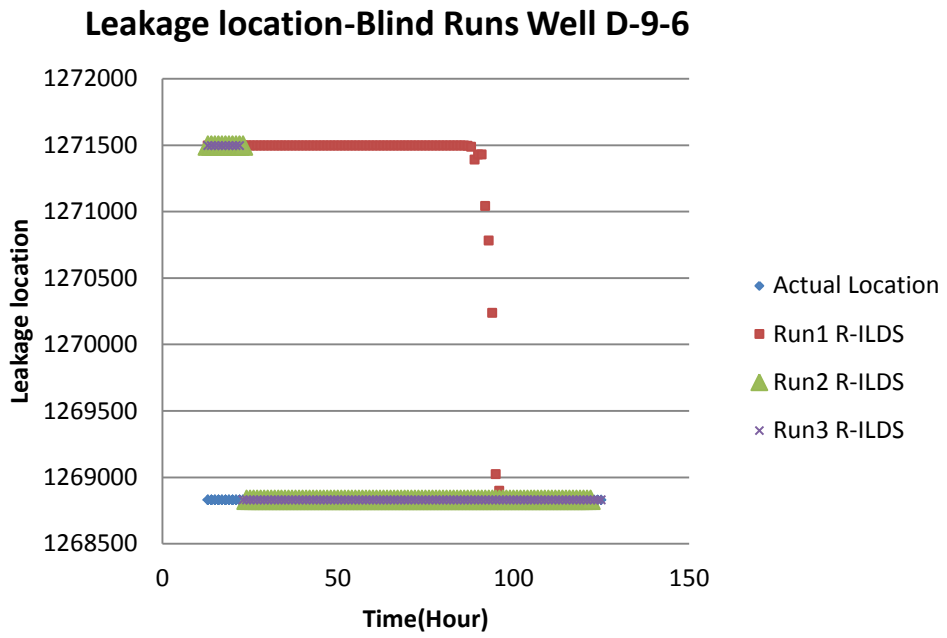

Figure 9-31: R-ILDS Leakage location prediction for well D-9-6, PDG in Injection well

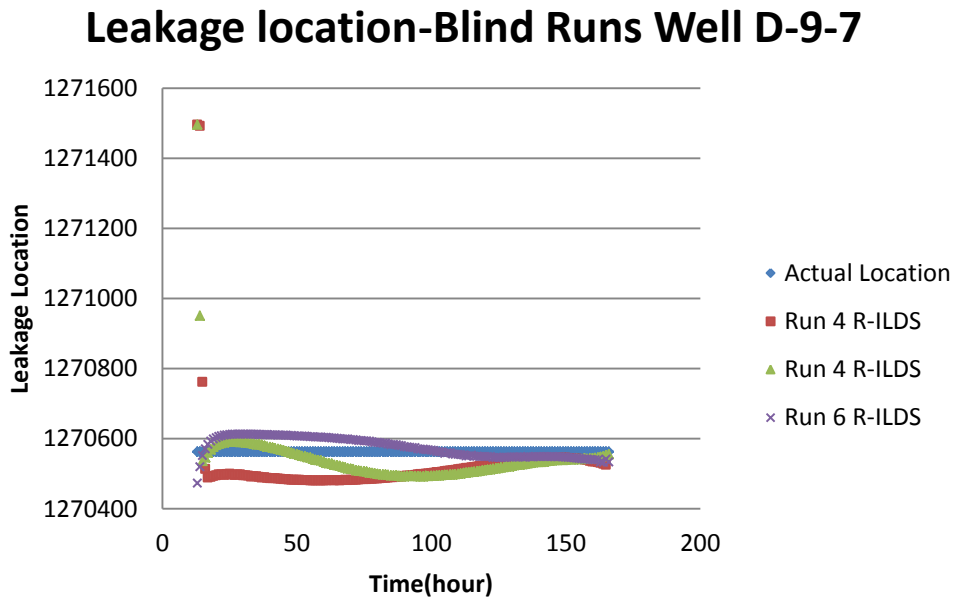

Figure 9-32: R-ILDS Leakage location prediction for well D-9-7, PDG in Injection well

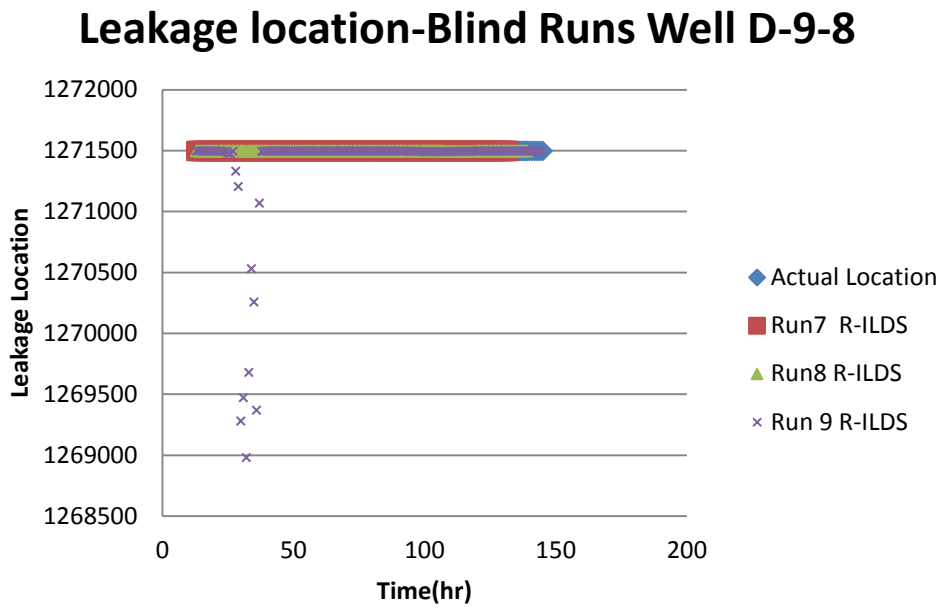

Figure 9-33: R-ILDS Leakage location prediction for well D-9-8, PDG in Injection well

Appendix 5 Cap-rock leakage results (Section6-9)

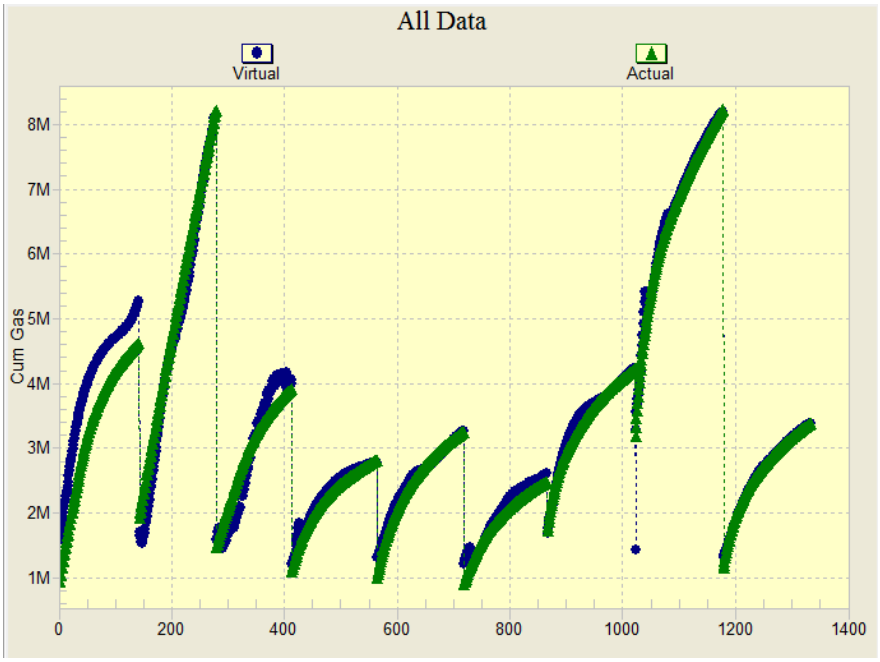

Figure 9-34: Neural network results for Cumulative leaked gas -cap-rock leakage

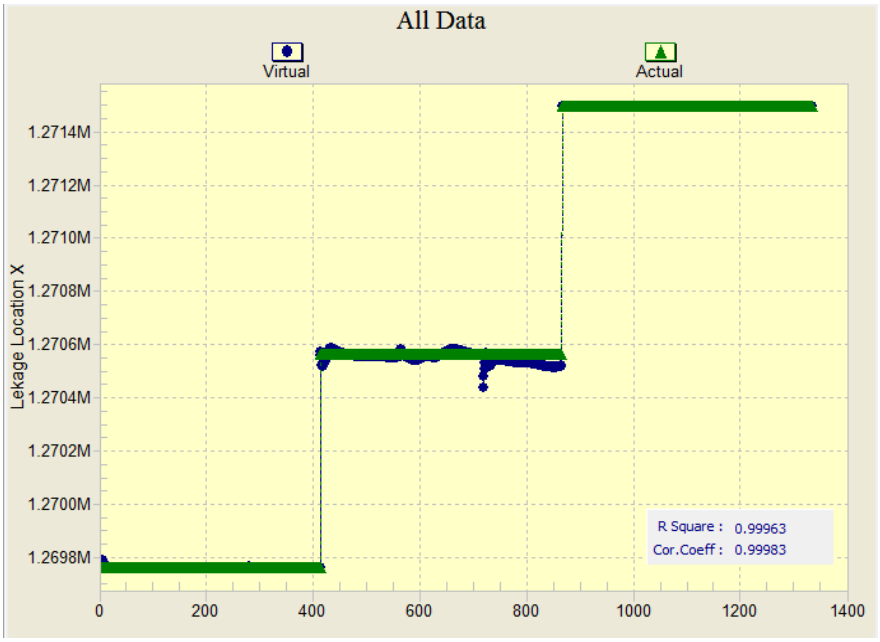

Figure 9-35: Neural network results for leakage location(X) -cap-rock leakage

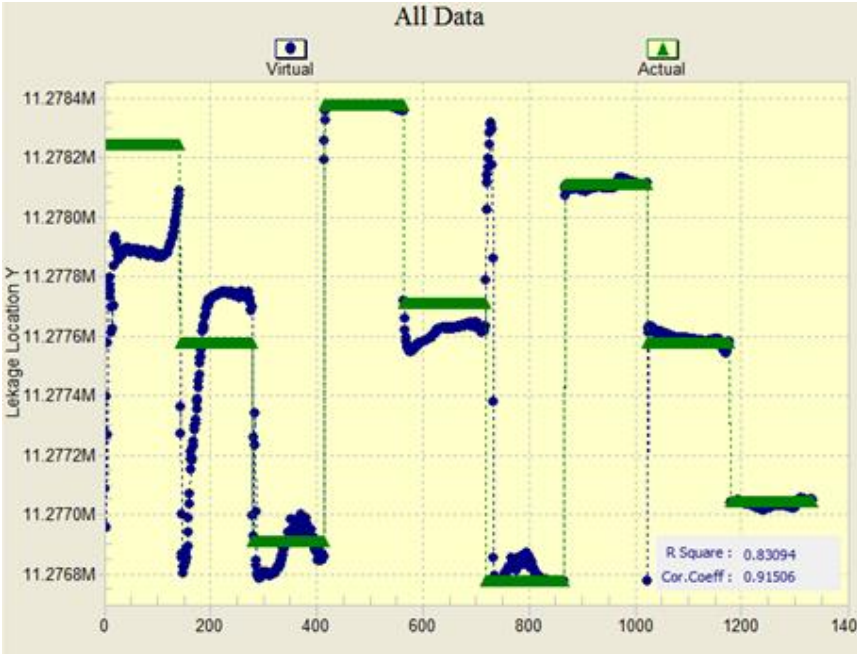

Figure 9-36: Neural network results for leakage location(Y) -cap-rock leakage

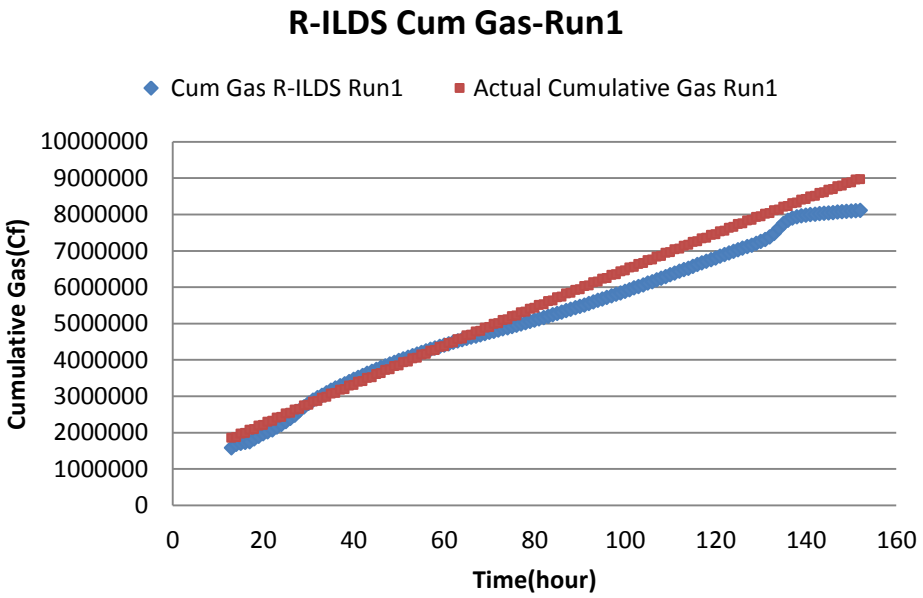

Figure 9-37: R-ILDS prediction for cumulative leaked gas, Blind Run 1(Cap-rock Leakage)

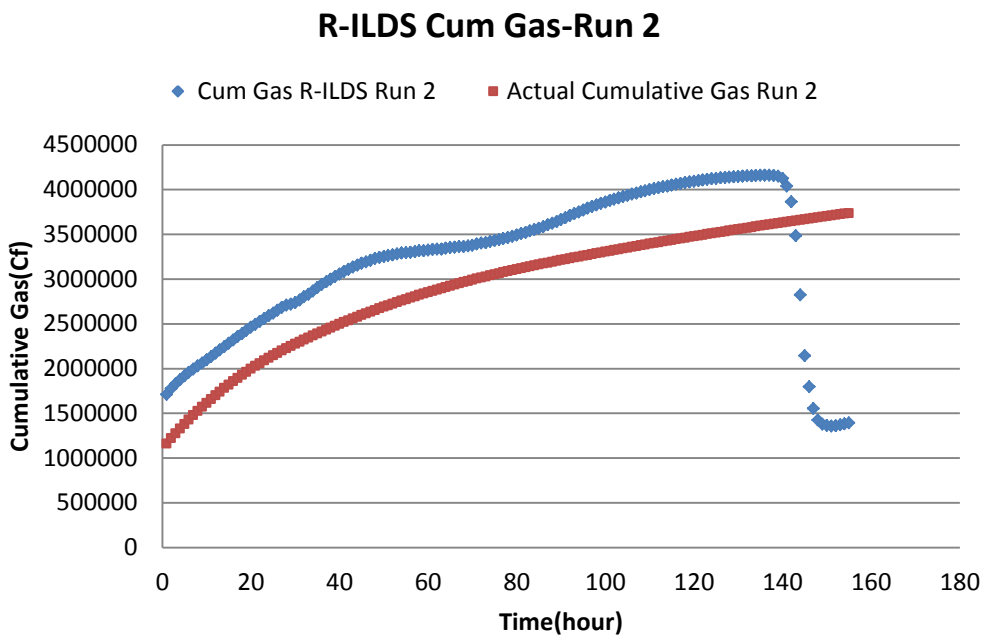

Figure 9-38: R-ILDS prediction for cumulative leaked gas, Blind Run 2(Cap-rock Leakage)

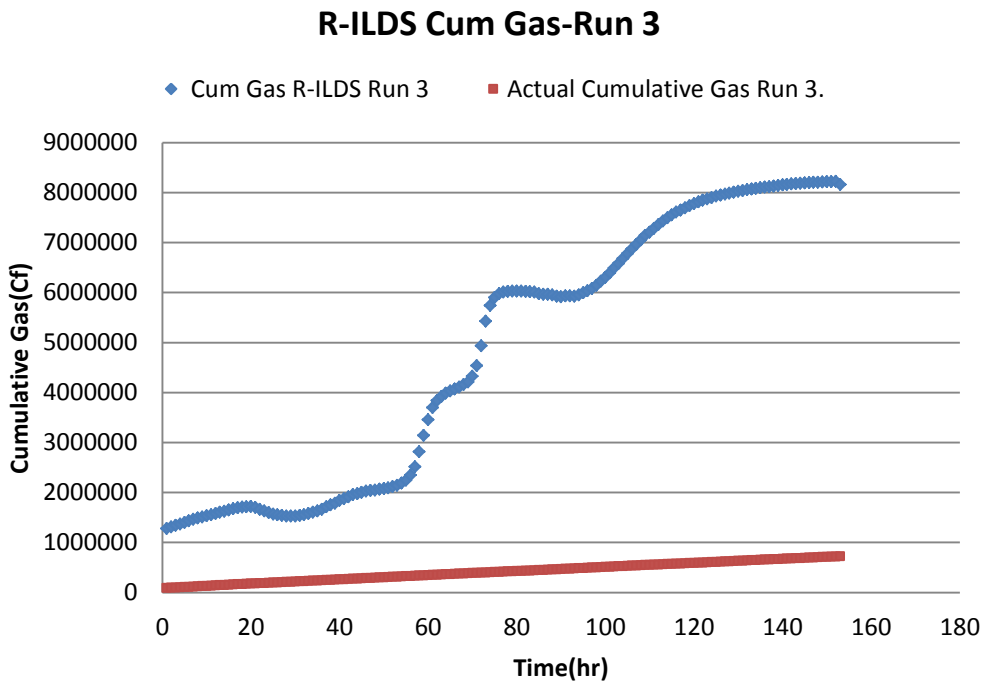

Figure 9-39: R-ILDS prediction for cumulative leaked gas, Blind Run 3 (Cap-rock Leakage)

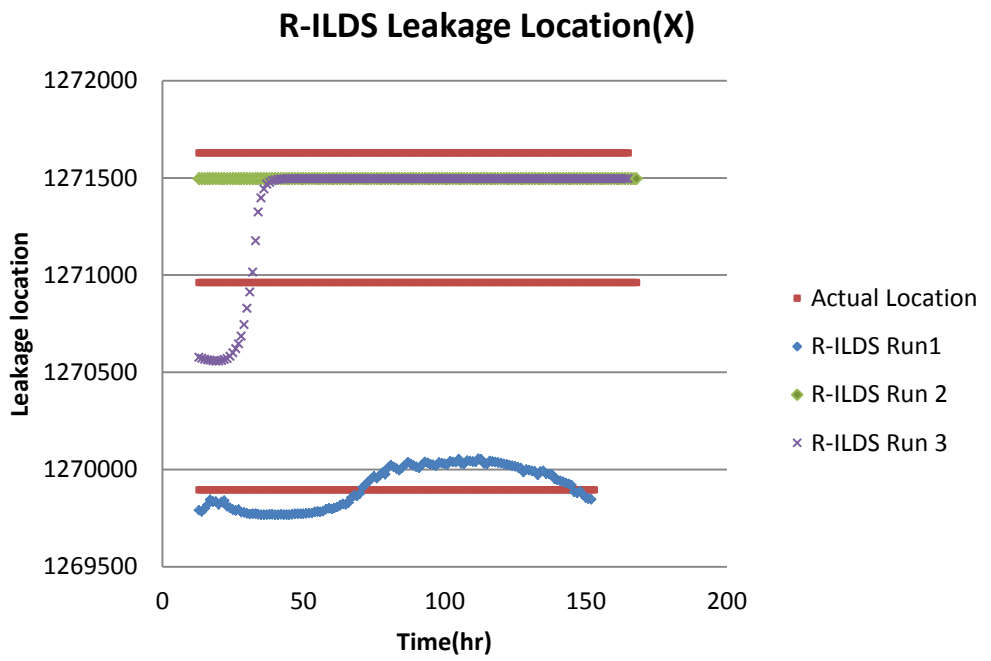

Figure 9-40: R-ILDS prediction for cumulative leaked gas, Blind Run 3 (Cap-rock Leakage)

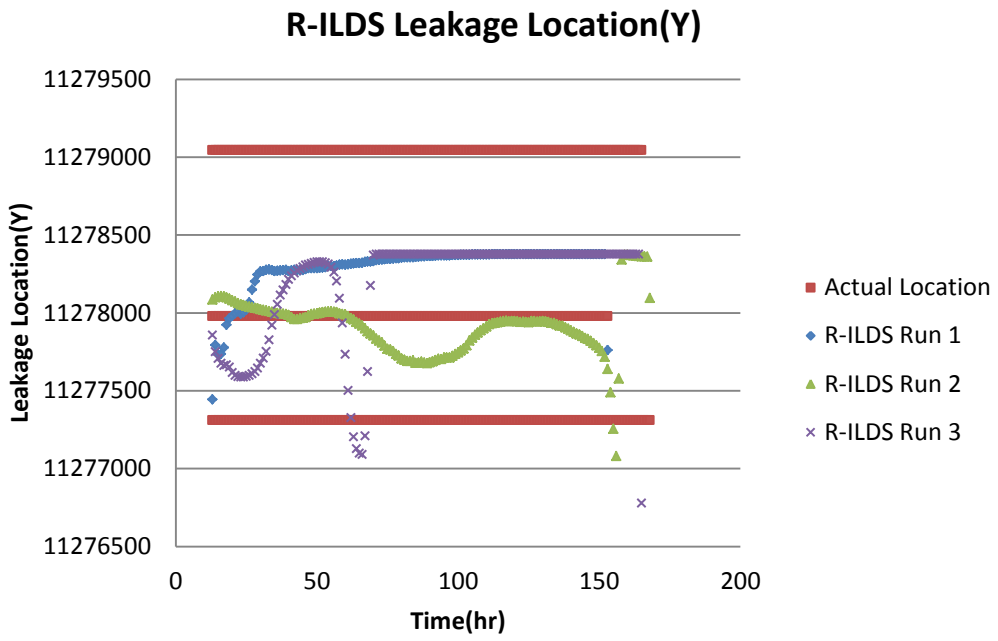

Figure 9-41: R-ILDS prediction for cumulative leaked gas, Blind Run 3 (Cap-rock Leakage)

Appendix 6 Multi-well Leakage Results (Section 6 -10)

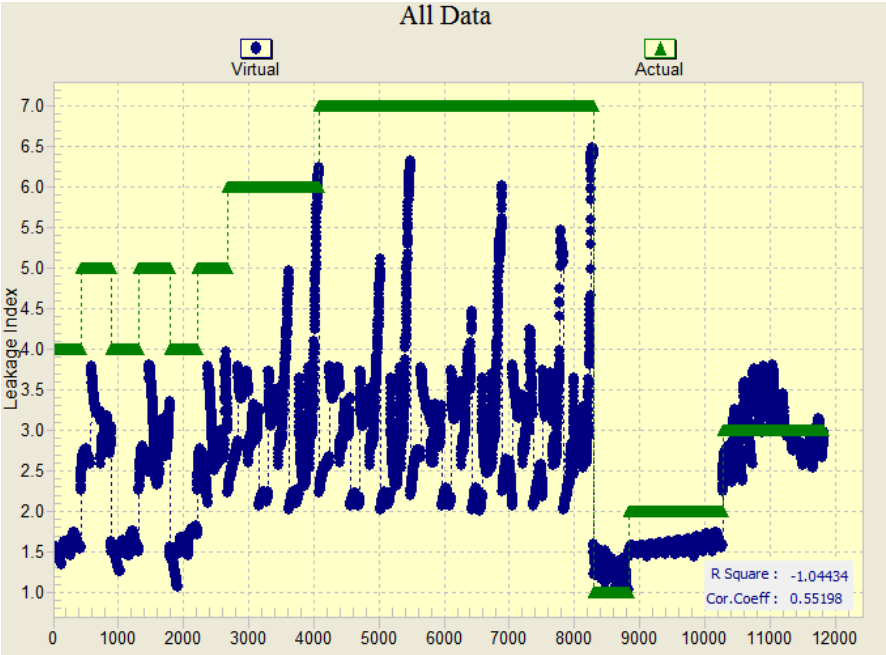

Figure 9-42: Neural network training results for Leakage Index (one, two and three-well leakage)

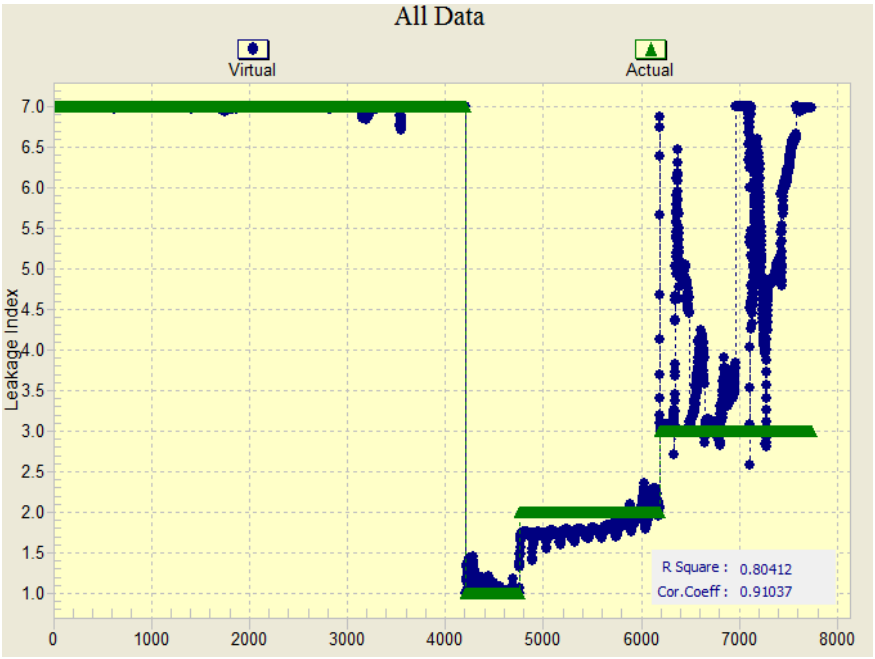

Figure 9-43: Neural network training results for Leakage Index (one and three-well leakage)